THE UNIVERSITY OF OKLAHOMA

GRADUATE COLLEGE

A Study of Directional Radiative Properties of Thermal Fire Barrier Materials

A Dissertation

SUBMITTED TO THE GRADUATE COLLEGE

in partial fulfillment of the requirements for the

degree of

Doctor of Philosophy

By

MAURICIO A. SANCHEZ
Norman, Oklahoma
2002

UMI Number: 3070640

ProQuest Information and Learning Company
300 North Zeeb Road
P.O. Box 1346
Ann Arbor, MI 48106-1346

A Study of Directional Radiative Properties of Thermal Fire Barrier Materials

A Dissertation APPROVED FOR THE
SCHOOL OF AEROSPACE AND MECHANICAL ENGINEERING

BY

Dr. William H. Sutton, Chair

Dr. Tom J. Love

Dr. Ramkumar N. Parthasarathy

Dr. Ajay Agrawal

Dr. Richard G. Mallinson

ACKNOWLEDGMENTS

I want to gratefully thank every one who contributed to this project. In particular, I express my deep gratitude to my advisor and friend Dr. William H. Sutton for his guidance, support, encouragement, and patience at every phase of this work.

I would like also to thank Dr. Tom J. Love Jr., Dr. Ramkumar N. Parthasarathy, Dr. Ajay Agrawal, and Dr. Richard Mallinson for their support and mentoring. My sincere appreciation is extended for taking the time to serve on my dissertation committee.

! am grateful to the University of Oklahoma and its resources as well as all the School of Aerospace and Mechanical Engineering staff.

A great deal of thanks shall be extended to all people who collaborated in some technical details during the research leading to this dissertation. Especially I thank Dr. Thomas Germer at NIST for his contribution and guidance in the reflectance function determination, Dr. Siu-Chun Lee at Applied Sciences Laboratory, CA for his invaluable comments in the radiation heat transfer through fibrous media, Dr. Timothy Tong at GWU, for allowing me to use his code to determine the radiative properties of fibrous insulation, Dr. Jayaraman Raja at UNCC for the metrology measurements, and Dr. Edgar A. O'Rear III and Harry Barraza at OU for allowing me to make use of the Atomic Force Microscope, and Carlos Borras, at OU, for helping me build the experimental scatterometer. Special thanks are expressed to Dr. S. R. Gollahalli for serving initially as one of my advisory committee member.

And finally, I dedicate this work to my parents Saulo and Amalfi, my twin brother Carlos, my wife Falia, and my precious daughter Mariajose. My sincere gratitude is expressed to them for their support, sacrifice, help, and encouragement.

TABLE OF CONTENTS

LIST OF TABLES

LIST OF FIGURES

Page

LIST OF SYMBOLS

A_m	Intensity of Radiation, Octant 1
B_m	Intensity of Radiation, Octant 2
C_m	Intensity of Radlation, Octant 3
D_m	Intensity of Radiation, Octant 4
E_m	Intensity of Radiation, Octant 5
F_m	Intensity of Radiation, Octant 6
G_m	Intensity of Radiation, Octant 7
H_m	Intensity of Radiation, Octant 8
G	Incident Radiation
I_m	Intensity of Radiation
I_b	Plank Function for Emission
lc	Autocorrelation Length
L	Observation Length of the Surface or Characteristic Length
m	RMS Surface Slope
$\overline{m}$	Optical Property Through Brugeman's Theory
n	Real Part, Complex Refractive Index
P	Power
R	Fresnel Intensity Reflection Coefficients
r	Fiber Radius
q	Heat Flux
(r)	Boundary Direction
V	Control Volume
$\hat{s}_i$	Directions of Quadrature
ϖ_i	Quadrature Weights
x	Cartesian coordinate
y	Cartesian coordinate
z	Cartesian coordinate
$a_{\lambda 1}$	Scattereing "Slope: Factor of Phase Function
b_λ	Back-Scattered Parameter
AL	Length in X coordinate
BL	Length in Y coordinate
CL	Length in Z coordinate
BRDF	Bi-angular Reflectance Distribution Function
F_3	Obliquity Factor, Equation 3.1
$F(x, y)$	Fiber Orientation
f	Spatial Frequency
f_v	Fractional Fiber Volume
$N[r(x, y)]$	Number of Radius between r and $r + dr$
$Q_{s\lambda}$	Scattering Efficiency

$Q_{e\lambda}$	Extinction Efficiency
$P(\Omega \rightarrow \Omega')$	Phase Function for Scattering
$S_2(\vec{f})$	Power Spectral Density (PSD)
S_m	Source Function
X_o	Sample Thickness

<u>Greek Letters</u>

α	Fiber Size Parameter
ε	Emissivity
β_λ	Volumetric Extinction Coefficient
ξ_m	Director Cosine DOM Quadrature
η_m	Director Cosine DOM Quadrature
μ_m	Director Cosine DOM Quadrature
κ_λ	Volumetric Absorption Coefficient
κ	Complex Part, Complex Refractive Index
λ	Wavelength
Φ	Azimuthal Angle
Θ	Polar Angle
η	Component Concentration
ρ	Reflectance
σ	RMS Surface Roughness
$\sigma_{s\lambda}$	Volumetric Scattering Coefficient
Λ	Optical Property Through Brugeman's Theory
ψ	Differencing Parameter
Ω	Directional Angle - Solid Angle
τ	Optical Thickness

<u>Superscripts</u>

$'$	Incoming or Incident
m	Quadrature Direction
d	Diffuse
s	Specular
+	Positive Direction
-	Negative Direction
net	Net Quantity

<u>Subscripts</u>

i	Incident
b	Backward Face
f	Forward Face

m	Quadrature Direction
n	North Face
s	South Face
e	East Face
w	West Face
o	Optical
p	Middle Point
s	Scattered
λ	Wavelength dependant

ABSTRACT

The objective of this work is to determine radiative properties of a fire barrier composed of metallic foils and a ceramic fiber blanket compatible with a commonly used model, which can account for multidimensional and angular effects. The reflectance function for the foils, ceramic fiber, and combinations among the materials must be determined in order to assess these properties. Several methods were evaluated to account for the reflectance function determination. A Kirchhoff-based relationship and a Raleigh-Rice Perturbation theory were two analytical methods that showed to be inconclusive at predicting reflectance function in rough surfaces. An experimental scatterometer based on the angular discretization of the discrete-ordinates or S_N method was built to account for the directional property of reflectance of the metallic materials and their interaction with the fiber insulation. The reflectance distribution function for the metallic surfaces showed to be good specular reflectors in the spectral/gray model.

The radiative properties of the fibrous material must be established to compile an accurate model for the scattering properties and spectral/gray properties of the insulation before solving the radiative transfer equation (RTE). This fiber insulation can be categorized as one material composed of fibers randomly oriented in space, with a near isotropic probability scattering distribution in both the wavelength range 1-12 μm and gray scale. Reflectance function measurements of the combination metallic surface-insulation showed that optically thin samples behave as optically thick upon positioning a metallic surface as a backing. Moreover, the influence in the type of backing is stronger in optically thin samples than in optically thick. Values in the measured reflectance function were larger with a reflective backing rather than a non-reflective one.

The solution of the RTE is given in terms of the discrete ordinate method taking into consideration the interactions between the foil and the fiber, assuming a linear-anisotropic scattering function for the scattering characteristics of the fiber, and including the directional properties of the foils as part of the boundary condition limits. The discretization of the boundary

is given in terms of a matrix form that accounts for the 144 possible incident-reflective directions using the S_4 quadrature. Prediction of the reflectance function in fiber insulation while using measured reflectance data of the type of backing utilized provided good qualitative agreement. The use of the linear anisotropic model does not account for the two-dimensional scattering effects of the fibers modeled as infinite cylinders, especially in the near grazing angles since the scattering directions of a single fiber and the slab medium are different except for angles of incidence near or equal at normal incidence. The equal weight quadrature utilized in the theoretical analysis tends to distribute the scattered energy evenly around the solid angle subtended by the hemisphere from its center, which is important in radiative heat transfer predictions when the inherent directional biasing of the quadrature has an adverse effect in the spatial orientation of the geometry. However, using the full directional reflectance data helps to diminish this directional biasing (even intensity hemispherical distribution), which in turn, will lead to better prediction of properties or attain accurate radiative transfer calculations.

CHAPTER 1

PROBLEM MOTIVATION

Safety and fire codes are written to provide occupants with a short time window to escape from a building before people are trapped, or prevail over deadly fumes from the burning materials. For this reason, fire barriers are utilized and designed explicitly to protect components, equipment, and most importantly the lives of the occupants from getting hot enough or exposed to flame and smoke. These barriers must protect the occupants for a period of time long enough to allow them to escape or shutdown important equipment safely.

Fire barriers are often manufactured by layering alternating blankets of ceramic fiber insulation with bounding thin metallic foil sheets. There are several factors that determine the effectiveness of these fire barriers. The barrier must meet the specifications given by either the ASTM standard E-119 or by fire marshal approval. This effectiveness is determined by the requirement of maintaining structural integrity by allowing some heat release while not permitting the fire flame to pass through. In some applications, fire barriers are large and form structures and partial enclosures. Virtually no data is available on the thermal interaction of 2-D and 3-D corners and splicing the layers for large barriers. It is expected that spatial and angular effects might either degrade performance or even cause "hot spots" in a barrier wall. Therefore, a better understanding of the radiative material properties motivates the current study.

Using the concepts of radiation heat transfer directional properties, the extended objective of this study is to develop thermal properties and methodologies for analyzing these type of fire barriers, which are often utilized in the expansion gaps or joints in walls or floors made of concrete. In its simplest form, these barriers are composed of two metallic foil surfaces that bound a blanket insulating material.

To account for the barrier effectiveness, analysis of the heat transfer modes is required. Due to the high temperatures involved in a fire (even at room temperatures in the opposing regions away from the fire), radiation heat transfer plays the most important role in the design of the barrier. Typically almost 60% of the heat transfer is accounted by radiation in thermal barriers and insulation materials; the rest is due to conduction and convection. Since thermal radiation heat transfer is such an influential factor, the radiative properties of both materials (metal and insulation) must be determined. A surface reflectance function must also be taken into consideration in the heat transfer analysis. These properties must be determined by experimental means, although some semi-analytical correlations exist based on experiments. Analytically, spectral extinction, absorption, and scattering efficiencies for fibrous insulations are calculated. These values must account for the orientation of the fibers, the type of material (complex refractive index), and the volumetric fraction related to thickness.

One task to be accomplished in the current research is to introduce a model to correctly determine both the radiative properties and the scattering model of the material. Depending upon the model used, scattering of fibrous materials can be simplified to include the effects of fiber orientation, angular symmetry and spectral characteristics. Analysis of modes of heat transfer interaction must include effects near the surface and the interactions between the metal and the fibrous material.

The metallic material of the barrier is a radiative boundary condition of the radiation problem. In the real world, many surfaces encountered in engineering practice possess a vast quantity of irregularities so that application of fundamental theories is neither practical to use nor accurate to obtain a complete representation of the reflectance distribution function. This is particularly true in the 1-4 μm wavelength range that is important in thermal radiation.

The significance of reliable thermo-physical property data for industrial research applications requires more accurate methods of determining them. In radiation heat transfer, the available properties of surfaces are scarce since they are strongly dependent upon several factors, such us wavelength, temperature, geometry position, surface finish, etc.

The accuracy of any prediction in combined modes of heat transfer is strongly dependent on the knowledge of the radiative properties of the matter involved in the energy exchange [1]. Despite the fact that considerable effort has been made in previous years to improve the theory behind thermal radiative property predictions, results are not valid for an entire range of surface and boundary conditions. In the case of surface conditions, complications arise from the surface roughness to contamination, whereas, in the case of boundary conditions, there are little data available that takes into account the interaction between surface properties with their surroundings. It is for the above reasons that the only reliable method of assessing thermal radiation properties and their interactions is thorough metrological (experimental determination) testing. It is also known that the data available for metallic foil materials is relatively scarce or not always reliable. The data to be investigated can be based on a spectral or non-spectral basis. If no accurate data is available, an experimental model can be constructed to determine the bi-directional properties (reflectance) for the thermal radiation wavelength characteristics.

Finally, a numerical evaluation of the barrier can be accomplished by utilizing the spectral/gray and directional/modeled data of each one of the components. This is done by coupling of the discrete ordinate method in radiation to the experimental data as a validation of the properties for fire barrier materials.

CHAPTER 2

PROBLEM DEVELOPMENT

2.1 Definitions

Thermal radiative properties are a measure of the tendency of a given surface or participating medium to reflect, or scatter, absorb, and emit radiation [1]. Knowing the actual qualitative and quantitative properties of the material, one can solve the related radiation problem. Exact definitions of the radiative properties can be found in the literature [1-5], however, a brief account will be given of the directional radiative properties that play an important role in the solution of radiation transfer problems that are applicable to a thermal fire barrier and its relationship to optical or energy scattering.

The most important radiative property, which describes the scattering of radiation from a surface, is known as the Bi-directional Reflectance Distribution Function, **BRDF**. This function is required to completely describe the radiative characteristics of any surface since all other property functions are related to it, i.e., the manner that a surface reflects radiation is in relation to the way that the same surface emits energy [1].

Assuming a beam of electromagnetic radiation of uniform cross section, an isotropic reflector (Figure 2.1), in which the scatter comes from the surface and not the bulk [6], then the reflectance function can be defined as the surface radiance normalized by the incident surface irradiance [4].

$$BRDF = \rho(\Theta_i, \Phi_i; \Theta_s, \Phi_s) = \frac{\partial P_s}{\partial \Omega} \frac{1}{P_i \cos(\Theta_s)} \tag{2.1}$$

where P_s is the scattered power flux per unit solid angle, P_i is the incident power, Θ_s and Θ_i are the scattering and incident polar angles, Φ_s and Φ_i are the scattering and incident azimuthal angles, and Ω is the solid angle defined as the projection of the surface onto a plane normal to the direction vector divided by the distance squared, as illustrated in Figure 2.1. It is noted that

BRDF has units of inverse steradians, and depending on the relative size of P_s and Ω_s, it can take on values that range from very large or very small [6].

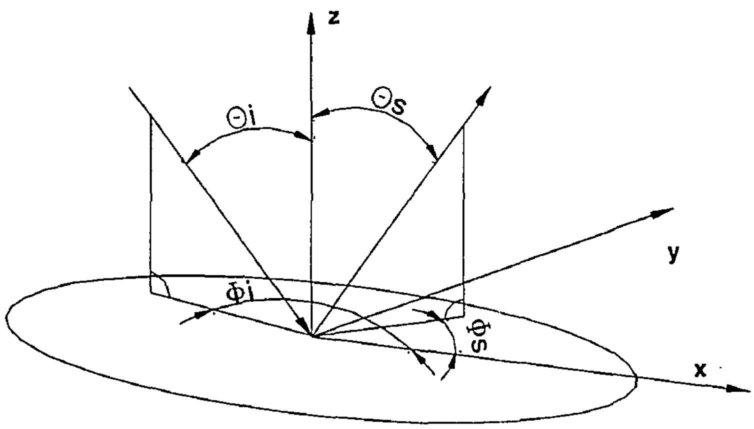

Figure 2.1. Surface Reflector Coordinate System

There are numerous ways in which one can obtain the reflectance function but all of them are based on the surface finish of the reflector. For instance, in geometric optics, a ray traces the energy incident on the rough surface as it leaves [7], assuming a Fresnel reflection from a locally optically smooth surface. BRDF is usually predicted for smooth surfaces by surface profile measurements plus information about the statistical symmetry of the surface reflector [8]. However, the best way to attain the function is by experimentation, since this provides the correct information from a surface reflector.

The necessity of reliable data on scattering from the solid materials is growing continually. Frequently, existing data on directional properties (especially for the materials that composed this fire barrier) cannot be used accurately unless some simplifying assumptions are made. Therefore, in many cases there is a need to correct and enhance these values, which allows proper use for existing numerical models. Again, this can be done is by the measurement of that given property.

2.2 Literature Review

Numerous studies and experiments have been developed in the area of optical or light scattering from rough and smooth surfaces [9-42]. In this part of the chapter some of the current state of knowledge on this subject will be reviewed in a chronological sense. The sections that follow will describe the methodology in the reflectance function determination of surface reflectors. Merits and shortcomings of the different models are discussed. Finally, a short review of radiative properties and transfer models in fibrous insulations will be given [43-52] since this material also composes a part of the fire barrier.

2.2.1 Radiation Characteristics of Surfaces

Many of the scattering and reflecting characteristics of surfaces have been based on relating a profile measurement with the theory of electromagnetic waves reflection. One of the first pioneers in this field was Davies [9]. Davies' work, which is based in connection to the scattering of radar waves from rough water surfaces, was fully enhanced by H.E. Bennet and J.O. Porteus [10,13]. They measured the scattered power from a surface and then normalized it to the reflected specular power; the ratio is defined as the total integrated scatter (TIS) [6]. Equation 2.2 shows the fractional scatter power for a smooth, conducting, and Gaussian height-distribution function surface.

$$TIS = \left(\frac{4\pi\sigma\cos(\Theta_i)}{\lambda} \right)^2 \tag{2.2}$$

where, λ is the wavelength of the incident power source and σ is the RMS surface roughness. Although the TIS development can be used as a source to measure the RMS roughness of a surface as a true measure of the area (2D), it fails to describe the true scattering properties of the reflector. For instance, it can only be used for angles close to normal incidence. It also assumes that both the specular angle is the same as the incident angle and a surface with a Gaussian-height distribution function. Finally, TIS neither accounts for polarization effects, nor it can be used for comparison with other profiling instruments.

Beckmann and Spizzinno [13] gave a more complete approach in which they made use of the Kirchhoff- based relationship to derive the function for isotropic surfaces with a normal Gaussian-height distribution. After Bennet et al. [10,11], Beckmann derived an expression called the auto-covariance length or autocorrelation function $lc = \sigma\sqrt{2}/m$. This function included the RMS slope *m* to give a more complete detail of the surface profile.

By 1965 similar works by Birkebak et al. [14], Torrance et al. [15], and Dunn [16] demonstrated the use of the work done by Bennet and Porteus [10] by conducting a series of experiments (using gonioreflectometers) and analysis (using electromagnetic theory correlations) in which the reflectance function was determined. Their numerical results agreed well with the experimental values for the different surface reflectors.

Although an off-specular shifting phenomenon has been evident in published reflectance data, but not fully reported due to the way the data was plotted, Torrance and Sparrow [17] and later Francis [18] provided a glimpse of this particular phenomenon in the experiments conducted using rough metallic and non-metallic surfaces. This phenomenon appears when the size of surface features is greater than the incident wavelength $(\sigma/\lambda) > 1$. In the same work, Torrance et al. [15] created a model using geometric optics to describe BRDF for very rough surfaces.

Houchens and Hering [17] compared the Davies [9] and Beckman [13] models. Both of these models work by separating the specular energy component and the diffuse component of the reflectance through the use of the optical roughness (σ/λ) and autocorrelation roughness parameters (lc/λ). It was demonstrated that the Beckman model was more accurate than the Davies' model, however both of these models fail to get an exact value of the reflectance since many different values of roughness and autocorrelation lengths can result in the same BRDF [6].

By the late 1960's a Monte Carlo solution for the determination of the BRDF was successfully performed by Look [20]. Although his results agree well with prior published data, the use of an extra parameter to accommodate for surface profile in his Monte Carlo approach can also result in different values for the reflectance.

It is interesting to note that the above models have used at least two profile measures (RMS slope and RMS surface roughness) to come up with the BRDF for roughened reflectors. Different models have also arisen for surfaces in the limit of slightly rough surfaces, and finally perfectly smooth surfaces while using profilometry. Except for the case of a perfectly smooth surface (no surface profile needed) the scattering is all in the specular direction and the reflectance function can be found using Fresnel theory.

While encountering a slightly rough surface, the reflectance function consists of a reduced specular component and a diffuse component, which is principally in off-specular directions. This function can still be found using the total integrated scatter (TIS) formulation but it now includes the diminished specular scatter and the diffuse scatter. The sum of the specular and diffuse scatter is less than one for a slightly rough surface made of a perfectly conducting material and for a non-perfectly-conducting material respectively. For the non-perfectly-conducting material case there are non-vanishing effects of the surface roughness [21].

If the surface reflector is in the limit of a slightly rough surface $[4\pi\sigma/\lambda]^2 << 1$, then both the specular and diffuse surface scatter and the total-integrated scatter can be expressed in terms of the two-dimensional power spectral density (PSD) of the surface roughness. The PSD can be found through the use of Fourier analysis and random signal theory from profile measurements. Equation 2.3 shows a particular equation obtained through the use of the Raleigh-rice perturbation theory [6,21], which describes the reflectance function (BRDF) for reflectors in slightly rough surface or smooth surfaces.

$$\rho(\Theta_i,\Phi_i;\Theta_s,\Phi_s)=\frac{16\pi^2}{\lambda^4}\cos(\Theta_i)\cos(\Theta_s)\cos^2(\Phi_s)\sqrt{R(\Theta_i)R(\Theta_s)}S_2(\vec{f}) \qquad (2.3)$$

where the angles $\Theta's$ and $\Phi's$ follow the description of figure 2.1, the R's are the Fresnel intensity reflection coefficients, the factor S_2 is the PSD which contains information about the surface roughness and f represents frequency of the spectrum.

There are important issues involving the smooth-perturbation results. For instance, many surfaces are fractal-like in that their PSD increases rather than rounds off at low spatial frequencies, thus the evaluation of the RMS roughness from real surface measurements is uncertain since real surface measurements gives information only down to the non-vanishing frequency (1/L) on the PSD, where L is the observation length on the surface [21].

Extended published literature about reflectance function prediction for smooth surfaces, which posses some micro roughness, has been done since the late 1970's [22-30]. John Stover [6] provided with an excellent treatise about optical scattering and BRDF predictions through the use of the power spectral density.

When the surface is rougher than permitted by the smooth-surface requirement (rough surfaces), meaning that the surface features are larger than the radiation wavelength, some different approaches can be taken for the reflectance function determination. As pointed out previously, geometric optics is a numerical method that has been used with success to determine biangular reflectance in very rough surfaces [7, 31-32]. However, for surfaces that are less than very rough with concentrated anisotropy in their profile, a common method to predict reflectance is by conducting light scattering experiments. Experimentation can capture the reflectance function of any surface; the data extracted from it can be used not only for surface profilometry and surface defect detection [27, 30] but also as a tool for computer graphics and image-based processes [33-35]. For instance, the main point of computer graphics and image-based measurements is to analyze the photographic data pixel by pixel of a 3D object around the hemisphere and converting it into BRDF data by normalizing it with the irradiance of the source.

As a conclusion, it can be stated that a spectral reflectance function (since it is also dependant of the wavelength of the radiation) can be predicted in several ways. From surface profile measurements (optical or mechanical), plus information about the symmetry of the surface adding a reflection theory (Kirchhoff, Perturbation, geometric optics, etc.) has been the most common method to obtain it, knowing that the function from one wavelength to another is model dependent. But direct reflectance measurements are more sensitive to the effects of surface defects than any other profile-based methods [25].

2.2.2 Radiative Heat Transfer in Fibrous Materials

The detailed study of radiative heat transfer in fibrous materials began around 1955. Despite the fact that many of the researches were concerned with only conduction through the gas and solid phases of high-porosity materials, all pointed out that radiation plays an important role in the determination of heat transfer rate even at low temperatures.

Some early studies [43] treated the radiation heat transfer by developing an analytical solution that includes experimental data and the "N" factor radiation to conduction. Tong [44], and Tong and Tien [45,46], developed a good approximation for the effects on radiation and conduction heat transfer in fibrous materials by including a radiation thermal conductivity as a diffusion equation model. Several authors [44-46] developed approximate solutions of the equation of transfer based on the Two-Flux Method including the scattering function and a linear anisotropic scattering function (using a back scattered fraction approximation) as an approximation for the scattering behavior of fibers randomly oriented by taking a scattering model as if the fibers were spheres. The above authors used the exact solution for the radiative properties of the material, which are based on the solution of the Maxwell's equations considering the material as an infinite cylinder. None of the above work has considered a reflectance function or Fresnel type of boundary conditions.

Lee [47-52], considering the two dimensional characteristics of a fiber and the orientation of the fiber, developed the phase function for scattering, and the integration of the radiative properties using the Maxwell's equations for electromagnetic scattering in infinite cylinders for any particular orientation. The phase function for scattering exhibits a strong peak in the direction of incident radiation [47], which is an indication of highly anisotropic material. By the same token, a new model for independent and dependent radiation heat transfer in fibrous material was developed which is more accurate than for previous investigators.

CHAPTER 3

SCOPE OF THE PROBLEM

As previously noted, determination of radiative properties of materials and radiation heat transfer analysis is interrelated. To establish an accurate model for a fire barrier, accurate determination of the reflectance function for all components of the barrier and accurate prediction of the fiber insulation radiation properties must be accomplished before attempting to solve the radiation transfer equation (RTE). An objective of this research is integrating these aspects and developing a numerical procedure to obtain an accurate estimation of the effectiveness of a fire barrier that can be used in any application.

3.1 Fire Barrier

The 1-D version of the layered fire barrier analyzed in this research has been designed, tested [53] and used [54] in previous occasions with good success. For fire protection, a ceramic fiber is used since it can withstand the high temperatures involved in a fire. The range of advantages attained by the usage of ceramic blankets is great since they are lightweight, thermally and structurally efficient, chemically inert to reactants, and resistant to thermal shock with low heat storage [53]. As for most insulating materials, ceramic fiber insulation actually blocks heat flow by attenuating thermal radiation and minimizing direct convection mixing.

Layers of metallic foil are often considered alone as thermal radiative shielding by reflecting heat. The foil also serves to minimize direct hot gas flow from the fireside of the layer(s). For the barrier, thin layers of foil are placed on the outside of the fire blanket. For a multi-layer fire barrier, the foils are used between layers of insulation and the outside boundaries. According to the design of the barrier, the foil layers provide both thermal radiation shielding and structural support [54].

As noted before, the main purpose of the foil layer is to reflect thermal radiation. To accomplish that, a highly reflective material would work best. Aluminum foil is a good candidate since it is highly reflective, but it cannot withstand the high fireside temperatures. Stainless steel foil can also be used in conjunction with the aluminum since this material can be positioned at the outer layers of the multi-layer fire barrier to withstand the direct temperatures involved in the fire. The foils materials chosen for this study are:

- Heavy Gauge Aluminum Foil, type 303-H14, 0.016" thick, corrosion resistant
- Stainless Steel Foil, type 321, 0.004" thick, corrosion resistant

Appendix A provides more details and characteristics of these foils.

Following the same design evaluated by Caplinger et al. [53], the chosen insulation material was a ceramic fiber blanket called Durablanket® S. Durablanket® ceramic fiber products are comprised of high strength, needled insulating blankets that are made from spun Fiberfrax® ceramic fibers. Some of the selected thermal properties of this material are listed in table 3.1. More details may be found in appendix A.

Table 3.1 Durablanket® S Properties

Continuous Use Temperature limit	1260°C
Density	128 Kg/m^3
Fiber Diameter	2.5 – 3.5 μm (mean)
Composition	53% - 57% SiO_2 43% - 47 % Al_2O_3
Specific Gravity	2.73 g/cm^3

3.2 Radiative Properties

To account for the barrier effectiveness, a study of the heat transfer modes must be accomplished. Due to the high temperatures involved in a fire (even at room temperatures initially and on the opposing air space), radiation heat transfer plays the most important role in the design of the barrier. Almost 60% of heat transfer is accounted for radiation related to the foil barriers and insulation materials; the rest is due to conduction and convection. Since this mode of heat transfer is such an influential factor, the radiative properties of both materials (metal and insulation) must be determined. Spectral (here, we will consider 2 thermal/wavelength ranges) Bidirectional reflectance must be taken into consideration in the heat transfer analysis. These properties can be determined by analytical or experimental means. Spectral/Gray extinction, absorption, and scattering efficiencies for fibrous insulations must be calculated. These values must account for the orientation of the fibers, the type of material (complex refractive index), and the volumetric fraction related to thickness. The wavelength range for property determination is chosen from 0.5 μm to 12 μm since almost 91% and 95% of the blackbody radiation energy is emitted at the average fire temperatures of 1000 K and 1600 K respectively [48].

3.2.1 Metallic Foil

The metallic material of the barrier would provide the radiative boundary condition of the radiation problem. Bi-directional properties (including surface characteristics) for stainless steel and or aluminum foil are to be determined either by literature search and/or experimentation. It is known that the data available for these types of materials is scarce or it is specialized to a specific solution method. The data to be investigated must be based on a spectral or non-spectral basis. If no accurate data is available, an experimental model must be constructed to determine the reflectance function with respect in some part to the thermal radiation wavelength characteristics.

Based upon the literature review, two attempts were evaluated in order to determine the reflectance function $\rho(\theta_i, \Phi_i; \theta_s, \Phi_s)$ for the metallic materials; Kirchhoff- based relationships using the Beckmann and Spizzinno models and the formulation for the slightly rough surface models (since the criterion for smoothness is often quoted as $(\sigma < \lambda/20)$, where λ is the wavelength, the metallic foils can be considered smooth in the infrared region [56]).

In order to make use of any of the above models, surfaces profilometry must be done in order to know the characteristics of the reflector. Three surface parameters must be considered for the above models. The RMS surface roughness σ, the RMS surfaces slope m for the first model, and the power spectral density $S_2(\bar{f})$ for the second one. The PSD can be considered as a surface roughness power per unit spatial frequency. Moreover, the RMS surface roughness is the integral of the PSD and the RMS slope is given by the square root of the integral of the PSD [6]. A more detail definitions of surface parameters can be defined, calculated from profile data [6] and in standardization references [57].

Figure 3.1 and 3.2 shows the surface profiles of one of the four aluminum and stainless steel samples using data collected by a Taylor Hubson® surface profilometer located at the Surface Metrology Lab at the Center for Precision Metrology in the Department of Mechanical Engineering and Engineering Science, University of North Carolina – Charlotte [58]. Table 3.2 lists the average surface profile data of the samples.

Table 3.2 Average Surface Profile Data of Metallic Foils

Surface Parameter	Aluminum	SS 321
σ [μm]	0.4484 ± 0.0099	0.2140 ± 0.003
RMS Slope Rdq [°]	4.5120 ± 0.1150	6.2013 ± 0.090

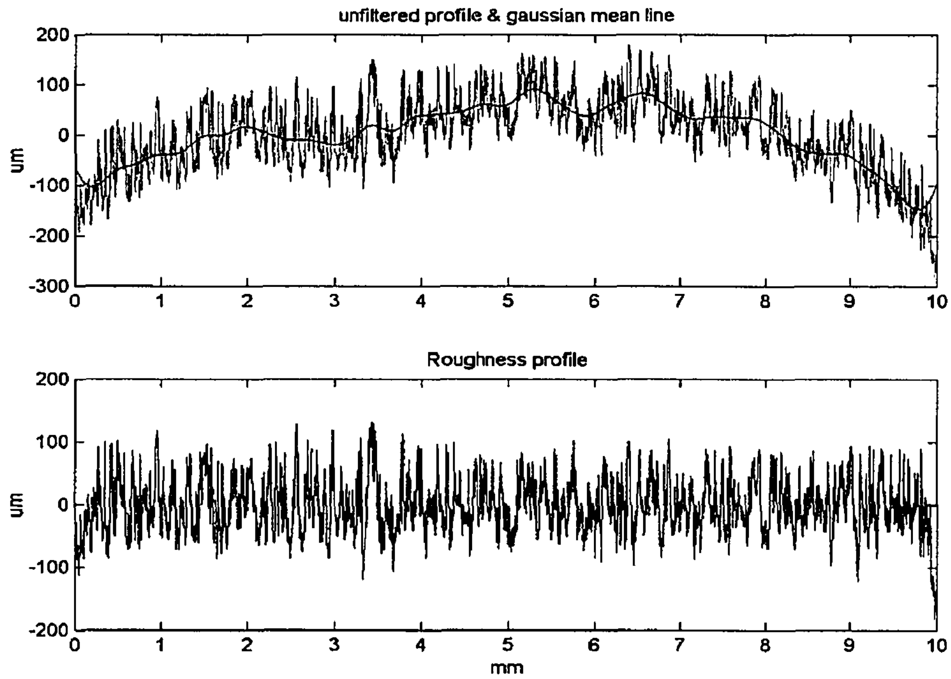

Figure 3.1 Unfiltered Roughness Profile and Gaussian Mean Line, Aluminum Foil. [Spacing between points 0.25 μm, cutoff 0.8] (Courtesy of UNCC Dimensional Metrology Laboratory)

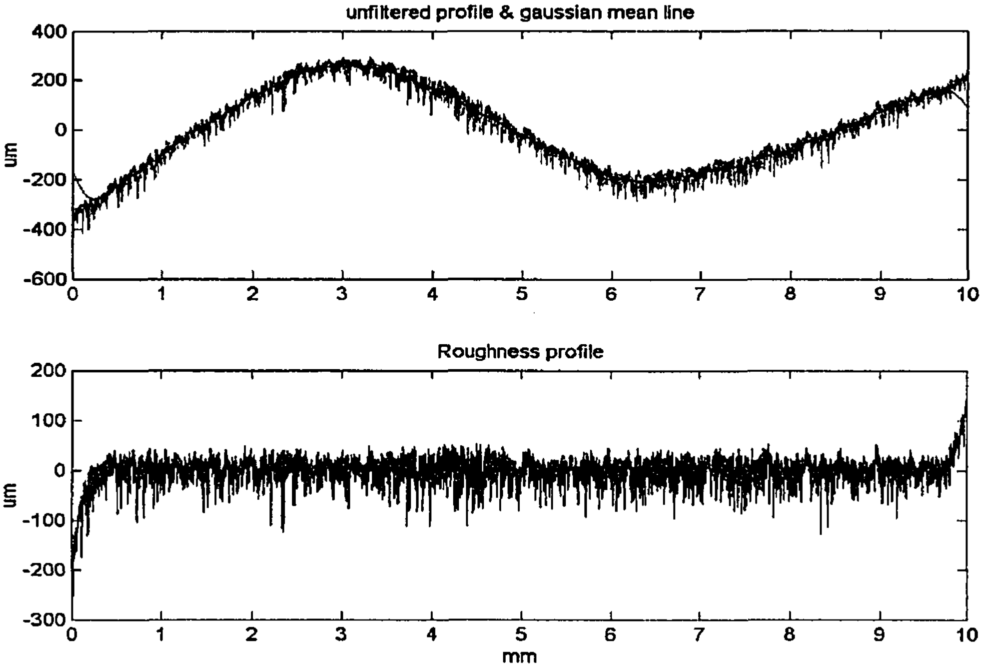

Figure 3.2 Unfiltered Roughness Profile and Gaussian Mean Line, SS 321 Foil [Spacing between points 0.25 μm, cutoff 0.8] (Courtesy of UNCC Dimensional Metrology Laboratory)

As seen in the above figures and table, the aluminum has almost twice the roughness of the stainless steel. It is to be expected that the stainless foil would have a much more specular scattering behavior than the aluminum material for certain wavelength ranges.

The Kirchhoff- based relationships using the Beckmann and Spizzinno model [6,19] state that the surface must be an isotropic random rough reflector with a Gaussian height distribution and autocorrelation function lc. This formulation results in six cases that cover smooth, general, and rough surface calculations for both one and two dimensional reflectors (the scattering surface is considered two dimensional such that spatial frequencies, which propagate in two directions, are necessary to represent surface and scatter pattern) [6]. Beckmann's 2D rough surface bidirectional reflectance distribution function can be expressed as shown in Equation 3.1

$$\rho(\Theta_i,\Phi_i;\Theta_s,\Phi_s) = \pi R(\Theta_i) F_3^2 (L/\lambda) \exp-(\pi f L)^2 \tag{3.1}$$

with,

$$F_3 = \frac{1+\cos(\Theta_i)\cos(\Theta_s) - \sin(\Theta_i)\sin(\Phi_s)}{\cos(\theta_i)\left[\cos(\Theta_i)+\cos(\Theta_s)\right]}$$

$$f = \frac{1}{\lambda}\left[\left(\sin(\Theta_i)\cos(\Phi_s) - \sin(\Theta_i)\right)^2 + \left(\sin(\Theta_s)\sin(\Phi_s)\right)^2\right]^{1/4}$$

$$L = \frac{lc\lambda}{2\pi\sigma\left[\cos(\Theta_i)+\cos(\Theta_s)\right]}$$

where F_3 is an obliquity factor, f is the spatial frequency and L is a characteristic length.

Since the terms σ and lc appear in Equation 3.1 as a ratio $\sqrt{2}\sigma / lc$ they become a single variable called RMS slope.

In order to validate Equation 3.1 with the metallic surfaces composing the fire barrier, experimental measurements of the BRDF were performed using a goniometric optical scatter instrument at the Bidirectional Optical Scattering Facility at the National Institute of Standards and Technology (NIST), Gaithersburg, MD [56].

In-plane measurements at 15, 40, and 65 degrees and out-of-plane measurements when incident and scattering angles equal to 65 degrees were carried out. All of the data represent the unpolarized reflectance at 0.633 μm. All measurements were performed for six different equally spaced sample rotations (sum of Θ_s and Θ_i from 0 to 150 degrees) [56].

Figures 3.3 to 3.5 show the reflectance function found by Equation 3.1 in comparison to the experimental data. Figures 3.6 to 3.7 show the experimental reflectance for stainless steel and aluminum samples.

Some remarks about the measurements [56]:

- It was difficult to ensure sample flatness due to thin samples. Data very close to the specular direction may be subject to large errors due to the resultant angular uncertainty.
- There are certain directions for which material blocks the incident or scattered beam.

- No uncertainties were provided for these NIST data. Systematic (instrument) uncertainties are less which is less than a percent. However, due to the sample alignment, the laser speckle (the biggest source of noise), and other related factors, the uncertainties in the data may be higher than that.

It can be noticed that the reflectance obtained by Equation 3.1 is not accurate since it was made for isotropic and Gaussian surfaces, something that does not correspond to the actual surfaces of the foils (at least the aluminum foil) since they present anisotropy in his surface profile (to be demonstrated later).

There seems to be no relation between the RMS slope measured by the profilometer and the RMS slope derived by the equation. Values of autocorrelation length were estimated in order to obtain a close fit to the data since the use of the RMS slope to obtain the autocorrelation function provided with a very poor reflectance function profile. Moreover, as pointed out by Houchens et al. [19] and Stover [6], the ratio σ/lc, obtained by many values of the RMS roughness and autocorrelation lengths will produce the same BRDF. Houchens et al.[19] also questioned the value of lc since it should be a constant parameter for all wavelengths of radiation, something that did not occur in the measurements conducted in references [10-15].

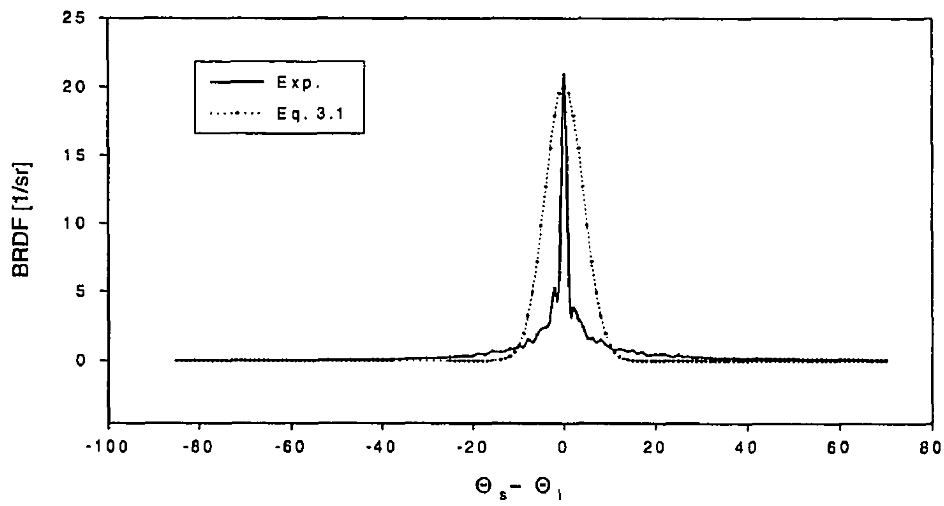

Figure 3.3 Stainless Steel Foil BRDF, $\Theta_i = 15'', \Phi_s = \Phi_i = 0''$, lc=6.231
(Courtesy of NIST Bidirectional Optical Scattering Facility)

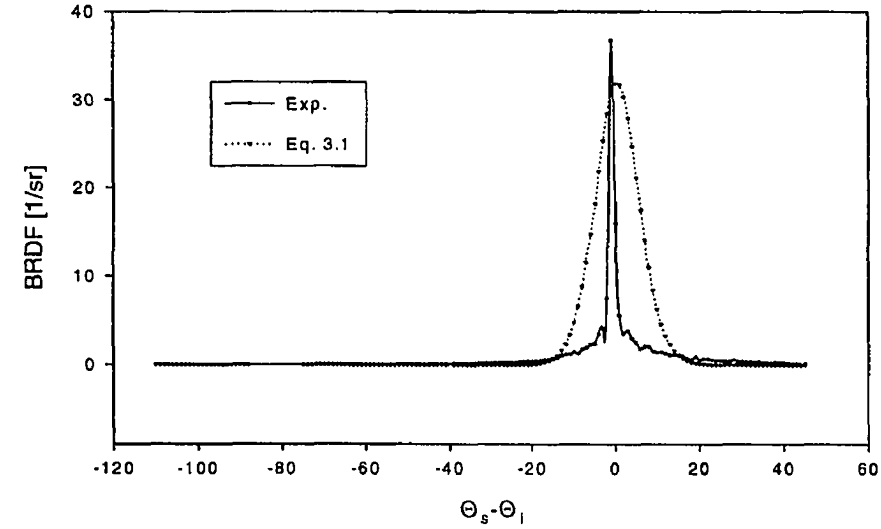

Figure 3.4 Stainless Steel Foil BRDF, $\Theta_i = 40''$, $\Phi_s = \Phi_i = 0''$, lc=6.231
(Courtesy of NIST Bidirectional Optical Scattering Facility)

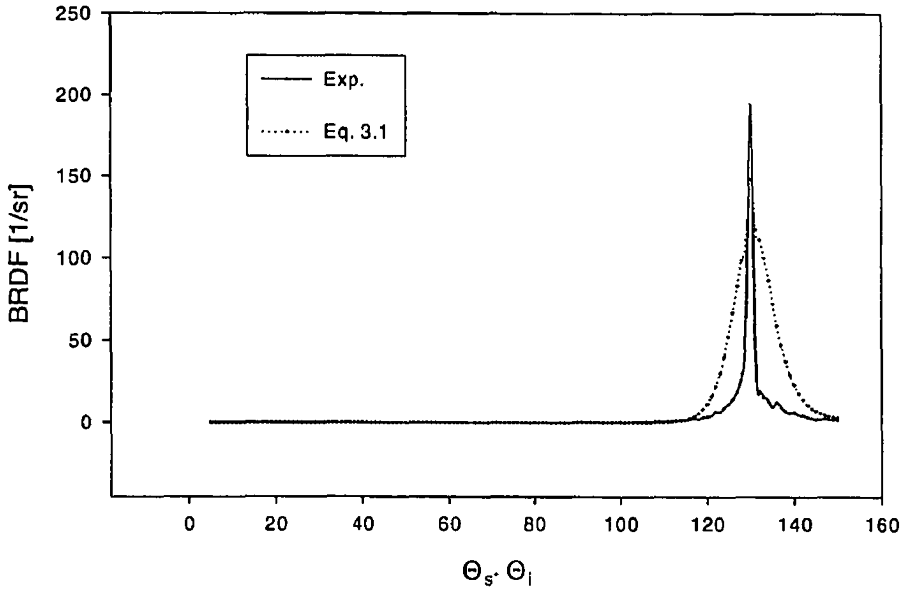

Figure 3.5 Stainless Steel Foil BRDF, $\Theta_i = 60''$, $\Phi_s = \Phi_i = 0''$, lc=6.231
(Courtesy of NIST Bidirectional Optical Scattering Facility)

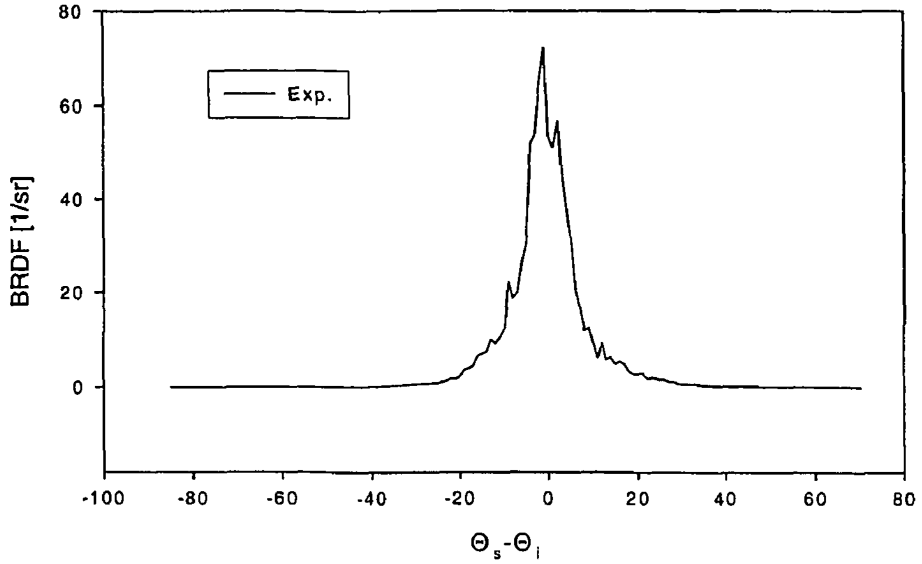

Figure 3.6 Aluminum BRDF Foil, $\Theta_i = 15^o, \Phi_s = \Phi_i = 0^o$
(Courtesy of NIST Bidirectional Optical Scattering Facility)

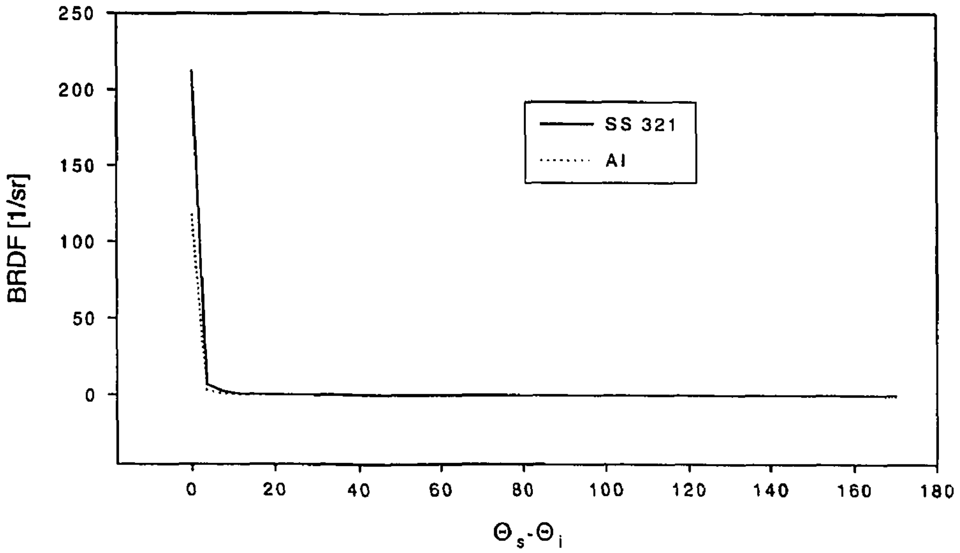

Figure 3.7 Aluminum Foil and Stainless Steel Foil BRDF, $\Theta_i = \Theta_s = 60^o, \Phi_i = 0^o$
(Courtesy of NIST Bidirectional Optical Scattering Facility)

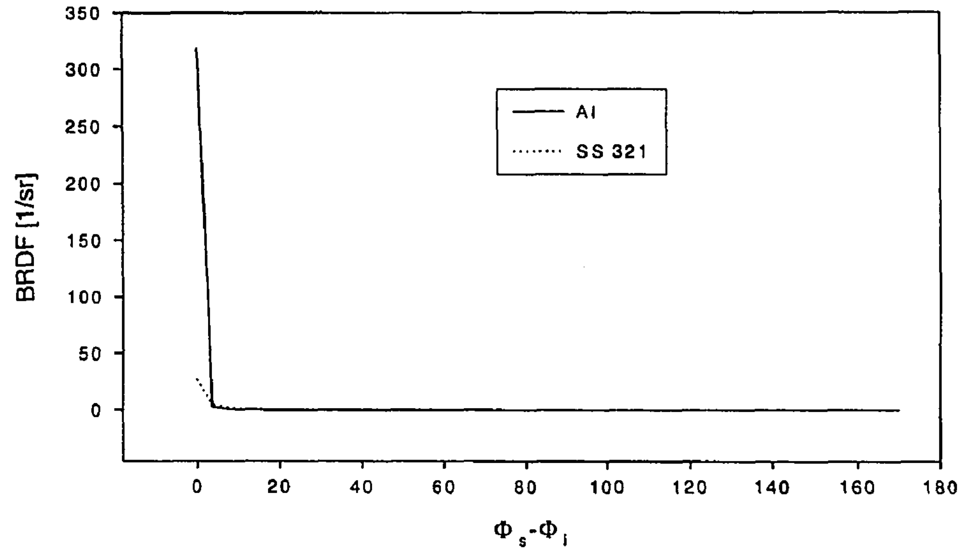

Figure 3.8 Aluminum Foil and Stainless Steel Foil BRDF, $\Theta_i = \Theta_s = 65^o, \Phi_i = 0^o$
(Courtesy of NIST Bidirectional Optical Scattering Facility)

The above results can be used to estimate the optical RMS roughness σ_o by making use of the TIS approach. By assuming that the surfaces are normally distributed and taking the specular component of the reflectance function for an angle of incidence of 15°, the optical RMS roughness σ_o is 0.414 µm for the aluminum foil sample and 0.332 µm for the stainless steel foil sample.

As previously indicated [14, 15] the above observations showed that when the angle of incidence is increased, the specular response of the roughened material increases. The same results also show the so-called off-specular shifting [17,18] where the specular reflected peak occurs at some leaving direction other than the specular direction, predicted by Fresnel equations. This shifting becomes more pronounced as the surface roughness or the anisotropy of the surface increases. For these metallic foils, the off-specular shifting is more pronounced for the aluminum foil rather than the much less rough stainless steel foil. However, this phenomenon is not greatly pronounced since these metallic surfaces have a mirror-like appearance. Table 3.3 shows in more detail both phenomena described above.

Table 3.3 Off- Specular Shifting Phenomenon for Fire Barrier Metallic Surfaces

	AL				SS-321			
Θ_i	Φ_i	Θ_s	Φ_s	$\rho(\Theta_i,\Phi_i;\Theta_s,\Phi_s)$	Φ_i	Θ_s	Φ_s	$\rho(\Theta_i,\Phi_i;\Theta_s,\Phi_s)$
-15	0	14	0	72.098	0	15	0	20.957
		15		53.561	30	14	30	13.445
	30	15	30	46.534		15		9.483
	60	15	60	45.949	60	14	60	22.838
	90	15	90	16.635		15		6.305
	120	14	120	53.095	90	14	90	12.073
		15		5.425		15		4.599
	150	13	150	39.325	120	14	120	5.042
		15		8.2148		15		3.187
					150	14	150	2.935
						15		2.825
-40	0	38	0	124.552	0	40	0	61.159
		40		114.903	30	39	30	36.782
	30	40	30	78.678		40		15.991
	60	40	60	84.494	60	39	60	73.275
	90	39	90	29.785		40		10.142
		40		22.088	90	39	90	19.738
	120	39	120	106.722		40		7.1386
		40		11.167	120	38	120	8.9823
	150	38	150	68.593		40		5.2198
		40		12.467	150	39	150	4.845
						40		4.802
-65	0	63	0	464.910	0	65	0	894.166
		65		415.405	30	64	30	733.152
	30	65	30	338.632		65		88.040
	60	65	60	345.664	60	64	60	907.935
	90	65	90	84.151		65		42.837
	120	64	120	303.551	90	64	90	614.297
		65		36.996		65		32.281
	150	63	150	281.063	120	64	120	29.545
		65		40.7163		65		29.136
					150	65	150	31.475

For the far infrared region, the surfaces will reach the limit of a slightly rough surface and the model for micro rough surfaces might be appropriate to use for the BRDF determination. This can be explained trough physical grounds since the ratio (λ/σ) determines the resulting directional distribution. For $(\lambda/\sigma) >> 1$ the surface will appear smooth and a strong reflected component and a weak non-specular component (diffuse) will occur, which is a similar trend to occur in the limit of slightly rough surface reflectors. As expressed in Equation 2.3, the power spectral density of the surfaces must be determined before calculating the reflectance function.

There are several ways to determine the PSD of a surface. Some profilometers are able to obtain the one dimensional PSD. However for a more detail description of a surface, different equipment is needed. Atomic force microscopy is a method capable of measuring the exposed surface of a material [30] and the 2D PSD can be obtained from these measurements since it is simply the square of the magnitude of the Fourier transform of the surface height function.

A Multi-Mode Atomic Force Microscope, Model MMAFM-153 was utilized to perform surface characterization and the obtaining of the isotropic 2D PSD for the foils. Different scan rates and spatial frequencies for the surface characterization had to be used because of the fact that the nano probe would tend to "jump" drastically while encountering some rough parts. (PSD is utilized as a metrological tool for evaluating extremely flat surfaces, something not accomplished with the foils.). Unfortunately due to the anisotropy and roughness of the material (Figures 3.9 – 3.10), the power spectral density extracted from the AFM (Figure 3.11-3.12), proved to be inconclusive since different PSD values were obtained for the same sample and scan rate which in turn might lead to non-unique BRDF.

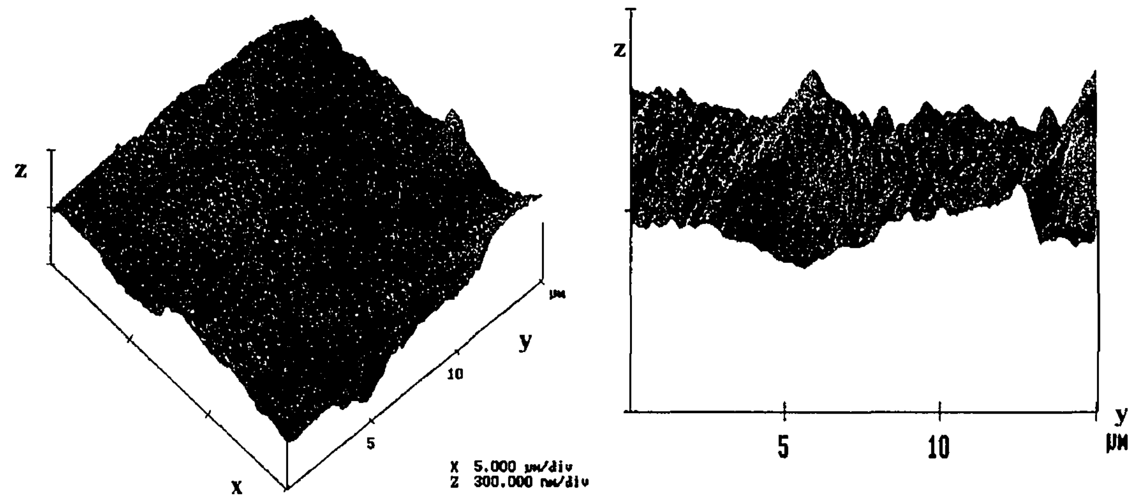

Figure 3.9 Three dimensional Surface profile Aluminum Foil,
Scan size 15 um, Scan rate 0.5003 Hz, Number of samples 256

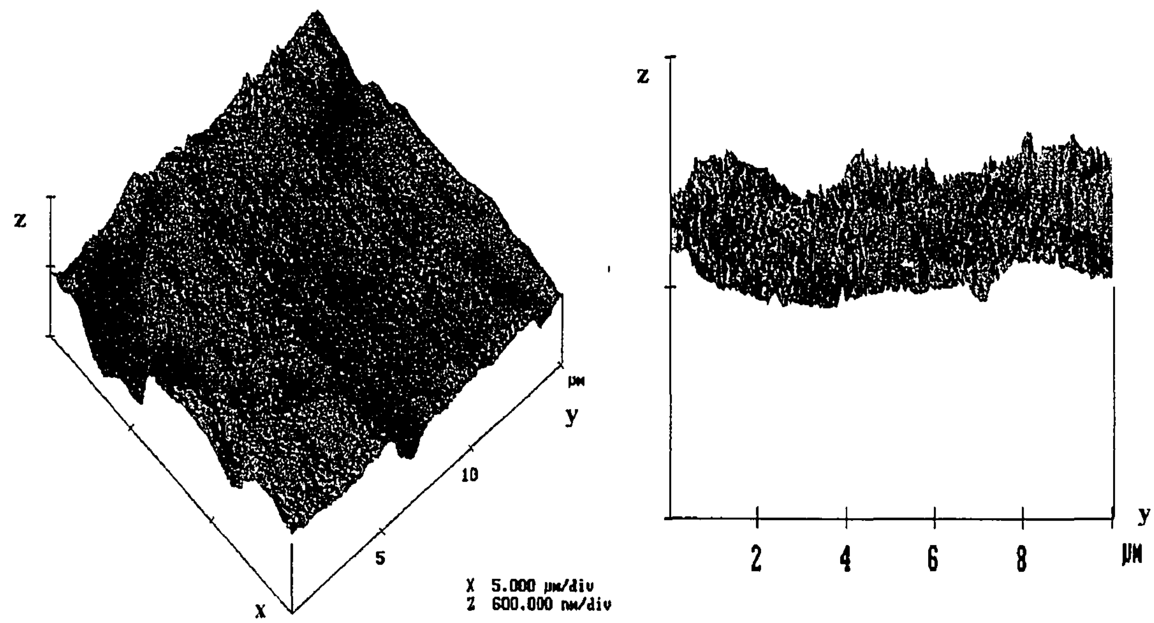

Figure 3.10 Three dimensional Surface profile SS 321 Foil,
Scan size 15 um, Scan rate 1.0001 Hz, Number of samples 256

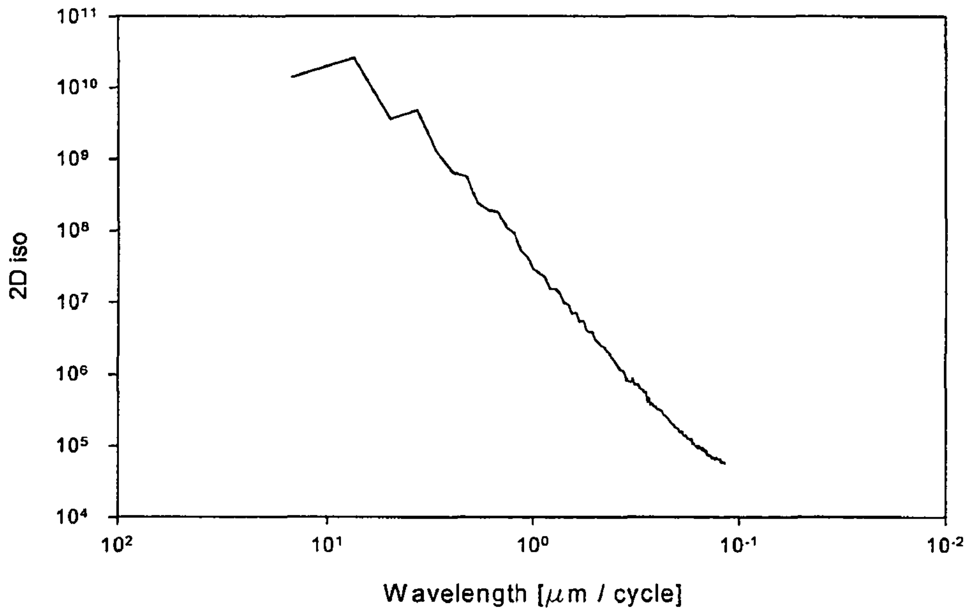

Figure 3.11 Isotropic Two-Dimensional Power Spectral Density
Aluminum Foil Scan size 15 μm, Scan rate 1.0001 Hz, Number of samples 256

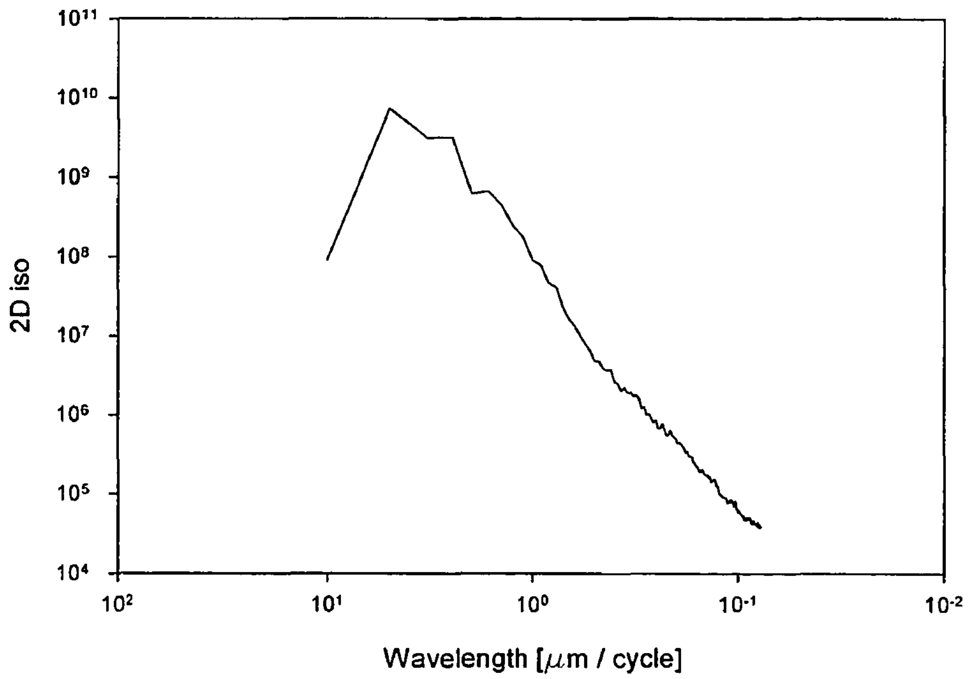

Figure 3.12 Isotropic Two-Dimensional Power Spectral Density
SS 321 Foil Scan size 15 μm, Scan rate 1.0001 Hz, Number of samples 256

3.2.2 Fiber Insulation

Another task to be accomplished is to introduce a good model to determine both the radiative properties and the scattering model of the material. Depending upon the model taken, scattering of fibrous materials can be simplified for an easy process, which should include the effects of fiber orientation, angular symmetry and spectral characteristics. Analysis of heat interaction must include effects near the surface. Accurate prediction of radiation heat transfer and radiation properties is a critical aspect in the design of fire barriers; therefore it is recommended the use of the correct radiation model [59].

Thermal insulations are typically composed of fibers of some millimeters in length and several micrometers in diameter. The usual modeling of a fiber is as an infinite long cylinder since the fiber length is much larger than both the diameter d and the wavelength λ of the radiation incident upon it. An infinite cylinder is considered as 2D region. It is usual to obtain dimensionless parameters to define the absorption, scattering and extinction parameters of the intensity in participating media, since these properties will help us to define some of the scattering modes. These models should also take into consideration the orientation, and size distribution of the fibrous material.

The spectral volumetric scattering coefficient $\sigma_{s\lambda}$ is defined as the fraction of incident radiation that is scattered by the particle in the hemisphere along the path of the beam. For a fiber, the scattering property is given in terms of the scattering efficiency $Q_{s\lambda}$, a dimensionless number to account for scattering of radiation. A fiber modeled as an infinite cylinder produces a scattered radiation along the surface of a cone, as depicted in Figure 3.13, where ξ_{ii} is the angle of incident radiation and γ is the observation angle measured on a plane normal to the fiber axis.

The spectral volumetric absorption coefficient k_{λ} is defined as the fraction of incident radiation that is absorbed by the matter along the path of the beam. The extinction coefficient β_{λ} is defined as the sum of the absorption coefficient and the scattering coefficient. Solutions of the scattering of an infinite long cylinder are well documented in the literature [59, 60]. The extinction and scattering efficiencies for unpolarized radiation at oblique incidence on an infinite cylinder as depicted in Figure 3.13 are given by [52, 61]

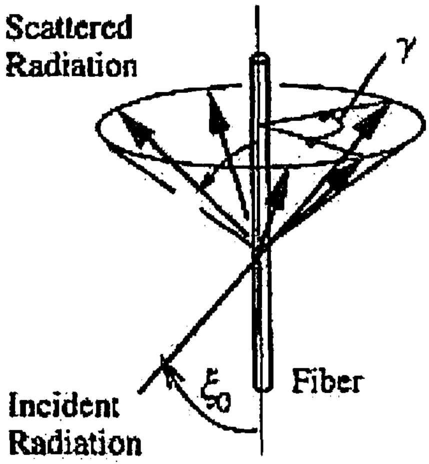

Figure 3.13 Scattering by a single fiber

$$Q_{e\lambda}(\xi_o) = \frac{1}{\alpha}\mathrm{Real}\left[b_{01} + 2\sum_{n=1}^{\infty} b_{n1} + a_{02} + 2\sum_{n=1}^{\infty} a_{n2}\right] \tag{3.2}$$

$$Q_{s\lambda}(\xi_o) = \frac{1}{\alpha}\left[|b_{01}|^2 + 2\sum_{n=1}^{\infty}|b_{n1}|^2 + |a_{02}|^2 + 2\sum_{n=1}^{\infty}|a_{n2}|^2 + 2\sum_{n=1}^{\infty}|a_{n1}|^2 + 2\sum_{n=1}^{\infty}|b_{n1}|^2\right] \tag{3.3}$$

where α is the size parameter defined as $\pi d/\lambda$ and the coefficients a_n and b_n are dependant of the incident angle, size parameter, and the complex refractive index.

Depending upon the type of fiber insulation, these can be classified according to the fiber orientation arrangement. For instance, the fibers of commercial house fiber insulation are randomly oriented in space while some thermal blankets could have fibers oriented or aligned with respect to a plane or the space. The specific orientation of the fiber has incidence in the radiative properties of the fiber, as demonstrated by Lee [47].

For determination of the spectral extinction or scattering coefficient in a fiber media, the respective radiative efficiencies must be weighted with respect to the size distribution and orientation, [52] resulting in

$$[\beta_\lambda, \sigma_{s\lambda}](x,y) = \int_0^{2\pi} \int_0^{\pi/2} \int_{r_1}^{r_2} \{Q_{e\lambda}(\xi_o), Q_{s\lambda}(\xi_o)\} 2rN[r(x,y)]F(x,y)\,dr\,dx\,dy \qquad (3.4)$$

$$\kappa_\lambda = \beta_\lambda - \sigma_{s\lambda} \qquad (3.5)$$

where x and y represent the directions of fiber orientation, $N[r(x,y)]$ is the number of fiber with radius between r and $r+dr$, and $F(x,y)$ specifies the fiber orientation. This equation implicitly assumes that the fibers scatter independently.

While solving the radiative heat transfer equation RTE, the phase function for scattering must be determined. Instead of finding the phase function, a linear anisotropic model is used [44-46] to replace the phase function. This model assumes that the scattering process of a fiber can be approximated to the scattering behavior of a sphere. Following Tong's model [44], the phase function for scattering is replaced by

$$P(\Omega \to \Omega') = 1 + a_{\lambda 1}\cos(\Omega) \qquad (3.6)$$

Equation 3.6 states the radiation energy scattered from incident direction Ω' to the scattered direction Ω has a linear behavior with a factor of "slope" $a_{\lambda 1}$ as

$$a_{\lambda 1} = 2(1 - 2b_\lambda) \qquad (3.7)$$

where the factor b_λ (Equation 3.8) is the back scattered parameter of the linearly anisotropic function, found by integrating Equation 3.6 over the backward hemisphere.

$$b_\lambda = \int_{\cup} P(\Omega \to \Omega') \qquad (3.8)$$

Following the same model to determine the radiative properties (coefficients) of the Durablanket® S using Equations 3.4, 3.5 and 3.8, some other physical properties have to be utilized, such the spectral complex refractive index m, the fiber size distribution $N[r(x,y)]$ and orientation $F(x,y)$, and the volumetric fraction fv.

The spectral complex index of refraction is $\overline{m} = n - ik$, where n is the real part, which accounts for the refraction of the radiation wave and k is an imaginary part accounting for absorption, depends of the composition of the material. Looking at table 3.1, Durablanket® S is made of a chemical combination of Silica and Alumina [63]. Refractive indeces for this combination have not been reported in the literature except for a work done by Tong et al. [55] in which a coating of alumina was applied to silica fibers. However, this treatment assumed separate refractive indexes. A crude approximation could perhaps describe the index of the small particles making up the material with an average of the indices of the two components or use effective medium theory [64]. An effective medium theory, though the use of the Brugeman's approximation [65], treats the components of the medium in a symmetrical way. For a binary composition Brugeman's approximation for a medium property can be stated as:

$$\overline{m} = \frac{1}{4}\left(\Lambda + \sqrt{\Lambda^2 + 8\overline{m}_1\overline{m}_2}\right) \tag{3.9}$$

where $\Lambda = (3\overline{\eta}_1 - 1)\overline{m}_1 + (3\overline{\eta}_2 - 1)\overline{m}_2$ and $\overline{\eta}_1$ and $\overline{\eta}_2$ are the concentration of the components.

Through the use of the indexes of refraction for Silica and alumina [66, 67], a new index of refraction for Durablanket® S using a composition of 55%, 45% silica, alumina respectively [65] is calculated and shown in Table 3.4.

The effective volumetric fraction fv can be estimated by taking the ratio of the insulation density to solid the mass density. For Durablanket® S fv yields a value of 4.27×10^{-2}.

Scanning electron microscopy and microscopic counting allow calculating not only the fiber size distribution but also serves as parameter to define the orientation of the fibers. Using an ETEC Auto scan SEM and coating the fibers with Carbon and Silver-Palladium the fiber orientation $F(x,y)$ of the insulation can be considered as fibers randomly oriented in space

(Figure 3.14). Fiber size distribution $N[r(x,y)]$ as shown in Figure 3.15 were measured using scanning electron microscopy (SEM). Several SEM photographs were analyzed and the number of individual fibers counted for the respective cases were greater than 80.

The size distributlon estimates a mean diameter of 1.578 μm while the product description sheet publishes a fiber mean diameter of 2.5 to 3.5 μm. This was brought to the attention of Unifrax® Corporation [62] and they noted that since the standard deviation of the fiber size distribution was very large and that the published value is only a crude estimate of the actual fiber sizes they place into this insulation. The surfaces of the individual fibers are relatively smooth and the fiber length- to diameter is large enough, which is consisted with the assumption of the property model as an infinite cylinder [48].

Table 3.4 Estimated Complex Refractive Index of Durablanket® S
[55% SiO_2, 45 % Al_2O_3]

λ [μm]	η	κ
0.500	1.598	0
0.633	1.594	0
1.0	1.583	0
2.0	1.568	0
3.0	1.640	0
4.0	1.513	0
5.0	1.464	0
6.0	1.396	0.001
7.0	1.254	0.002
8.0	0.780	0.257
9.0	1.137	1.175
10.0	1.741	0.214
11.0	1.024	0.257
12.0	0.929	0.759

Knowing that the fibers are randomly oriented in space, there is no correlation between the size and orientation. Also, the radiative coefficients can be average over all angles of incidence due to the same reasons explained above. Equation 3.10 shows the well-established formulae for the cases of fibers randomly oriented in space [44-52] to calculate the radiative properties of infinite cylinders.

$$\{\beta_{\lambda r}, \sigma_{s\lambda r}\} = \frac{2fv}{\pi}\sum_{i=1}^{N}\frac{x_i}{r_i}\int_0^{2\pi} Q_{e\lambda}(\xi_o, r_i)\cos(\xi_o)\,d\xi_o \qquad (3.10)$$

Equations 3.2 and 3.6 were solved using an algorithm created by Swathi and Tong [68] and cross-correlated with the help of the Applied Sciences Laboratory Inc., CA [59] (except backscatter factor, Figure 3.16) and the results are shown below.

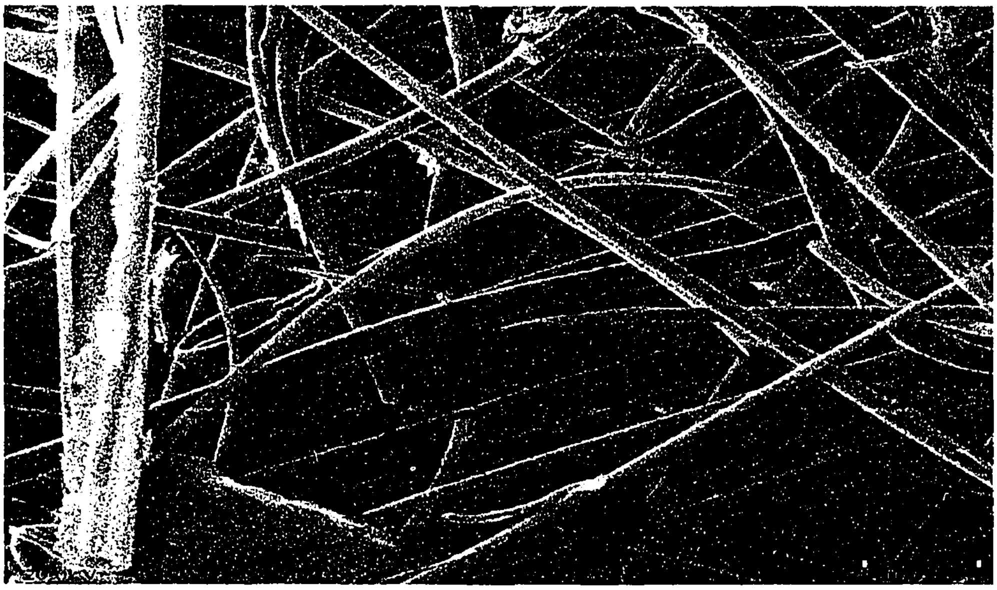

Figure 3.14 SEM of Durablanket® S Fibers

Figure 3.17 shows the single scattering albedo, which is the ratio between the scattering (Figure 3.18) and extinction efficiencies. These results have the same trend characteristics as the values found by Cunnington et al. [62]. The small values of the spectral scattering coefficient obtain trough Equation 3.10 at large wavelengths are produced by the closeness of the absorption coefficient in the refractive index range 8 to 10 μm. Furthermore, the values of the linear anisotropic parameter $a_{\lambda 1}$, represented through the backscatter factor show that the anisotropic part of the scattering phase function is small which lead to the conclusion that most of the scattering would be isotropic. Finally, the average gray values coefficients in over the above wavelength range were determined and compared [53]: [0.74 - 0.93] for the single scattering albedo, 4864 [1/m] for the extinction coefficient. The average backscatter factor is 0.470.

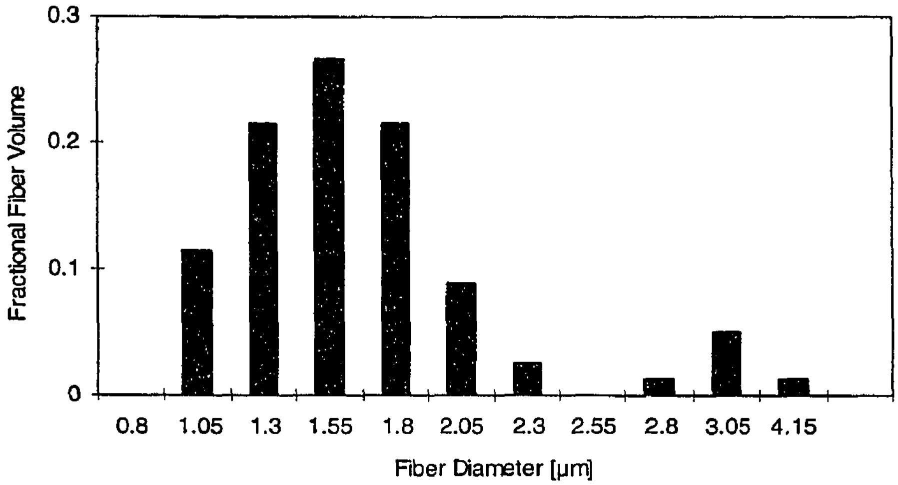

Figure 3.15 Fiber Size Distribution Durablanket® S

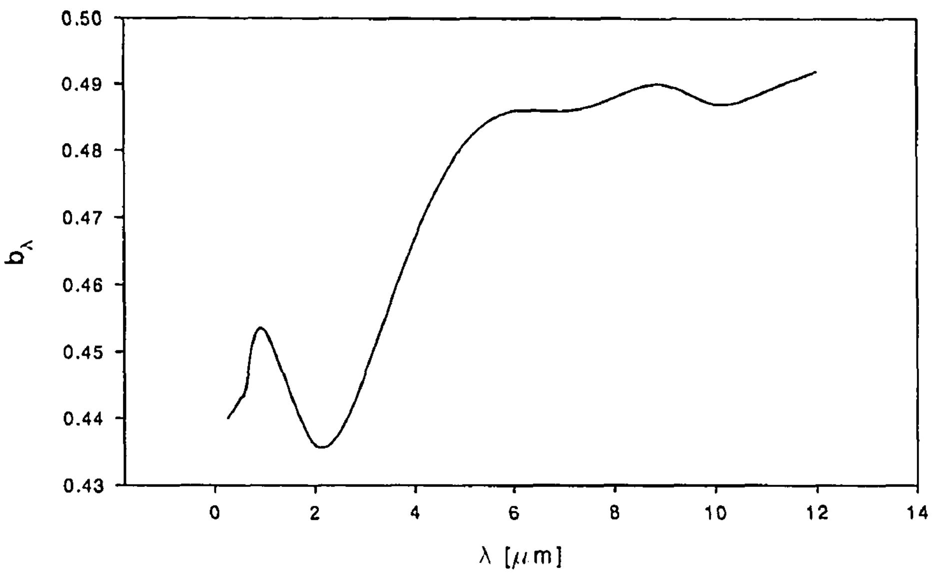

Figure 3.16 Back Scatter Factor

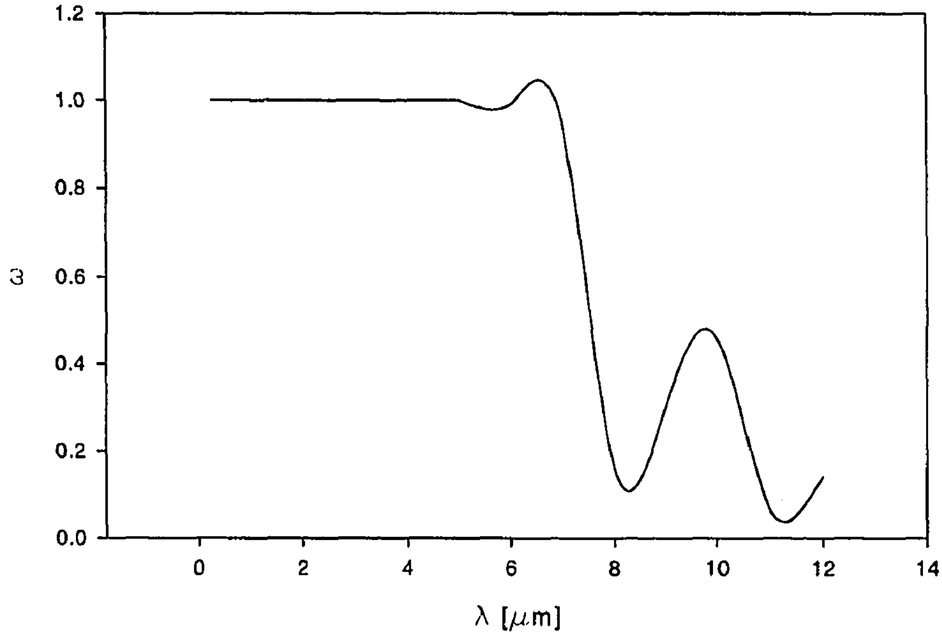

Figure 3.17 Single Scattering Albedo Durablanket® S

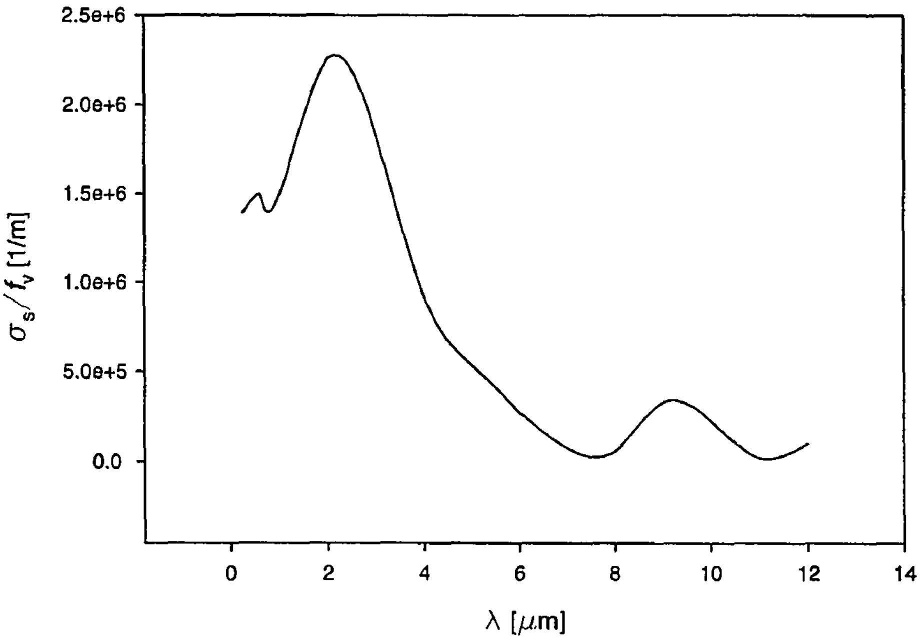

Figure 3.18 Spectral Scattering Coefficients for Durablanket® S

3.3 Conclusions

The results of this chapter may be summarized as follows. The reflectance function of any surface is dependant on several parameters; among them are the RMS surface roughness, incident energy wavelength and direction. If the magnitude of the surface anisotropy is sufficiently large (comparing to the energy incident wavelength), the off-specular shifting occurs which might be used as a reference parameter to describe its surface properties. As the angle of incidence increases, the surface becomes very specular and surface roughness and or wavelengths effects are minimized

Since the surface is rougher than permitted by the smooth-surface requirement, the PSD of the surface peaks or be non-existent at zero frequency, so that it cannot be extrapolated to another frequency. Furthermore, some non-existent PSD values at certain frequencies appear in the peridogram, which leads to the use of a different more complete theory requiring numerical evaluation [21].

Another possible complication comes from the fact that some of the textbook calculations usually take the surface to be an infinite half space of homogeneous material rather than, say, a layered structure without considering subsurface complications or they are too cumbersome to apply. The result is the that actual measurement of the reflectance function is the best way to determine this radiative property and measure it in such manner that could also be applied to radiation heat transfer solution method.

By also getting the scattering characteristics of the insulation, a heat transfer analysis of the insulation can be accomplished by any standard method. If the reflectance function is included into the solution of the RTE, these measurements of the insulation must be generated. The only way to obtain the data would be by also performing measurements with application to some approximate solution. In the next chapter an attempt is made to measure directional properties extracted from the solution of the radiative transfer equation (RTE). This method should help account for multiple dependent scattering in the insulation.

CHAPTER 4

EXPERIMENTAL MEASUREMENT OF REFLECTANCE FUNCTION

The primary objective of this chapter is to describe the experiment design to obtain the Reflectance Function (BRDF) for the materials that composed the fire barrier.

Development of the experimental apparatus has been based on the directions of quadrature $\hat{s}_i$ and weights ϖ_i for the method of discrete-ordinates or S_N approximation. An explanation of the method of discrete ordinates and the selection of the discrete ordinate quadrature will be given prior the explanation of the experimental design. The discrete-ordinates method is one of the most regularly used analysis tools for participating thermal radiation; a version of the method is given in Fluent Inc[1]. The current analysis is formulated in the appendices.

4.1 Selection of the Discrete Ordinate Quadrature

Although the selection or choice of the quadrature scheme is arbitrary [5], a good quadrature should be one that not only integrates well the integrals in the radiative transfer equation (RTE) but also a system that satisfy accurately the zeroth, first, and second moments of scattering phase functions of high complexity.

The S_4 quadrature approximation has been shown to work well for multidimensional heat transfer problems with isotropic or simple scattering phase functions including some of higher complexity [69]. Different sets of directions and weights, which satisfy the above criteria, have been created and tabulated [5, 69, 70]. The choice of the quadrature scheme for this experiment is the completely symmetric quadrature originally developed by Larthrop and Carlson [70] and extended by Fiveland [69].

[1] Fluent: A worldwide flow modeling company headquartered in Lebanon, New Hampshire, USA.

4.1.1 Discrete-Ordinates Method

Following Fiveland's development [5], the RTE in Cartesian coordinates can be written in the following form:

$$\xi\frac{\partial I}{\partial x}+\eta\frac{\partial I}{\partial y}+\mu\frac{\partial I}{\partial z}=-\beta I+\frac{\sigma_s}{4\pi}\int_{4\pi}P(\Omega\to\Omega')Id\Omega+\kappa I_b \tag{4.1}$$

where the phase function is approximated by a linear anisotropic phase function as shown in Equation 3.6. The S_N approximation of equation 4.1 can expressed as:

$$\xi_m\frac{\partial I_m}{\partial x}+\eta_m\frac{\partial I_m}{\partial y}+\mu_m\frac{\partial I_m}{\partial z}=-\beta I_m+S_m \tag{4.2}$$

where the source function term S_m in equation 4.2 is approximated by:

$$S_m=\kappa I_b+\frac{\sigma_s}{4\pi}\sum_{m'}\varpi_{m'}(1+a_1(\xi_m\xi_{m'}+\eta_m\eta_{m'}+\mu_m\mu_{m'})I_{m'} \tag{4.3}$$

For a discrete direction, Ω_m, the values of ξ_m, η_m, and μ_m define the direction cosines of Ω obeying the condition $\xi_m^2+\eta_m^2+\mu_m^2=1$. The prime in Equation 4.3 denotes the direction of incoming radiation.

The directions ξ_m, η_m, and μ_m span over the 4π steradians of solid angle. Assuming a completely symmetric quadrature (invariant sets to 90° rotation), description of the points in one octant suffices to describe the points in the rest of the octants. Table 4.1 describes a S_4 quadrature, which would integrate well for highly reflective materials, small forward scattering, and some refractory materials [69]. The same quadrature direction in terms of degree angles is depicted in the positive octant of the hemisphere (Figure 4.1). Due to rotational symmetry and invariance, it is required that if (ξ_m,η_m,μ_m) for the first octant, then $(-\xi_m,\eta_m,\mu_m)$ for the second, $(-\xi_m,-\eta_m,\mu_m)$ on the third octant and so forth until completion of the entire sphere.

Table 4.1 Discrete-Ordinates Completely Symmetric Quadrature [69]

	Ordinates			Weights
Order of Approximation	ξ	η	μ	ϖ
S_4	0.2958759	0.2958759	0.9082483	0.5235988
	0.2958759	0.9082483	0.2958759	0.5235988
	0.9082483	0.2958759	0.9082483	0.5235988

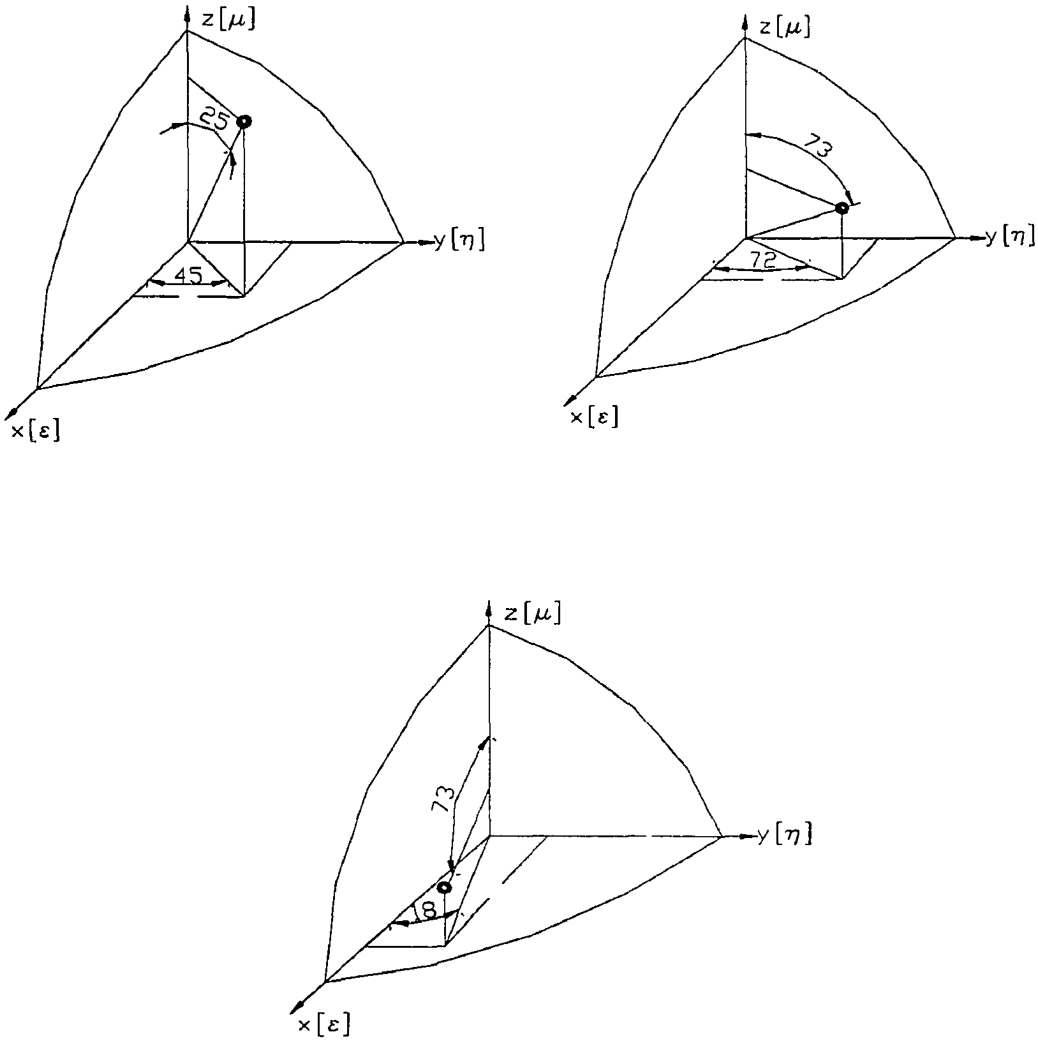

Figure 4.1 Symmetric S_4 quadrature in terms of Approximate Degree Angles

4.2 DOM-Hemispherical BRDF Scatterometer

Measurement of Biangular Reflectance Distribution function BRDF has usually been performed using goniometric optical scattering instruments [14, 15, 17, 18, 33-35, 71, 73-75] since this apparatus can readily perform in-plane and out-of-plane measurements in simple manner. However, with the aim of demonstrating a practical application, a simple prototype hemispherical optical scattering instrument has been designed based on the discrete ordinate method (DOM). The reflectance data obtained from this device can be directly applied to an S_4 scheme code when solving the RTE. The basic concept of the device is to measure the energy scattered from the surface from each detector and obtain the reflectance function by dividing the amount of scattered light by the incident amount of energy. Other similar instruments [76,77] have been designed for the purpose of determining surface defects.

A description of the DOM-Hemispherical Scatterometer is given below. The following section details the instrumentation and construction of the instrument. Further sections complement the chapter by finding the calibration procedures and the BRDF experimental results.

4.2.1 Instrument Description

In the above section, the location of the direction cosines for an S_4 quadrature scheme have been established (Figure 4.1) by converting the numerical quadrature in Table 4.1 into degree angles. Angles located at the bottom of the hemisphere (45°, 71.96°, 18.04°) represent the azimuthal angles Φ. The other angles (24.74°, 72.79°, 72.79°) represent the polar angles (Θ) measured from the z-axis.

Figure 4.2 a) shows a top view of the collection shell of the DOM-Hemispherical Scatterometer. This hemispherical shell is made of spun aluminum and has an outside radius of 62 mm and a thickness of 1.3 mm. This shell was flat black-anodized to obtain a near black body configuration. Each octant of the hemispherical shell has three opening ports to locate either the sensor or as a coupling mean to the source light. Thus, while 11 ports hold detection systems, one port is being use as an incident source. The shell is attached to a black-anodized base where the samples would be placed. Each of the twelve sensors is laser aligned to point at the center of the sampling holding base.

In Figure 4.2 b) the coordinate system is depicted for the incident and scattering directions. The polar incident and scattering angles Θ_i and Θ_s are measured from the normal surface angle (axis z) whereas the azimuthal incident and scattering angles Φ_i and Φ_s are defined with respect to the plane of incidence [77]. Table 4.2 shows the actual location of the ports throughout the hemisphere.

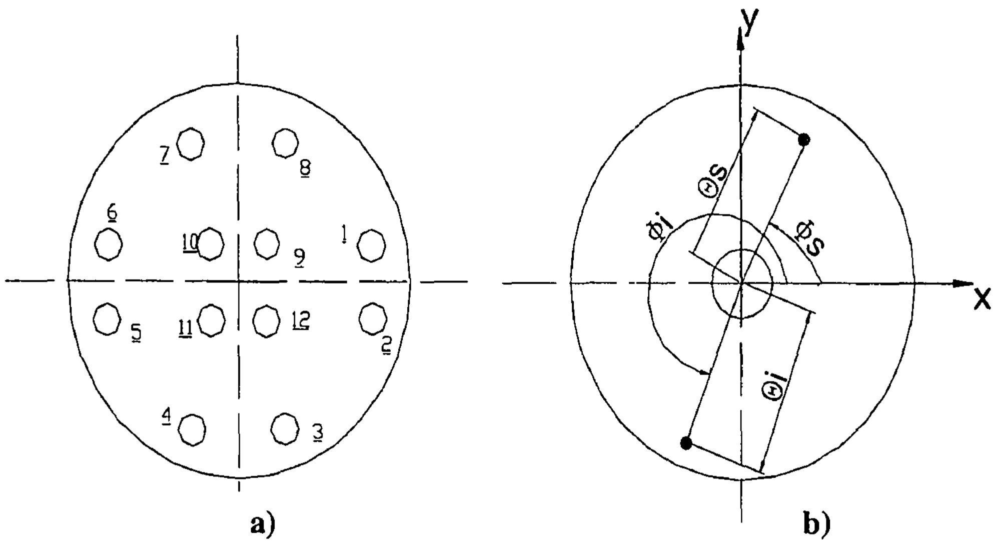

Figure 4.2
a) Top View of the Hemispherical Detection Holder showing multiple detection port positions.
b) Coordinate system projected into the holding surface used to describe the incident $\hat{i}$ and scattering $\hat{s}$ angles position.

Table 4.2 Direction of the Detector Center Point

Port	θ [°]	φ[°]
1	73	18
2	73	342
3	73	288
4	73	252
5	73	198
6	73	162
7	73	108
8	73	72
9	25	45
10	25	135
11	25	225
12	25	315

Figure 4.2b also depicts the center support surface (base of the hemisphere) in which the specimen material will be aligned and placed. This surface region (see Figure 4.3) is an adjustable section that will allow alignment, measurement, and assessment of light reflected from the metallic sample alone (Figure 4.3a) and light transmitted and reflected from the a second sample, which is placed beneath a primary sample at the top of the surface in the center region (Figure 4.3b).

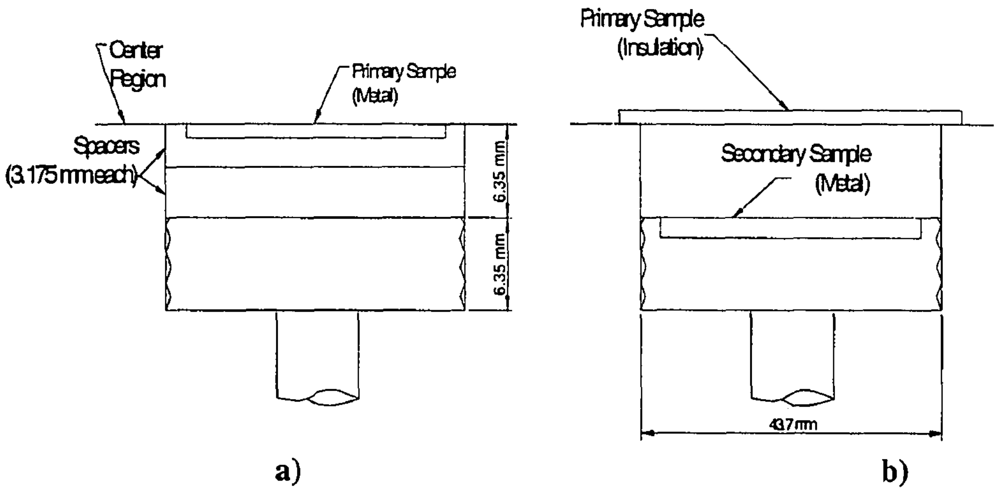

Figure 4.3 Sample-Holder Sections

The detection system consists of a thin film based thermopile detector (Dexter Research®) model 2M with KBr window with argon encapsulating gas. Figure 4.3 shows one of the detectors mounted in a cylindrical threaded black-anodized case. The voltage signal taken from the detectors is amplified through a low noise amplifier and acquired and recorded by a National Instrument® Data Acquisition System.

Three Ion Optics® sources that works separately depending upon the wavelength range provide incident power were used. These light sources emit infrared energy. Two windowless broad infrared light sources provide power for a wavelength range from 2 to 20 μm. (ReflectIR-P1N and TO-5). The output patterns of these sources are depicted in Appendix B. The third light source is a collimated-light-source with a range in wavelength from 2 to 5.25 μm (ReflectIR-P1S) with an output pattern similar to the other sources. An evaluation kit (drive board and software) is used to adjust the, temperature, amplitude and frequency range of these infrared sources.

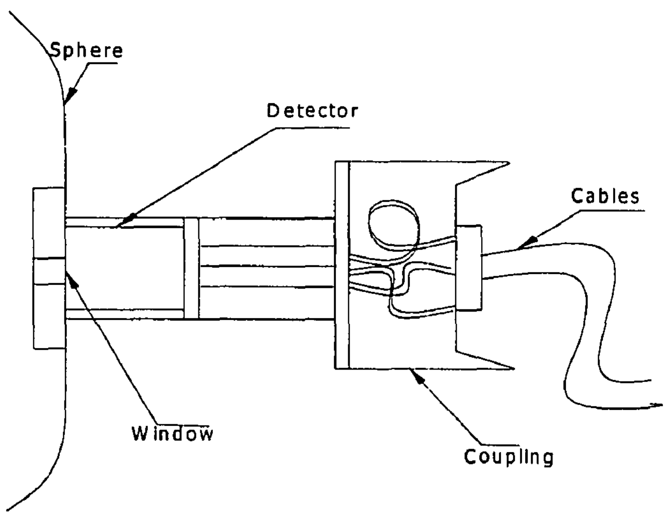

Figure 4.4 Detection Systems and Mounting

All light sources were set up at the same amplitude and frequency in order to increase the life expectancy of the source. However, the un-collimated and third light sources were set up to work at a temperature of 600°C whereas the second light source had a working temperature of 400°C. This temperature range was selected in order to obtain two working wavelength bands, taking into account the concepts of blackbody radiation functions and Wien's law.

The data acquisition set up consists not only of the National Instrument system but also of an electro-mechanical multiplexing system, which allows scanning of twelve digital inputs using an eight bit digital board and a Digital Tektronix® Oscilloscope. By using the same mechanism, temperature monitoring in the system is required in order to maintain isothermal during operation. Figure 4.5 shows the experimental instrument to measure the reflectance function.

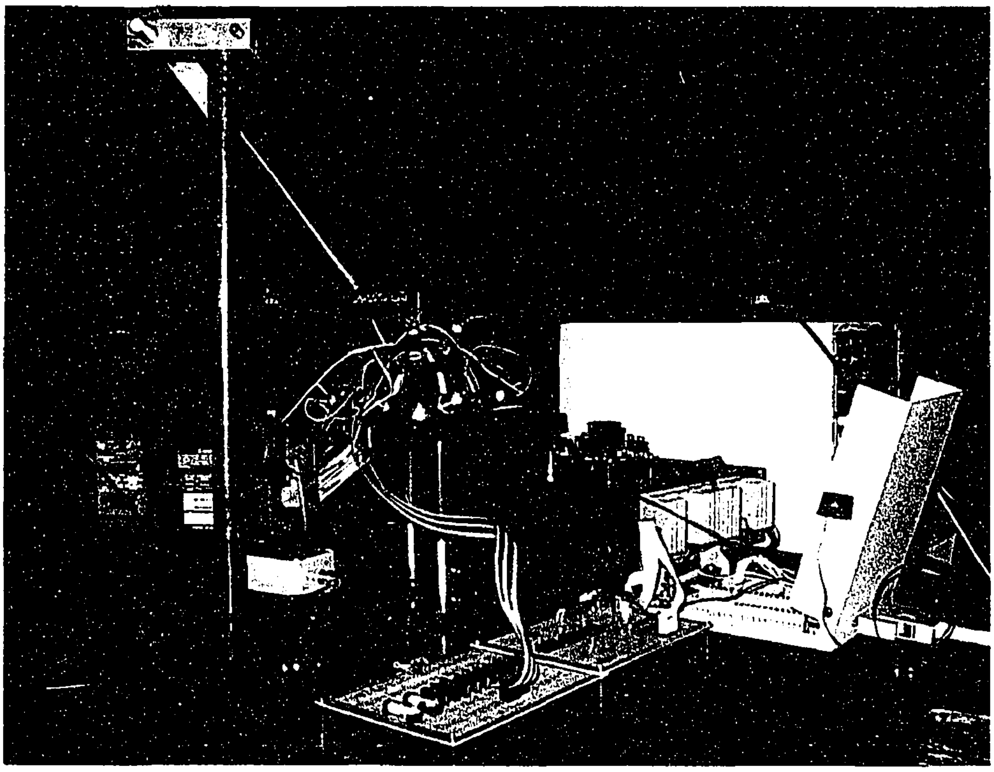

Figure 4.5 A Photograph of the DOM-Hemispherical BRDF Instrument

4.3 System Calibrations and Experimental Procedure

According to the American Society for Testing and Materials designation E-1392-90 [78], the biangular reflectance can be measured and normalized using four types of normalizations. It is the choice of this work to normalize the scattered power to the incident power in a relative manner. This relative technique normalizes the sample data to that of a reference standard or highly reflectance diffuse surface [74, 78] with a known spectral reflectance function.

Due to the quality and characteristics of the detection system, the reflectance function can be obtained through the voltage signal ratio between the scattered and incident light intensity. Thus, there is no necessity to calibrate the sensors [75] in an absolute basis. The normalization method for the Scatterometer is accomplished by normalizing the instrument voltage response with the reference standard bi-directional reflectivity. The following can now be calculated [74]:

$$\frac{\rho_{\lambda,spl}\left(\Theta_i,\Phi_i;\Theta_s,\Phi_s\right)}{\left[\rho_{\lambda,ref}\left(\Theta_i,\Phi_i;\Theta_s,\Phi_s\right)\right]}=\frac{V_{spl}}{V_{ref}} \tag{4.4}$$

where, $\rho_{\lambda,spl}\left(\Theta_i,\Phi_i;\Theta_s,\Phi_s\right)$ and V_{spl} stand for the values measured by the Scatterometer for the material sample to be investigated.

The theory behind the experiment follows. Voltage measurements were first taken in a black anodized standard coupling with a length equal to the radius of the shell. By placing the light source at one side and the thermopile sensor at the other side, the registered voltage obtained from the sensor gives the incidence or reference voltage. The ratio between the thermopile detector area and the light source area is 1:1.35. Once the average incidence voltage is obtained, the light source is repositioned and aligned with respect to the DOM-Hemispherical shell and measurements can be repeated.

Measurements were taken for all angles described in Table 4.2. After a series of repeated measurements yielded similar values, the data run was considered accepted. Each measurement takes a large number of samples, which are averaged.

4.3.1 Reference Standard

Due to the fact that the working wavelength region is between the NIR to MIR, an Infragold® diffuse reflectance standard, from Labsphere, Inc., was selected. It is a typical material with a high hemispherical reflectance value for this spectral region and provides sufficient energy levels over the entire range of incident angles [75].

Despite the fact that the calibration from 2.5 μm to 15 μm every 50 nm is traceable to the current National Institute of Standards and Technology (NIST) the biangular reflectance for the Infragold® had to be measured due to the type of infrared sources used during the experiments. Figures 4.6 and 4.7 show the Reflectance R for the reflectance standard for different types of source. Out-of-plane measurements for this material yield small values of reflectance similar to one another, which agrees well with the calibration.

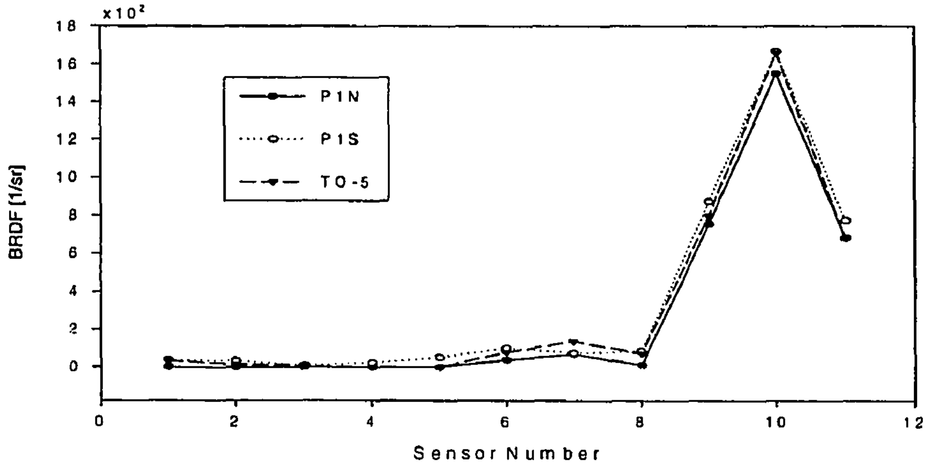

Figure 4.6 Biangular Ellipsometry reflectance of Infragold® using various light sources with incident angle of $\Theta = 25°, \Phi = 315°$ (Port 12)

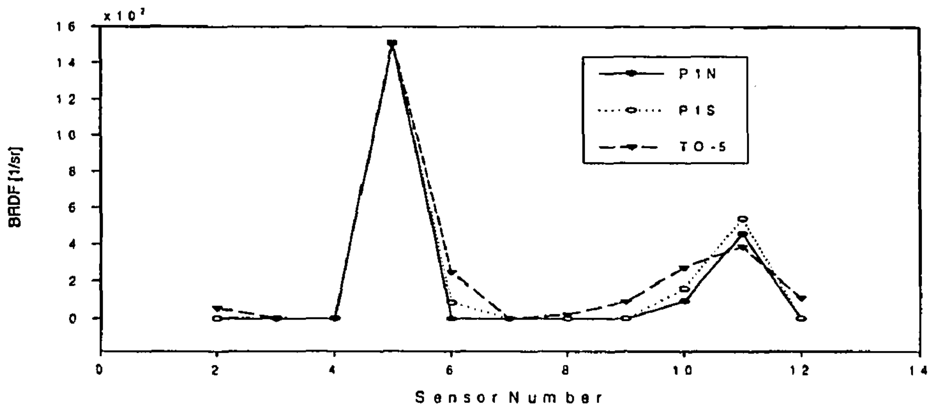

Figure 4.7 Biangular Ellipsometry reflectance of Infragold® using various light sources with incident angle of $\Theta = 73°, \Phi = 18°$ (Port 1)

In order to verify that the measured reflectance function values are correct, the hemispherical reflectance of the Infragold® is calculated using the un-normalized measured data. The hemispherical reflectance is defined as the fraction of the total irradiation from all directions reflected into all directions [5] and expressed as:

$$\rho(r) = \frac{\int\limits_{2\pi}\int\limits_{2\pi} \rho(r,\Omega_i\Omega_s) cos(\Theta_s) I(r,\Omega_i) cos(\Theta_i) d\Omega_s d\Omega_i}{\int\limits_{2\pi} I(r,\Omega_i) cos(\Theta_i) d\Omega_i} \quad (4.5)$$

where $\rho(r,\Omega_i\Omega_s)$ is the biangular reflectance distribution function BRDF and $I(r,\Omega_i)$ is the incident intensity per direction per established direction. However, Equation 4.5 is not suitable for the measurements taken by the DOM scatterometer since it involves directional intensity effects.

A method of integrating the diffuse part of the all reflectance function produced by the 12 different intensities and adding the weighted summation of the all specular components produced by the 12 different intensities should lead a value similar to the calibrated hemispherical reflectance. Thus,

$$\rho(r) = \sum_{j=1}^{N}\sum_{i=1}^{N} w_j w_i \rho^d(r,\Omega_i,\Omega_s)\cos(\Omega_i) + \frac{1}{\pi}\sum_{i=1}^{N} w_i \frac{\rho^s(r,\Omega_i,\Omega_s)}{\cos(\Omega_i)} \quad (4.6)$$

N represents the number of incident directions. By solving Equation 4.6 using the DOM integration method and the quadrature expressed in Table 4.1, the calculated hemispherical reflectance of Infragold® was 0.975, a 1.2% error with the average calibrated hemispherical reflectance provided by the manufacturer. This error falls in the uncertainty of the measured data for the scatterometer calculated in the next section.

Since the highest values of reflectance showed in the specular direction, this was taken as the relative reference value for the other reflectance functions of each one of the materials composing the barrier as expressed in equation 4.4.

4.3.2 Uncertainty

Since the reflectance function is obtained through the ratio of voltage signals, there is great reduction in the overall uncertainty of the experiment. However, the contributions to this value can be summarized in the following paragraphs.

As described in the previous chapter the sample materials to be analyzed are the 97% aluminum foil, the 321-stainless steel, and the Durablanket® S. Both metallic surfaces were carefully attached to the blackened holders (cleaned with acetone to remove dust and dirt between samples). Ensuring complete flatness of all samples was not possible. Reflectance measured values might be dependent of the flatness of the sample materials.

Erroneous readings can be generated if light enters at a different angle since the light might miss the center of the specimen. Great care was placed in the construction of the light source and all receiving area couplings to ensure that the light beam always enters normally and directly to the specimen center. Due to the machining process of the hemispherical shell, the scattering or receiving angles (see figure 4.2) have an average deviation of ±¼ of a degree (±0.005 radians) with respect to the exact values of the S_4 approximation. The contribution of this angular uncertainty and the solid angle uncertainty can be considered small since each detector has the same solid angle and a good size hole aperture that guarantees an that the filed of view of the detector include the entire sample irradiated area. However, this entire area might contain some small areas of the black surface where the samples are attached. This could contribute in the overall uncertainty of the reported reflectance values. The above factors, in addition to incident energy measurement, source and detector output variations (amplifier) and external set up components, add approximately 6% to the overall bias of the uncertainty.

In order to eliminate noise signal from the detectors and contamination by other types of incident light all measurements were taken at night in the previously darkened laboratory. In order to report accurate values of reflectance and to avoid noise equivalent reflectance (NEBRDF) the measured voltage readings were compared against voltage readings when no sample holder section is placed at the bottom of the hemispherical shell. Depending upon the type of source (especially the un-collimated one), some sensors detect incident light when no sample holder section was in place. These readings were subtracted from the actual sample readings in order to obtain the true reflectance for the respective sample.

To ensure more accurate and less noisy signals through the detectors, the signals were also recorded using Wavestart®, a software package that connected the oscilloscope with the PC. These readings were compared with the Labview™ readings and the less noisy signals were taken. By using a Gaussian filtering approach the signals were denoised to obtain a smooth reading without losing the inherent details of the main signal. An average of 1400 data points per sample was collected through the oscilloscope acquisition for each detector to guarantee uniformity of the signals.

The use of the reference standard can also be a factor that increments the uncertainty of the data. Bias of the signals was calculated for each one of the obtained readings. Combining all the factors mentioned above plus the bias of the detectors, and following the guidelines by Kim et al. [72] the calculated measurement uncertainty at 4.2 percent.

4.4 Results and Discussion

Reflectance function measurements were performed on a series of sample materials that form a composite fire barrier. These measurements include all twelve-port positions as incident angles. The samples were placed in the sample holder in the same direction in order to show if the anisotropy of the material possessed some effect in the reflectance.

In order to determine system effects between the insulation material and the metallic boundary or black boundary, biangular reflectance measurements were performed not only for the single materials but also for each one of the possible combinations among the material, i.e., aluminum - insulation material, black boundary - insulation, etc. The insulation material was rotated 90 degrees to determine if there was any influence in the orientation position while keeping the bottom surface at the same orientation. All results were normalized using the specular value of the Infragold® reflectance standard according to the incident port and light source used. However, in order to enhance the resolution of the results and reduce the uncertainty of the reflectance function of the Infragold® the data is re-normalized using the average of the hemispherical reflectance of the standard provided by the manufacture's calibration report.

Since the surface of the porous insulation is poorly defined, the physical thickness Xo is difficult to measure directly. Appendix B describes the method to determine this value and experimentally determine the respective optical thickness τ for the insulation samples, based on [79]. This range in thickness (between optically thin and optically thick) was designed to show effects of single and multiple scattering presented in this fire blanket.

4.4.1 Aluminum

Figures 4.8 through 4.11 show the experimental data for the refection function for different incident positions and different light sources. It is noted that due to the random distribution of the surface material the reflectance is different for opposite specular positions. This trend is similar for the rest incident position angles. The data also unveils a slight difference in reflection between the two wavelengths ranges. This difference is likely due to the fact that at longer wavelengths the surfaces tend to behave more specularly. However, due to the precision of the calculations, even a small difference is an indication of surface anisotropy (random orientation). Illuminating the sample with an un-collimated source does not provide sufficient evidence of surface description.

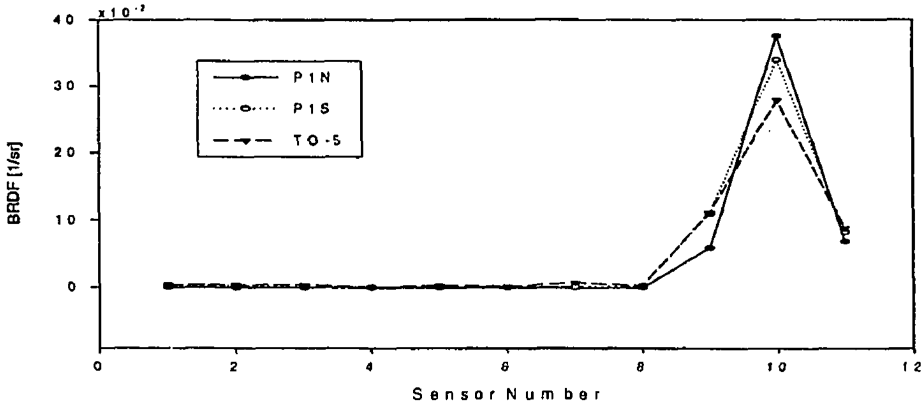

Figure 4.8 Biangular Ellipsometry reflectance as a function of the detector number of Aluminum foil using various light sources with incident angle of $\Theta = 25°, \Phi = 315°$ (Port 12)

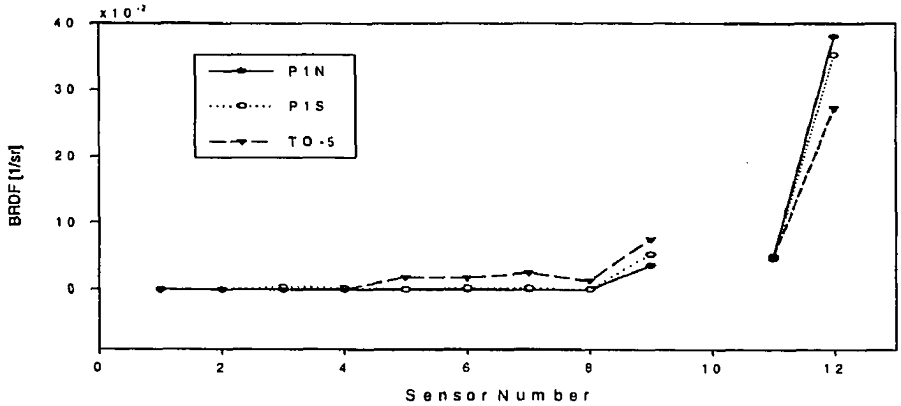

Figure 4.9 Biangular Ellipsometry reflectance as a function of the detector number of Aluminum foil using various light sources with incident angle of $\Theta = 25°, \Phi = 135°$ (Port 10)

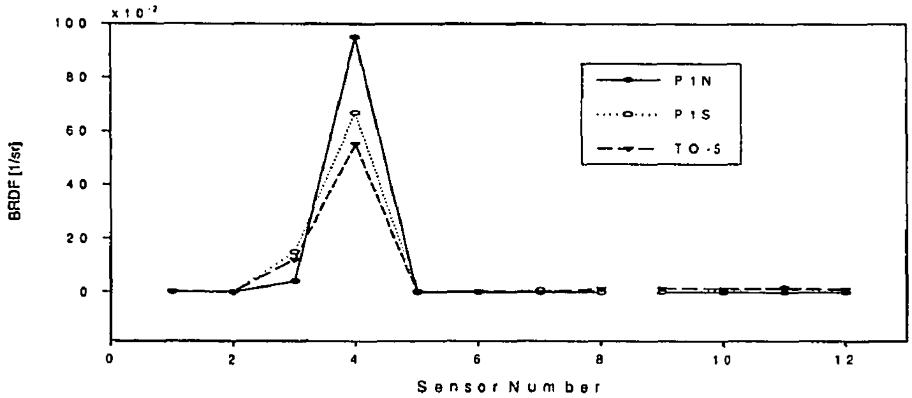

Figure 4.10 Biangular Ellipsometry reflectance as a function of the detector number of Aluminum foil using various light sources with incident angle of $\Theta = 73°, \Phi = 72°$ (Port 8)

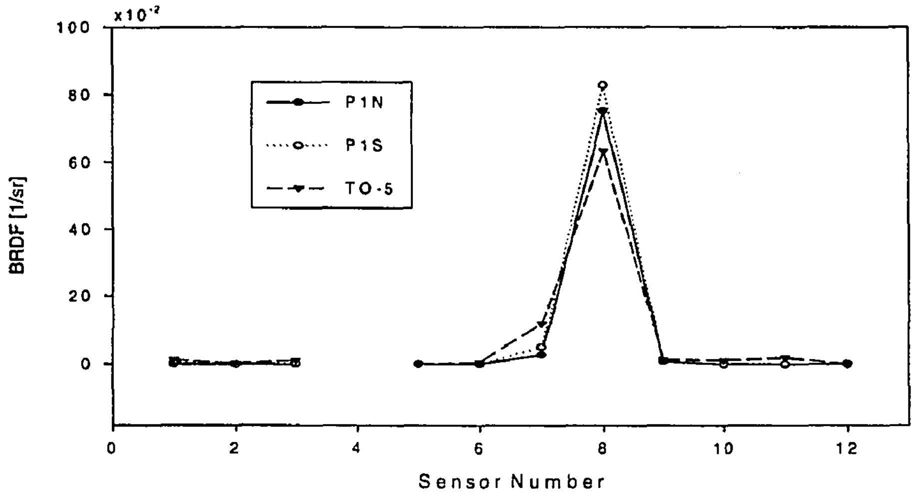

Figure 4.11 Biangular Ellipsometry reflectance as a function of the detector number of Aluminum foil using various light sources with incident angle of $\Theta = 73°, \Phi = 252°$ (Port 4)

4.4.2 Stainless Steel

As pointed out previously for the aluminum sample, the data obtained for the less rough steel foil follows the same trends with respect to the port positions. For this particular case, the angle positions of the quadrate reflect different trends in reflectance function. Since this material is less rough than the aluminum foil, the specular reflection effects depending upon the wavelength range are more noticeable than the aluminum foil. The data obtained for the 2-20 μm range are slightly bigger than the range from 2 to 5.25 μm, something that agrees with the literature data [14-20]. Also, the reflectance function obtained for angles of incidence for the upper positions of the S_4 quadrature are much lower than the respective reflectance function values of the mirror-like aluminum foil for the same positions. The inverse trend happens for the lower incident position angles since at these bigger incident polar angles, the surfaces tend to reach a specular behavior. That is, the more smooth the surface is, the bigger the reflection obtained, as shown in Figures 4.14 and 4.15 in comparison to 4.10 and 4.11

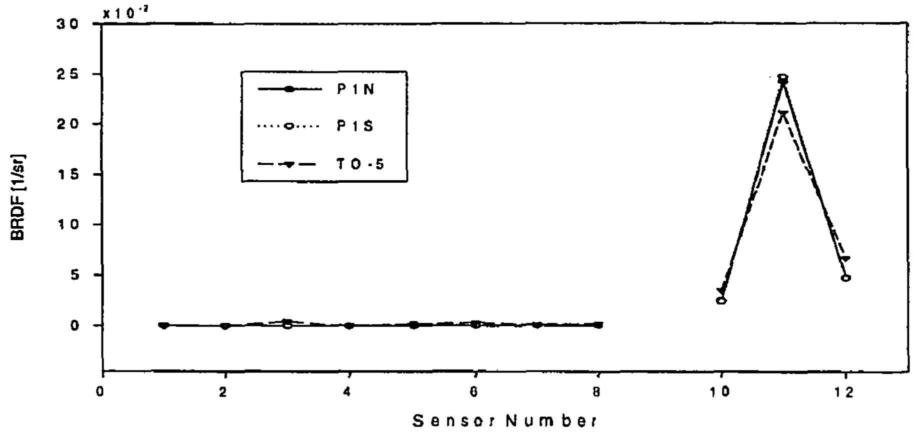

Figure 4.12 Biangular Ellipsometry reflectance as a function of the detector number of Stainless Steel foil using various light sources with incident angle of $\Theta = 25°, \Phi = 45°$ (Port 9)

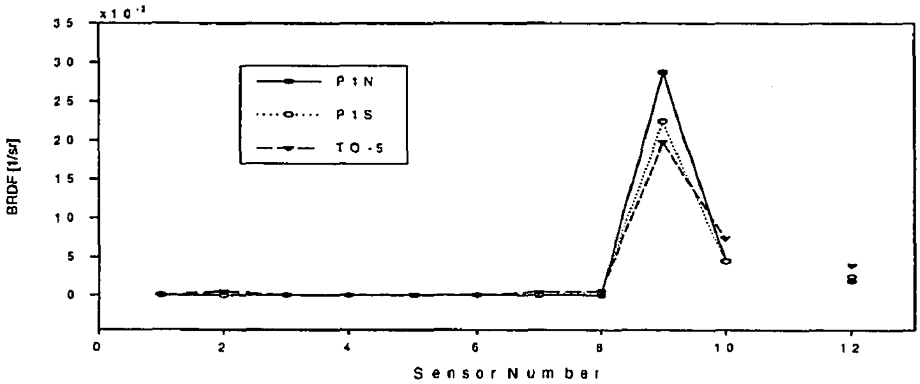

Figure 4.13 Biangular Ellipsometry reflectance as a function of the detector number of Stainless Steel foil using various light sources with incident angle of $\Theta = 25°, \Phi = 225°$ (Port 11)

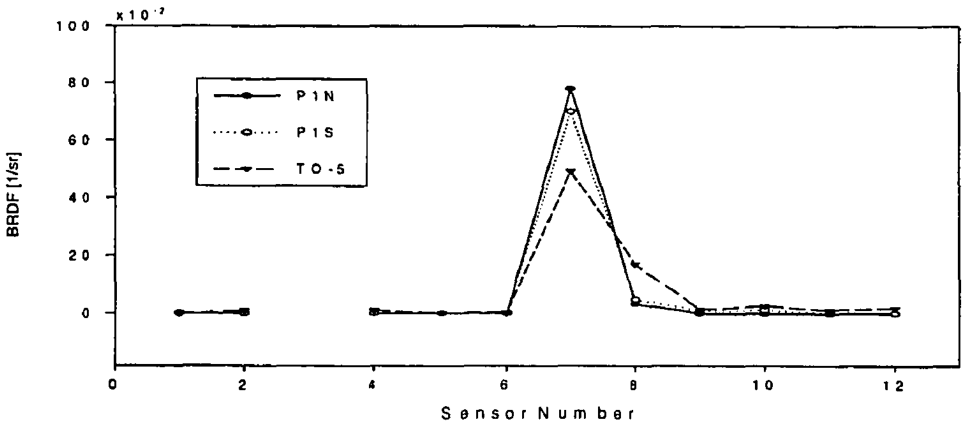

Figure 4.14 Biangular Ellipsometry reflectance as a function of the detector number of Stainless Steel foil using various light sources with incident angle of $\Theta = 73°, \Phi = 288°$ (Port 3)

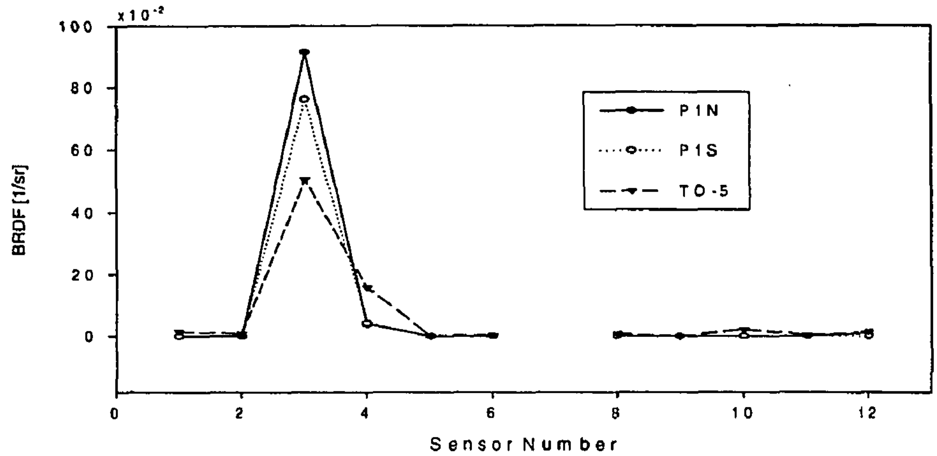

Figure 4.15 Biangular Ellipsometry reflectance as a function of the detector number of Stainless Steel foil using various light sources with incident angle of $\Theta = 73^{\circ}, \Phi = 108^{\circ}$ (Port 7)

4.4.3 Black Anodized Aluminum Surface

As part of the reflection function analysis in the materials composing the fire barrier, a black anodized aluminum surface also underwent the same measurement of the reflection function since this one serves as a surface backing when analyzing the fiber insulation alone. This anodizing does not have the anti-reflecting coating characteristic that some other anodizing could have. Figure 4.16 shows an interesting feature of the reflectance function for this particular material when the incident angle is located at the upper positions of the hemispherical shell. For these four incident positions, the reflectance function produced for the ReflectIR-P1N (2-20μm) is lower than the other two type data produced by the other sources. This is contrary from the behavior exhibit by the two metallic surfaces. For the other lower positions the reflectance behavior with respect to wavelength range and angular positions the tendency is similar to the metallic surfaces. In spite of the black coating used to simulate a black body, the coating does not get rid of imperfections due to the machining of the metal pieces, a common incorrect perception of the general public, which lead to different values of reflectance depending upon the incident position.

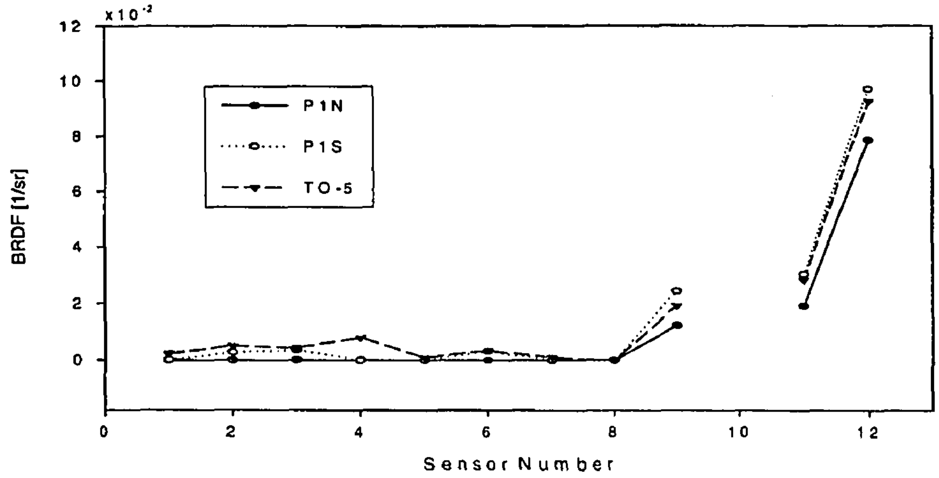

Figure 4.16 Biangular Ellipsometry reflectance as a function of the detector number of Black Anodized Aluminum Surface using various light sources with incident angle of $\Theta = 25^\circ, \Phi = 135^\circ$ (Port 10)

4.4.4 Fiber Insulation

Reflectance data were taken for the Durablanket® S fiber insulation for three different optical thicknesses using the different light sources. This reflectance data was taken using different materials as a backing as described above in the experimental design of the sample holder section, Figure 4.3. Table 4.3 shows the different types of optical insulation thicknesses and their designation according to their mass. Appendix B details the manner in which these were calculated.

Table 4.3 Durablanket® S Samples

Mass [g]	Xo [cm]	τ_o []	Designation $fvXo$
1.4	0.424	5.064	0.0181
0.8	0.242	3.759	0.0103
0.4	0.121	2.738	0.0052

Xo describes the measured and calculated thickness of each insulation sample. τ_o is the optical thickness of the insulation for these experimental measurements. The above designation [52] (fiber volume fraction-thickness product ($fvXo$) is chosen since it is adequate for analytical and numerical computations. fv is the fiber volumetric fraction of the insulation.

ReflectIR-P1N Source

Utilizing this collimated source at an emission temperature of 400°C, the reflectance function of the fiber insulation for the thickness of $fvXo$=0.0103 and 0.0181 with 3 types of different backings were measured through the hemispherical scatterometer.

This experimental data illustrates different features about the reflection function of the insulation material. Firstly, the effect of specimen orientation on reflectance function for the upper angles of the scatterometer is negligible, as shown in Figure 4.17. For the different optical thicknesses and type of backings, the reflectance was measured in two specific positions with the second rotated 90 degrees with respect of the first one.

Another feature of the above measurements is the small reflectance difference among the type of backings. This experimental data suggests that the backing influence on the insulation is small for the components of the fiber barrier. By also placing a surface backing beneath of an optically thin insulation, the behavior is the same as if it were an optically thick sample.

Figures 4.18 a) and b) show the difference in reflectance trend when the incident angle is located at the bottom part of the scatterometer. In this case, the reflectance trend follows a similar path for the different orientations but the values are bigger from one orientation to the other, for the different types of backings. For almost all incident angles when the metallic surfaces (Aluminum (AL) and Stainless Steel (SS)) act as surface insulation backings, the reflectance of the insulation tends to give a homogenous behavior, as opposed to what happens with the black (B) surface backings.

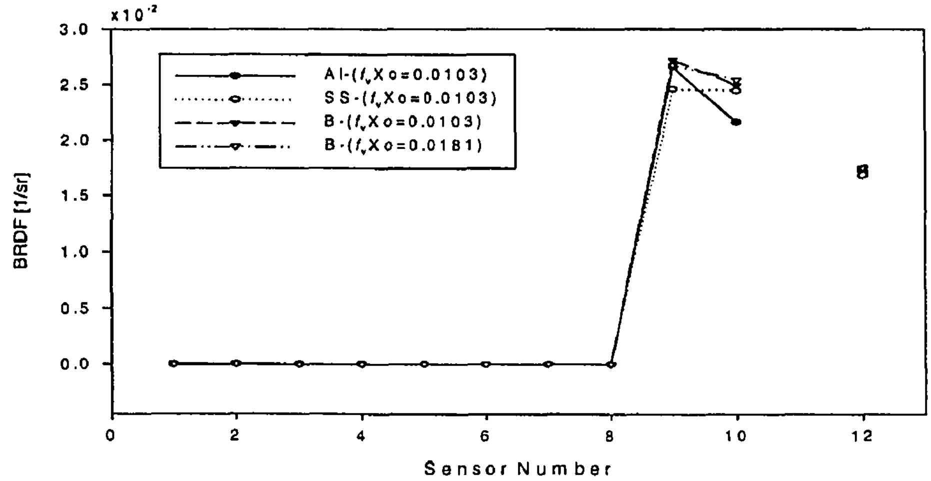

a)

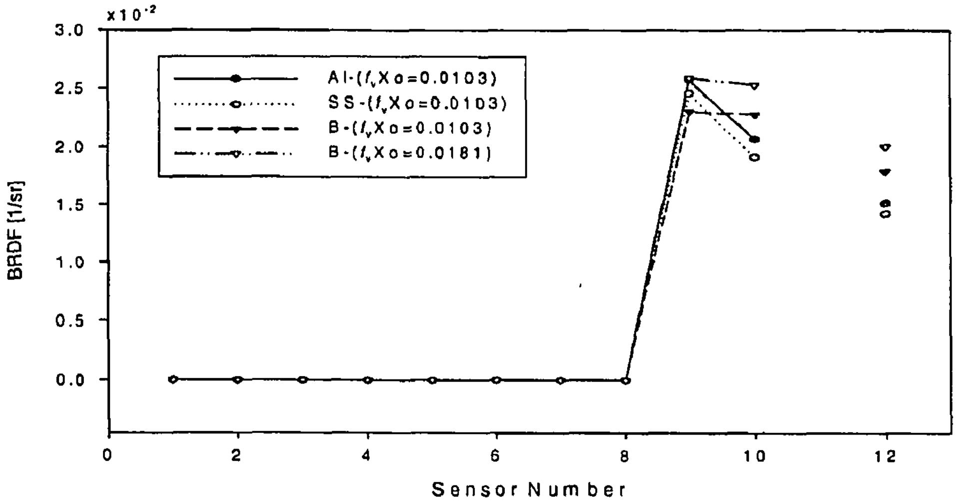

b)

Figure 4.17 Biangular Ellipsometry reflectance as a function of the detector number of Durablanket® S insulation using various backing (secondary) surfaces with incident angle of $\Theta = 25^{\circ}, \Phi = 225^{\circ}$ (Port 11). a) Position 1, b) Position 1+ 90° CW

ReflectIR-P1S Source

In spite of the 200°C of difference in the emission temperature from this collimated source, the behavior of the reflectance trend of the fiber insulation is similar for the different surface backings and orientation for the upper angles of the quadrature. Figure 4.19 presents the reflectance data among the combinations of fiber insulation and secondary surfaces. In this figure, it is seen that the backing makes an optically thin sample look like an optically thick one. The effect or fiber orientation with respect to the reflectance is small.

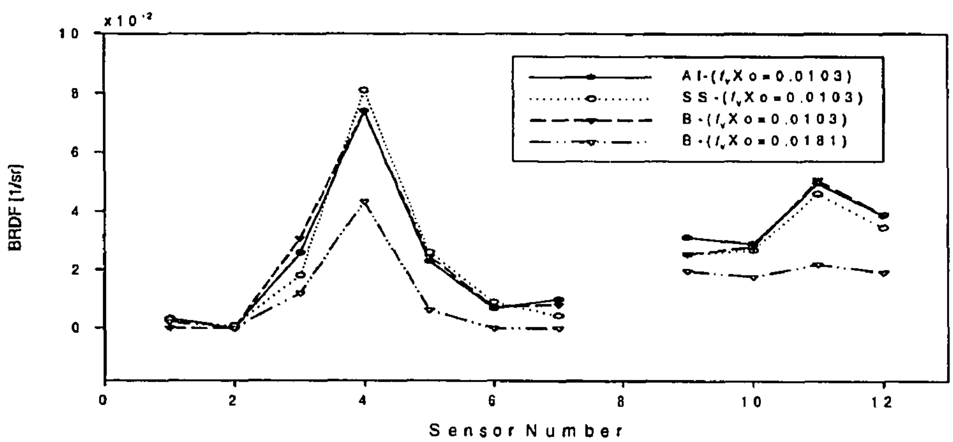

a)

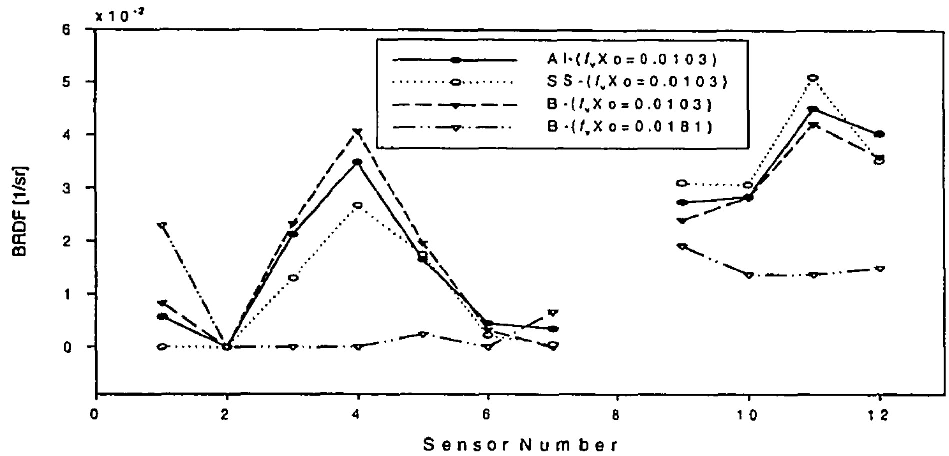

b)

Figure 4.18 Biangular Ellipsometry reflectance as a function of the detector number of Durablanket® S insulation using various backing (secondary) surfaces with incident angle of $\Theta = 73^{\circ}, \Phi = 72^{\circ}$ (Port 8). a) Position 1, b) Position 1+ 90° CW

For this spectral region, the insulation reflectance behavior trend was different when the angle of incidence was located at the bottom part of the scatterometer (see Figures 4.20 and 4.21). In some instances, difference of reflectance with respect to the orientation of the fiber was much more noticeable for some angles whereas in others that difference was small. However, there was always reflectance difference with respect to the orientation, something that agrees with the assumption of fibers randomly oriented.

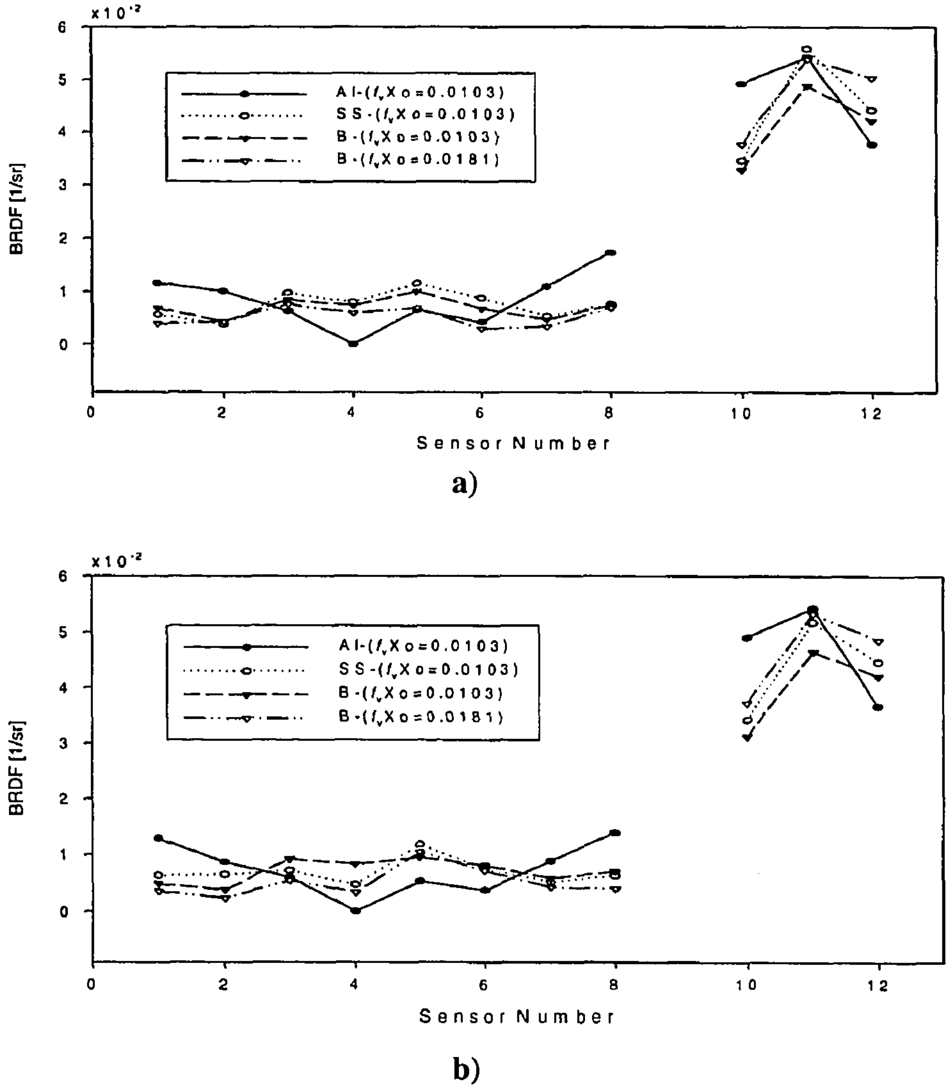

Figure 4.19 Biangular Ellipsometry reflectance as a function of the detector number of Durablanket® S insulation using various backing (secondary) surfaces with incident angle of $\Theta = 25^{\circ}, \Phi = 45^{\circ}$ (Port 9). a) Position 1, b) Position 1+ 90° CW

These experimental trials also show that for an optically thin sample ($fvXo$ =0.0052) there were non-zero values of reflectance around the hemisphere (with respect to the 12 quadrature points). Since this particular sample has more transmittance than the others, the backing (secondary) surface seems to enhance the relative reflection function of the insulation.

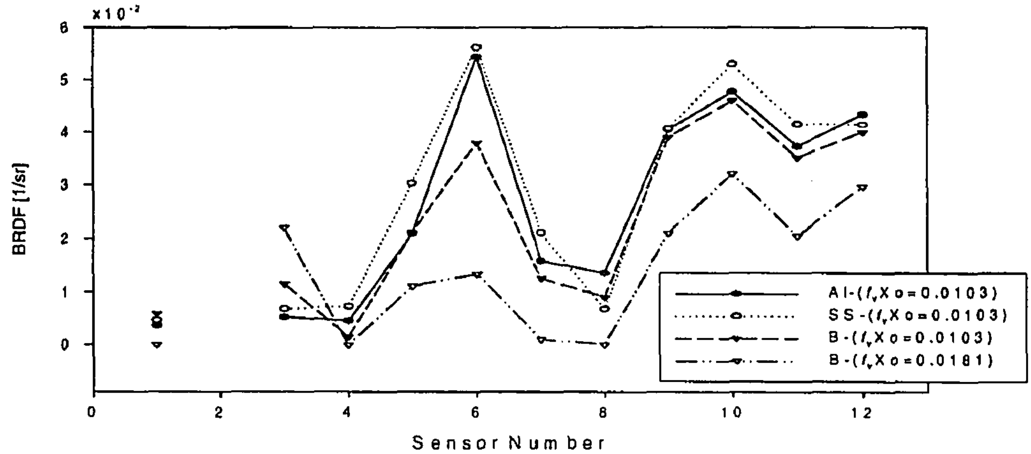

a)

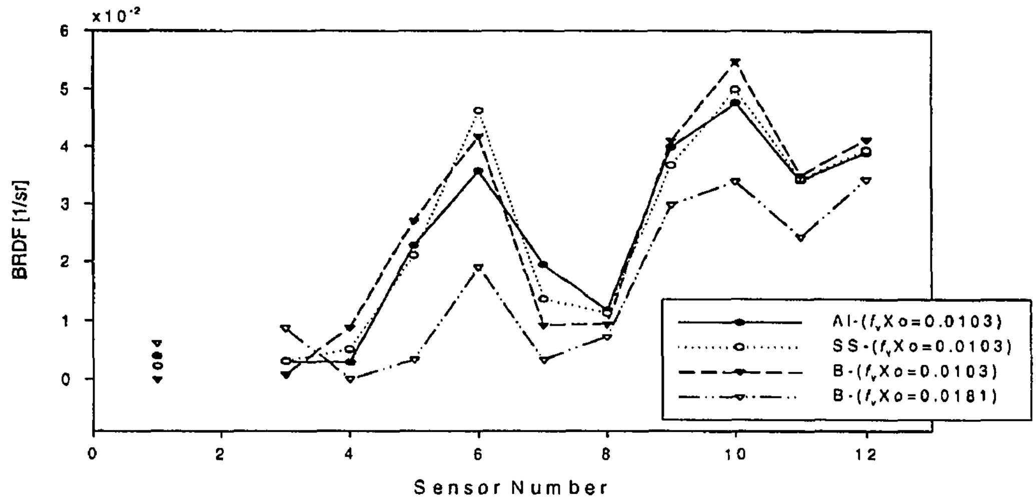

b)

Figure 4.20 Biangular Ellipsometry reflectance as a function of the detector number of Durablanket® S insulation using various backing (secondary) surfaces with incident angle of $\Theta = 73°, \Phi = 342°$ (Port 2). a) Position 1, b) Position 1+ 90° CW

TO-5 Source

Using an un-collimated infrared source at an emission of 600°C produced more homogenous reflectance values than the previous sources. This is due to the fact that the sample and some sensors are partially illuminated. In order to obtain the reflectance function for this source, the scattering data had to be subtracted from the reference data taken previously. Placing the source at each angle position in the shell and measuring the signal readings from the sensors when no sample holder was in place.

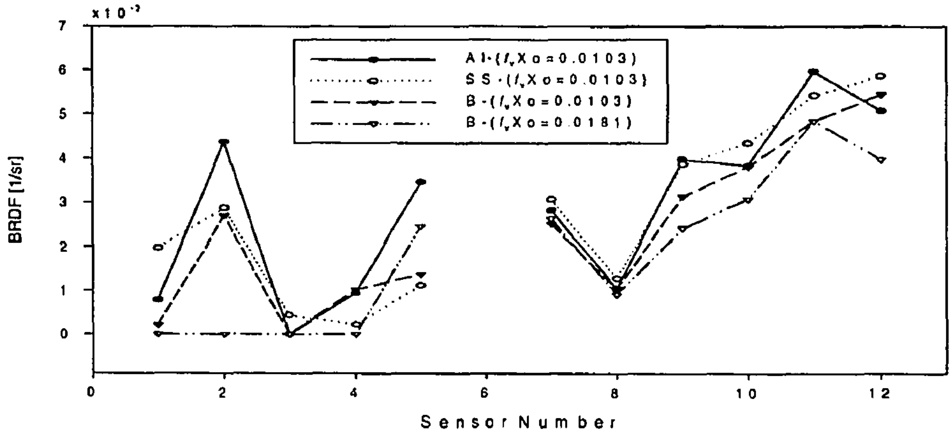

a)

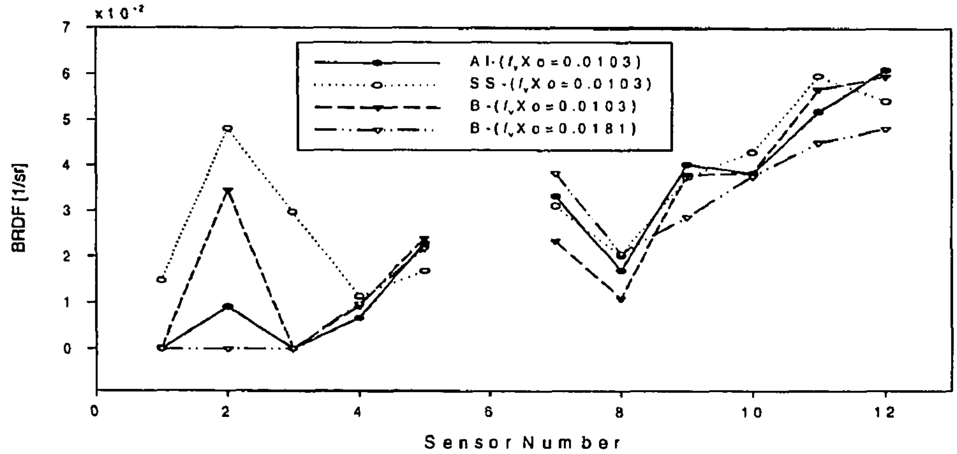

b)

Figure 4.21 Biangular Ellipsometry reflectance as a function of the detector number of Durablanket® S insulation using various backing (secondary) surfaces with incident angle of $\Theta = 73^\circ, \Phi = 162^\circ$ (Port 6). a) Position 1, b) Position 1+ 90° CW

As for the above data, Figure 4.21 shows that for the upper angles of the hemispherical shell the reflectance distribution function does not change with the orientation of the fiber. For the bottom angie positions, the data presented shows that, for most of the incident angle positions, the reflectance data follows a similar trend while for others the data between fiber orientations is sparse. However, this experimental data (Figure 4.22) demonstrates the bulk effects or fiber orientation with respect to the backing used.

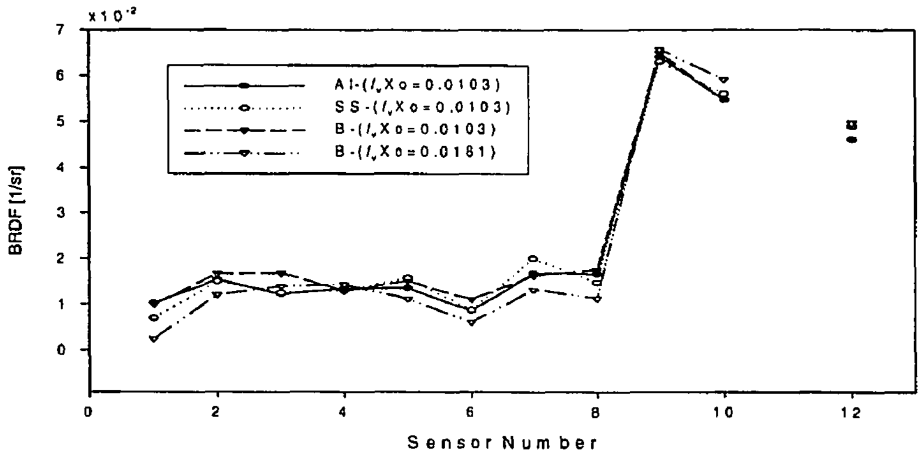

a)

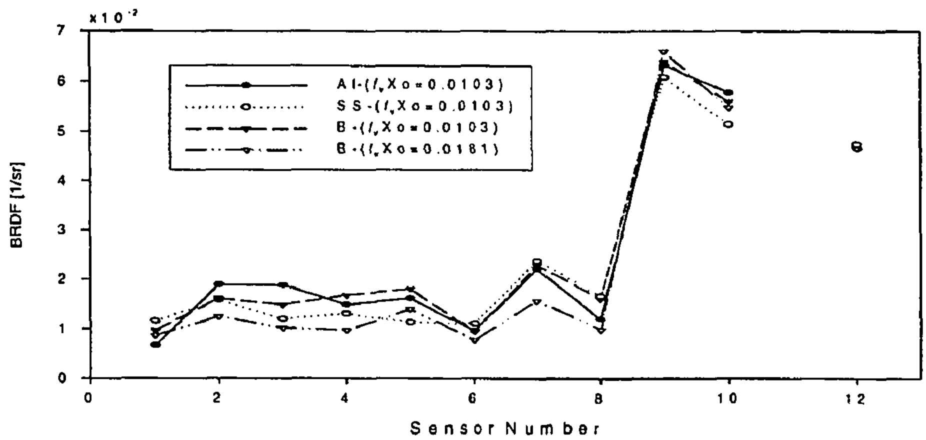

b)

Figure 4.22 Biangular Ellipsometry reflectance as a function of the detector number of Durablanket® S insulation using various backing (secondary) surfaces with incident angle of $\Theta = 25^{\circ}, \Phi = 225^{\circ}$ (Port 11). a) Position 1, b) Position 1+ 90° CW

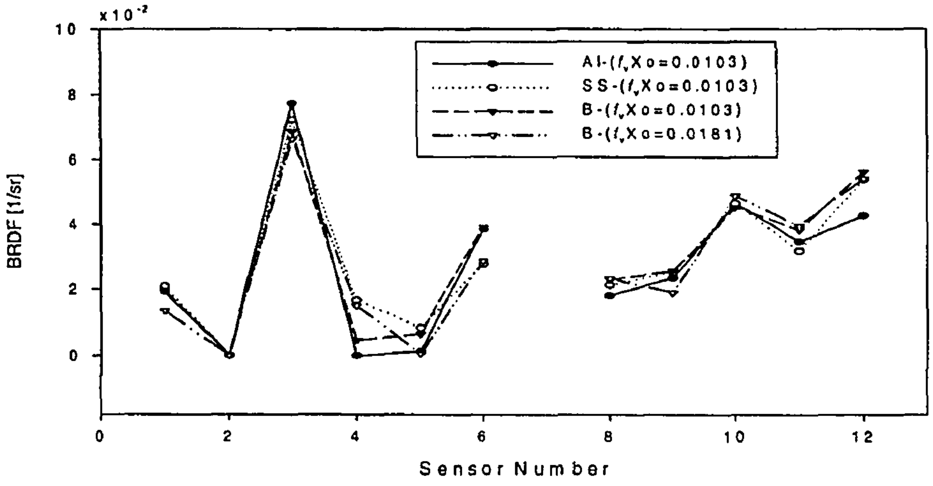

a)

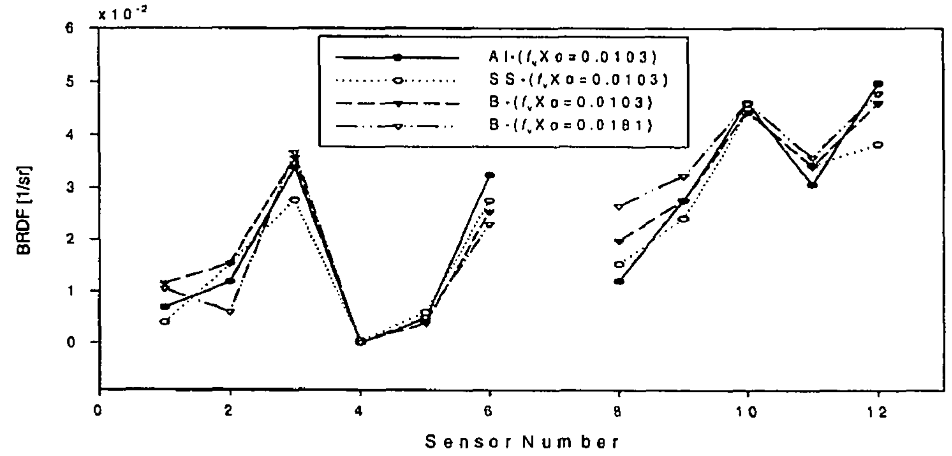

b)

Figure 4.23 Biangular Ellipsometry reflectance as a function of the detector number of Durablanket® S insulation using various backing (secondary) surfaces with incident angle of $\Theta = 73^{\circ}, \Phi = 108^{\circ}$ (Port 7). a) Position 1, b) Position 1+ 90° CW

4.5 Conclusions

The DOM-hemispherical scatterometer prototype has proved itself as a device to measure the reflectance function but also to investigate the surface defects and scattering effects in the infrared region. The versatility of choosing a discrete ordinates quadrature can make the apparatus as an experimental tool to be included in heat transfer calculations using the discrete ordinates method.

Despite the fact that the quadrature angles are similar for each quadrant, the experimental data has shown that there are preferential directions for scattering. For instance, angle positions labeled by port 1, 5 and, 7 always showed greater scattering values than the other ports. Perhaps these could be also enhanced by irregularities of the spinning of the shell. However, another possibility is that there exist preferential angles of scattering in the quadrature since for all light sources utilized in this research the same trend was observed for all sample materials. In order to better assess this claim, more in-depth experimentation must be carried out, perhaps using a bigger quadrature scheme, or a precision goniometer.

These results provide a simplified measure of scattering data for surface and pattern recognition and can be used as a reference tool for machining and surface finish process [76, 77] using gray scale data.

Measuring the reflectance data at each of the twelve port positions has produced an enormous amount of data that can be easily classified and retrieved as a reference tool for later use in any specific industrial, research, and academic investigation

By the use of the scatterometer it was discovered the manner in which a mirror-like surface behaved at different incident angles with respect to a much smoother one for the same incident angles. All metallic samples composing the fire barrier show a similar trend, which guarantees the uniformity of the data. Using the collimated light sources it was possible to assess a position, which produced the highest specular reflection. This in turn could be used to establish a position pattern of the fire barrier in order to increase its effectiveness.

By measuring the reflectance function of the fire insulation blanket it was possible to determine the preferable direction of scattering and the kind of fiber orientation. For this blanket, the SEM photography show that the fibers are nearly randomly oriented and the variability of the reflectance values around the hemisphere has proven this circumstance.

The type of surface backing has shown that an optically thin sample can be "enhanced" to become an optically thick sample. The above data has also demonstrated that placing a mirror like surface or a smooth surface instead of a regular material increases the reflectance of the incoming intensity of radiation.

Perhaps using a more collimated light source, such as a laser, could have better supported the data as stated before. The apparatus can easily be adapted more powerful type of sensors and light sources which in turn will make it as a important tool for studies purposes. Furthermore, increasing the quadrature scheme to a one of higher order will uncover more surface effects, i.e. off specular shifting and will be an excellent parameter for theoretical comparisons.

Finally, the changes with respect to the spectral bands are not strong and barely noticeable. As stated above, the results and claims will be greatly enhanced with the use of well define spectral sources.

CHAPTER 5

NUMERICAL ANALYSIS

This chapter presents the formulation for a rectangular Cartesian three-dimensional problem using the method of discrete ordinates. This formulation includes a linear anisotropic participating medium with biangular reflectance boundaries. Model and results have been obtained for the S_4 approximation, which can be extended easily to a different flux approximation.

Note that the experiment sample is a very short cylinder. To avoid edge effects and to simulate one-dimension the 3-D rectangular model is used instead of cylindrical, for ease of application. A 3-D model is needed to allow non-axisymetric angular simulation even for a quasi-one-dimensional geometry. In this chapter a similar 1-D problem is also posed based on published results for comparison of 3-D that requires some averaging of radiative intensity (for 1-D).

Finally, a CFD package (FLUENT®) is used to predict thermal performance in a one-layer fire barrier inverted L-shape (corner) geometry exposed to fire conditions based on the E-119 ASTM standard fire procedure.

5.1 Introduction

The discrete ordinates method is an approach used extensively by the heat transfer community since the late 1980's, although developed almost more than 50 years ago for astrophysical radiation and neutron transport applications. The range of problems solved using this method is extensive, [70,80] from the analysis of nuclear reactor shielding [70] to the analysis of combustion furnaces [81]. The resulting numerical finite difference/quadrature solution of the RTE is simple and gives good accuracy.

The discrete ordinate method (DOM) gives a solution by solving the RTE for a scheme of directions that span the full range 4π [83]. The DOM has become one of the most popular current methods to solve radiative heat transfer problems involving scattering [84]. Due to its ease of application it can be incorporated with commercial CFD codes and it requires similar formulation if accuracy needs to be increased.

Early application of DOM noted a redistribution of radiative energy in angular directions unless careful attention was given to representation of angular integration. Such effects sires in the ray effects problems involving directed beams in multi-dimensional geometries (such as with lasers), and Fresnel type reflective boundaries. Enhancements of the DOM have been applied to overcome these effects [84] by splitting the directional integrals into sub-intervals taking into account the critical angles.

Since the DOM has been tested and applied in many radiation problems, the objective of this work is to enhance the use of the method to solve radiative heat transfer problems in which realistic biangular reflectance boundary conditions exits. The concept is to better match experiment and theory. Several numerical schemes in which a biangular reflectivity or Fresnel type boundary is applied have been developed for one-dimensional Cartesian geometries [85-87] and cylindrical coordinates [84]. Roux et al. [85] make use of discrete ordinates method to obtain biangular reflectance on a 1-D substrate. Using the Ambarzumian's method, Rokhasaz et al. [86] obtain a solution for radiative transfer within a homogeneous, 1-D absorbing, isotropically scattering media with reflecting interfaces. An enhancement of the discrete ordinate method (DOM) was proposed for a radiative transfer medium with Fresnel boundaries [87]. This current work applies DOM to three-dimensional problems in a participating medium by using a combination of a control volume formulation with a method to avoid singularities in the RTE. The RTE is used with a completely symmetric angular quadrature scheme. Although this type of formulation is only applied to rectangular coordinates, it can be extended to any geometry.

By using the BRDF obtained from the previous chapter, the heat transfer analysis for a fire barrier or to any of its components can be enhanced in order to get a more exact prediction of the radiation heat transfer phenomena. Stability and accuracy of the solution is discussed for the problems presented here. Advantages and shortcomings of the solution are also noted.

5.2 Descriptive Analysis

Considering the solution of the radiative heat transfer equation (RTE) in a rectangular enclosure containing a participating medium as shown in Figure 5.1. The RTE for this type of configuration cam be written as:

$$(\Omega \bullet \nabla) I_\lambda(r,\Omega) = -(\kappa_\lambda + \sigma_{s\lambda}) I_\lambda(r,\Omega) + \kappa_\lambda I_b(r) + \frac{\sigma_{s\lambda}}{4\pi} \int_{\Omega' \to 4\pi} I_\lambda(r,\Omega) P(\Omega' \to \Omega) d\Omega' \quad (5.1)$$

where $P(\Omega' \to \Omega)$ is the phase function of radiative energy transfer from the incident direction Ω' to the scattered Ω direction as depicted in Figure 5.1. The intensity of black body radiation for the medium at a given temperature is defined by the symbol $I_b(r)$; the spectral radiation heat transfer coefficients are defined by the scattering coefficient $\sigma_{s\lambda}$ and the absorption coefficient κ_λ, where the sum of the two yields the spectral extinction coefficient β_λ.

The Biangular Reflectance Distribution Function (BRDF) governs non-ideal radiative reflective properties. The boundary condition for intensity when the reflector is an opaque surface with arbitrary properties [5] can be written as:

$$I_\lambda(r,\Omega) = \varepsilon_\lambda I_b(r) + \int_{\Omega'<0} |n \bullet \Omega'| \rho''_\lambda(r,\Omega',\Omega) I_\lambda(r,\Omega') d\Omega' \quad (5.2a)$$

where $I_\lambda(r,\Omega)$ is the intensity leaving a surface at a certain boundary location, $\rho(r,\Omega',\Omega)$ is the biangular reflectance distribution function, n is the unit normal vector at the boundary location, and ε_λ is the emissivity of the surface.

However, the above equation cannot directly handle specularly reflecting surfaces [1] unless some modifications are made. For such cases, the boundary conditions of the problem must be restated as [5]:

$$I_\lambda(r,\Omega) = \varepsilon_\lambda I_b(r) + \rho^s(r) I_\lambda(r,\Omega_s) + \frac{\rho^d(r)}{\pi} \int_{\Omega'<0} |n \bullet \Omega'| I_\lambda(r,\Omega') d\Omega' \quad (5.2b)$$

where Ω_s is the "specular direction, defined as the direction from which a light beam must it the surface in order to travel into the direction Ω after the specular reflection [5].

5.2.1 Discrete Ordinates Method

Following Fiveland's development [80], Equation 5.1 in Cartesian coordinates can be written for monochromatic or for gray radiation as:

$$\xi\frac{\partial I}{\partial x}+\eta\frac{\partial I}{\partial y}+\mu\frac{\partial I}{\partial z}=-\beta I+\frac{\sigma_s}{4\pi}\int_{4\pi}P(\Omega\rightarrow\Omega')Id\Omega+\kappa I_b \tag{5.3}$$

where the phase function is approximated to a linear anisotropic phase function as shown in Equation 3.6. The S_N approximation of Equation 4.1 in the m direction can expressed as:

$$\xi_m\frac{\partial I_m}{\partial x}+\eta_m\frac{\partial I_m}{\partial y}+\mu_m\frac{\partial I_m}{\partial z}=-\beta I_m+S_m \tag{5.4}$$

where the source function term S_m, representing radiation entering a beam in the m direction, in Equation 4.2 is approximated by:

$$S_m=\kappa I_b+\frac{\sigma_s}{4\pi}\sum_{m'}\varpi_{m'}(1+a_1(\xi_m\xi_{m'}+\eta_m\eta_{m'}+\mu_m\mu_{m'})I_{m'} \tag{5.5}$$

For a discrete direction, Ω_m, the values of ξ_m, η_m, and μ_m define the direction cosines of Ω obeying the condition $\xi_m^2+\eta_m^2+\mu_m^2=1$. The prime in Equation 5.5 denotes the direction of incoming radiation contributing to the m direction.

The discrete boundary conditions can be formulated such i.e., for a non-emitting reflecting west boundary:

$$I^m(r,\Omega)=\sum_{\substack{m' \\ \eta_{m'}<0}}\varpi_{m'}\eta_{m'}\rho''(r,m',m)I^{m'} \qquad y=0 \tag{5.6}$$

The second term of the right hand side in Equation (5.6) represents the reflected radiation flux, extended over the 2π incoming directions.

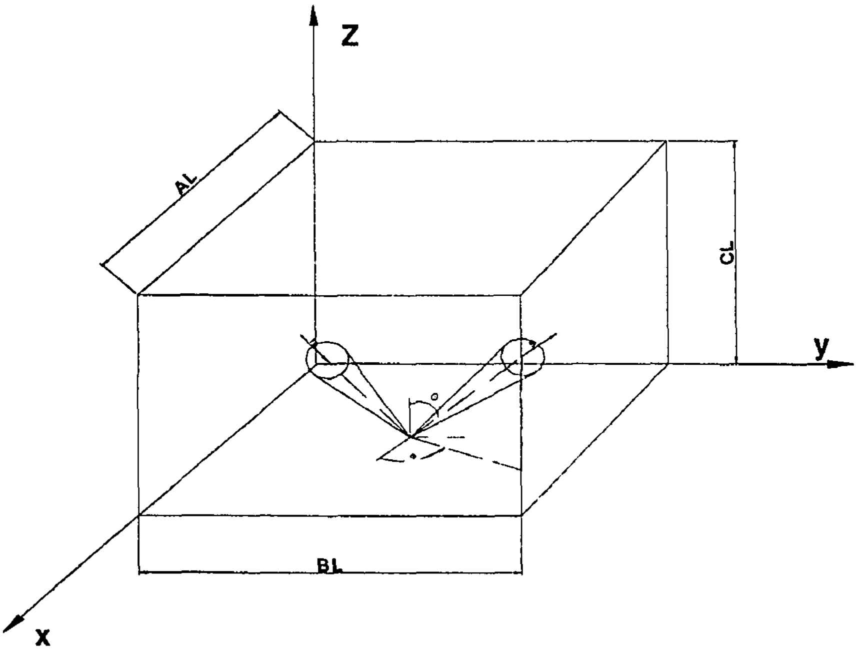

Figure 5.1 Rectangular Coordinate System

For a specular and diffuse reflecting surface on the west wall boundary, Equation 5.2b is transformed as:

$$I^{m}(r,\Omega)=\varepsilon I_{b}+\frac{\rho^{d}}{\pi}\sum_{\substack{m' \\ \eta_{m'}<0}}\varpi_{m'}.\eta_{m'}.I^{m'}+\rho^{s}I_{m^{s}} \tag{5.7}$$

with $I_{m^{s}}$ as the intensity leaving in the specular direction. Note that, in general, it is not possible to numerically extract the specular term from the bi-directional term under the integral in Equation 5.6. Therefore, the specular angle must be manually removed even if the reflectance remains under the integral.

5.2.2 Discretization of Equations

Integrating Equation 5.4 over the control volume depicted in Figure 5.2, a discretized equation is generated as

$$\xi_m A_x\left(I_f^m - I_b^m\right) + \eta_m B_y\left(I_e^m - I_w^m\right) + \mu_m C_z\left(I_n^m - I_s^m\right) =$$
$$-\beta V_p I_p^m + \kappa V_p I_{bp} + V_p \frac{\sigma_s}{4\pi}\sum_{m'} \varpi_{m'} P(m',m) I_p^{m'} \tag{5.8}$$

where A_x, B_y, and C_z are the control volume areas normal to the axis and V_p is the volume of the control at the point of analysis.

Each of the control volume intensities can be related to one another by interpolation as the following equation [80, 83, 84]

$$I_p^m = \Psi I_f^m + (1-\Psi) I_b^m = \Psi I_n^m + (1-\Psi) I_s^m = \Psi I_e^m + (1-\Psi) I_w^m \tag{5.9}$$

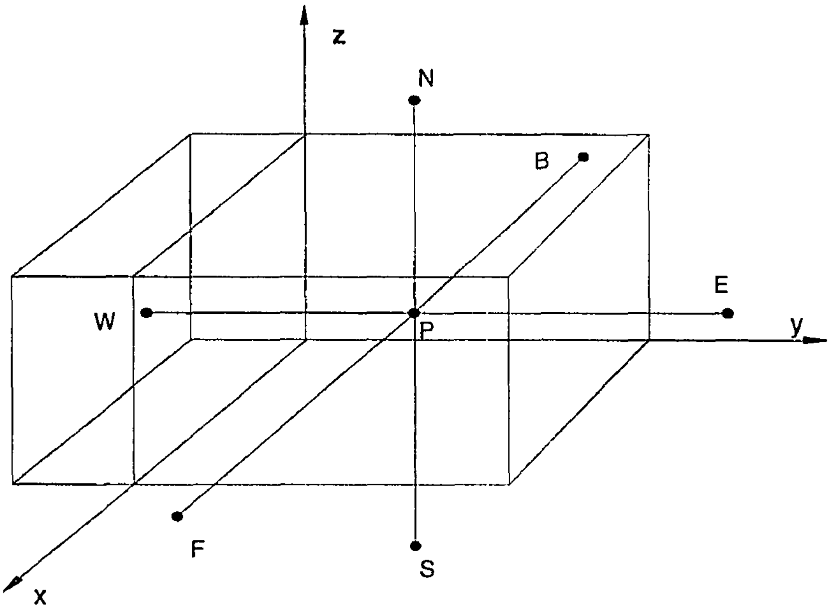

Figure 5.2 Control Volumes

The above equations are used to solve for the unknown intensities at the forward, north, and east sides of each one of the control volumes that compose the medium. Thus,

$$I_p^m = \frac{\xi_m A_x I_b^m + \eta_m B_y I_w^m + \mu_m C_z I_s^m + \Psi S_m V_p}{\xi_m A_x + \eta_m B_y + \mu_m C_z + \Psi \beta V_p} \tag{5.10}$$

where the quantity S_m is defined by Equation 5.5.

Positive direction cosines are to be used in Equation 5.14. The scalar ψ represents a differencing scheme. For ψ = ½ Lathrop's [70] second order differencing scheme is obtained. Different schemes are obtained for ½ < ψ < 1.

5.2.3 Solution

Continuing using reference [80], Equation 5.10 is re-written with the aim to preserve stability while using different types of quadrature schemes

$$I_p^m = \frac{|\xi_m| A_x I_x^m + |\eta_m| B_y I_y^m + |\mu_m| C_z I_z^m + \Psi S_m V_p}{|\xi_m| A_x + |\eta_m| B_y + |\mu_m| C_z + \Psi \beta V_p} \tag{5.11}$$

with

$$I_p^m = \Psi I_{ie}^m + (1-\Psi) I_{ir}^m \tag{5.12}$$

Subscript i in the above equation symbolizes one of the three coordinate directions (x, y, z) whereas e and r stand for end and reference face values of the coordinate cell.

To avoid singularities while using some direction schemes, the radiation intensity in Equation 5.1 is split into eight octants [88]; this is equivalent to applying the absolute values in Equation 5.11. Intensities for each of the octants, A through H, are denoted and described in Appendix C where A represents the natural (x, y, z) octant arising from positive direction cosines.

Thus, eight sets of intensity equations based on Equation. 5.12 can be created. For instance, the intensity equation for octant 1 would be

$$A_p^m = \frac{|\xi_m| A_x A_b^m + |\eta_m| B_y A_b^m + |\mu_m| C_z W_s^m + \Psi S_m V_p}{|\xi_m| A_x + |\eta_m| B_y + |\mu_m| C_z + \Psi \beta V_p} \tag{5.13}$$

with

$$A_p^m = \Psi A_f^m + (1-\Psi) A_b^m = \Psi A_n^m + (1-\Psi) A_s^m = \Psi A_e^m + (1-\Psi) A_w^m \tag{5.14}$$

and $$I(x,y,z,\theta,\Phi) = A(x,y,z,\theta,\Phi)\,;\ 0<\theta<\pi/2\,;\ 0<\Phi<\pi/2$$

where the reference faces for octant 1 are the backward, south, and west sides of the cubical geometry. For the other octal intensities the equations would look similar to Equation 5.18 and 5.19 but the reference faces are the faces adjacent to the axis of the coordinate systems according to Figure 5.3, and as shown on Appendix C.

Using the new set of octal intensities Equation 5.5 can be expanded to obtain:

$$S_{ip}^{m} = \kappa I_b + \frac{\sigma_s}{4\pi}\Big[\sum_{m'} \varpi_{m'}(1 + a_1(\xi_m\xi_{m'} + \eta_m\eta_{m'} + \mu_m\mu_{m'}))\cdot (A_p^{m'} + B_p^{m'} + C_p^{m'} + D_p^{m'} + E_p^{m'} + F_p^{m'} + G_p^{m'} + H_p^{m'})\Big] \tag{5.15}$$

where i represents the octal intensity (from A to H) in this discussion. Equation 5.15 must be set for each one of the eight octal intensities in order to account for the angular variation in linear anisotropic phase function. Appendix C shows the description for each one of the octal source functions in which the same development is done for the rest of the source functions except that the signs of the director cosines change in relation to the specific intensity in consideration.

As seen for Equations 5.11 through 5.15, for each of the cosines directions, there is an iterative solution since the source term is dependent of the intensity of radiation.

5.2.3.1 S_4 Approximation

In the previous chapter a quadrature scheme was chosen due to its unique qualities to integrate the source function for a good variety of phase functions, including simple scattering functions as the linear anisotropic scattering phase function. This quadrature scheme establishes three directions per octant to make a total of 12 for a hemisphere from which the boundary analysis is made.

To explain the above concept further, the boundary condition at the west side is expanded. The octal incident and leaving intensities at the west boundary are the intensities pointing at the negative and positive y direction respectively. Thus,

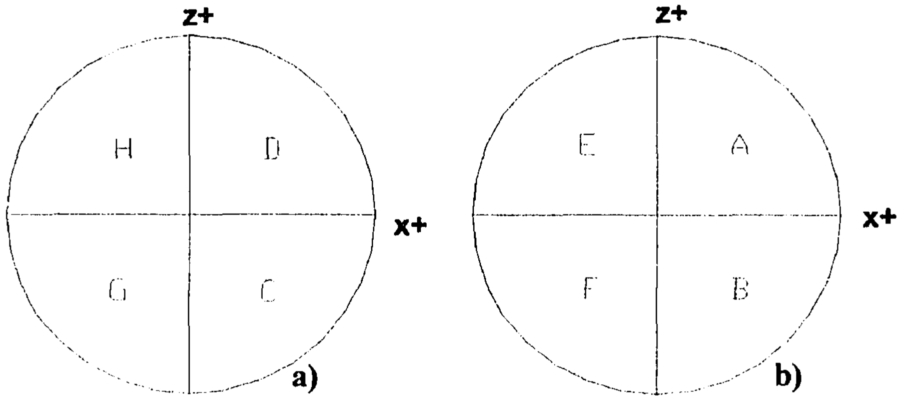

Figure 5.3 a) Incident and b) Leaving Octal Intensities at the West Boundary Side

For leaving intensity A, with BRDF Equation 5.8 is transformed into:

$$A_p^m(r,\Omega) = \sum_{\substack{m' \\ \eta_{m'}<0}} \varpi_{m'}\eta_{m'}\rho''(r_p, m', m)\left[C_p^{m'} + D_p^{m'} + G_p^{m'} + H_p^{m'}\right] \tag{5.16}$$

where r_p symbolizes that the reflectivity depends also of the octal intensity. Separating the second term of right hand side of Equation 5.21 into its components, then for the S_4 approximation one obtains

$$\sum_{\substack{m' \\ \eta_{m'}<0}} \varpi_{m'}\eta_{m'}\left[\rho_C(m',m)C_p^{m'} + \rho_D(m',m)D_p^{m'} + \rho_G(m',m)G_p^{m'} + \rho_H(m',m)H_p^{m'}\right] \tag{5.17}$$

Expanding for all leaving and incident directions, one obtains (see Appendix C), a directional reflectance matrix that considers the reflection from all incident and leaving intensities. Thus, the biangular reflectance distribution function for a particular octal intensity can be represented as a uniform matrix

$$\rho_{i,l}(\Omega_{m'},\Omega_m) = \begin{bmatrix} \rho_{i,l}(1,1) & \rho_{i,l}(1,2) & \rho_{i,l}(1,3) \\ \rho_{i,l}(2,1) & \rho_{i,l}(2,2) & \rho_{i,l}(2,3) \\ \rho_{i,l}(3,1) & \rho_{i,l}(3,2) & \rho_{i,l}(3,3) \end{bmatrix} \tag{5.18}$$

with i representing the boundary side of incidence and l representing the intensity striking the wall of incidence i. There are 144 possible reflectance combinations in a boundary, including 12 of retro-reflection. These reflectance directions are expressed in 16 - 3x3 matrices, which will complete the 144-reflectance combinations.

For the specularly reflecting, diffusively emitting opaque boundary conditions model, the boundary is discretized by taking into account the incoming direction intensity for the respective octant that will produce a specular reflection at the octal concerning the boundary and summing all contributions for diffuse reflection. At the west boundary wall, intensity A is formulated as:

$$A_w^m = \varepsilon I_b + \rho^s H_p^m + \frac{\rho^d}{\pi} \sum_{\substack{m' \\ \eta_{m'}<0}} \varpi_{m'} \eta_{m'} \left[C_p^{m'} + D_p^{m'} + G_p^{m'} + H_p^{m'} \right] \tag{5.20}$$

Intensity H_p^m is the intensity that will produce a specular reflection leaving in direction of A_w^m. This intensity was selected by taking into account the spherical geometry of radiation intensities (all octal intensities forming a sphere), and the plane of incidence of the specular ray leaving in the desired direction of intensity A. Section 3 in Appendix C describes the rest of the specularly reflecting, diffusively emitting opaque boundary conditions.

Since the solution in DOM is through continuous iteration, the calculations must be performed by step-by-step process in which the source term is initially set to zero and the walls conditions are radiatively black. After center node calculations are obtained for each one of the directions coordinates (ξ_m, η_m, μ_m) the source term and incident radiation are re-calculated. Scattering and boundaries are introduced in subsequent iterations. Comparisons for the source term and incident radiation for current and previous iterations are made until convergence agreement of less than 0.01%.

To ensure a stable solution two procedures have been established. The first step is to make zero all negative intensities encountered in the solution and also to avoid unwanted oscillations due to the finite differencing procedure (computational grid domain), the following standards are set as [80]

$$\Delta x < \frac{|\xi|}{\beta(1-\Psi)}\varphi \quad ; \quad \Delta y < \frac{|\eta|}{\beta(1-\Psi)}\varphi \quad ; \quad \Delta z < \frac{|\mu|}{\beta(1-\Psi)}\varphi \tag{5.21a}$$

where

$$\varphi = \frac{\Psi^3 + (1-\Psi)^2(2-5\Psi)}{\Psi} \tag{5.21b}$$

Equations 5.21 ensure that physically unwanted intensities will not occur. A caveat about this set of criteria is that in one or two-dimensional problems they must be modified in order to obtain a solution. To ensure an accurate solution a successively finer grid domain should be used to compare with others such that when small variations are presented a solution can be considered physically realistic.

Once the intensity distribution along the center nodes is determined, quantities of engineering interest (i.e. heat flux, incident intensity, source term distributions) are readily computed. For instance, the heat flux at the positive and negative z directions in terms of the octal intensities are:

$$q_z^+ = \sum_m \varpi_m \mu_m \left(A_p^m + D_p^m + E_p^m + H_p^m\right) \tag{5.23}$$

$$q_z^- = \sum_m \varpi_m \mu_m \left(B_p^m + C_p^m + F_p^m + G_p^m\right) \tag{5.24}$$

where the net radiation heat flux is calculated as $q_z^{net} = q_z^+ - q_z^-$. The above procedure, with appropriate direction cosines, is applied to the heat fluxes in the x and y directions.

Finally, the incident radiation distribution in terms of octal intensities and the quadrature scheme is

$$\overline{G} = \sum_m \varpi_m (A_p^m + B_p^m + C_p^m + D_p^m + E_p^m + F_p^m + G_p^m + H_p^m) \tag{5.25}$$

5.2 Performance Results

In order to assess the DOM basic performance, it has been evaluated and compared with some basic reliable cases [89-93] using the S_4 and S_8 quadrature.

The first test refers to a one-dimensional media for which different scattering albedo ω optical thickness, directional boundaries and type of scattering are used. The bottom wall of the 1-D medium is black with diffuse entering intensity equal to one while the opposite boundary is successively set to black, specular or diffuse boundary. Tables 5.1, and 5.2 verify the S_4 DOM results for transmissivity and reflectivity of a 3-D medium with dominant z direction against the one-dimensional exact solution or iterative solution for the isotropic and backward scattering [89].

Despite the fact that Sutton and Özisik [89] use Legendre polynomials to account for the scattering function, the linear anisotropic model follows their trend with an average error of approximately 5%. Figure 5.4 shows the comparison against the exact solution [3] for the hemispherical reflectivity for a purely scattering slab with anisotropic forward scattering (a_1=0.5) using the S_8 approximation using a 3D formulation with dominant z direction and a 1-D DOM formulation.

The second case is similar to case 1 but for a two dimensional medium. The results obtained with the S_4 method for dominant y and z directions agree well with the results found by Sutton and Özisik, [90]. Table 5.3 shows the comparison results.

The final benchmark result is for an absorbing-emitting cubic medium with an emissive power of unity. Boundary conditions are considered black and cold. A computational grid of 30x30x30 was selected. Figure 5.5 depicts the dimensionless surface radiative heat flux along the centerline of the north wall. The results are compared with the exact solution and several DOM approximate solutions [91, 92] for different optical thickness (τ_o).

Table 5.1 Comparisons of Hemispherical Transmissivity and Reflectivity for a 3D S_4 DOM results (with z dominant direction) with Sutton and Özisik [89] for Isotropic Scattering

	Wall Reflectivity			Hemispherical Reflectivity		Hemispherical Transmissivity	
τ_o	ρ_s	ρ_d	ω	Exact	3D	Exact	3D
2	0	0	0.7	0.2506	0.2521	0.1551	0.1549
2	0	0	0.8	0.3294	0.3281	0.1973	0.1937
5	0	0	0.9	0.4841	0.4722	0.0534	0.0551
5	0	0	1	0.7910	0.7787	0.2077	0.2001
2	0.5	0	0.7	0.2657	0.2678	0.0880	0.0877
2	0.5	0	0.8	0.3527	0.3522	0.1172	0.1140
5	0.5	0	0.9	0.4783	0.4742	0.0349	0.0353
5*	0.5	0	1	0.8264	0.8077	0.1696	0.1553
2	0	1.0	0.7	0.2827	0.2836	0.0	0.0017
2	0	1.0	0.8	0.3859	0.382	0.0	0.0017
5	0	1.0	0.9	0.4818	0.4777	0.0	0.0008
5*	0	1.0	1	0.9946	0.9138	0.0	0.0002

* Iterative solution with P-1 initial guess

Table 5.2 Comparisons of Hemispherical Transmissivity and Reflectivity for a 3D S_4 DOM results (with z dominant direction) with Sutton and Özisik [89] for anisotropic backward scattering (a_1=-0.8)

	Wall Reflectivity			Hemispherical Reflectivity		Hemispherical Transmissivity	
τ_o	ρ_s	ρ_d	ω	P-Eleven	3D	P-Eleven	3D
2	0	0	0.7	0.2805	0.2896	0.1373	0.1312
2	0	0	0.8	0.3594	0.3702	0.1738	0.1633
5	0	0	0.9	0.5072	0.5108	0.0280	0.0384
5	0	0	1	0.8190	0.8163	0.1810	0.1677
2	0.5	0	0.7	0.2909	0.3013	0.0793	0.0760
2	0.5	0	0.8	0.3791	0.3880	0.1053	0.0987
5	0.5	0	0.9	0.5072	0.5118	0.0280	0.0258
5	0.5	0	1	0.8471	0.8374	0.1529	0.1341
2	0	1.0	0.7	0.3049	0.3127	0.0	0.0026
2	0	1.0	0.8	0.4060	0.4092	0.0	0.0025
5	0	1.0	0.9	0.5096	0.5140	0.0	0.0010
5	0	1.0	1	1.0000	0.9293	0.0	0.0002

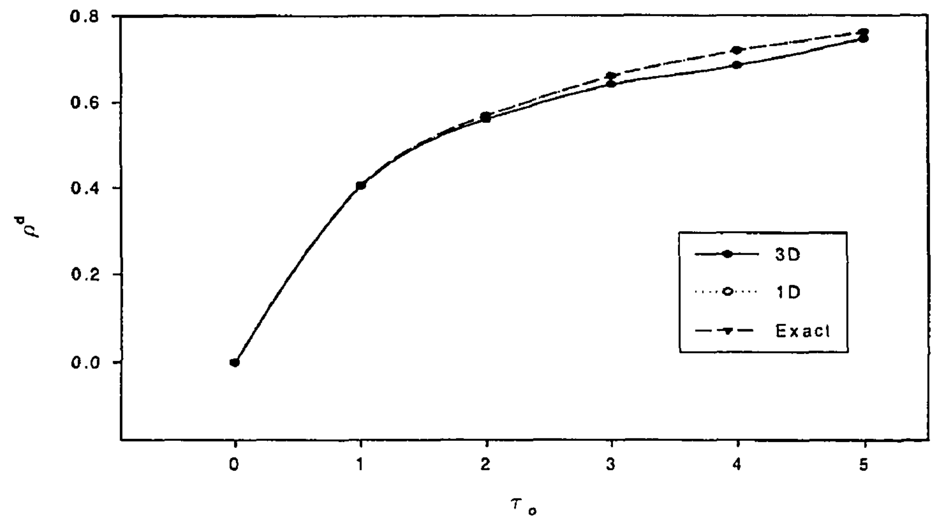

Figure 5.4 Comparison of Hemispherical Reflectivity for a slab with transparent boundaries for anisotropic forward scattering (a_1=0.5), with Özisik [3] for a phase function $1+a_1\mu$, using S_N method (N=8) for a 1D formulation and 3D formulation (Dominant z direction). (ω=1).

Table 5.3 Comparison of Transmissivity for a 3D S_4 DOM results (y and z dominant) with 2D results from Sutton and Özisik [90] results (isotropic scattering) AL=20, BL=2, CL=1, ω = 0.5

YL/BL	0.25		0.5		0.8		1	
ZL/CL	2D	3D	2D	3D	2D	3D	2D	3D
0	0.948	0.9359	0.914	-	0.898	-	0.981	-
0.25	0.63	0.6589	0.643	0.7199	0.6109	0.6776	0.331	0.3506
0.5	0.421	0.4468	0.455	0.4684	0.427	0.4536	0.229	0.2504
0.75	0.287	0.2917	0.321	0.3011	0.3079	0.2837	0.167	0.15
1	0.201	0.2623	0.23	0.2558	0.201	0.2708	0.123	0.1268

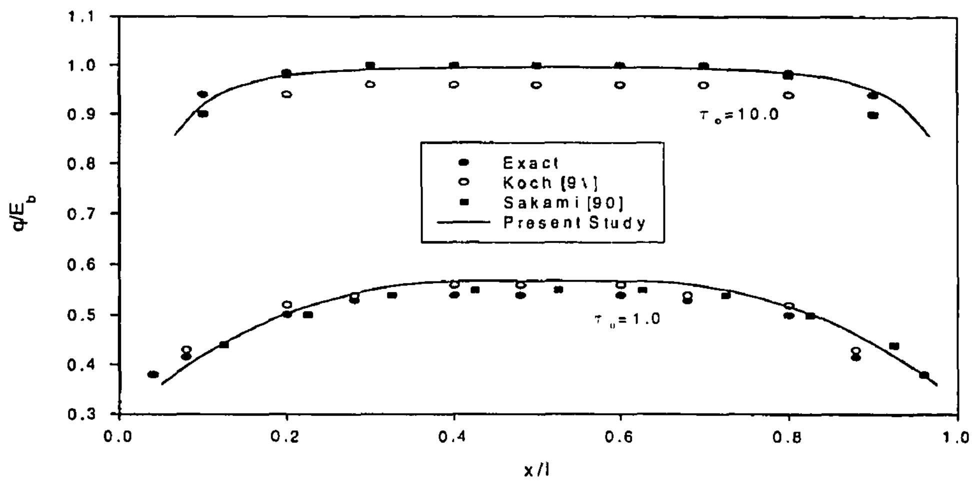

Figure 5.5 Heat Fluxes at Centerline of North Surface for a 3-Dimensional Media

These solutions agree really well with the cited references even for the higher optical dimension, which proves the accuracy of the code.

All the results shown above have a maximum discrepancy of nearly 5% in comparison to the exact solutions.

5.4 Treatment of Collimated Irradiation to Determine the Reflectance Function

There exist many situations when a collimated mono-directional flux is incident to a scattering boundary layer such as surface coatings, a planetary atmosphere, insulation shielding, etc. for which the radiation transfer is not azimuthally symmetric. For the current work, the experiment consists of this condition (while the motivating fire barrier problems does not).

Considering the problem of a collimated incident flux of magnitude q_o incident on a medium with suspended particles (or fibers) having a relative refractive index of unity with respect to the surrounding boundaries as depicted in Figure 5.6.

The direction of incidence is given by the coordinate system (ξ_o, η_o, μ_o). Treating the collimated irradiation flux as a source term in the transfer equation then $q_o \exp\left(\int \beta d(C_L - z) \right)$ is the attenuated flux at any specific depth. The contribution to the scattered radiation field in the direction (ξ_o, η_o, μ_o) is [95,96]

$$Sc = \frac{\sigma_s}{4\pi} P(\Omega' \rightarrow \Omega) q_o \exp\left(\int \beta d(C_L - z) \right) \tag{5.26}$$

and the RTE becomes

$$(\Omega \bullet \nabla) I_\lambda(r,\Omega) = -(\kappa_\lambda + \sigma_{s\lambda}) I_\lambda(r,\Omega) + \kappa_\lambda I_b(r) + \frac{\sigma_{s\lambda}}{4\pi} \int_{\Omega' \rightarrow 4\pi} I_\lambda(r,\Omega) P(\Omega' \rightarrow \Omega) d\Omega' + Sc \tag{5.27}$$

Discretizing the above equation leads to the same octal equations as shown before except that the source function will have the collimated term to be evaluated. Since the intensity was spilt into eight octants the collimated incident flux of magnitude q_o must also be divided into the same number of octants. Thus, Equation 5.15 is transformed into:

$$S_{ip}^{m} = \kappa I_b + \frac{\sigma_s}{4\pi}[\sum_{m'} \varpi_{m'}(1 + a_1(\xi_m \xi_{m'} + \eta_m \eta_{m'} + \mu_m \mu_{m'})) \cdot \\ (A_p^{m'} + B_p^{m'} + C_p^{m'} + D_p^{m'} + E_p^{m'} + F_p^{m'} + G_p^{m'} + H_p^{m'})] + \\ \frac{\sigma_s}{4\pi}\left(q_o/8\right)\exp\left(\int \beta d(C_L - z)\right)\left((1 + a_1(\xi_m \xi_o + \eta_m \eta_o + \mu_m \mu_o)\right) \quad (5.28)$$

The last term in Equation 5.28 is the source function due to the collimated irradiation flux. Where i represent the octal intensity (from A to H) in discussion. Equation 5.28 must be set for each one of the eight octal intensities in order to account for the angular variation In linear anisotropic phase function. Refer to Appendix C for the source function development.

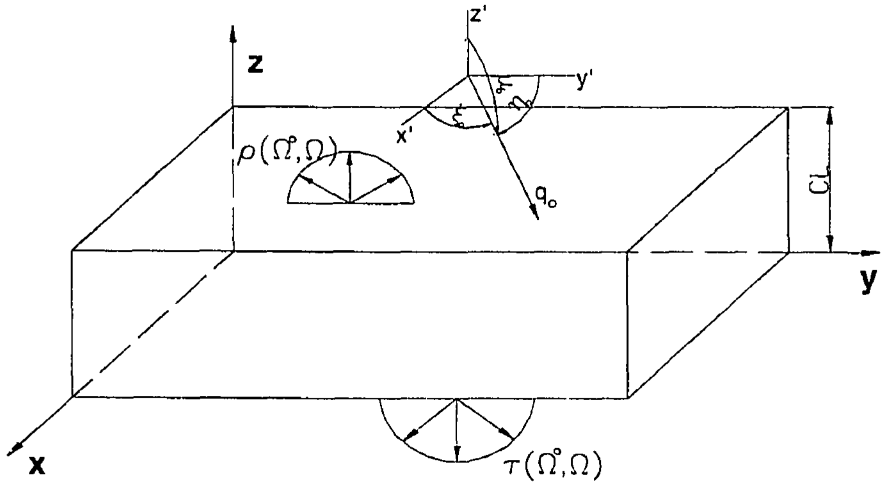

Figure 5.6 Three-dimensional Medium Subject to Collimated Mono-directional Flux

Following the same analysis as in reference [95], for some situations in which the emission term is non-existent and the mono-directional collimated incident flux is the only source of radiation; the scattered intensities leaving the top and low boundaries are the unknowns to the problem. These unknowns are represented by the reflectance function and a bi-directional transmissivity for the respective boundary. Thus,

$$\rho(\theta_o,\phi_o;\theta_s,\phi_s)=\frac{\pi I\left(C_L,(\theta_s,\phi_s>0)\right)}{(\theta_o,-\phi_o)q_o} \tag{5.29}$$

$$\tau(\theta_o,\phi_o;\theta_s,\phi_s)=\frac{\pi I\left(0,(\theta_s,\phi_s<0)\right)}{(\theta_o,-\phi_o)q_o} \tag{5.30}$$

The intensity I in Equation 5.29 represents the octal intensities A, D, E, and H whereas in Equation 5.30 the octal intensities are B, C, F, and G.

To validate the accuracy of the three-dimensional formulation with collimated irradiation at the top boundary, the diffuse reflectivity and diffuse transmissivity were calculated for a purely scattering slab (ω=1) subject to normal incident flux (ξ_o=0, η_o=0, μ_o=-1) for different types of scattering situations. These results were compared with reference [95] (except the anisotropic backward scattering) and to a 1D formulation using the S_8 quadrature. The result for the 3D formulation with dominant-z direction agrees very well with the other two comparison parameters. The diffuse transmissivity for the forward scattering is off by 2% due to geometrical effects and since the some intensity rays are leaving to the other 4 boundaries.

Reference [95] results are overlapped by the exact math from the 1D formulation results. τ_c' is defined as the collimated irradiation transmissivity, defined as $\exp\left(\beta\left(C_L/\mu_o\right)\right)$[95].

5.5 Reflectance Results and Discussion

Biangular reflectance data for a specimen of Durablanket® S with a thickness of $fvXo$=0.0052 is shown in Figure 5.8. The solid curve is the data calculated using the above theoretical model for the same value of the of the fiber volume fraction-thickness product $fvXo$ as was measured for the test specimen. The calculation was performed setting the semi-transparent boundaries at the top and bottom of the 3D media using the gray values for the insulation. The magnitude of the irradiation flux was specified altogether with the beam width and the cosine vector values that specify the beam direction. A specular fraction value is given to the incoming irradiation beam.

Setting up a value less than 1 will provide with a portion of the ray to reflect specularly at the impinged wall while the rest is transmitted to the media and reflected diffusively.

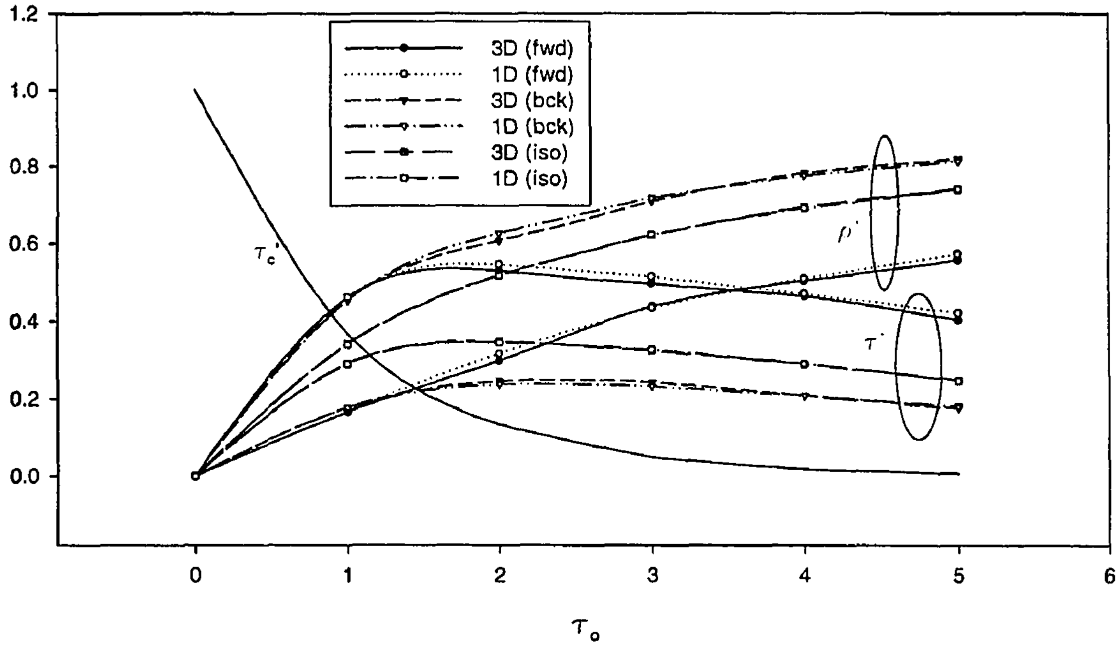

Figure 5.7 Comparison of Reflectivity and Transmissivity for a slab subject to collimated incident irradiation with Brewster [95] for conservative isotropic (a_1=0), anisotropic forward scattering (a_1=0.5), and anisotropic backward scattering (a_1=-0.5), using S_N method (N=8) for a 1D formulation and 3D formulation (Dominant z direction). (ω=1, ξ_o=0, η_o=0, μ_o=-1)

Experimental data (using the Reflect IR-P1S) sets above the calculated values in the diffuse part (Directions 1 through 8) while a better match is obtained at the specular directions (directions 9 to 11). Although the orientation effect is small for the test materials, the same figure also shows that the linear anisotropic model (LAS) model does not account for the effects of specimen orientation.

Experimental data illustrating the reflectance function for a different fiber volume fraction-thickness product *fvXo* are presented in Figure 5.9. The results show that the calculated reflectance follows the trend obtained in the experimental trials but with larger diffuse values and lower specular values. The calculated result shows that the discrete ordinates method tries to distribute the scattered energy evenly around the hemisphere most notoriously when large optical thicknesses are provided. The specular fraction value for the calculated data was lower than the one used in data depicted in Figure 5.8

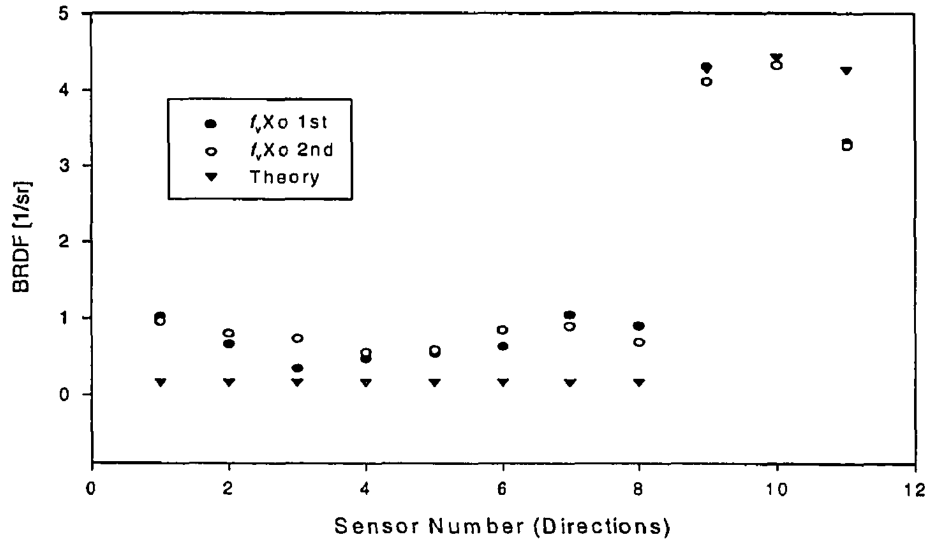

Figure 5.8 Biangular Ellipsometry reflectance as a function of the detector number of Durablanket® S insulation with incident angle of $\Theta = 25°, \Phi = 315°$ (Port 12), $fvXo$=0.0052

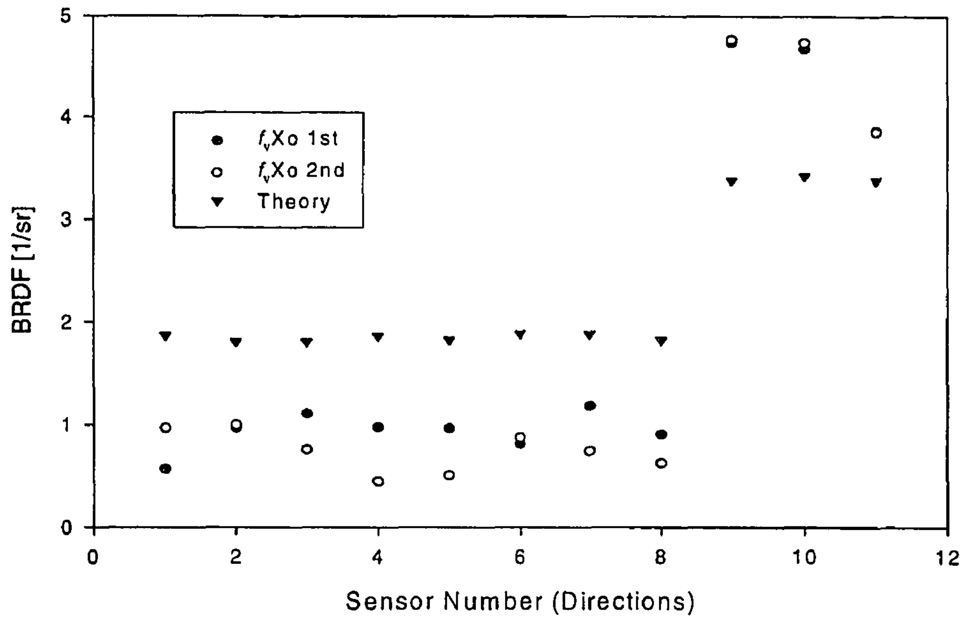

Figure 5.9 Biangular Ellipsometry reflectance as a function of the detector number of Durablanket® S insulation with incident angle of $\Theta = 25°, \Phi = 315°$ (Port 12), $fvXo$=0.0181

Comparisons of theoretical model predictions using the 144 different reflectance directions at the bottom boundary with the experimental data for the biangular reflectance for two different values of $fvXo$ are shown in Figure 5.10. The agreement between the experiment (using the Reflect IR-P1S) and theory for the case of using the black backing surface reflectance is shown in Figure 5.10a. Figure 5.10b depicts the agreement between the experimental data and the calculated data using the reflectance directions of the aluminum foil as backing at the bottom boundary for the same fiber volume fraction-thickness product $fvXo$ as Figure 5.10a. Theoretical and experimental results for a different insulation thickens are presented in Figure 5.10c. The agreement between experimental data and theory is the same, showing that a similar trend with respect to the experiment is accomplished based upon the fiber volume fraction-thickness product $fvXo$.

Poor agreement between the experimental data and the theory is found for the biangular reflectance data when the incoming radiation is at the lower angles of the quadrature as shown in Figure 5.11. Figure 5.11a shows that a similar trend is followed by the calculated results in comparison to the experimental data while using the reflectance directions for the blacked surface at the bottom boundary. The same agreement is found while using the aluminum foil reflectance directions. One of the reasons of the poor agreement could be that the method tends to redistribute the energy evenly around the hemisphere as stated before. Additionally, the simple form of the phase function does not usually capture the two-dimensional scattering behavior of fibers [59] as shown in Appendix B, which at near grazing angles becomes important.

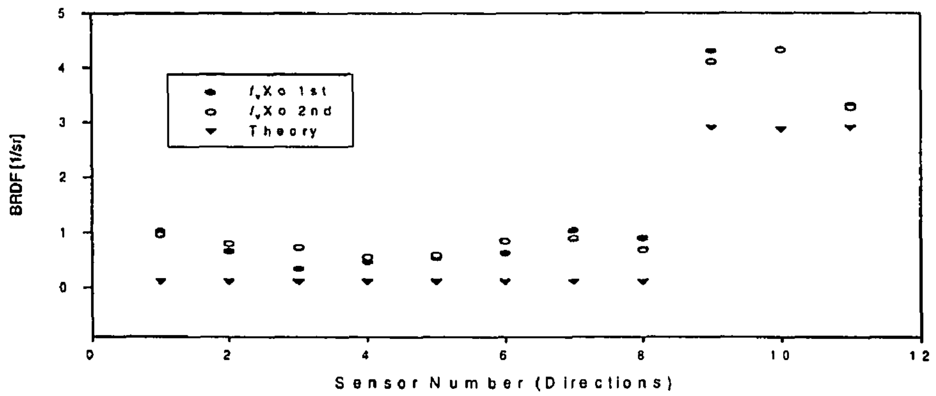

a)

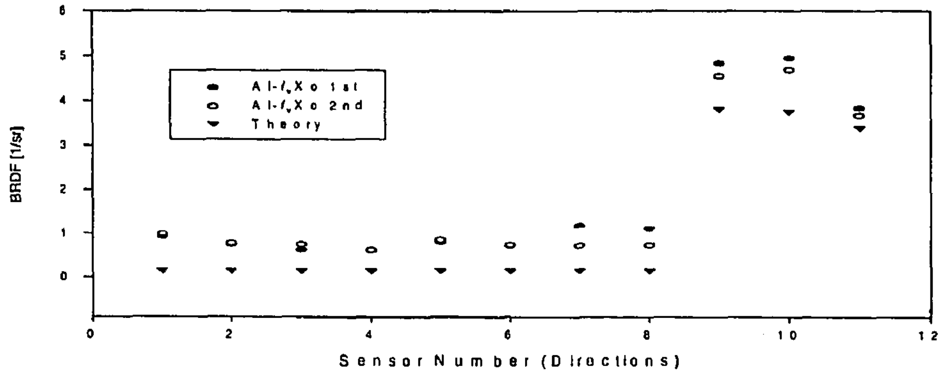

b)

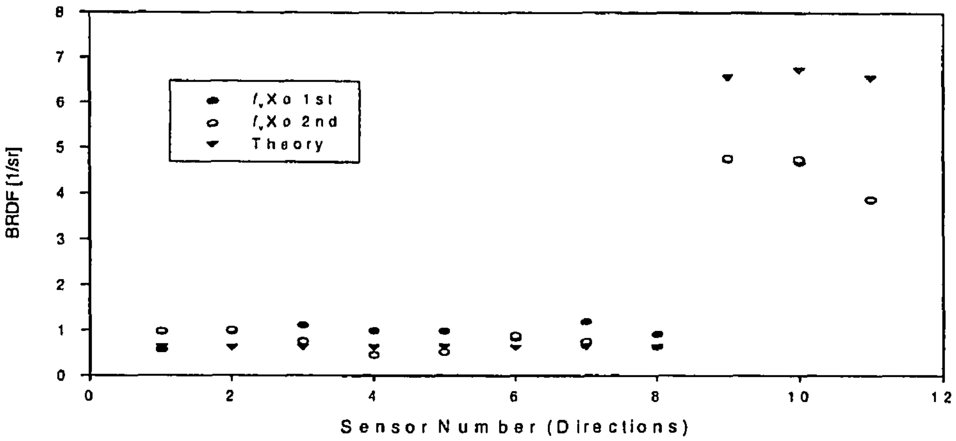

c)

Figure 5.10 Biangular Ellipsometry reflectance as a function of the detector number of Durablanket® S insulation with incident angle of $\Theta = 25^{\circ}, \Phi = 315^{\circ}$ (Port 12), f_vXo=0.0052
a) Black Surface Backing. b) Aluminum Foil Surface Backing.
c) Black Surface Backing f_vXo=0.0181

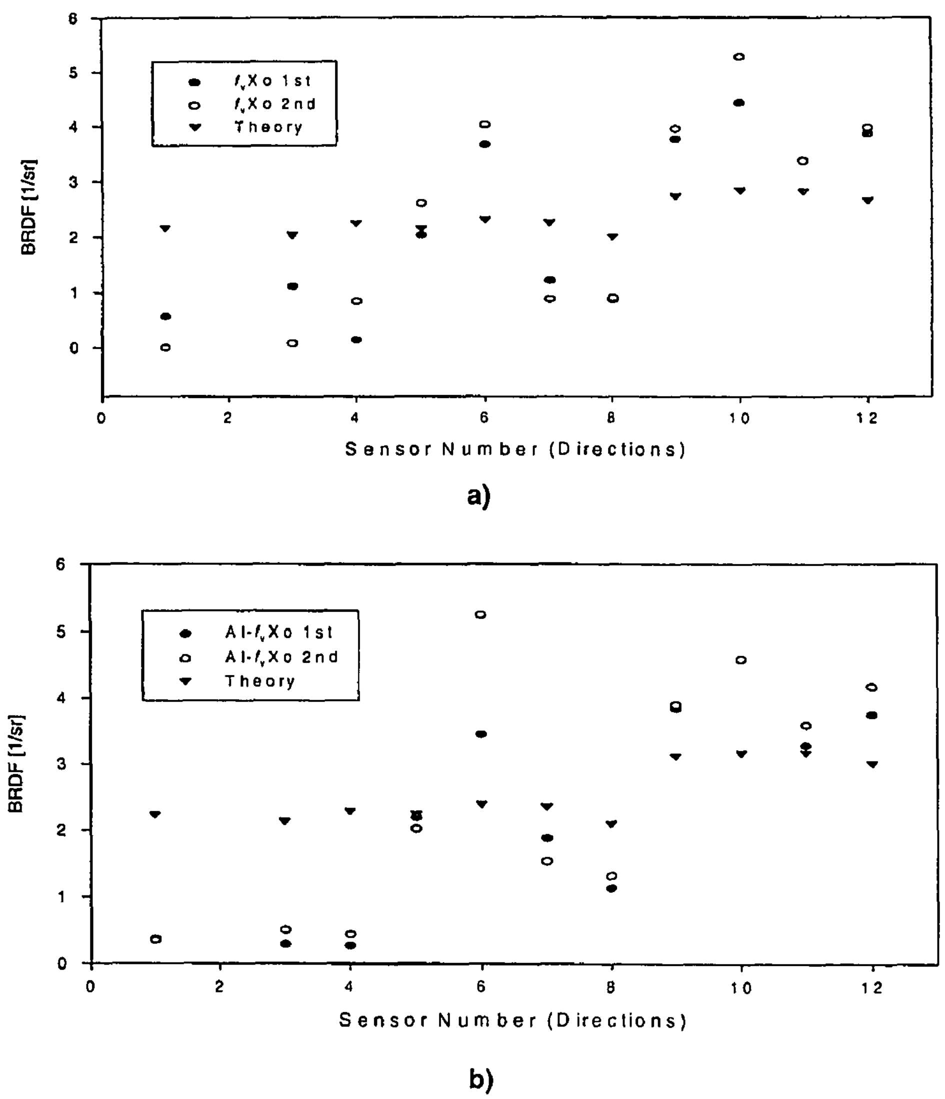

Figure 5.11 Biangular Ellipsometry reflectance as a function of the detector number of Durablanket® S insulation with incident angle of $\Theta = 73°, \Phi = 342°$ (Port 2), $fvXo$=0.0052
a) Black Surface Backing. b) Aluminum Foil Surface Backing.

5.6 Fire Barrier Assessment

The *ASTM Standard E-119* or "Standard Method of Fire Tests of Building Construction and Materials" prescribes a transient fire of a given severity for full non-load bearing walls. According to this test, in slab geometry, some thermal performance criteria are established at the opposite (unexposed) side of the barrier. The barrier is then rated as satisfying the standard for some period of time [53]. This specification is necessary to account the fire resistive properties of the materials, the integrity of the fire barrier according to the standard, and that it can be applied to a variety of different case scenarios.

Caplinger et al. [53] examined the 1-D version of the layered fire barrier made of aluminum foil and Durablanket® S fiber insulation. They obtained results for different cases of single or multiplayer fire barrier obtained thorough the variation of the insulation thickness, the number of foil layers, and material properties. However, there is no data is available on thermal interaction of 2-D corners and splicing the layers for large barriers. It is expected that spatial and angular effects might either degrade performance or even cause "hot spots" in a barrier wall. Therefore, this part of the chapter details the thermal performance of single-layer corner geometry of the fire barrier analyzed in this study.

5.6.1 Thermal Analysis

In order to determine the heat transmission and transient temperature behavior the sample barrier, a thermal analysis utilizing a CFD package (FLUENT®) is performed. Appendix D illustrates the input values and grid generation for the problem. The fire barrier is considered as an inverted L shaped geometry of single thickness, as shown in Figure 5.12. The thermal and physical properties of the Durablanket® S fiber insulation are taken constant in the gray region area as described in Chapter 3 and Appendix A. The corner shape is taken as an absorbing, emitting, anisotropic (linear anisotropic scattering) medium. The convective heat transfer coefficient was varied with temperature difference between the surface and the ambient air. Two different models for the heat transfer coefficient are selected. One model is based on the hot plate facing up, or cold plate facing down for the horizontal faces, the other one is a the vertical hot plate model for the vertical faces with $Nu_L = c(Gr\,\mathrm{Pr})^a$.

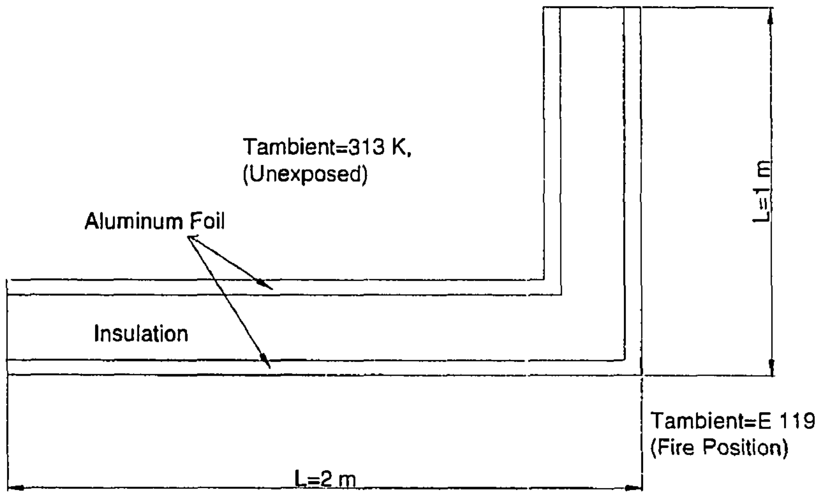

Figure 5.12 Corner-Shape Fire Barrier

For simplicity the boundary conditions of the problem are set for one side to be exposed to the flame represented by the E-119 standard [53]. The other boundary is exposed to a constant temperature of 313K. For both boundaries, natural convection, conduction, and radiation are considered. Only conduction and radiation are considered in the fire barrier (convection is set to be negligible). The two foil layers, on both the fireside and the unexposed side, consider both reflective properties and conduction. Appendix D details the problem specifics, problem set up, and boundary conditions.

The boundary intensities are set to reflect specularly since according to the previous experiments most of the energy is scattered in the specular direction of the incoming ray. Finally, the thickness of the insulation (distance between layers) is set to 1 in (0.0254 m).

5.6.2 Sensitivity Analysis and Results

To validate the numerical computations obtained by the CFD code, a comparison was made against to the results obtained by Caplinger et al. [53] for a single layer one-dimensional barrier, as shown in Figure 5.13. The parameters in the CFD code were the same as stated in reference [53]. The angular discretization of the DOM model was set up for three angles, which makes it similar to the S_4 approximation. The effect of foil thickness is included something that was not taken into account in Caplinger's work.

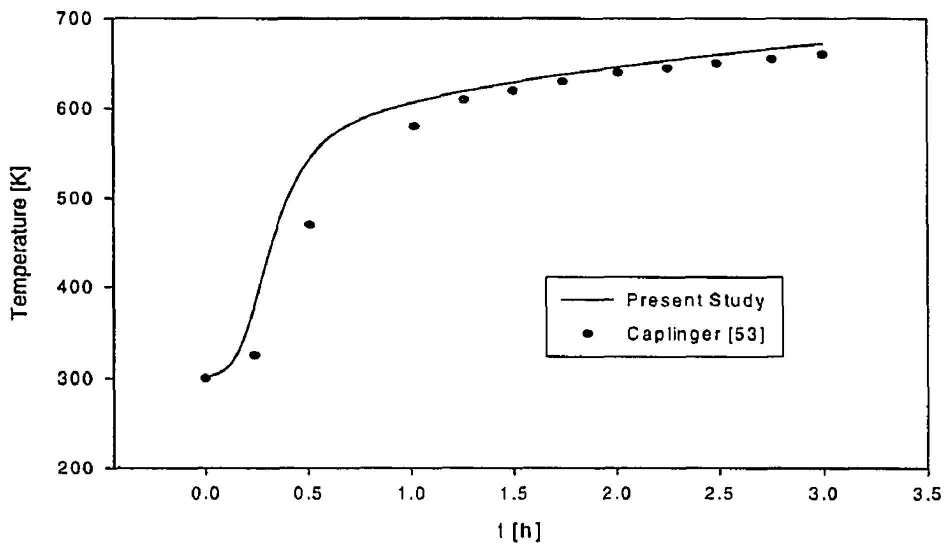

Figure 5.13 Comparison in Temperature Distribution at the exposed boundary for a slab subject to a fire according to E-119 at one of its sides with Caplinger [53]

As seen In the above figure, the agreement between the two solutions is good which demonstrates the validity of the numerical computations carried by the commercial package in the determination of the thermal performance of this type of fire barriers.

Utilizing the above setting parameters, the 1 layer corner shape fire barrier problem is analyzed. The next series of Figures shows the effect of the fire incident upon the corner shaped barrier. Figure 5.14 depicts the transient average temperature distribution for the unexposed and fireside of the barrier. It is noticed on the figure that the temperatures are close one to another. This is an indication that the 1-layer corner shaped fire barrier is not able to impede the heat flow as in the case depicted in Figure 5.12. After 3 hours the temperature is more than 1000K, which eventually lead to the destruction of the sample. These high temperatures are also enhanced due to the large area for heat to conduct from the fireside to the unexposed boundary.

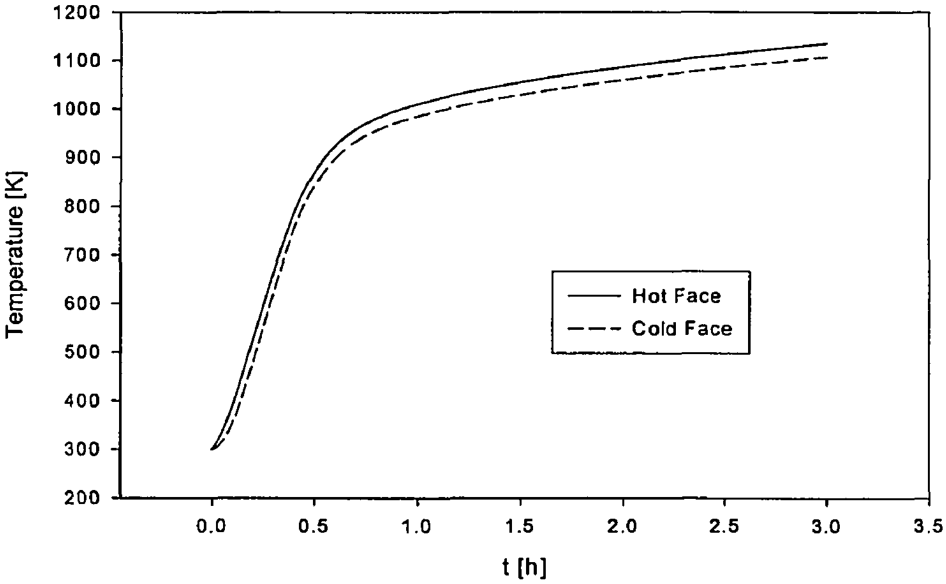

Figure 5.14 Average Face Temperature Distribution at the exposed and fireside boundary for 1 layer corner shaped geometry

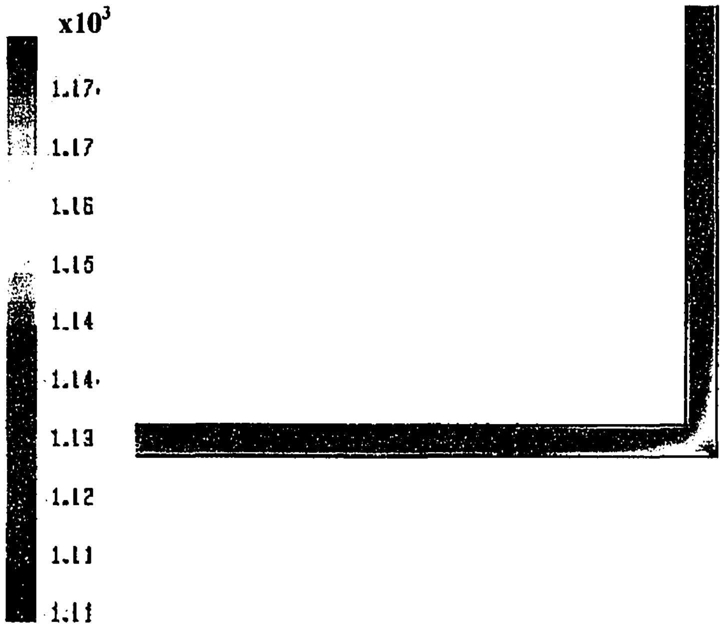

Figure 5.15 Total Temperature Color Contour Plot, (t=3h)

It is also noticed that the hot spots along the barriers are concentrated in the corner edge. A similar simulation showed that when the fire is at the inside (smaller sides of the barrier) the temperature concentration is at the away from the union between the horizontal and vertical faces (corner edge), suggesting that there is some preferential orientation or position of barrier to better contain the fire. Appendix D shows another results when the fire is located at the inside of the inverted L geometry fire barrier.

From these initial calculations it was found that a fire barrier consisting of this geometry exposed to a fire would collapse easier than a slab of the same characteristic aspect ratio. More calculations are to be performed to verify the above claim. However, the above data demonstrates that several layers of insulation must be added to protect the unexposed side in order to allow sufficient time to save people or shut down vital equipment.

5.7 Conclusions

This biangular reflectance model has demonstrated its potential to resolve Cartesian radiation heat transfer problems in more depth than other particular models. It has shown the capabilities to set up most common boundary conditions including the biangular reflectance model it a straightforward manner. It can also be easily adapted to more complicated phase functions.

The good agreement among the theoretical data demonstrates the validity of the theoretical formalisms expressed by Fiveland [80-82] and Sutton [88] for their respective radiation heat transfer situations. It has also shown good promise with respect to the easily development of biangular reflectance boundary conditions for the S_4 approximation.

In spite of the use of a simpler anisotropic function, the good qualitative agreement for the prediction of reflectance function values in randomly oriented fibrous materials throughout the hemisphere when for near normal incident angles has been demonstrated. However, at bigger incident angles fiber surface effects and the difference between the scattering directions around the hemisphere (forward and backward) relative to the slab geometry and those in relation with a single fiber are of great consideration, which could translate into disparities in the scattering phenomena [55]. Also, the scattering mechanisms of the fiber with respect to the boundary are related to the radiation scattered into the opposite hemisphere from that containing the incident direction [49], which results in uncertainties of the reflectance data. The scattering phenomena cannot be provided just by a single number (scattering coefficient) and the use of the exact phase function would probably enhance the agreement between the experimental and the theoretical data [50]. However, the use of the biangular reflectance function data as boundary condition help to diminish in some degree the considerable uncertainty of the model.

For this type of calculations the S_4 DOM method has shown to distribute the energy around the hemisphere. This happens due to the single weighting value to describe the hemisphere of radiation and to the inherent directional biasing of the quadrature scheme. A different or higher scheme could help to overcome this situation at the expense of grater computational effort [92].

The initial numerical calculations for the assessment of a L-shaped fire barrier corner show that the large planar area of the barrier enhanced the flow of heat transfer from the fireside to the unexposed side. One-layer barrier will only be effective for the first 25 minutes after the commencement of the fire since the temperature will reach a value of 453K, the safe limit temperature condition set by the E-119 standard [53]. Perhaps, the use of a multi-layer barrier would allow enhancing the effectiveness of the barrier for this type of geometry

CHAPTER 6

CONCLUSIONS

The enhancement of directional and surface properties and radiative heat transfer in fire barrier materials has been investigated. Experimental and numerical methods are employed for predicting scattering and radiation fields for the metallic surfaces, the fiber insulation, and their interaction.

A simple but effective scattering model was introduced to account for the scattering behavior of the fibrous insulation material Durablanket® S. By performing standard experimental methods it was determined that the fibers of the materials lie randomly, which asserts more the use of a simple scattering (Linear Anisotropic Scattering) model in comparison to the exact phase function for scattering.

By making use of the theory behind the angular distribution of the S4 discrete-ordinate method, a new apparatus was created to measure the reflectance function of the materials that composed the fire barrier. The same equipment can be used to measure other properties and other materials and it has been envisioned as a tool to determine surface defects through surface scattering characterization for in-line process manufacturing. In spite of the fact that the scattering results are small since they are out-of-plane measurements, a small change in the parameters might lead to an indication of a different scattering patterns around the hemisphere.

The same apparatus provided reliable information about the scattering characteristics of the metals composing the barrier, the insulation material, the scattering parameters of the combination of metals and insulation. It was shown that at higher incidence temperatures all materials tend to scattered with higher intensity. Also, reducing the optical thickness of the insulation affect the characteristics of scattering in some degree while using different types of backing. The opposite occurs when optically thick samples are used, no change in scattering behavior is highly present while using any surface backing.

The scattering phenomena in the metallic surfaces have been established using the DOM scatterometer. Other types of experimental and numerical methods were tried for property determination but neither of them yielded good results. Through the use of the DOM scatterometer it was found that the reflectance function of the aluminum foil tends to be more mirror like with respect to the stainless steel 321 foil despite the fact it is twice as bigger in surface roughness in the gray area. The contrary occurred at certain spectral range, in which the stainless steel showed mirror-like performance.

The new biangular reflectance model based on the S_4 discretization scheme yield good qualitative results in the determination of reflectance patterns for the fibrous insulation material. The use of a more comprehensive scattering function could possibly lead into better performance. However, the use of the 144 scattering directions leads to promising results and the manner it was set up can be extended to higher schemes and different geometrical configurations.

A simple approximation of the thermal performance in a corner shaped fire barrier has shown that there is a preferential orientation for the barrier to be positioned when a fire must be expected to occur since hot spots can be set at the trailing edges or at the union of faces of the barrier. These initial calculations have also shown that more layers of insulation material must be added to contain and increase the effectiveness of the barrier.

This research has sought to work as a further guide for fire barrier design. Knowing the surface characteristics of the metallic foil and determining the scattering characteristics of the insulation proved that the combination of stainless steel and the fire blanket would enhance the radiative response of the barrier at the extreme fire temperatures. This in turn could lead to better assessment and prediction of thermal response in a barrier as well as obtain more cost effective benefits for the application being pursued.

REFERENCES

1. Love, T.J., *Radiative Heat Transfer*, Merrill, Ohio, 1968

2. Siegel R., Howell, J.R., *Thermal Radiation Heat Transfer*, McGraw-Hill, New York, 1972

3. Ozisik, M.N., *Radiative Heat Transfer*, Wiley, New York, 1973

4. Wolfe, W. L. (Editor), *Handbook of Military Infrared Technology*, Naval Research Laboratory, 1965

5. Modest, M.F., *Radiative Heat Transfer*, McGraw-Hill, New York, 1993

6. Stover, J.C., *Optical Scattering, Measurement and Analysis*, 2nd Edition, Proc. SPIE, 1995

7. Tang, K., Dimenna, R. A., Buckius, R.O., " Regions of Validity of the Geometric Optics Approximation for Angular Scattering from Very Rough Surfaces, " International Journal of Heat and Mass Transfer, Vol. 40, No. 1, pp. 49-59, 1997

8. Church, E.L., Tacks, P.Z., Leonard, T.A., " The Prediction of BRDFs from surface profile measurements, " SPIE, Vol. 1165, pp. 136-150, 1989

9. Davies, H., " The Reflection of Electromagnetic Waves From a Rough Surface, " Proceedings of the Institution of Electrical Engineers, Vol. 101, No. 4, pp. 209-214, 1954

10. Bennet, H.E., Porteous, J.O., " Relation Between Surface Roughness and Specular Reflectance at Normal Incidence, " Journal of the Optical Society of America, Vol. 51, No. 2, pp. 123-129, 1961

11. Bennet, H.E., " Specular Reflectance of Aluminized Ground Glass and the Height Distribution of Surface Irregularities, " Journal of the Optical Society of America, Vol. 53, No. 12, pp. 1389-1394, 1963

12. Porteous, J.O, " Relation Between the Height Distribution of a Rough Surface and the Reflectance at Normal Incidence, " Journal of the Optical Society of America, Vol. 53, No. 12, pp1394-1402, 1963

13. Beckmann, P., Spizzinno A., *The Scattering of Electromagnetic Waves from Rough Surfaces*, Pergamon, New York, 1963

14. Birkeback, R.C., Eckert, E.R.G., " Effects of Roughness of Metal Surfaces on Angular Distribution of Monochormatic Reflected Radiation, " Journal of Heat Transfer, Vol. , pp. 65-94, 1965

15. Torrance, K., E., Sparrow, E.M., " Biangular Reflectance of an Electric Non-Conductor as a Function of Wavelength and Surface Roughness, " Journal of Heat Transfer, Vol. 87, pp. 283-289, 1969

16. Dunn, S. T., " A Possible Approach to Evaluation of Flux Scattered by Roughened Surfaces, " AIAA paper No. 66-20, 1966

17. Torrance, K., E., Sparrow, E.M., " Theory for Off-Specular Reflection From Roughened Surfaces, " Journal of the Optical Society of America, Vol. 9, No. 9, pp. 1105-1111, 1967

18. Francis R. E., *The Experimental Determination of Reflectance Functions for Type 302 Stainless Steel*, M.S. Thesis, Oklahoma University, Norman, 1967

19. Houchens, A.F., Hering, R.G., " Bidirectional Reflectance of Rough Metal Surfaces, " Thermophysics of Space Craft and Planetary Bodies, Edited By G.B. Heller, New Orleans, 1967

20. Look, D.C., *Investigation of Effects of Surface Roughness Upon Reflectance*, PhD Dissertation, School of Aerospace and Mechanical Engineering, The University of Oklahoma, Norman, 1969

21. Church, E.L., Personal Communications

22. Church, E.L., Jenkinson, H.A., Zavada, J.M., " Measurement of the Finish of Diamond-Turned metal Surfaces by Differential Light Scattering, " Optical Engineering, Vol. 16, No.4, pp. 360-374, 1977

23. Harvey, J.E., " Light Scattering Characteristics of Optical Surfaces, " Proceedings of SPIE Vol. 107, pp. 41-47, 1977

24. Church, E.L., Jenkinson, H.A., Zavada, J.M., " Relationship between Surface Scattering and Micro Topographic Features, " Optical Engineering, Vol. 18, No.2, pp. 125-136, 1979

25. Soto-Crespo, J.M., Nieto-Vesperonas, M., " Electromagnetic Scattering from Very Rough Surfaces and Deep Reflection Gratings, " Journal of the Optical Society of America A, Vol. 6, No. 3, pp. 367-384, 1989

26. Drolen, B.L., " Bidirectional Reflectance and Specularity of Twelve Spacecraft Thermal Control Materials, " Journal of Thermophysics and Heat Transfer, Vol. 6, No. 4, pp. 672-679, 1992

27. Dimenna, R., Buckius, R.O., " Quantifying Specular Approximations for Angular Scattering from Perfectly Conducting Rough Surfaces, " Journal of Thermophysics and Heat Transfer, Vol. 8, No. 3, pp. 393-399, 1994

28. Dimenna, R., Buckius, R.O., " Electromagnetic Theory Predictions of the Directional Scattering from Triangular Surfaces, " Journal of Heat Transfer, Vol. 116, pp. 639-645, 1994

29. Church, E.L., Takacs, P.Z., Leonard, T.A., " The Prediction of BRDF from Surface Profile Measurement, " Proceedings SPIE, Vol. 1165, pp.137-150, 1989

30. Harnisch, B., Weigel, T., " Microroughness, Statistical Surface Models and BRDF-Functions of Smooth Surfaces, " Proc. SPIE, Vol. 2210, pp. 533-542, 1994

31. Germer, T.A., " Angular Dependence and Polarization of Out-of-Plane Optical Scattering from Particulate Contamination, Surface Defects, and Surface Microroughness, " Applied Optics, Vol. 36, No. 3, pp. 8798-8805, 1997

32. Cohn, D.W., Tang, K. Buckius, R.O., " Comparison of theory and Experiments for Reflection from Microcontoured Surfaces, " International Journal of Heat & Mass Transfer, Vol. 40, No. 13, pp. 3223-3235, 1997

33. Tang, K. Buckius, R.O., " Bi-Directional Reflection Measurements from Two-Dimensional Microcontoured Metallic Surfaces, " Microscale Thermophysical Engineering, Vol. 2: pp. 245-260, 1998

34. Germer, T.A., " Characterizing Interfacial Roughness by Light Scattering Ellipsometry, " Characterization and Metrology for ULSI Technology: 2000 International Conference, Edited by D.G. Seilier, et al., Proceedings AIP, Vol. 550, pp. 186-190, (AIP, New York), 2001

35. Tang, K., Buckius, R.O, " The Geometric Optics Approximation for Reflection from Two-Dimensional Random Rough Surfaces, " International Journal of Heat & Mass Transfer, Vol. 41, No. 13, pp. 2037-2047, 1998

36. Greffet, J. –J., Nieto-Vesperinas, M., " Field Theory for Generalized Bidirectional Reflectivity: Derivation of Helmholtz's Reciprocity Principle and Kirchhoff's law, " Journal of the Optical Society of America A, Vol. 15, No. 10, pp. 2735-2744, 1998

37. Carminati, R., Greffet, J. -J., Sentenac, A., " A Model for the Radiative Properties of Opaque Rough Surfaces, " Heat Transfer 1998, Proceedings of the 11th Heat Transfer Conference, Vol. 7, pp. 427-432, August 1998

38. Tang, K., Kawka, P.A., Buckius, R.O, " Geometric Optics Applied to Rough surfaces Coated with an Absorbing Thin Film, " Journal of Thermophysics and Heat Transfer, Vol. 13, No. 2, pp. 169-175, 1999

39. Tang, K., Yang, Y, Buckius R.O., " Theory and Experiments on Scattering from Rough Surfaces, " in *Annual Review of Heat Transfer*, Vol. 10, pp. 101-140, 1999

40. Marschner, S.R., Westin, S.H., Lafortune, E.P.F., Torrance, K.E., Greenberg, D.P., " Image-Based BRDF Measurement Including Human Skin, " Technical report PCG-99-1, Program of Computer Graphics, Cornell University, 1999

41. Marschner, S.R., Westin, S.H., Lafortune, E.P.F., Torrance, K.E., " Image-Based BRDF measurement, " Applied Optics, Vol. 36, No. 16, pp. 2592-2600, 2000

42. Lafortune, E.P.F., Foo, S-C., Torrance, K.E., Greenberg, D.P., " Non-Linear Approximation of Reflectance Functions, " Technical report, Program of Computer Graphics, Cornell University, 2000

43. Larkin, B.K., Churchill, S.W., "Heat Transfer by Radiation Through Porous insulations, " A.I.Ch.E. Journal, Vol. 5, pp. 467-474, 1965

44. Tong, T.W., *Thermal Radiation in Fibrous insulations*, Ph.D. Dissertation, Dept. of Mechanical Engineering, University of California, Berkeley, CA, Oct 1980

45. Tong, T.W., Tien. C.L., " Radiative Heat Transfer in Fibrous Insulations-Part I: Analytical Study, " J. Heat Transfer, Vol. 105, pp. 70-85, 1983

46. Tong, T.W., Tien. C.L., " Radiative Heat Transfer in Fibrous Insulations-Part II: Experimental Study, " Journal of Heat Transfer, Vol. 105, pp. 76-81, 1983

47. Lee, S.C., " Radiative Transfer Through a Fibrous Medium: Allowance for Fiber Orientation, " Journal of Quantitative Spectroscopy and Radiative Transfer, Vol. 36, No. 3, pp. 253-263, 1986

48. Lee, S.C., " Radiation Properties of Fibrous Insulations: Theory Versus Experiment, " Journal of Thermophysics, Vol. 2, No. 4, pp. 303-308, 1988

49. Lee, S.C., " Effects of Fiber Orientation on Thermal Radiation in Fibrous Media, " International Journal of Heat & Mass Transfer, Vol. 32, No. 2m pp. 311-319, 1989

50. Lee, S.C., " Scattering Phase Function for Fibrous Media, " International Journal of Heat & Mass Transfer, Vol. 33, No. 10, pp. 2183-2190, 1990

51. Lee, S.C., Cunnington, G.R., " Heat Transfer in Fibrous Insulations: Comparison of Theory and Experiment, " Journal of Thermophysics & Heat Transfer, Vol. 12, No. 3, pp. 297-303, 1998

52. Lee, S.C., Cunnington, G.R., " Conduction and Radiation Heat Transfer in High Porosity Fiber Thermal Insulation, " Journal of Thermophysics, Vol. 14, No. 2, pp. 121-136, 2000

53. Caplinger, G., D., Sutton, W.H., Spindler, R., Golke, H.," Transient Heat Transfer for Layered Ceramic Insulation and Stainless Steel Foil Fire Barriers, " Journal of Heat Transfer, Vol. 121, pp. 1059-1066, 1999

54. Sánchez, M.A., Borrás, C., Hergenrether, D., Sutton, W.H., Chandra H., " Super-Gas™ Fueling Stations, " Fuel Cells & Alternative Fuels/Energy Systems, SAE SP-1635, pp. 9-14, 2001

55. Cunnington, G.R., Tong, T.W., Swathi, P.S., " Angular Scattering of Radiation from Coated Cylindrical Fibers, " Journal of Quantitative Spectroscopy and Radiative Transfer, Vol. 48, No. 4, pp. 353-362, 1992

56. Germer, T.A., NIST, Personal Communications

57. ANSI B46.1, *Surface Texture: Surface Roughness, Waviness and Lay*, 1978

58. Muralikrishnan, Bala, University of North Carolina-Charlotte, Personal Communications

59. Lee, S.C., Applied Sciences Laboratory Inc., Personal Communications

60. Kerker, M.C., *The Scattering of Light and Other Electromagnetic Radiation*, Academic Press, New York, 1969, Chap. 6

61. Van de Hulst, H.C., *Light Scattering by Small Particles*, Dover, 1981, Chap. 15

62. Cunnington, G.R., Tong, T.W., Swathi, P.S, " Comparison of Radiative Heat Transfer in Several Fibrous Insulations, " Journal Of Thermal Insulation, Vol. 14, pp. 107-122, 1990

63. Unifrax Corporation, Personal Communications

64. Kaplan S., Personal Communications

65. Choy, T.C., *Effective Medium Theory. Principles and Applications*, Claredon Press, Oxford, 1999

66. Palik, E.D, *Handbook of optical constants of solids*, AP, New York, 1985

67. Palik, E.D, *Handbook of optical constants of solids II*, AP, New York, 1991

68. Swathi, P.S, Tong, T.W., " A New Algorithm for Computing the Scattering Coefficients of Highly Absorbing Cylinders, " Journal of Quantitative Spectroscopy and Radiative Transfer, Vol. 40, No.4, pp. 525-530, 1988

69. Fiveland, W.A., " The Selection of Discrete Ordinate Quadrature Sets for Anisotropic Scattering, " Fundamentals of Radiation Heat Transfer, Vol. HTD-160, ASME, pp. 89-96, 1991

70. Larthrop, K.D., Carlson, B.G., " Discrete Ordinates Angular Quadrature of the Neutron Transport Equation, " Los Alamos Scientific Laboratory Report 3186, Los Alamos, New Mexico, 1965

71. Sacadura, J. – F., " Measurement Techniques for Thermal Radiation Properties, " Heat Transfer 1990, Proceedings of the Ninth International Heat Transfer Conference, Vol. 1, pp. 207-218, 1990

72. Kim J.H., Simon, T.W., Viskanta R., " Journal of Heat Transfer Policy on Reporting Uncertainties in Experimental Measurements and Results, " Journal of Heat Transfer, Vol. 115, pp. 5-6, 1993.

73. Germer, T.A., " A Goniometric Optical Scattering Instrument for Bidirectional Reflectance Distribution Function Measurements with Out-of-Plane and Polarimetry Capabilities, " Proceedings SPIE 3141, pp. 220-231, 1997

74. Ford, J.N., Tang, K., Buckius, R.O., " Fourier Transform Infrared System Measurement of the Bidirectional Reflectivity of Diffuse and Grooved Surfaces, " Journal of Heat Transfer, Vol. 117, pp. 955-962, 1995

75. Zaworski, J.R., Welty, J.R., Drost, M.K., " Measurement and Use of Bi-Directional Reflectance, " International Journal of Heat & Mass Transfer, Vol. 39, No. 6, pp. 1149-1156, 1996

76. Stover, J.C, Skurdal, V., Bender, J., Chausse, P., " Design Review of a Hand Held Scatterometer, " Proceedings SPIE, Vol. 1331, pp. 195-200, 1990

77. Germer, T.A., " Multidetector Hemispherical Polarized Optical Scattering Instrument, " Proceedings SPIE 3784, pp. 304-313, 1999

78. ASTM Designation: E 1392-90, " Standard Practice for Angle Resolved Optical Scatter Measurements on Specular or Diffuse Surfaces, " 1991

79. Saboonchi, A., *A Method For The Determination of Thermal Radiation Properties of Fiber Insulation*, PhD Dissertation, School of Aerospace and Mechanical Engineering, The University of Oklahoma, Norman, 1986

80. Fiveland, W.A., " Three-Dimensional Radiative Heat Transfer Solutions by the Discrete Ordinates Method, " Journal of Thermophysics & Heat Transfer, Vol. 2, No. 4, pp. 309-316, 1988

81. Fiveland, W.A., Jamaludin, A.S., " Three-Dimensional Spectral Radiative Heat Transfer Solutions by the Discrete Ordinates Method, " Journal of Thermophysics and Heat Transfer, Vol. 5, No. 3, pp. 335-339, 1991

82. Fiveland, W.A., " Discrete Ordinate Solutions of the Radiative Transport Equation for Rectangular Enclosures, " Journal of Heat Transfer, Vol. 106, No. 4, pp. 699-706, 1984

83. Thynell, S.T., " Discrete Ordinates Method in Radiative Heat Transfer, " International Journal of Engineering Science, Vol. 36, pp. 1651-1675, 1998

84. Wu, C-Y., Liou, B-T., " Discrete-Ordinate Solutions for Radiative Transfer in a Cylindrical Enclosure with Fresnel Boundaries, " International Journal of Heat & Mass Transfer, Vol. 40, No. 10, pp. 2467-2475, 1997

85. Roux, J.A., Smith, A.M., " Biangular Reflectance for an Absorbing and Isotropically Scattering Medium, " AIAA Journal, Vol. 23, No.4, pp. 624-628, 1985

86. Rokhsaz, F., Dougherty, R.L., " Radiative Heat Transfer within a Finite Plane-Parallel Medium Exhibiting Fresnel Reflection at a Boundary, " in Heat Transfer Phenomena in Radiation, Combustion and Fires, Shah R.K. Editor. HTD - Vol. 106, 1989

87. Wu, C-Y., Liou, B-T., Liou, J-H., " Discrete Ordinate Solution For Radiative Transfer in a Scattering Medium with Fresnel Boundaries, " in Radiation and Combustion Measurements Techniques, Numerical Techniques and Modeling, Hewitt, G.F., Editor. Vol. 2, 1994

88. Sutton, W.H., Kamath, R.S., " Participating Radiative Heat Transfer in a Three-Dimensional Rectangular Medium with Layered Properties, " ASME Paper 86-HT-25, AIAA/ASME Thermophysics Heat Transfer Conference, Boston, Massachusetts, June 1986

89. Sutton, W.H., Özisik, M.N., " An iterative Solution for Anisotropic Radiative Heat Transfer in a Slab, " Journal of Heat Transfer, Vol. 101, 695-698, 1979

90. Sutton, W.H., Özisik, M.N, " An Alternative Formulation for Radiative Heat Transfer in Isotropically Scattering Two-Dimensional Bar Geometry and Solution Using the Source Function Expansion Method, " ASME Paper 84-KT-36, ASME/AIChE, 22nd National Heat Transfer Conference, Niagara Falls, NY, August 1984

91. Sakami, M. Charette, A., Dez Le, V., " Radiative Heat Transfer in Three-Dimensional Enclosures of Complex Geometriy by Using the Discrete-Ordinate Method, " Journal of Quantitative Spectroscopy and Radiative Transfer, Vol. 59, No. 12, pp. 117-136, 1998

92. Koch, R. Krebs, W. Witting, S., Viskanta, R., " A Parabolic Formulation of the Discrete Ordinates Method for the Treatment of Complex Geometries, " in Radiative Heat Transfer I, edited by M. Pinar Menguc, Begekk House, New York, 1995

93. Selcuk, N., Kayakol, N., " Evaluation of Discrete Ordinates Method for Radiative Transfer in Rectangular Furnaces, " International Journal of Heat & Mass Transfer, Vol. 40, No. 2, pp. 213-222, 1997

94. Hanssen, L. M., Kaplan, S., " Infrared Diffuse Reflectance Instrumentation and Standards at NIST, " Analytica Chimica Acta, Vol. 380, pp. 289-302, 1999

95. Brewster, M.Q., *Thermal Radiative Transfer and Properties*, Wiley-Interscience, February 1992

96. Ho, J.R., Grigoropoulos, C.P, Humphrey, J.A.C., " Gas Dynamics and Radiation Heat Transfer in the Vapor Plume Produced by a Pulsed Laser Irradiation of Aluminum, " Journal of Applied Physics, Vol. 79, No. 9, 7205-7215, 1996

APPENDIX A

FIRE BARRIER MATERIALS

This section provides general information about the materials that composed the fire barrier.

A.1 Aluminum Foil

MSC Industrial Supply Co.
Heavy Gauge Aluminum Foil
Type 303-H14 Aluminum
0.016" (0.41 mm) thick

GENERAL PROPERTIES

Corrosion Resistant
Typical applications: Heating and duct work, any type of patchwork

CHEMICAL PROPERTIES

Si	Fe	Cu	Mn	Zi	Others	Al
0.6	0.7	0.05-0.20	1.0-1.5	0.10	0.05Each/0.15Total	96.75 - 97.5

A.2 Stainless Steel Foil

Falcon Stainless & Alloys Corp
Stainless Steel Foil
Type 321
0.004" (0.10 mm) thick

GENERAL PROPERTIES

Type 321 is a stabilized stainless steel, which offers as its main advantage an excellent resistance to intergranular corrosion following exposure to temperatures in the chromium carbide precipitation range from 800 to 1500° F (427 to 816° C). Type 321 is stabilized against chromium carbide formation by the addition of titanium.

CHEMICAL PROPERTIES

C	Mn	P	S	Si	Cr	Ni	Mo	Cu	N	Other
0.08	2.00	0.045	0.30	0.75	17.00-19.00	9.00-12.00	0.75	0.75	0.10	Ti=5x(C+N) min 0.70 max

A.3 Durablanket® S

Unifrax Corporation
Density 128 kg/m^3
0.25" thick

GENERAL PROPERTIES:
Typical Applications:

Infrared panels and ovens, Furnace, kiln, reformer and boiler linings, Investment casting mold wrappings, High temperature gasketing, Atmosphere furnace linings, Expansion joint seals, Flexible high temperature pipe insulation, Furnace insulation, seals and repairs, Removable insulating blankets for field stress relieving welds, Reusable insulation for steam and gas turbines, Pressure and cryogenic vessel fire protection

AL_2O_3	SiO_2	ZrO_2	Fe_2O_3	TiO_2	MgO	CaO	Na_2O_3	Alkali	Chlorides	Other
43 - 47	53 - 57	-	Trace	Trace	-	-	<0.5	0.05	< 10 ppm	0.85

Continuous Use Temperature limit	1260°C
Density	128 Kg/m^3
Specific Heat	1130 J/KgK
Thermal Conductivity	0.2 W/mK
Fiber Diameter	2.5 – 3.5 μm (mean)
Composition	53% - 57% SiO_2 43% - 47 % Al_2O_3
Specific Gravity	2.73 g/cm^3

APPENDIX B

REFLECTANCE MISCELLANEOUS PARMAMETERS AND RESULTS

The discussion that follows is a representative of the approximations taken to determine the biangular ellipsometry reflectance for the fire barrier materials and some combinations among them.

B.1 Light Sources

As previously stated three types of light sources are utilized to evaluate the reflectance function of the fire barrier materials. Each one of these sources possesses unique characteristics, which can be summarized as follows.

Wavelength: Two of the light sources, ReflectIR-P1N and TO-5, (both windowless) emit infrared energy in the wavelength region of 2-20 μm according to the manufacturer. The other light source, ReflectIR-P1S, possesses a sapphire window, which allows transmitting 80% of infrared energy in the 2-5.25 μm range as described in figure B.1.1, supplied by the manufacturer.

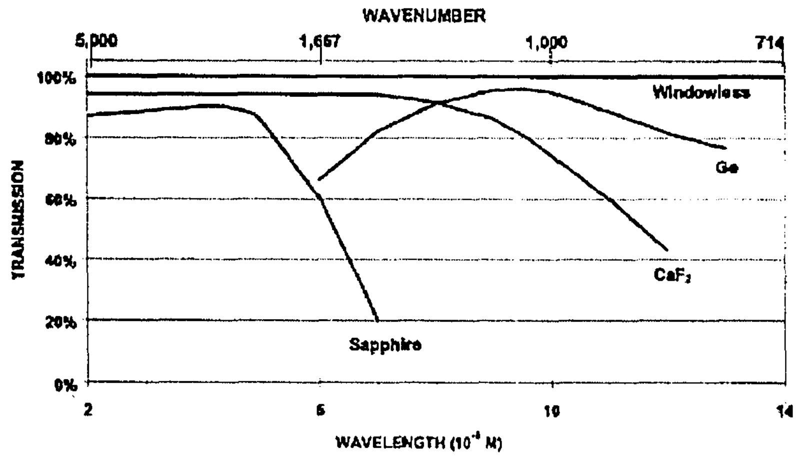

Figure B.1.1 Ion-Optics® Light Sources Wavelength Region

B. <u>Output Pattern</u>: In spite of the fact that the normalized output pattern of the sources was provided by the manufacturer, it was necessary to verify how the sources emitted their energy since it was discovered during the testing period of the DOM-Hemispherical Scatterometer that the sensors were picking up signals when the sample holder was not positioned in the shell.

By performing a simple rotation experiment, the incident voltage was measured from the sources by keeping them in a fixed position and rotating the sensor 180 degrees, every 4 degrees. The distances between the sensors and the source were 25.4 mm and 62 mm. The light source was rotated 90 degrees with the aim of verifying output anomalies with none found. Figure B.1.2 and B.1.3, shows the output pattern of the sources. As shown in Figure B.1.2, the collimated sources concentrated most of the energy in the first 8 to 10 degrees from the normal. The other un-collimated source (TO-5) emits a broader pattern of energy in comparison to the collimated sources. It was not possible to determine the output pattern of the TO-5 source due to equipment constrains to hold the source in alignment, therefore Figure B.1.3 is the normalized output pattern provided by the manufacturer.

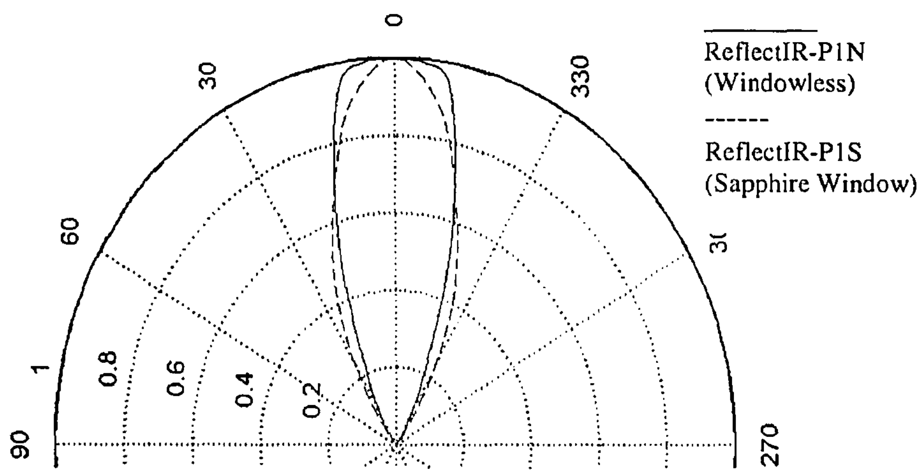

Figure B.1.2 Normalized Output Pattern Collimated Sources

The above results are somewhat close to the manufacturer's data. The window in the ReflectIR-P1S source tends to affect the output signal. This event was present during the experiment trials.

It was also determined that 77% of the energy of both collimated sources reached the sensor at normal position while 35% of the energy of the un-collimated source reached the sensor at the same normal position.

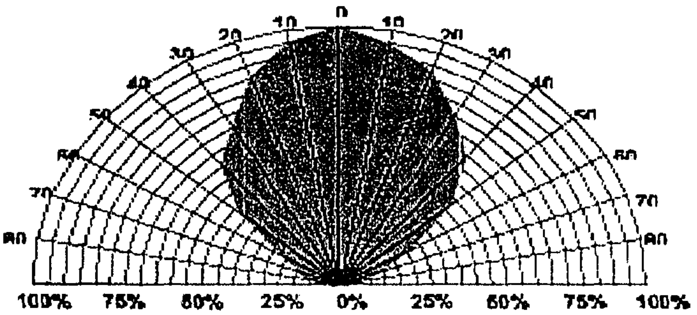

Figure B.1.3. Normalized Output Pattern T0-5 Source [Courtesy of Ion-Optics]

B.2 Incident Voltage

In order to measure the incident voltage, which represent the incident intensity of radiation, a simple hollow aligned device (Figure B.2.1) was built in which the sensor and source are place normally to one another at a distance equal to the radius of the hemispherical shell.

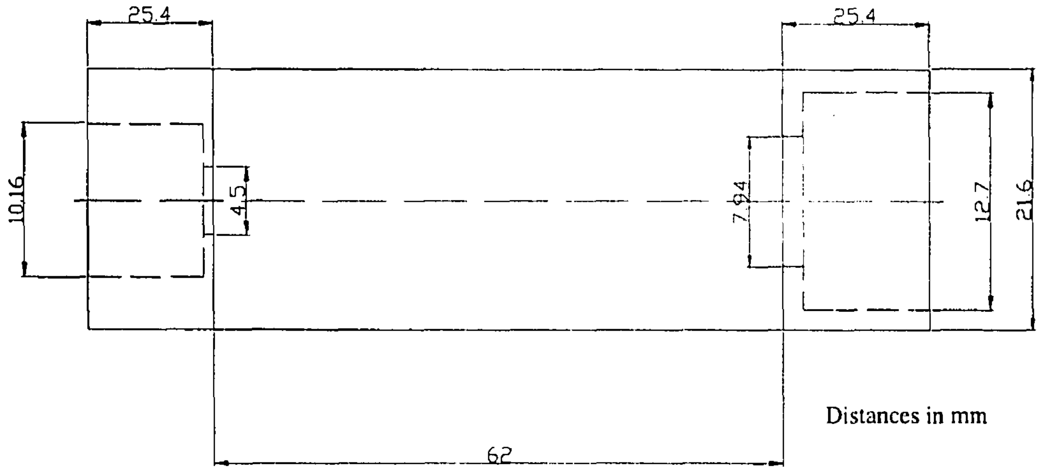

Figure B.2.1 Incident Intensity Alignment System

This is a direct-type of measurement, which assumes that the light coming out of the sensor is collimated. Since this is not the case for either of the sources, the incident voltage was multiplied by the cosine of the incident polar angle Θ_i to account for the geometry variations and the reflected target area, as usually done in the calculation of solid angle. Table B.2.1 summarizes incident voltage measurements for each one of the discrete ordinates positions.

Table B.2.1 Direct type- measurement results of the incident intensity for the S_4 angles

Port	Incident Voltage		
	P1N (400°C)	P1S (600°C)	TO-5 (600°C)
1-8	0.02591	0.05571	0.03202
9-12	0.07935	0.17055	0.09804

B.3 Insulation Properties

B.3.1 Thickness

The optical thickness τ of an insulation material is defined by:

$$d\tau = \rho\beta dX \tag{B.1}$$

Equation B.1 allows defining the optical variable in a more suitable way since the quantity ρXo is determined more accurately by measuring the mass divided by the relatively large planar area. Xo is previously determined by dividing the quantity ρXo over the density of the insulation Therefore, the optical thickness of the insulation slab is

$$\tau_o = \rho\beta Xo \tag{B.2}$$

where β is the volumetric extinction coefficient. This property was previously obtained using the electromagnetic scattering analysis in chapter 2. Table B.3.1 shows the optical thickness of the Durablanket® S insulation material for gray measurements. The same table provides the data of the transmission measurements and the volumetric extinction coefficient for each one of the samples calculated through Beer's law. This was accomplished by measuring the sample normal transmittance using the collimated light sources. Transmittance is calculated from the ratio of the detector signal with and without the specimen placed in a fixed position set up. This range in thickness goes from an optically very thin sample to a very thick sample. Some other values of thickness were analyzed in order to seek the possible changes in scattering properties, although not reported here.

Table B.3.1 Durablanket® S Samples

Mass [g]	Area [cm^2]	Xo [cm]	Normal Transmittance	β [1/cm]	τ_o [ ]
1.4	25.81	0.424	0.006	11.951	5.064
0.8	25.81	0.242	0.024	15.522	3.759
0.4	25.81	0.121	0.065	22.614	2.738

This transmittance results are in accordance with the spectral hemispherical transmittance results (Figure B.3.1) taken with a spectrophotometer system [93] at the NIST Optical Technology.

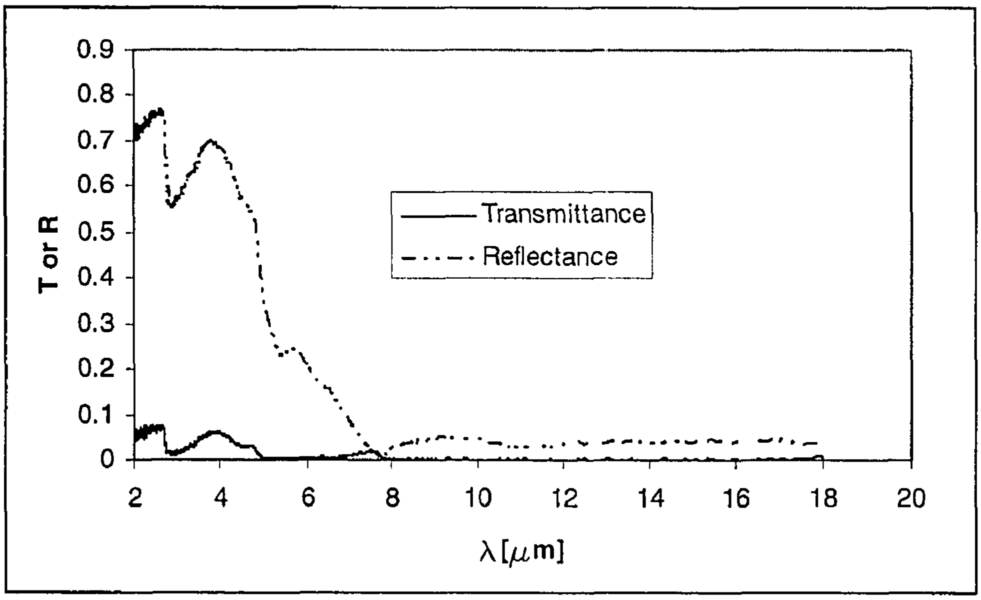

Figure B.3.1 Spectral Hemispherical Transmittance and Reflectance for 0.635 cm-thick sample of Durablanket® S

Despite the fact that the measured transmittance agrees with the values measured at NIST, the discrepancy in the values of the extinction coefficient touches on the aspect of radiative transfer that is very simple but yet often overlooked. Beer's law is so often applied incorrectly to calculate the extinction coefficient from transmission data. When an absorbing/scattering medium such as one containing particles (e.g., fibers or spheres) is subjected to collimated irradiation, the emerging intensity consists of both the collimated and the diffuse parts. The total intensity is given by:

$$I_{total} = I_{diffuse}(s,\Omega) + q_o \exp(s_t - s) \qquad \text{(B.3)}$$

The first term is due to attenuation of the incident radiation, and the second term is due to scattering by the particles. It is obvious that Beer's law is exact if the medium is purely absorbing, and its application to measured normal transmittance would give the absorption (extinction since scattering is zero) coefficient. However, for an absorbing/scattering medium, the extinction coefficient cannot be determined from Beer's law, as contribution from the scattered radiation can be significant as shown in Figure B.3.2. This Figure shows the forward and backward intensity distributions for the collimated incidence. Results are shown for two thickness values of 0.635cm and 0.0635cm. Because the fibers are non-absorbing at the wavelength of 0.25 micron, extinction is due to scattering only, thus resulting in the highly diffuse pattern of the transmitted and reflected intensity distributions. In essence, transmission of the original irradiation along the incident direction is all but non-existent. This should not be too surprising, as the fibers do not absorb and all incident radiation on the fibers are scattered. [59]

The same Figure shows the comparison of the true extinction coefficient, i.e. based on EM theory, and those calculated by utilizing the predicted normal transmittance. The calculated extinction coefficients utilizing Beer's law on the normal transmittance are different from the EM value, as the application violated the inherent assumption of Beer's law. It can be easily seen that by taking the logarithm of the RHS of equation B.3 and dividing it by S would not give you the extinction coefficient unless the diffuse term vanishes. But here there is the case that the first term on the RHS vanishes. Making transmission measurements on specimens of the same material but with different thickness, it will be found that Beer's law would give you different values of the extinction coefficient. This is an obvious inconsistency that tells that application of Beer's law to calculate the extinction coefficient of a scattering medium is incorrect. Note that the values beyond 7-micron wavelength show better agreement, because the collimated term becomes the fibers are more absorbing, resulting in the collimated term comparable to or even dominant over the diffuse scattering term. The difficulty of measurement at such long wavelengths is that the signal has become too small for detection [59]

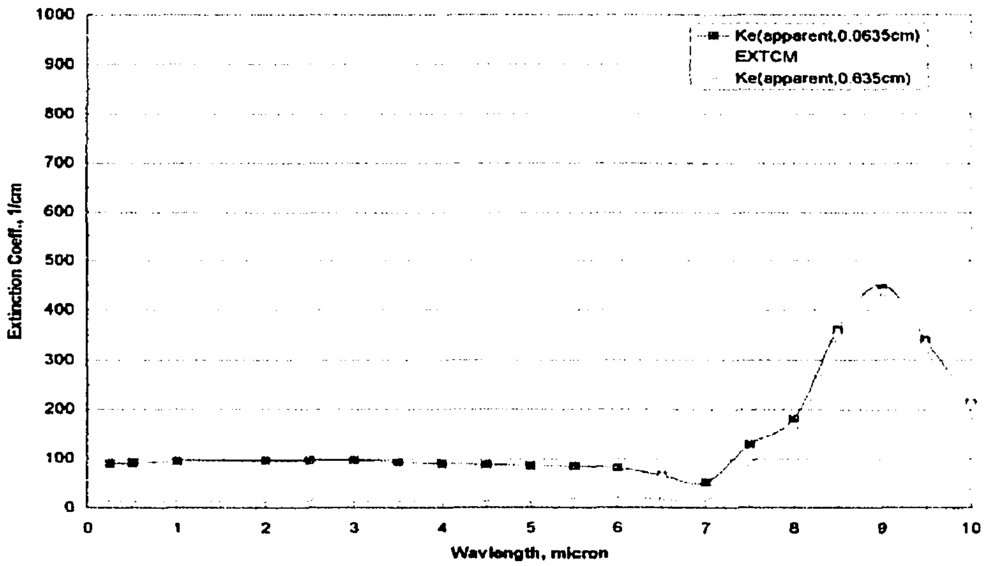

Figure B.3.2 Comparison of True Extinction Coefficient Kext (β) from Normal Transmittance, for Durablanket® S fv=0.0427. [59]

B.3.2 Phase Function[1]

The exact formulation for the scattering phase function of randomly oriented fibers has been published in reference 50. It is important to use that in the solution method, although one is tempted to use the simpler forms of either the anisotropic or linear anisotropic phase function. These simple forms of the phase function do not usually capture the two-dimensional scattering behavior of fibers at all. More importantly, they do not have any physical correspondence to fibers, as the characteristics of fiber scattering are not included in these simple phase functions. Note that the scattering behavior and therefore the phase function are strongly influenced by the value of the size parameter. In the case of Durablanket® S that has a fiber size distribution

[1] From reference 59

containing 9 radii, the size parameter for each wavelength varies widely, as shown in Figure B.3.3 This means that the phase function for each fiber radius is different, resulting in different amount of contribution to the scattered radiation.

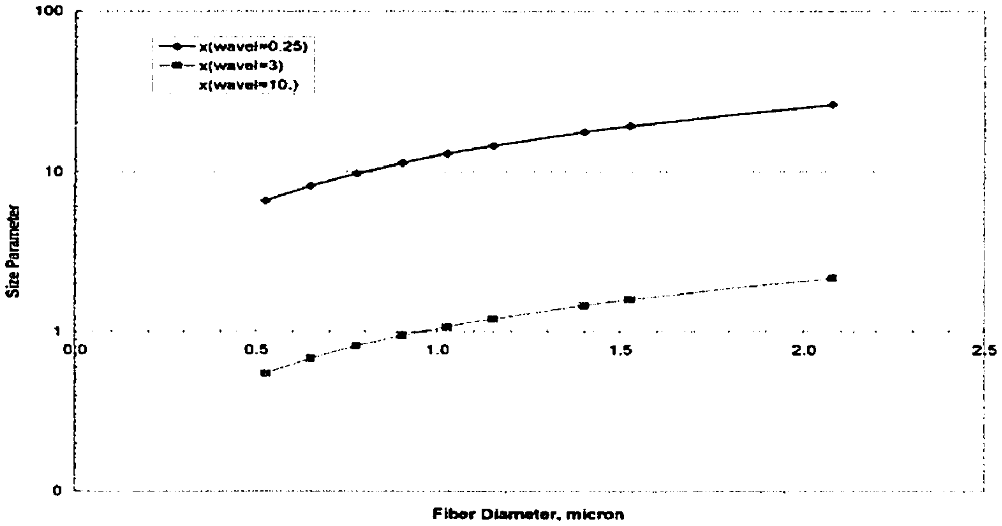

Figure B.3.3 Size Parameter vs. Fiber Diameter for Durablanket® S

These numerical analyses utilized the fiber phase function [50] (as shown in Figure B.3.4) for each fiber diameter at the specific wavelength, and the calculated fiber size distribution and optical constants, and a 40-point Gaussian quadrature discrete ordinates method to solve the RTE.

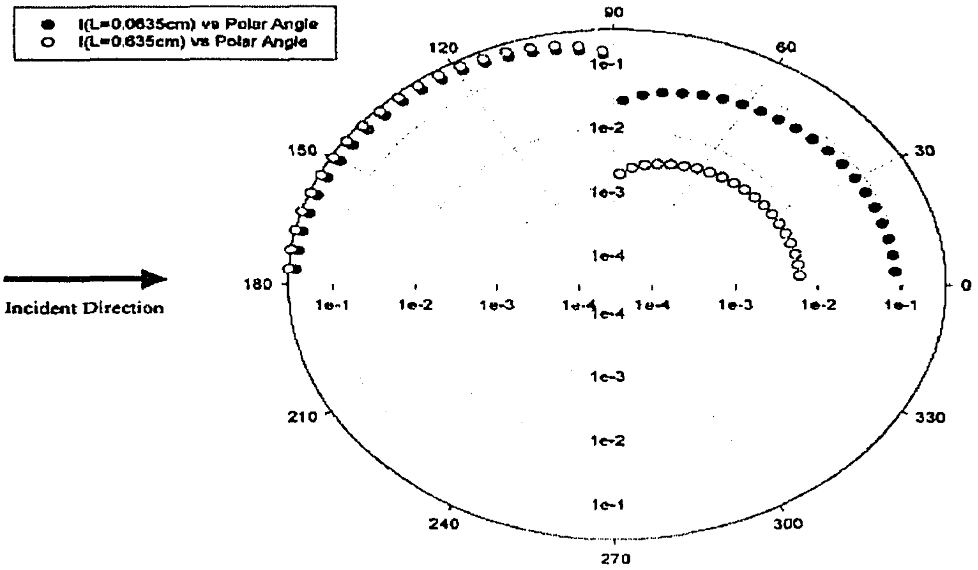

Figure B.3.4 Scattered Intensity Distribution due to Collimated Incidence on a Slab L=0.0635 cm, and 0.635cm, λ=2.5 μm, (θ=0 refers to forward direction) [59]

B.4 Results

The series of reflectance results presented in this section will not be numbered. These plotted results begin with the metallic materials including black surface, reflectance standard and continue with fiber insulation interactions (first and second rotation appearing consecutively). They begin from incident angle 1 to finish at incident angle 12 (the missing point on the x axis). R, in the vertical axis stands for BRDF.

The specular angle of reflectance is apparent in the figures. For example, it is clear from the 1st and 5th figures that they are specular pairs of ports on the hemisphere. Similarly, 2-6, 3-7, 4-8, 9-11, and 10-12 form specular pair ports. Recall from Chapter 4 that ports 9, 10, 11, and 12 are arranged closed to the normal axis, symmetrically about the normal to the sample at 25° polar angle. The other ports are also symmetric about the normal to the sample at a 73° polar angle. Again. P1N and P1S are collimated light sources, while TO-5 is a diffuse source. Also, recall that the diffuse source required subtraction of interaction with the scatterometer with no sample or backing plate. In addition, the TO-5 required special procedures for mounting (size mismatch).

Aluminum

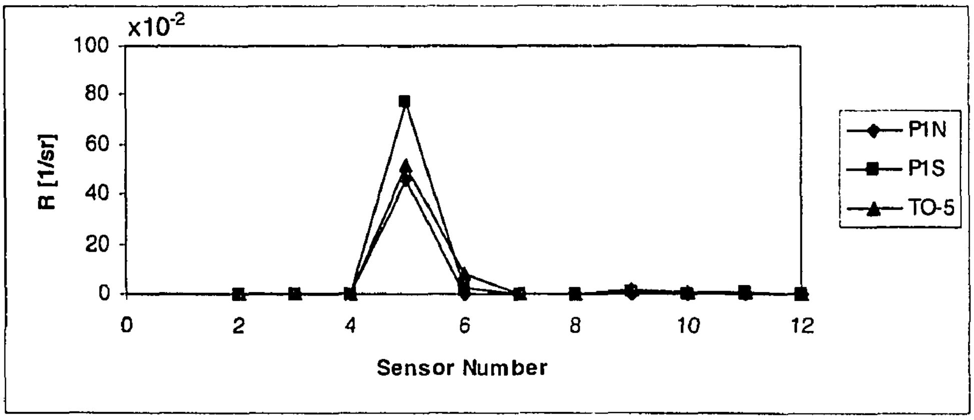
x10^-2
100
80
60
40
20
0
R [1/sr]
0
2
4
6
8
10
12
Sensor Number
P1N
P1S
TO-5

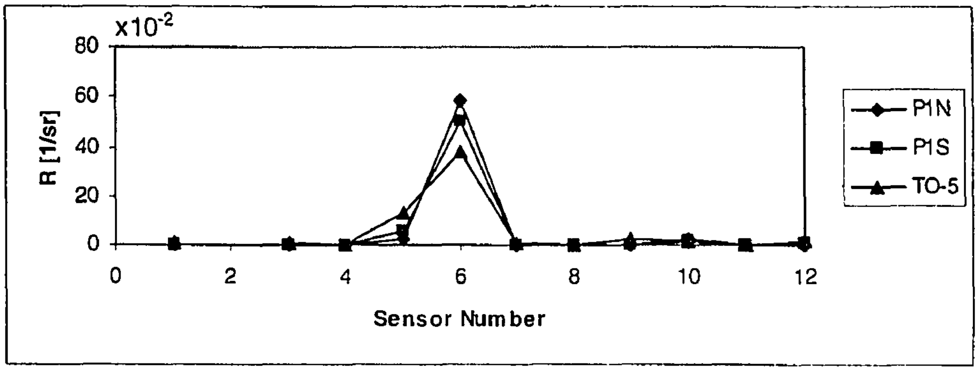
x10^-2
80
60
40
20
0
R [1/sr]
0
2
4
6
8
10
12
Sensor Number
P1N
P1S
TO-5

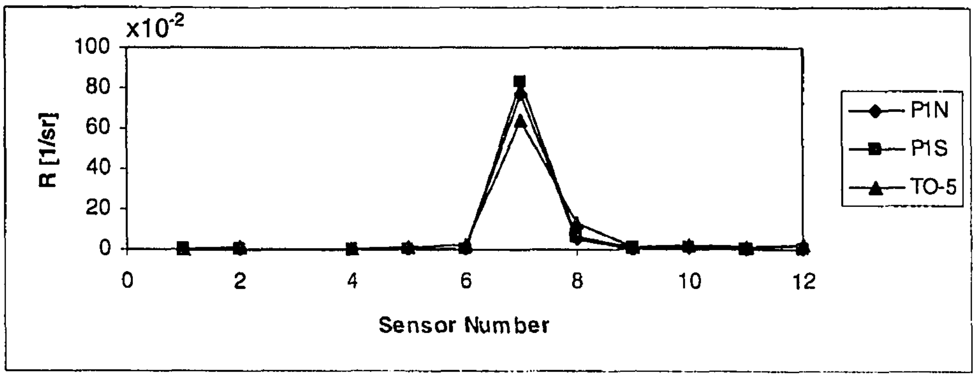
x10^-2
100
80
60
40
20
0
R [1/sr]
0
2
4
6
8
10
12
Sensor Number
P1N
P1S
TO-5

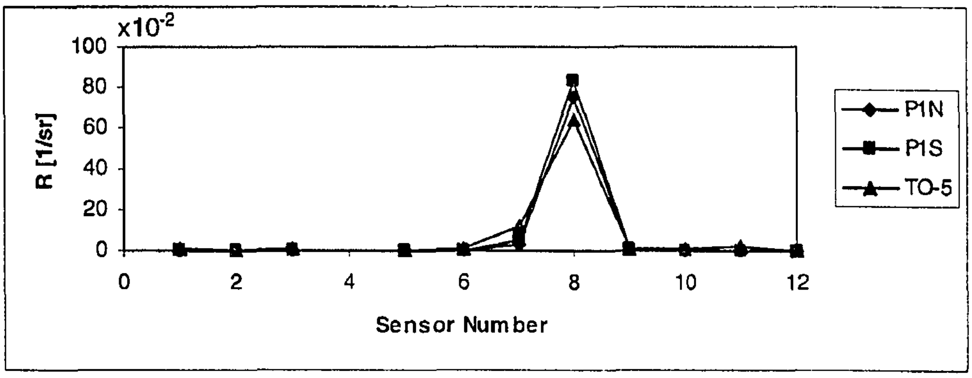
x10-2
R [1/sr]
Sensor Number
P1N
P1S
TO-5

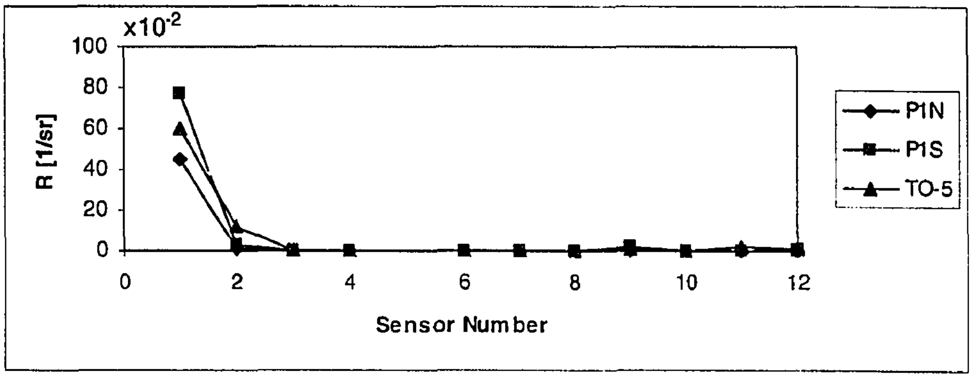
x10-2
R [1/sr]
Sensor Number
P1N
P1S
TO-5

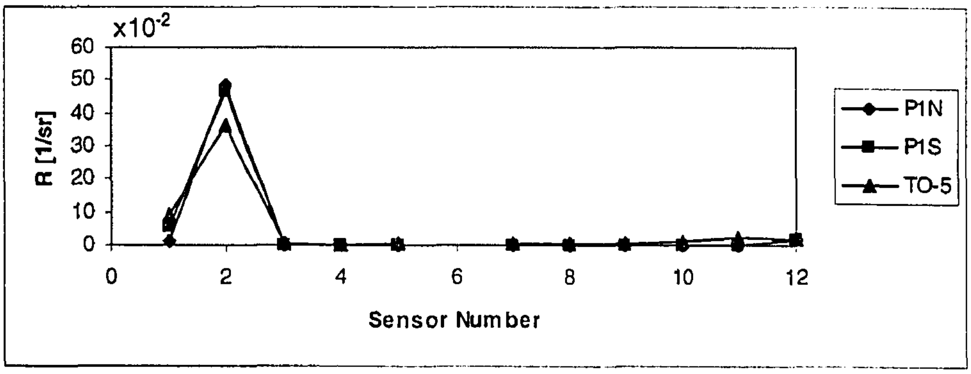
x10-2
R [1/sr]
Sensor Number
P1N
P1S
TO-5

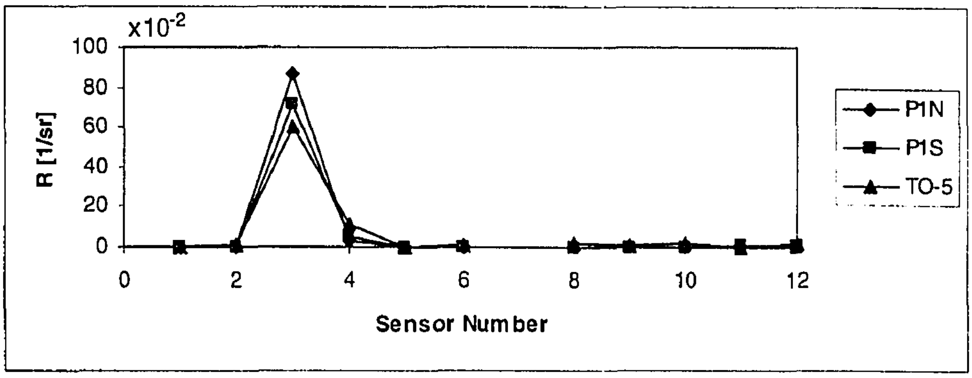
x10-2
R [1/sr]
Sensor Number
P1N
P1S
TO-5

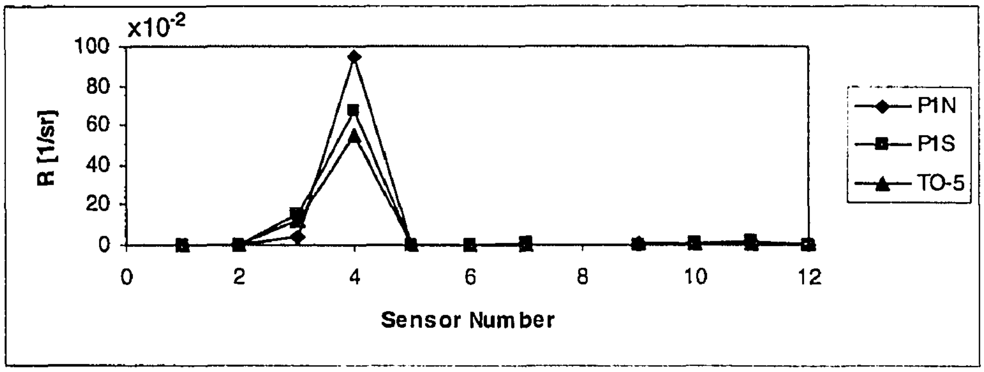

x10-2
R [1/sr]
Sensor Number
P1N
P1S
TO-5

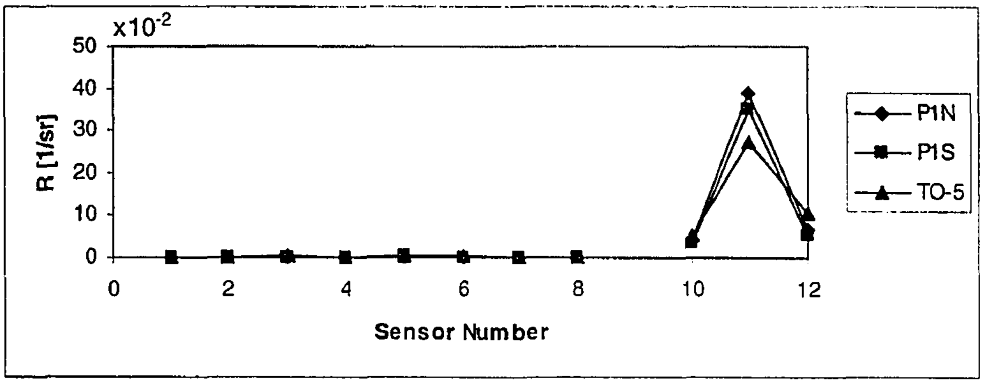

x10-2
R [1/sr]
Sensor Number
P1N
P1S
TO-5

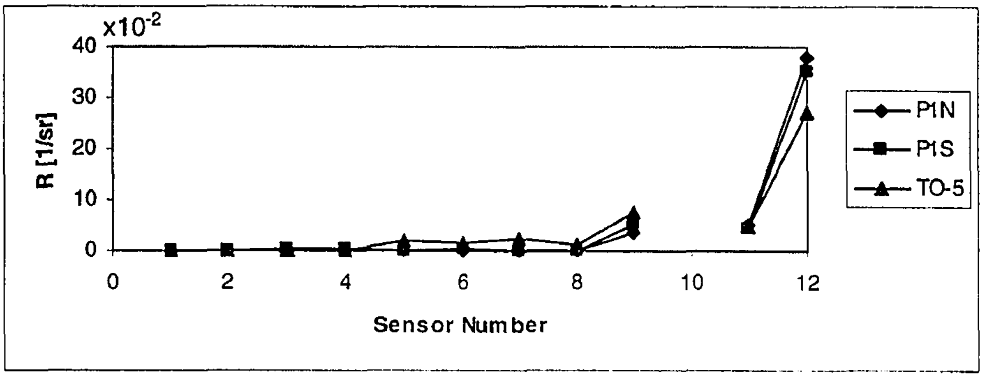

x10-2
R [1/sr]
Sensor Number
P1N
P1S
TO-5

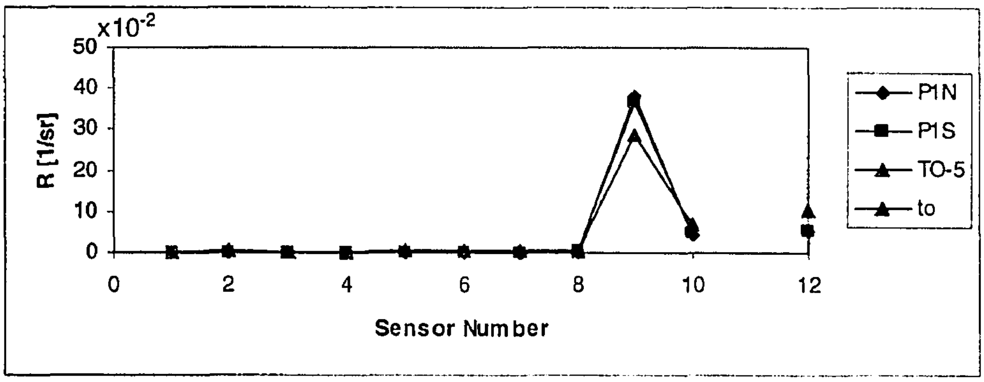

x10-2
R [1/sr]
Sensor Number
P1N
P1S
TO-5
to

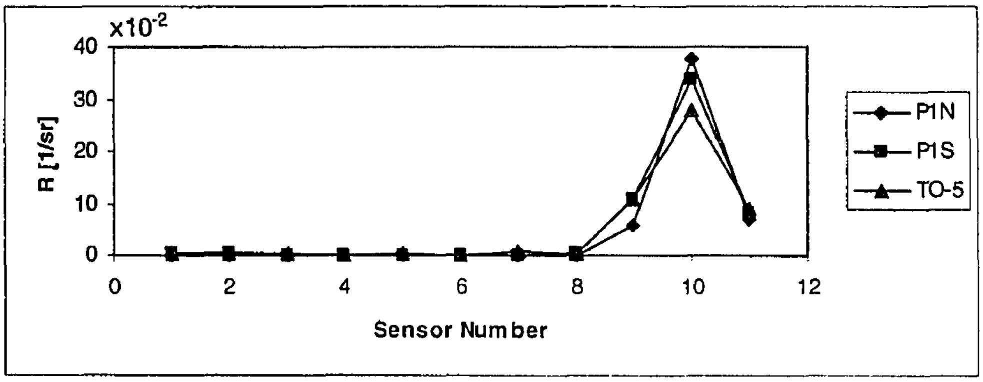

Stainless Steel

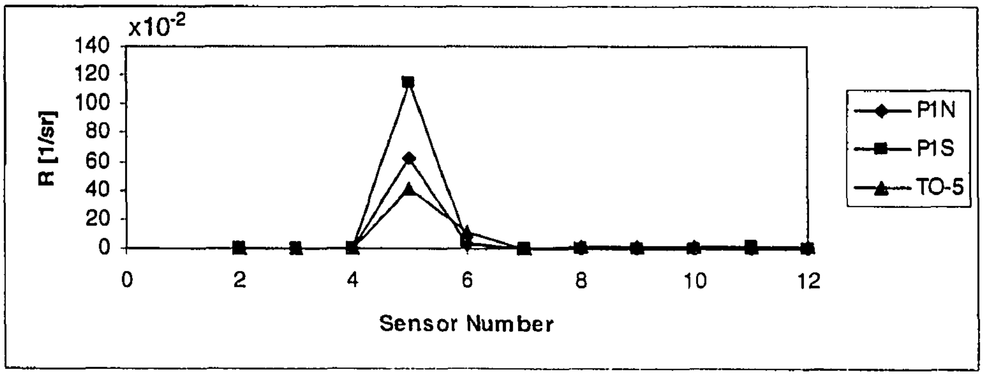

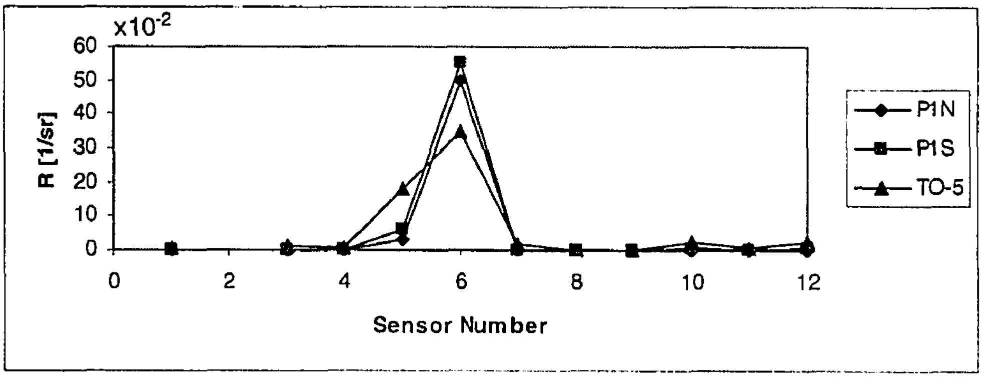

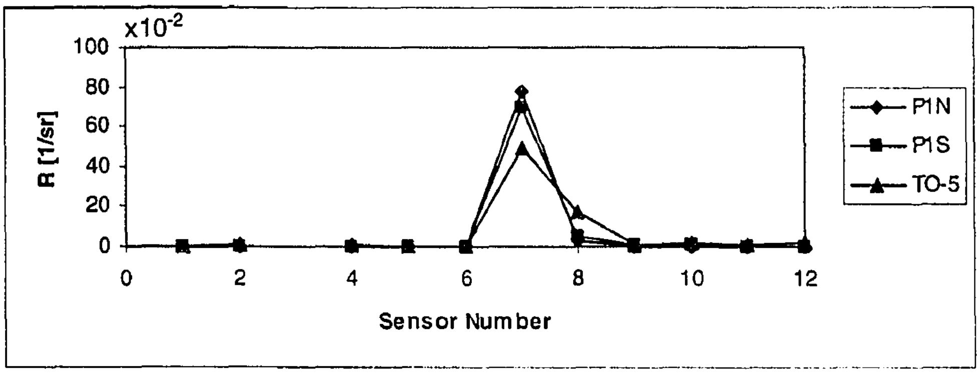
x10-2
R [1/sr]
Sensor Number
P1N
P1S
TO-5

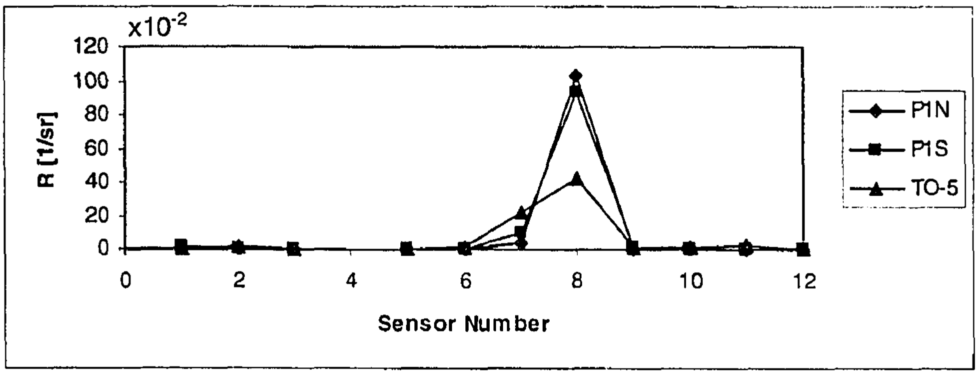
x10-2
R [1/sr]
Sensor Number
P1N
P1S
TO-5

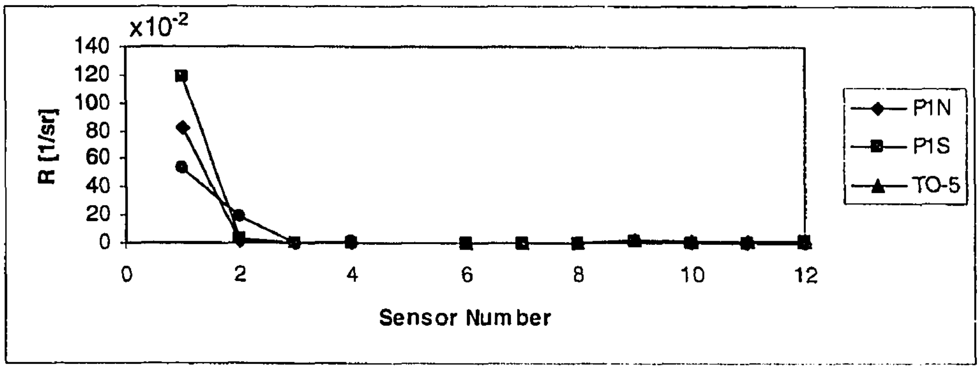
x10-2
R [1/sr]
Sensor Number
P1N
P1S
TO-5

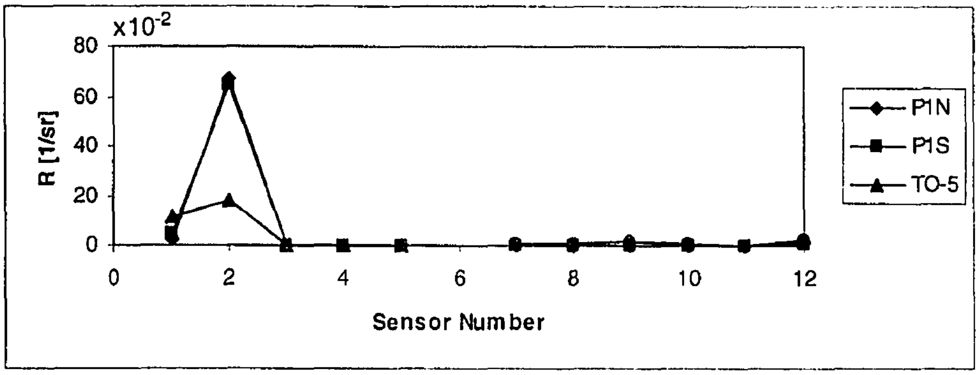
x10-2
R [1/sr]
Sensor Number
P1N
P1S
TO-5

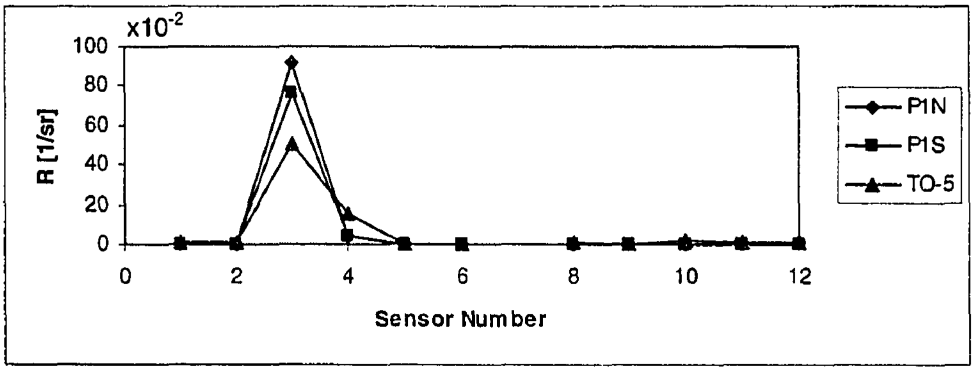
x10-2
R [1/sr]
Sensor Number
P1N
P1S
TO-5

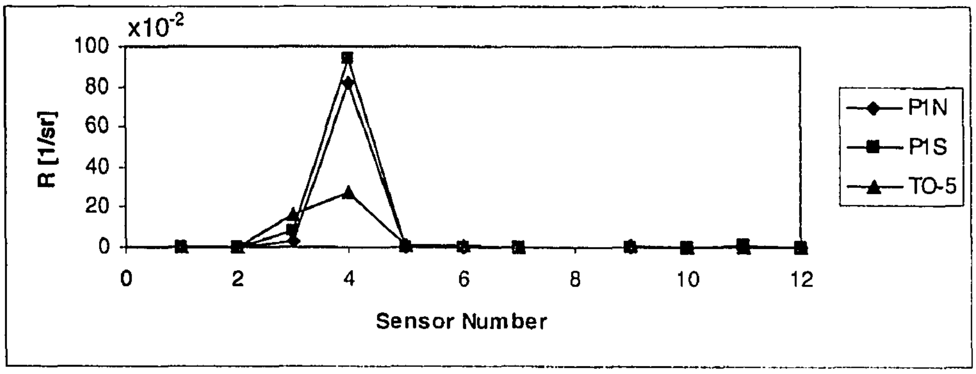
x10-2
R [1/sr]
Sensor Number
P1N
P1S
TO-5

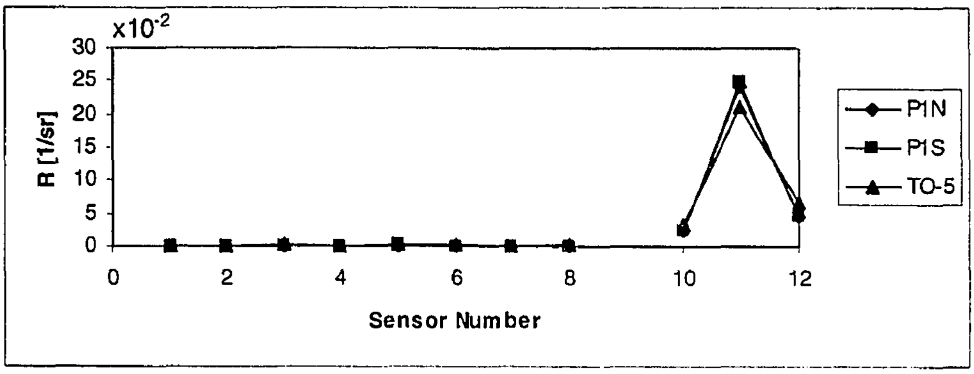
x10-2
R [1/sr]
Sensor Number
P1N
P1S
TO-5

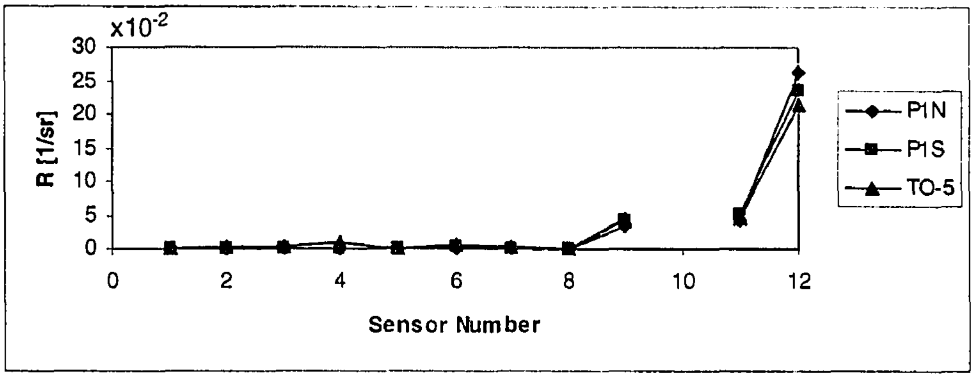
x10-2
R [1/sr]
Sensor Number
P1N
P1S
TO-5

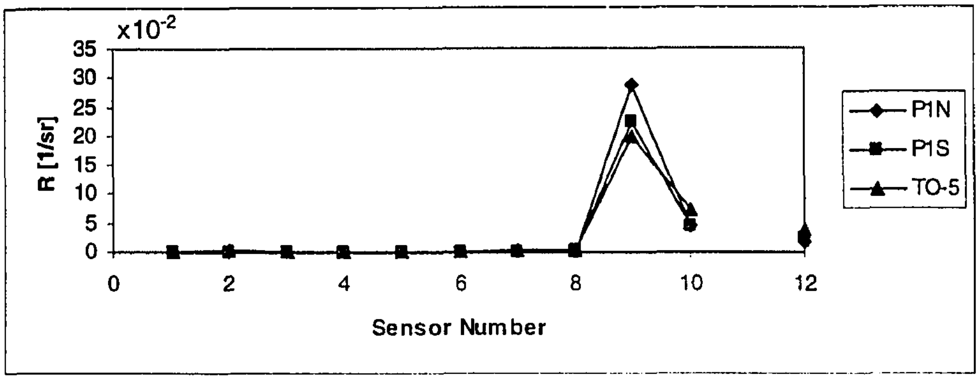

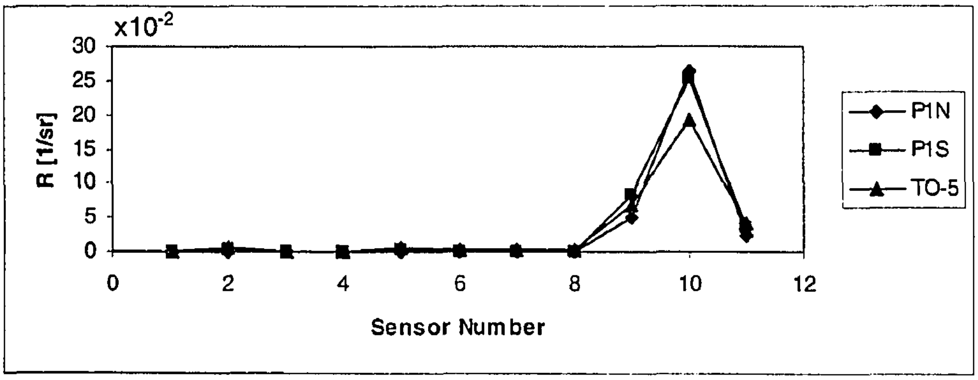

Black Anodized Surface

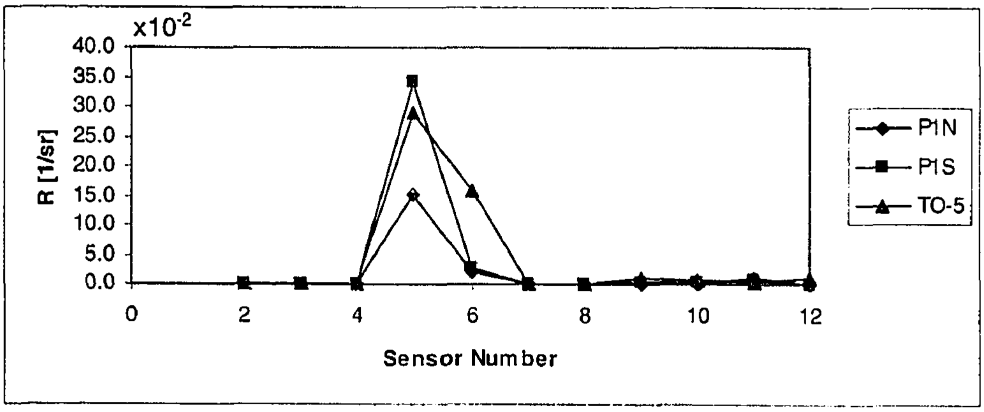

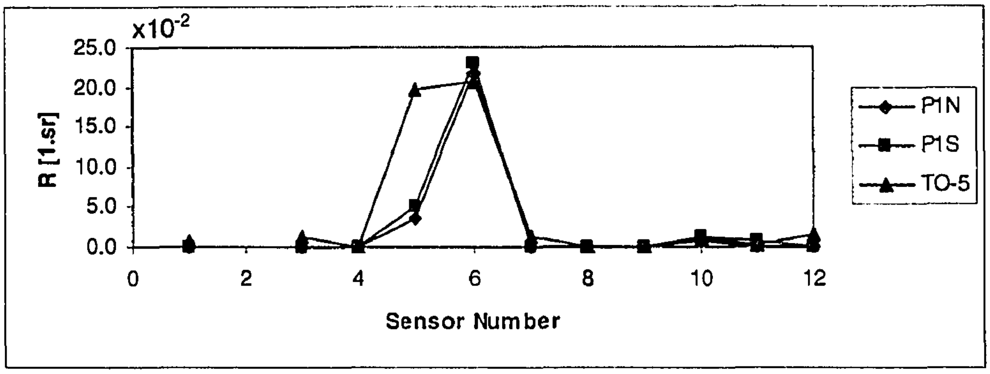
x10-2
R [1.sr]
Sensor Number
P1N
P1S
TO-5

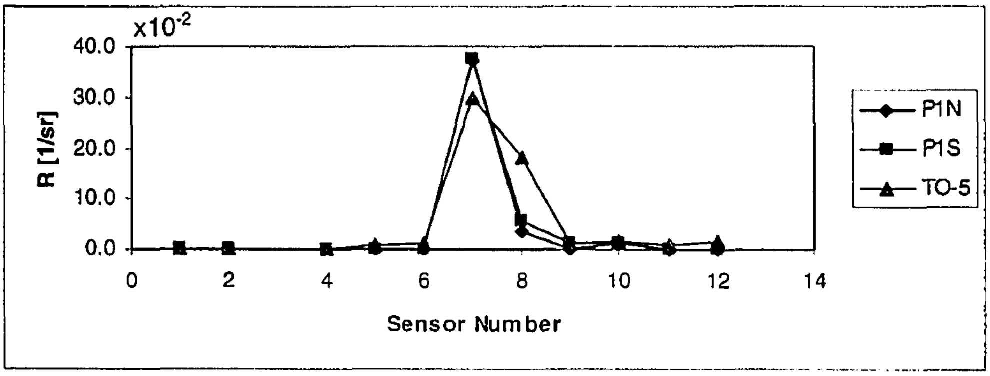
x10-2
R [1/sr]
Sensor Number
P1N
P1S
TO-5

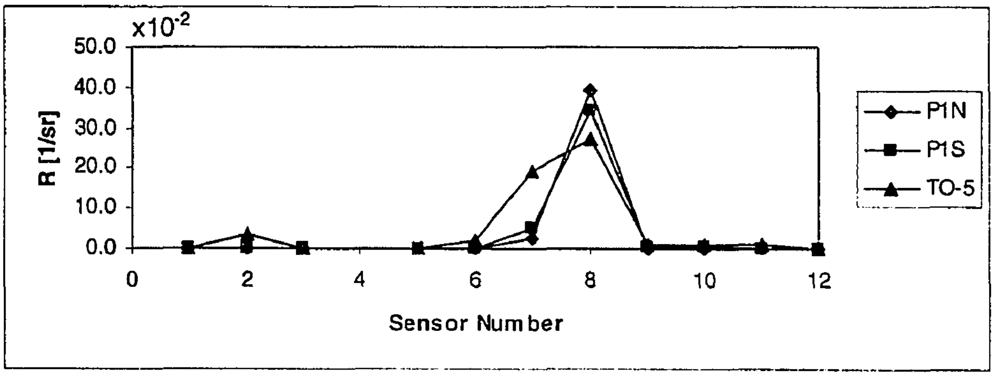
x10-2
R [1/sr]
Sensor Number
P1N
P1S
TO-5

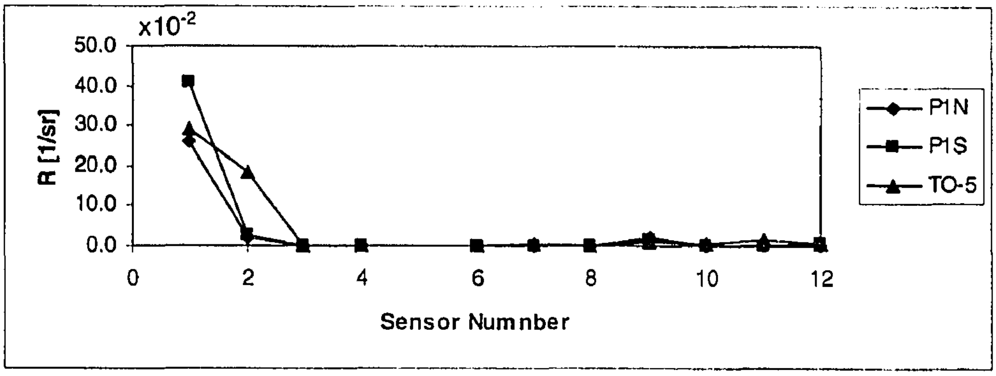
x10-2
R [1/sr]
Sensor Numnber
P1N
P1S
TO-5

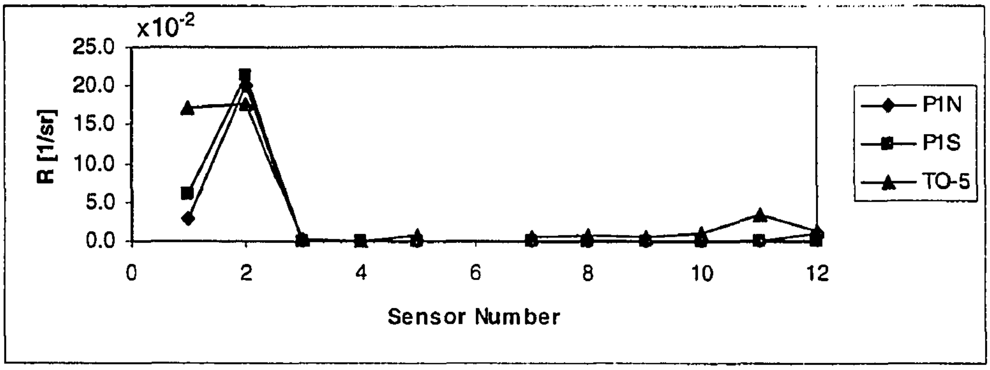
x10^-2
R [1/sr]
Sensor Number
P1N
P1S
TO-5

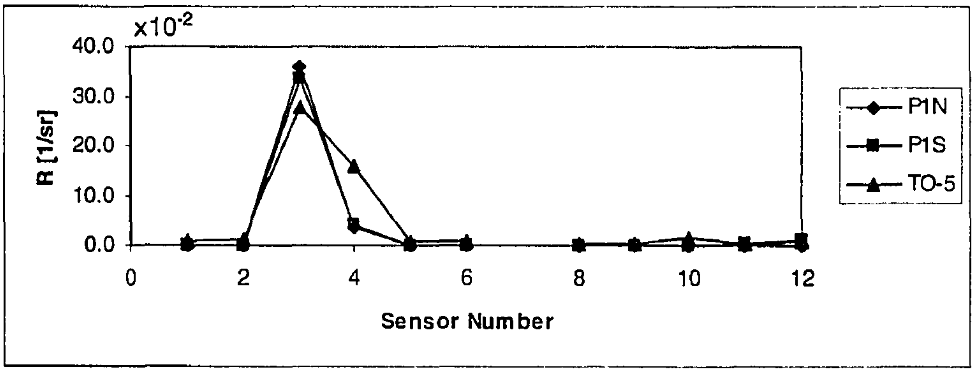
x10^-2
R [1/sr]
Sensor Number
P1N
P1S
TO-5

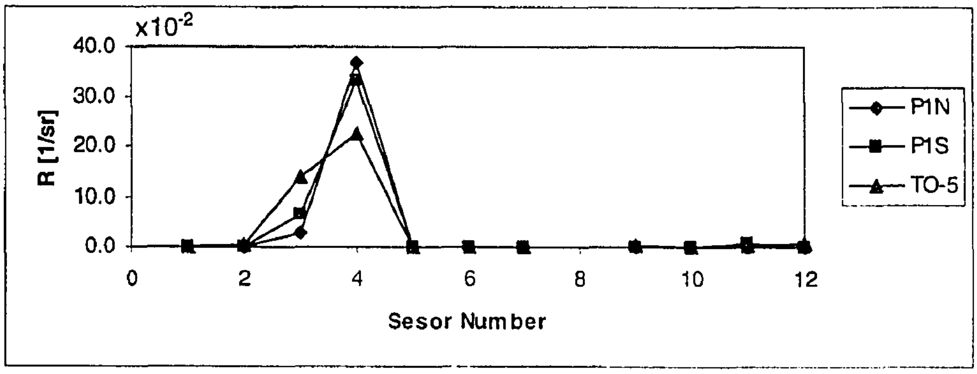
x10^-2
R [1/sr]
Sesor Number
P1N
P1S
TO-5

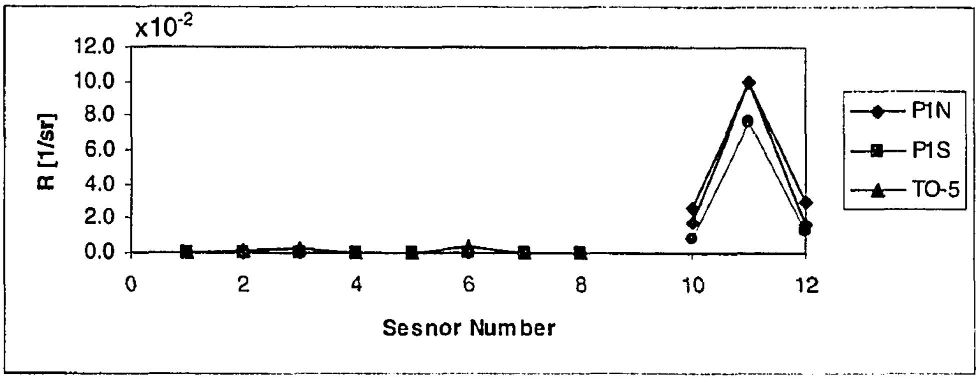
x10^-2
R [1/sr]
Sesnor Number
P1N
P1S
TO-5

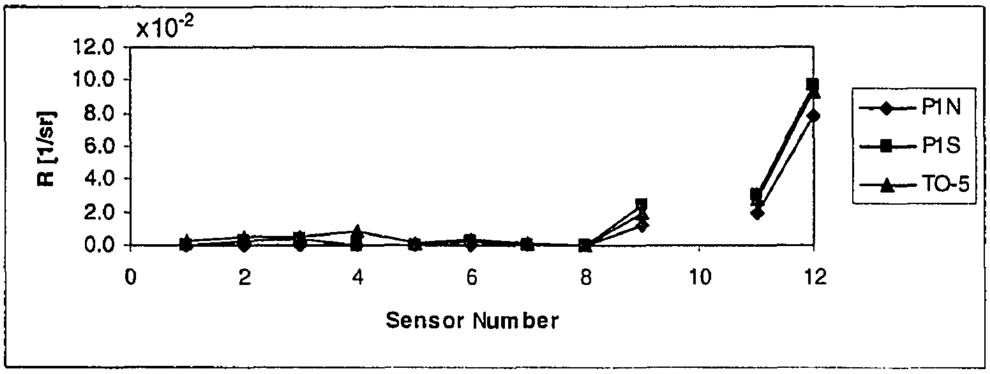
x10-2
R [1/sr]
Sensor Number
P1N
P1S
TO-5

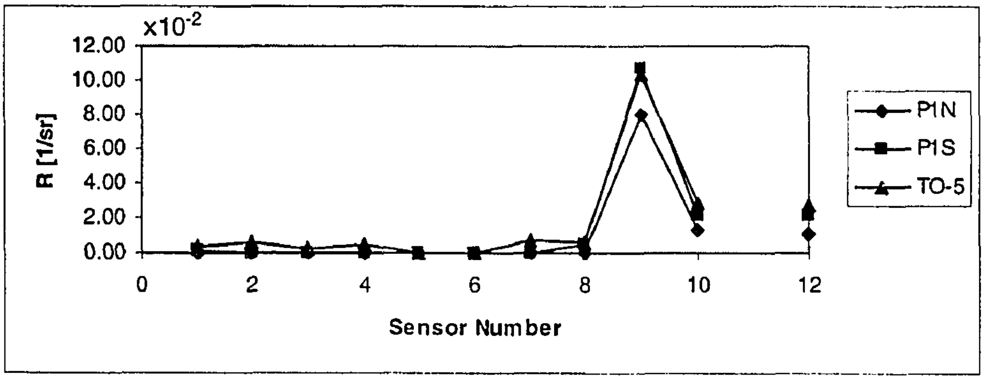
x10-2
R [1/sr]
Sensor Number
P1N
P1S
TO-5

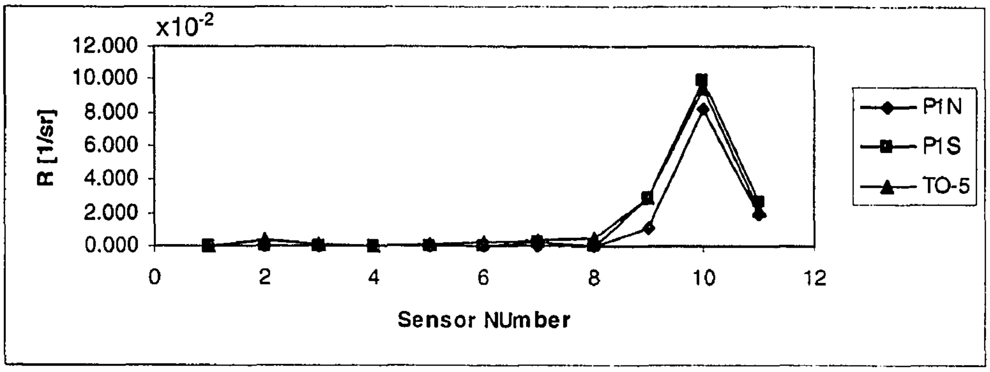
x10-2
R [1/sr]
Sensor NUmber
P1N
P1S
TO-5

Infragold® Reflectance Standard

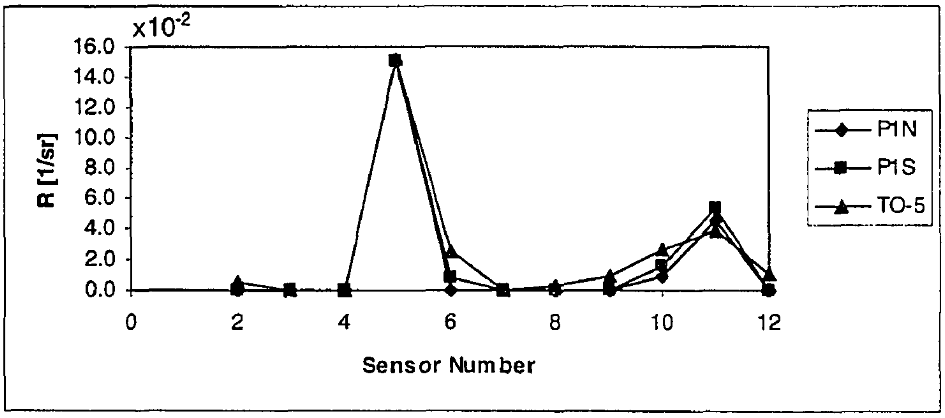

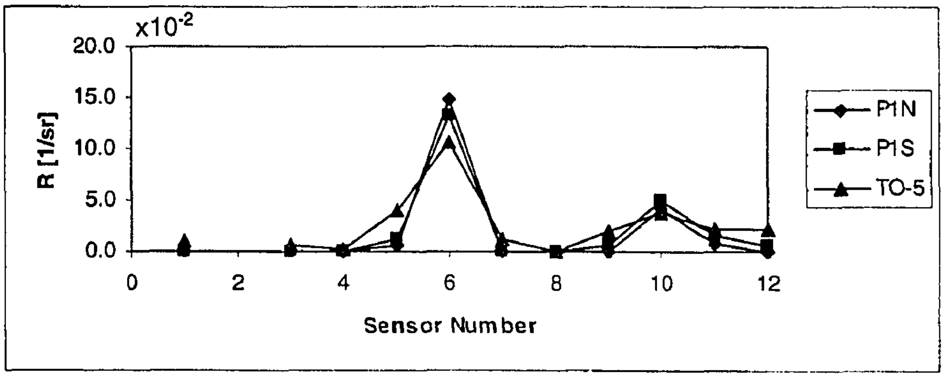

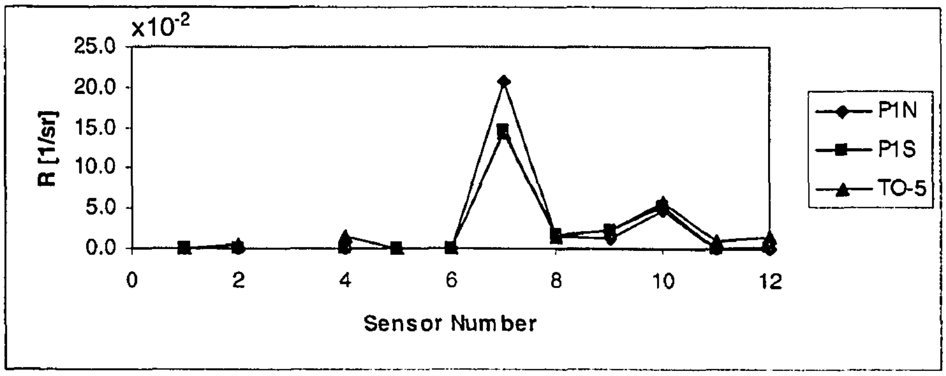

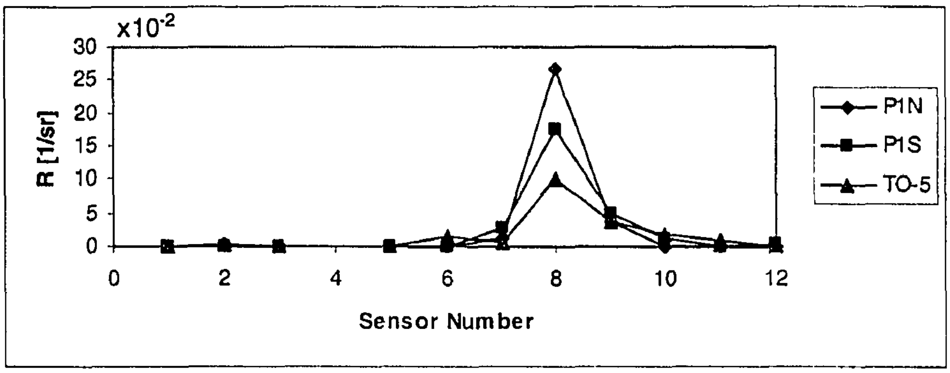

x10-2
R [1/sr]
Sensor Number
P1N
P1S
TO-5

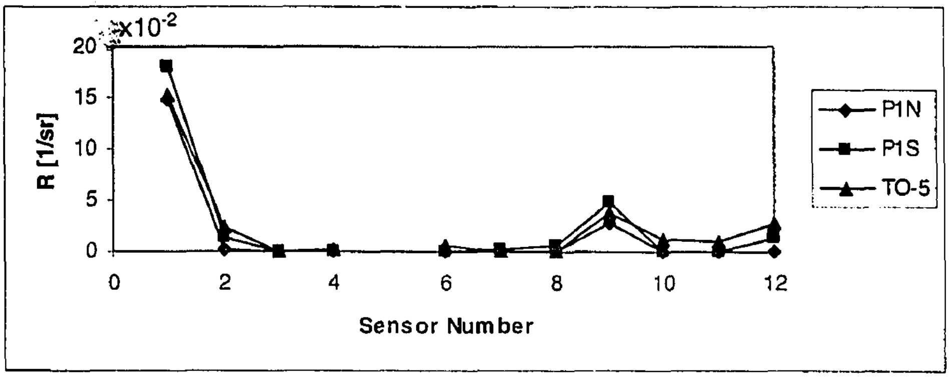

x10-2
R [1/sr]
Sensor Number
P1N
P1S
TO-5

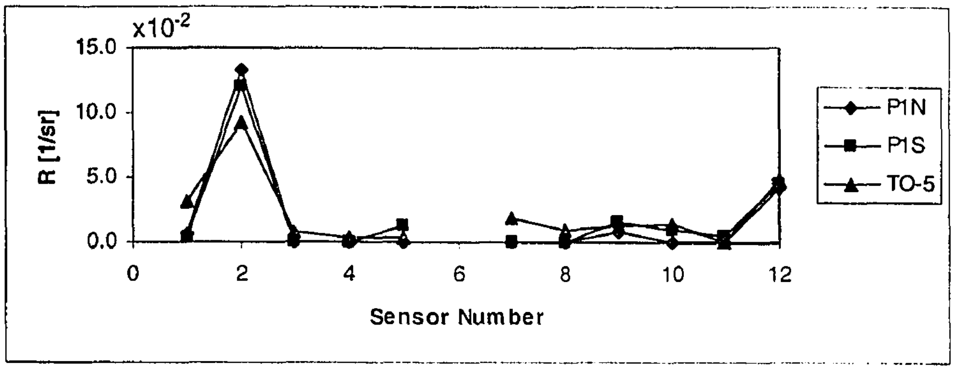

x10-2
R [1/sr]
Sensor Number
P1N
P1S
TO-5

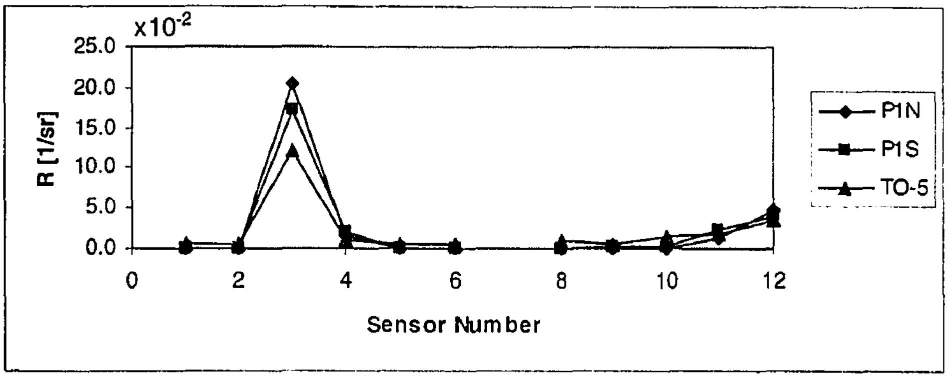

x10-2
R [1/sr]
Sensor Number
P1N
P1S
TO-5

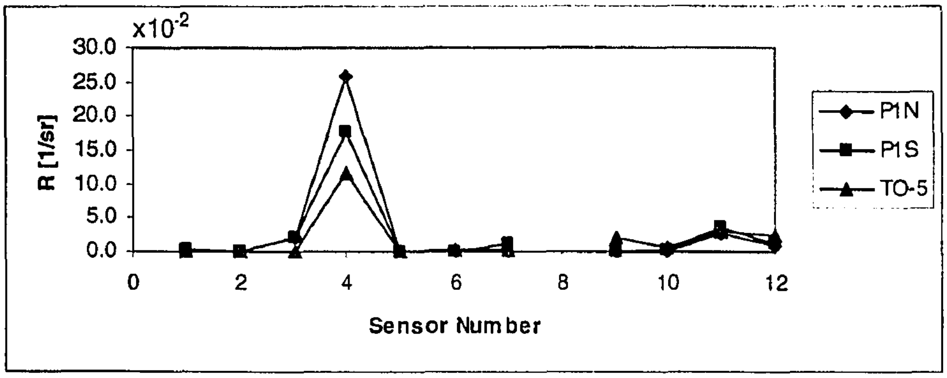
x10-2
R [1/sr]
Sensor Number
P1N
P1S
TO-5

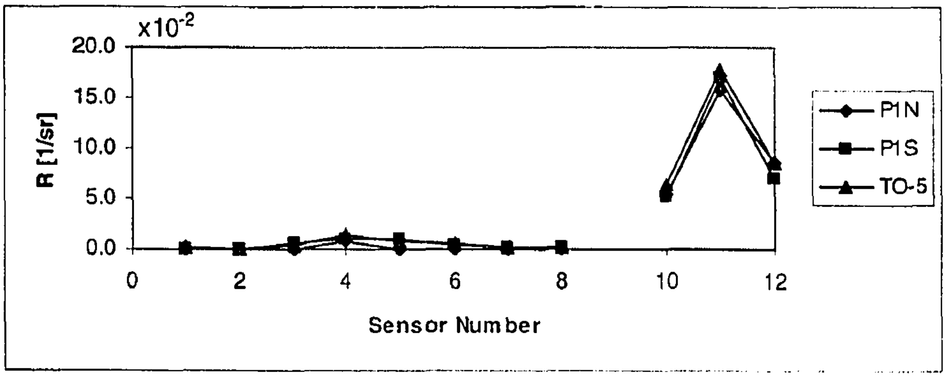
x10-2
R [1/sr]
Sensor Number
P1N
P1S
TO-5

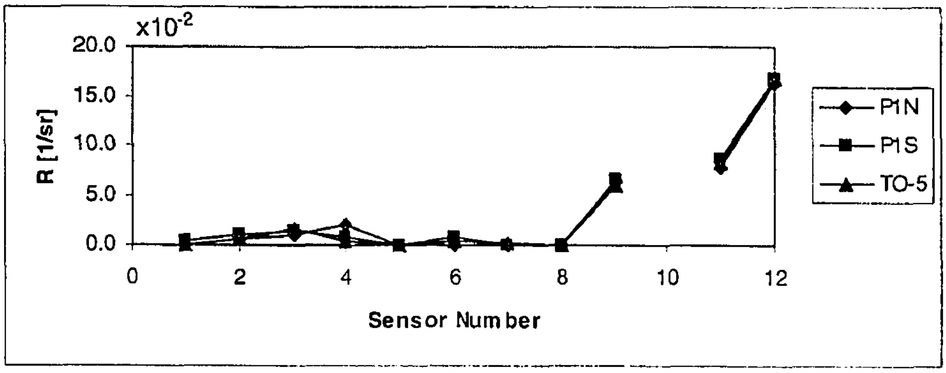
x10-2
R [1/sr]
Sensor Number
P1N
P1S
TO-5

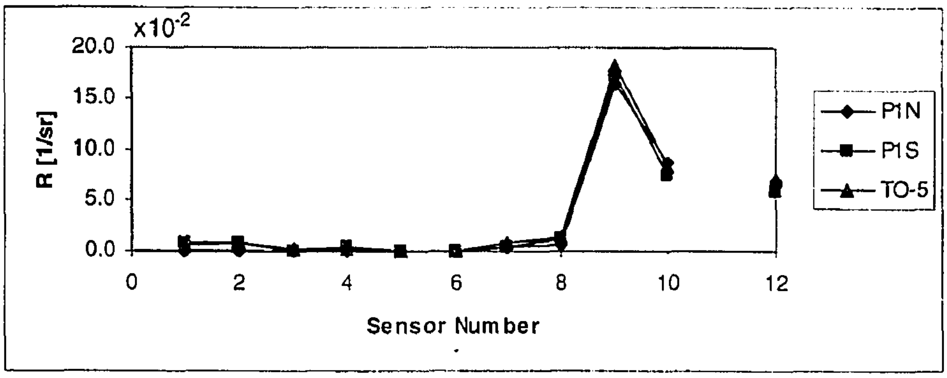
x10-2
R [1/sr]
Sensor Number
P1N
P1S
TO-5

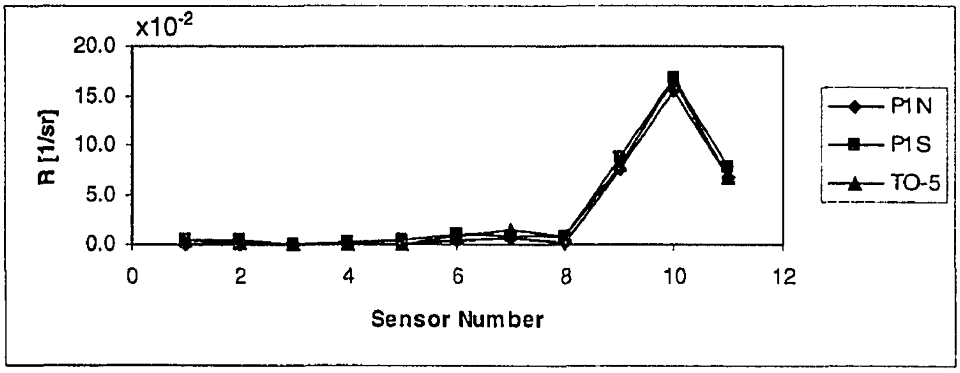

Fiber Insulation (ReflectIR_P1N)

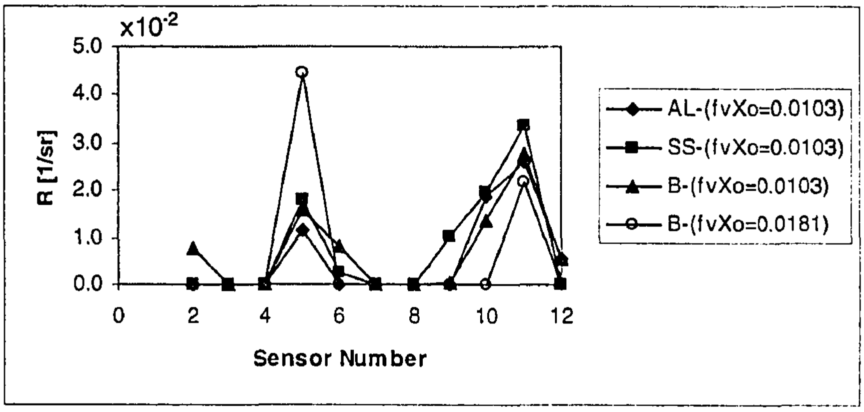

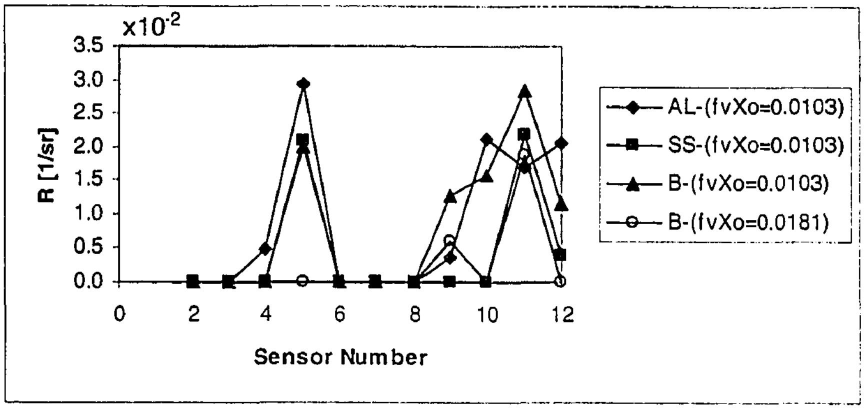

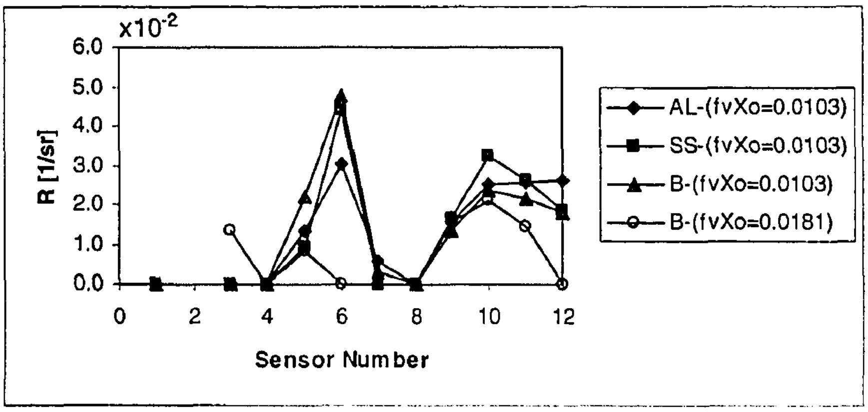
x10^-2
R [1/sr]
Sensor Number
AL-(fvXo=0.0103)
SS-(fvXo=0.0103)
B-(fvXo=0.0103)
B-(fvXo=0.0181)

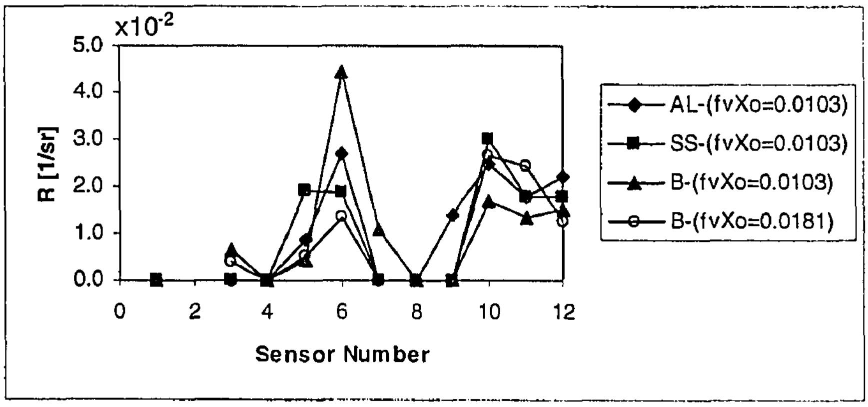
x10^-2
R [1/sr]
Sensor Number
AL-(fvXo=0.0103)
SS-(fvXo=0.0103)
B-(fvXo=0.0103)
B-(fvXo=0.0181)

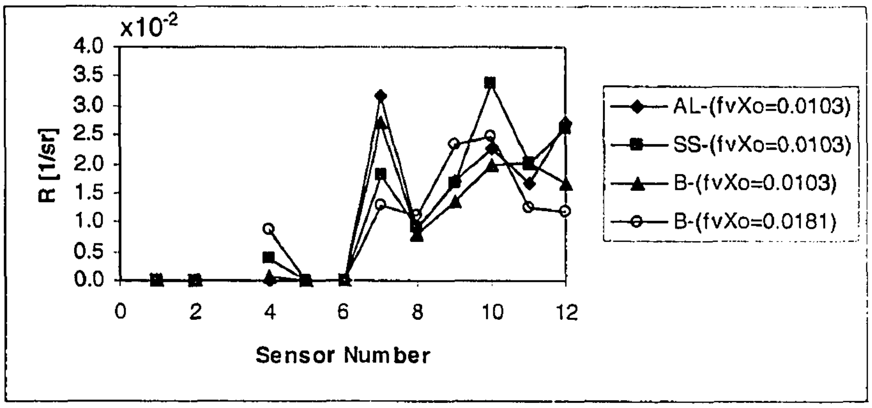
x10^-2
R [1/sr]
Sensor Number
AL-(fvXo=0.0103)
SS-(fvXo=0.0103)
B-(fvXo=0.0103)
B-(fvXo=0.0181)

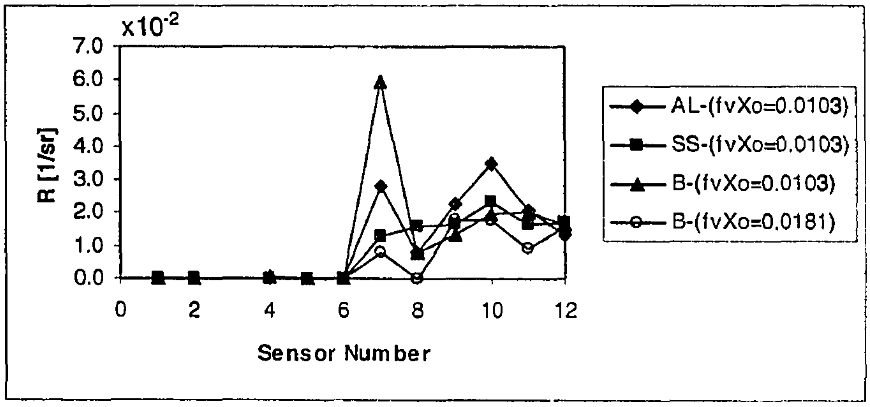
x10^-2
R [1/sr]
Sensor Number
AL-(fvXo=0.0103)
SS-(fvXo=0.0103)
B-(fvXo=0.0103)
B-(fvXo=0.0181)

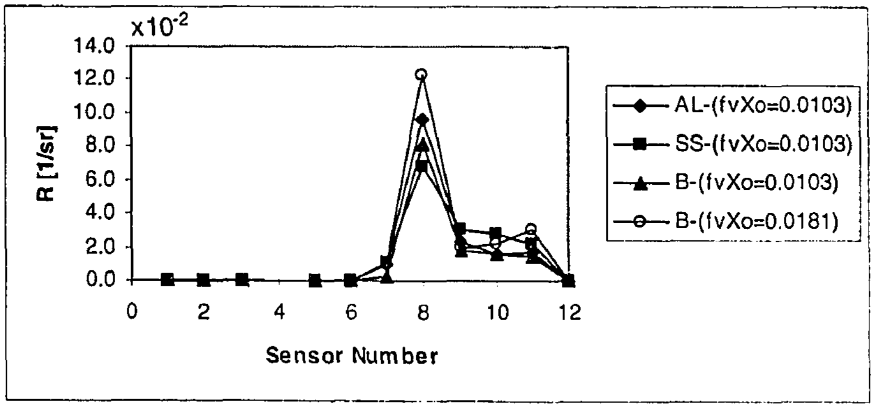
x10^-2
R [1/sr]
Sensor Number
AL-(fvXo=0.0103)
SS-(fvXo=0.0103)
B-(fvXo=0.0103)
B-(fvXo=0.0181)

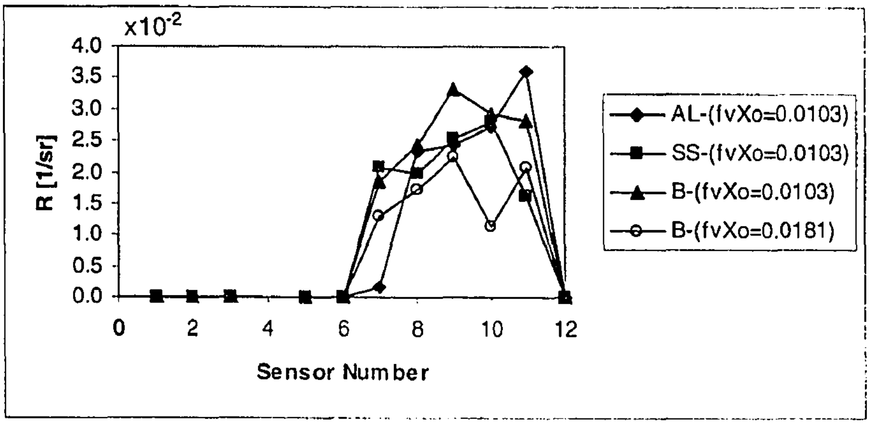
x10^-2
R [1/sr]
Sensor Number
AL-(fvXo=0.0103)
SS-(fvXo=0.0103)
B-(fvXo=0.0103)
B-(fvXo=0.0181)

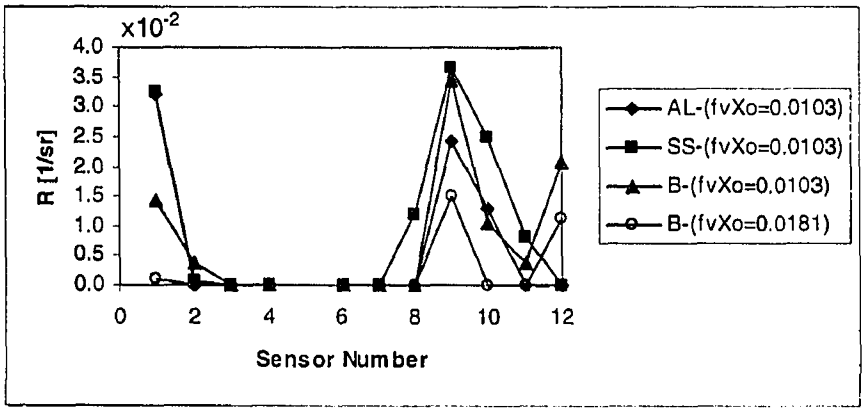

x10^-2
R [1/sr]
Sensor Number
AL-(fvXo=0.0103)
SS-(fvXo=0.0103)
B-(fvXo=0.0103)
B-(fvXo=0.0181)

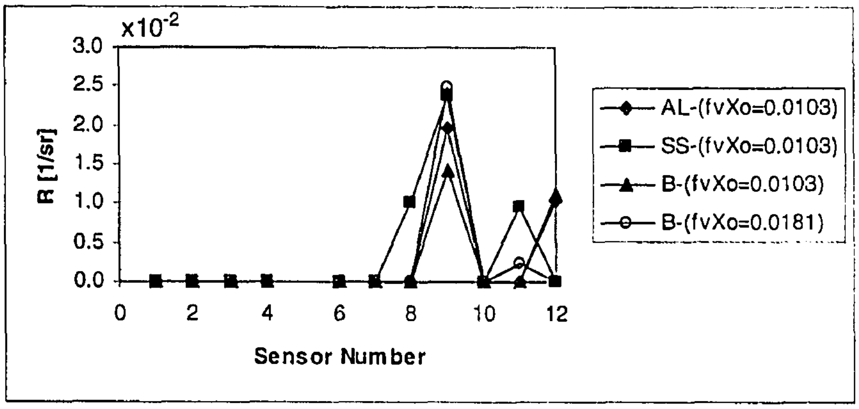

x10^-2
R [1/sr]
Sensor Number
AL-(fvXo=0.0103)
SS-(fvXo=0.0103)
B-(fvXo=0.0103)
B-(fvXo=0.0181)

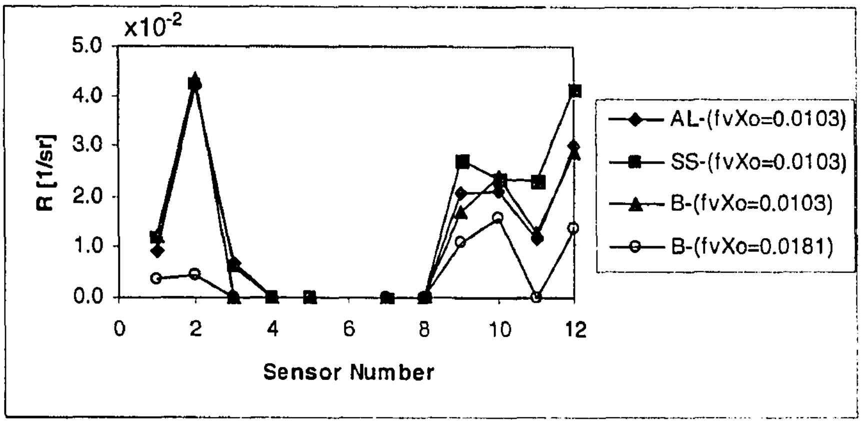

x10^-2
R [1/sr]
Sensor Number
AL-(fvXo=0.0103)
SS-(fvXo=0.0103)
B-(fvXo=0.0103)
B-(fvXo=0.0181)

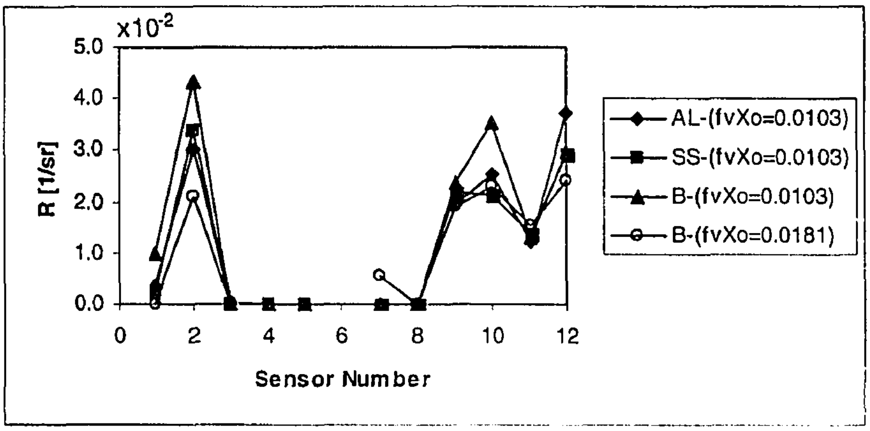
x10-2
R [1/sr]
Sensor Number
AL-(fvXo=0.0103)
SS-(fvXo=0.0103)
B-(fvXo=0.0103)
B-(fvXo=0.0181)

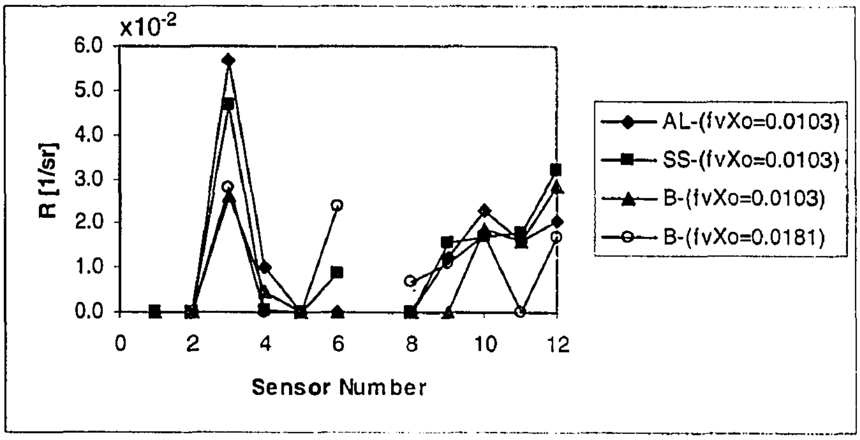
x10-2
R [1/sr]
Sensor Number
AL-(fvXo=0.0103)
SS-(fvXo=0.0103)
B-(fvXo=0.0103)
B-(fvXo=0.0181)

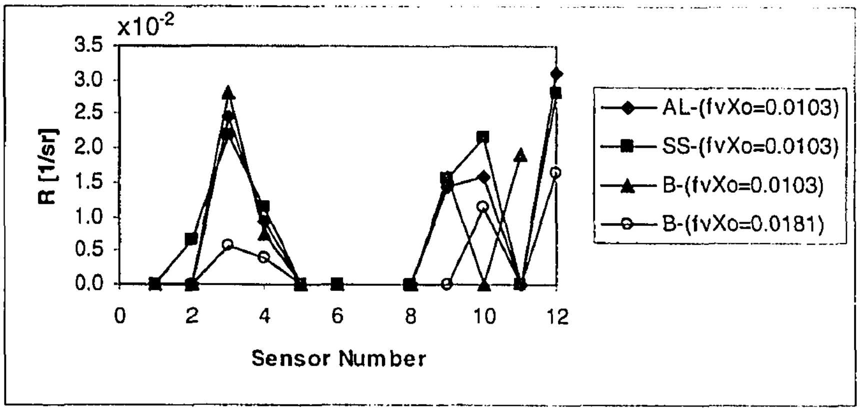
x10-2
R [1/sr]
Sensor Number
AL-(fvXo=0.0103)
SS-(fvXo=0.0103)
B-(fvXo=0.0103)
B-(fvXo=0.0181)

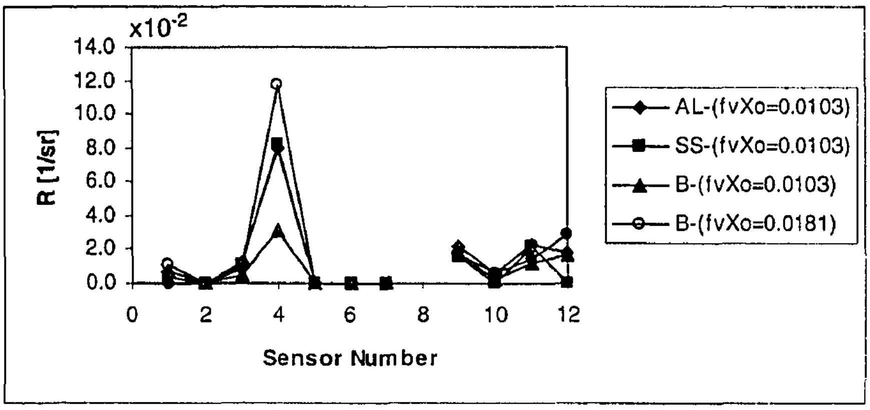

x10^-2
R [1/sr]
Sensor Number
AL-(fvXo=0.0103)
SS-(fvXo=0.0103)
B-(fvXo=0.0103)
B-(fvXo=0.0181)

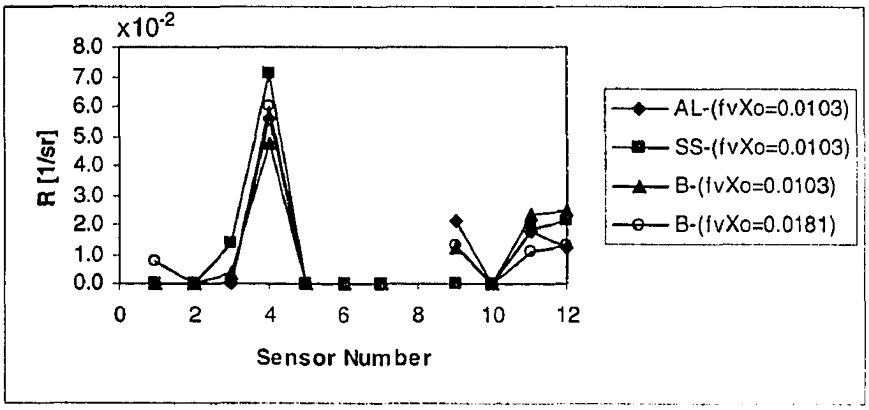

x10^-2
R [1/sr]
Sensor Number
AL-(fvXo=0.0103)
SS-(fvXo=0.0103)
B-(fvXo=0.0103)
B-(fvXo=0.0181)

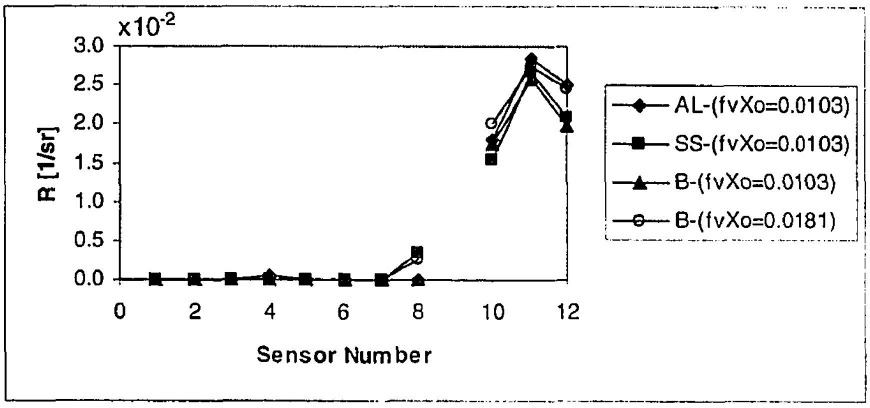

x10^-2
R [1/sr]
Sensor Number
AL-(fvXo=0.0103)
SS-(fvXo=0.0103)
B-(fvXo=0.0103)
B-(fvXo=0.0181)

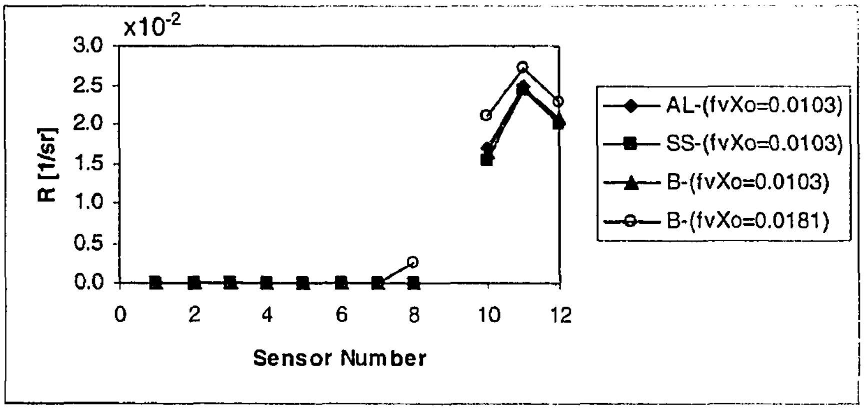
x10-2
R [1/sr]
Sensor Number
AL-(fvXo=0.0103)
SS-(fvXo=0.0103)
B-(fvXo=0.0103)
B-(fvXo=0.0181)

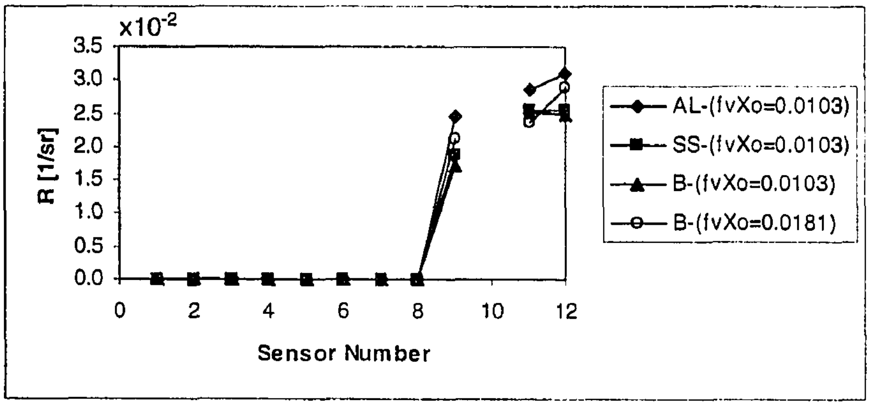
x10-2
R [1/sr]
Sensor Number
AL-(fvXo=0.0103)
SS-(fvXo=0.0103)
B-(fvXo=0.0103)
B-(fvXo=0.0181)

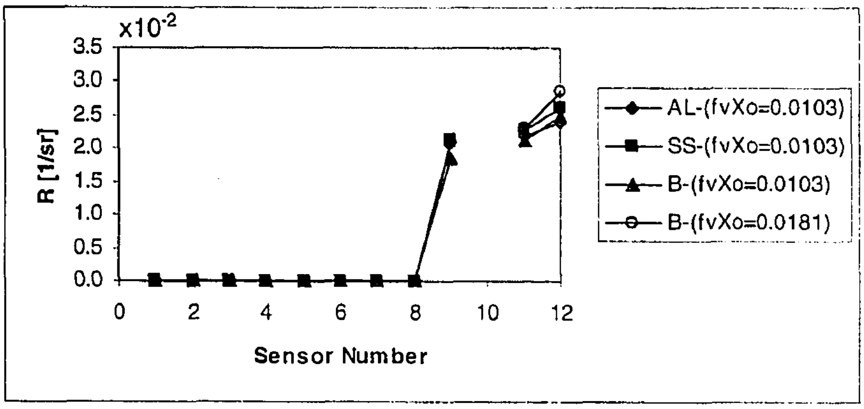
x10-2
R [1/sr]
Sensor Number
AL-(fvXo=0.0103)
SS-(fvXo=0.0103)
B-(fvXo=0.0103)
B-(fvXo=0.0181)

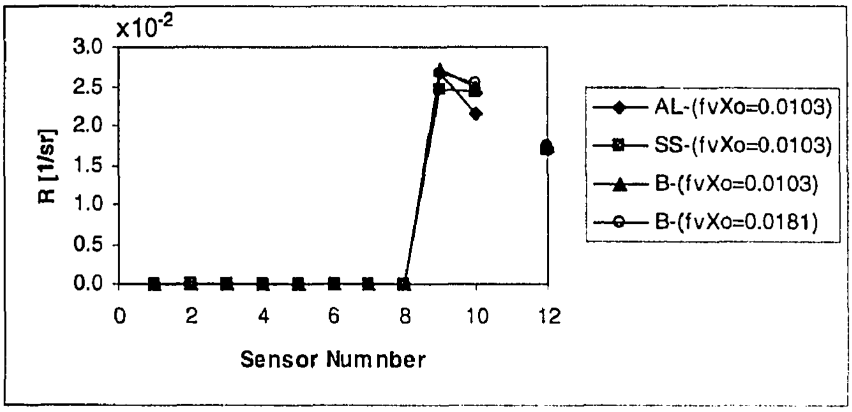
x10-2
R [1/sr]
Sensor Numnber
AL-(fvXo=0.0103)
SS-(fvXo=0.0103)
B-(fvXo=0.0103)
B-(fvXo=0.0181)

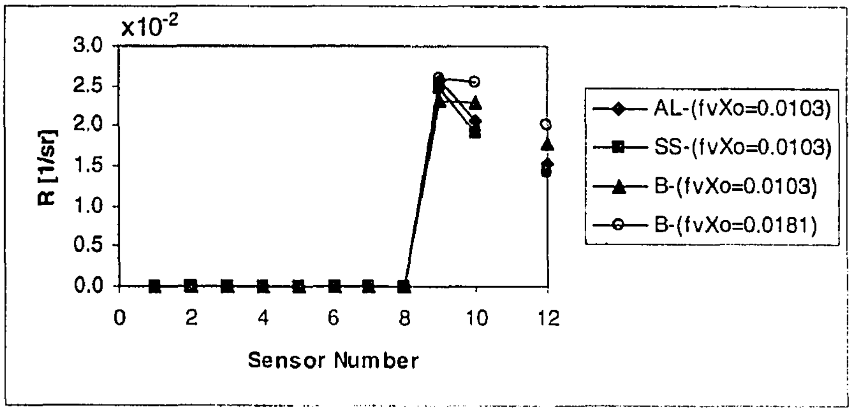
x10-2
R [1/sr]
Sensor Number
AL-(fvXo=0.0103)
SS-(fvXo=0.0103)
B-(fvXo=0.0103)
B-(fvXo=0.0181)

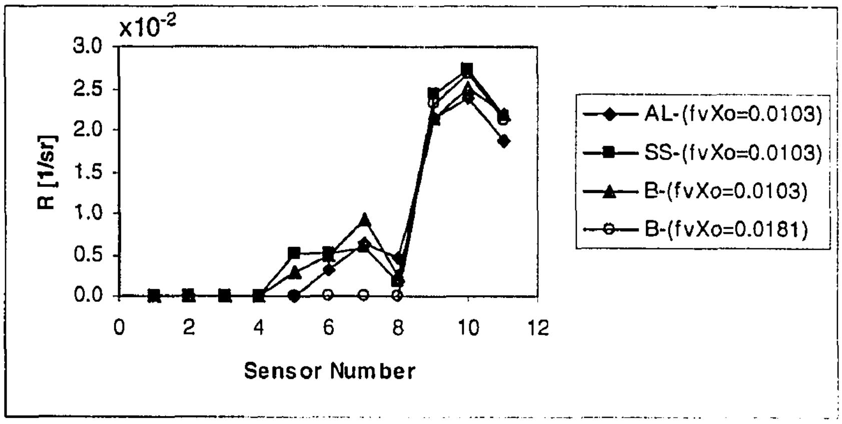
x10-2
R [1/sr]
Sensor Number
AL-(fvXo=0.0103)
SS-(fvXo=0.0103)
B-(fvXo=0.0103)
B-(fvXo=0.0181)

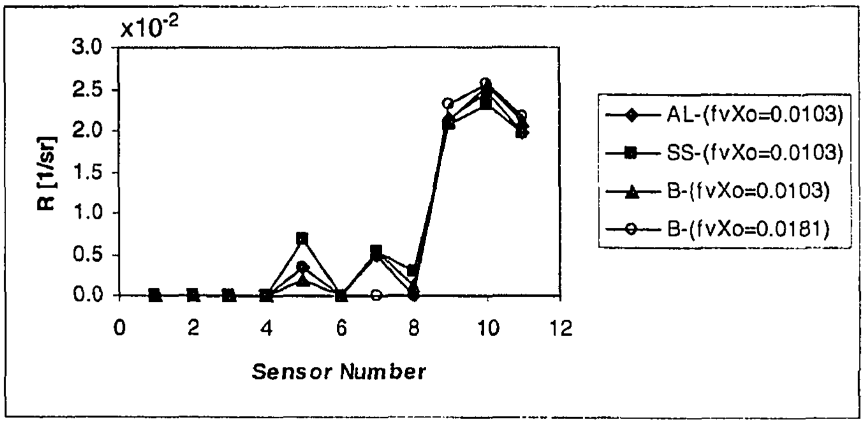

Fiber Insulation (ReflectIR P1S)

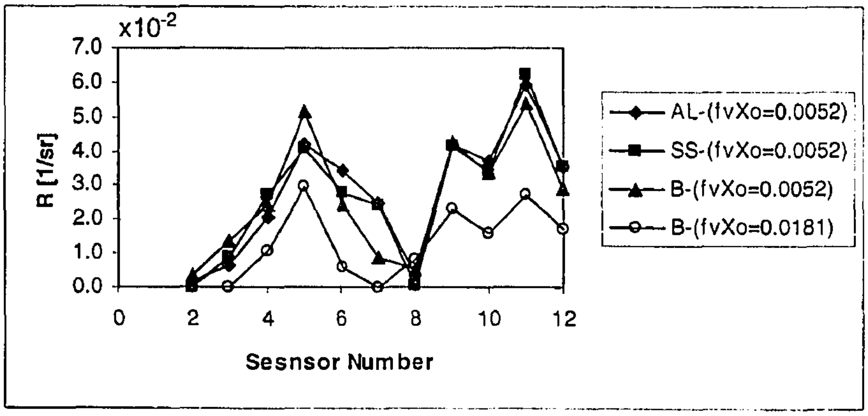

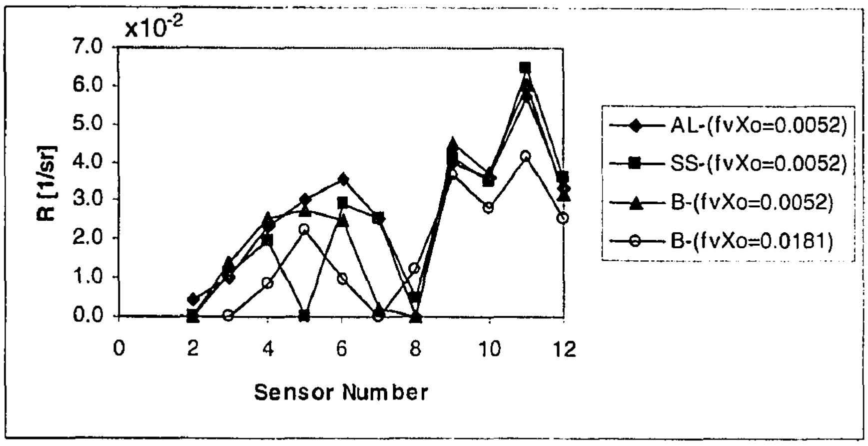

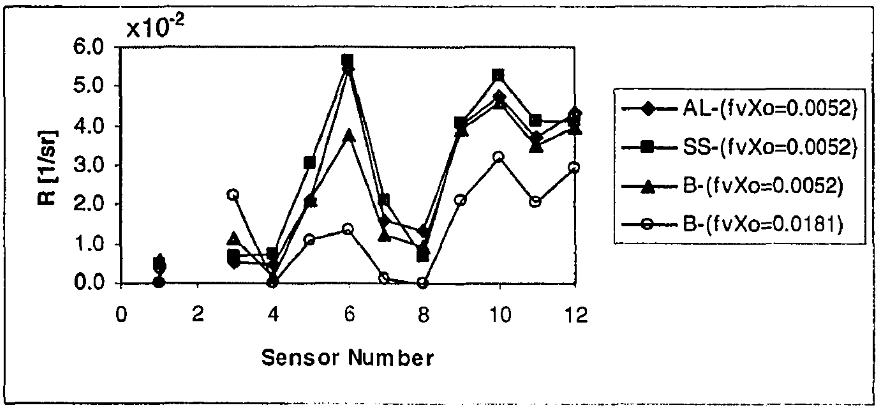
x10-2
R [1/sr]
Sensor Number
AL-(fvXo=0.0052)
SS-(fvXo=0.0052)
B-(fvXo=0.0052)
B-(fvXo=0.0181)

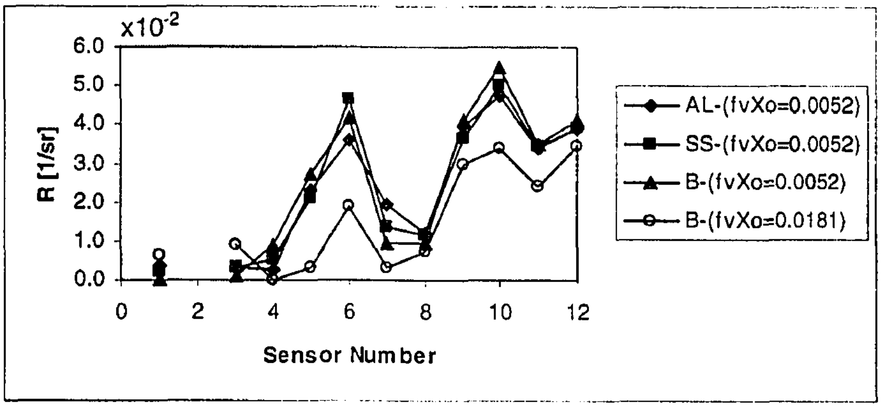
x10-2
R [1/sr]
Sensor Number
AL-(fvXo=0.0052)
SS-(fvXo=0.0052)
B-(fvXo=0.0052)
B-(fvXo=0.0181)

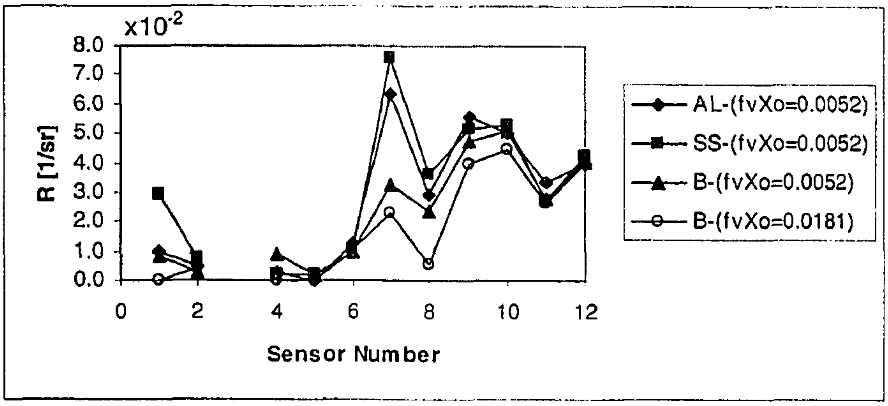
x10-2
R [1/sr]
Sensor Number
AL-(fvXo=0.0052)
SS-(fvXo=0.0052)
B-(fvXo=0.0052)
B-(fvXo=0.0181)

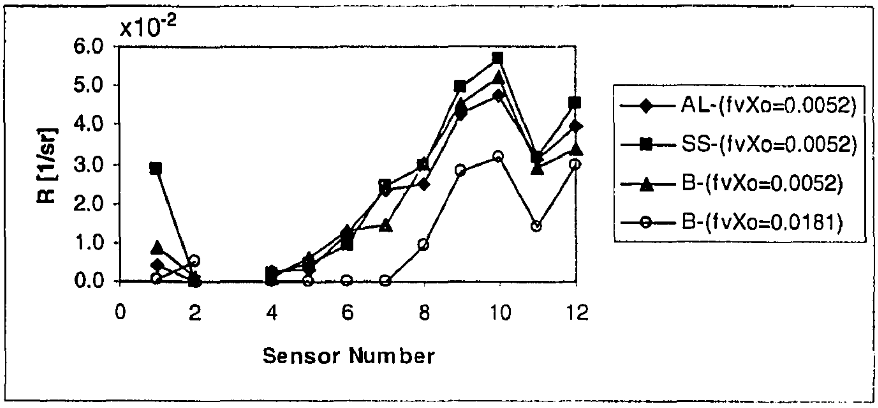
x10^-2
R [1/sr]
Sensor Number
AL-(fvXo=0.0052)
SS-(fvXo=0.0052)
B-(fvXo=0.0052)
B-(fvXo=0.0181)

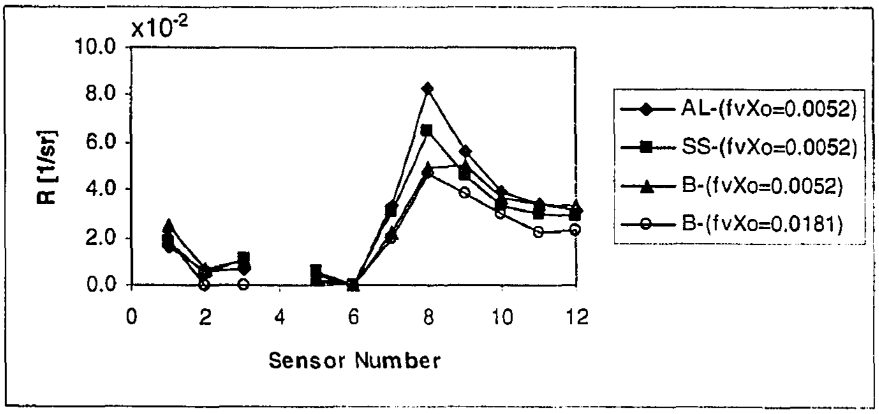
x10^-2
R [1/sr]
Sensor Number
AL-(fvXo=0.0052)
SS-(fvXo=0.0052)
B-(fvXo=0.0052)
B-(fvXo=0.0181)

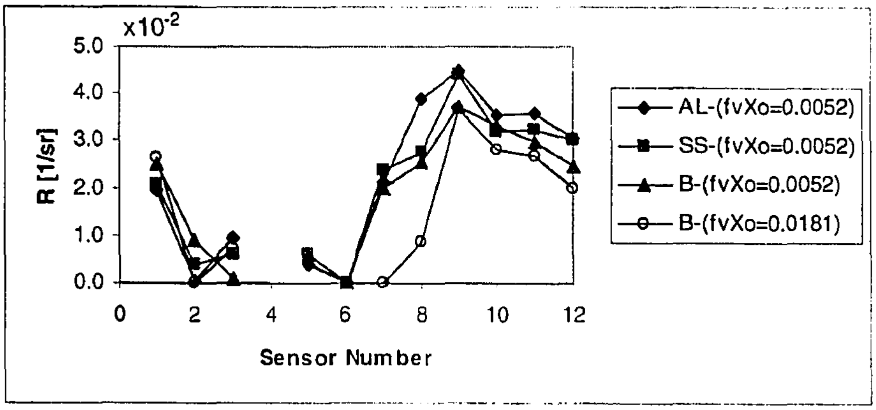
x10^-2
R [1/sr]
Sensor Number
AL-(fvXo=0.0052)
SS-(fvXo=0.0052)
B-(fvXo=0.0052)
B-(fvXo=0.0181)

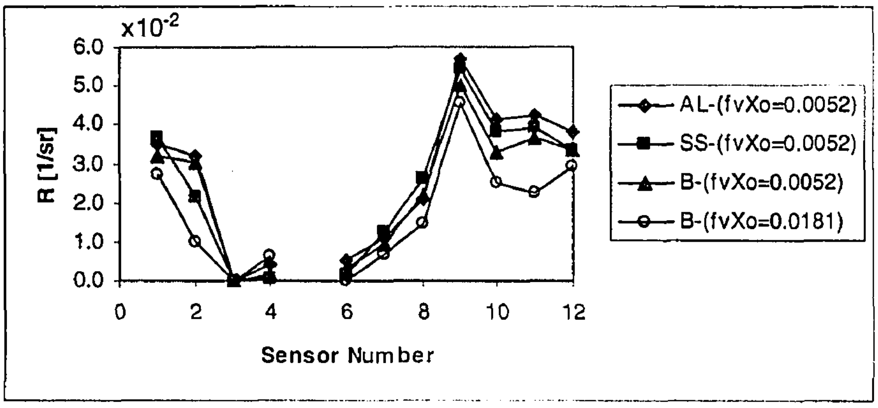
x10^-2
R [1/sr]
Sensor Number
AL-(fvXo=0.0052)
SS-(fvXo=0.0052)
B-(fvXo=0.0052)
B-(fvXo=0.0181)

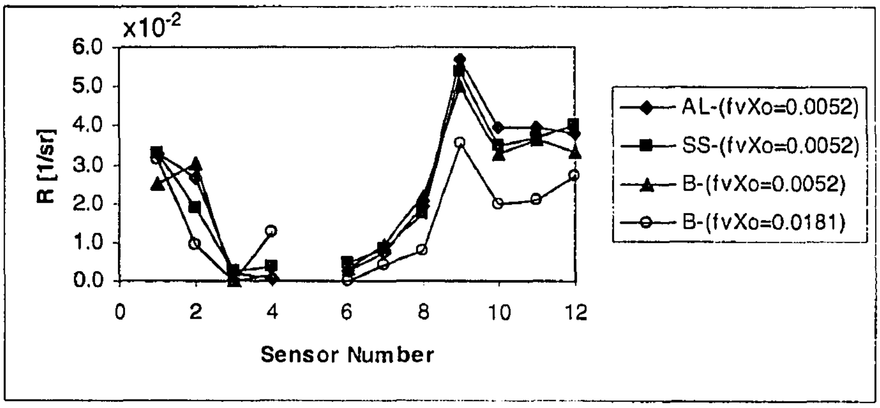
x10^-2
R [1/sr]
Sensor Number
AL-(fvXo=0.0052)
SS-(fvXo=0.0052)
B-(fvXo=0.0052)
B-(fvXo=0.0181)

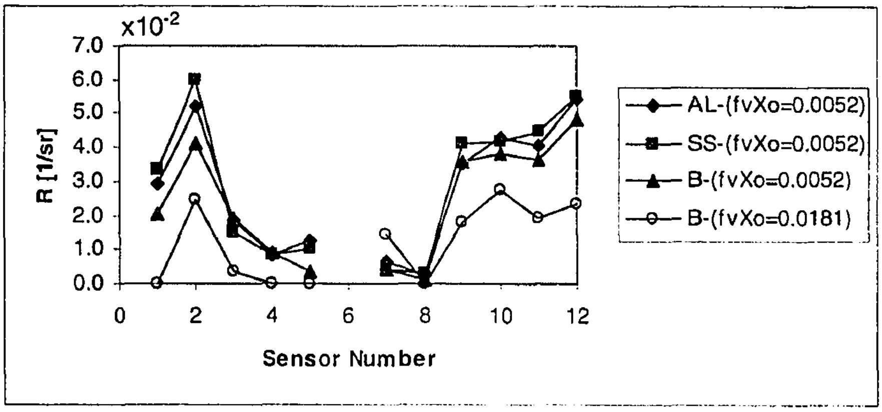
x10^-2
R [1/sr]
Sensor Number
AL-(fvXo=0.0052)
SS-(fvXo=0.0052)
B-(fvXo=0.0052)
B-(fvXo=0.0181)

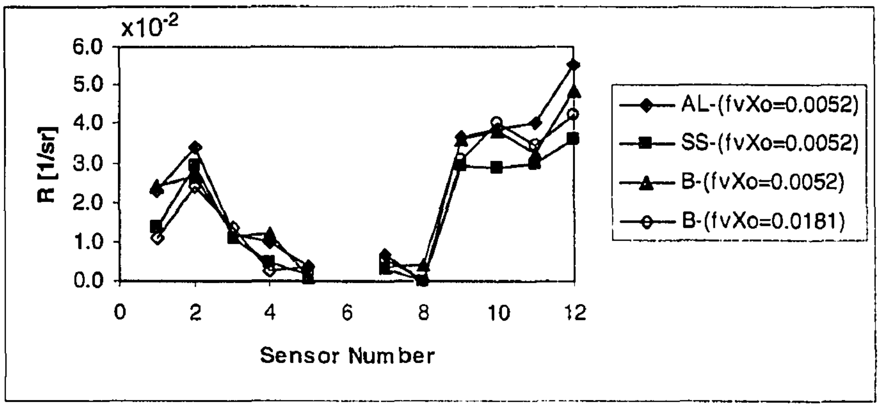
x10-2
R [1/sr]
Sensor Number
AL-(fvXo=0.0052)
SS-(fvXo=0.0052)
B-(fvXo=0.0052)
B-(fvXo=0.0181)

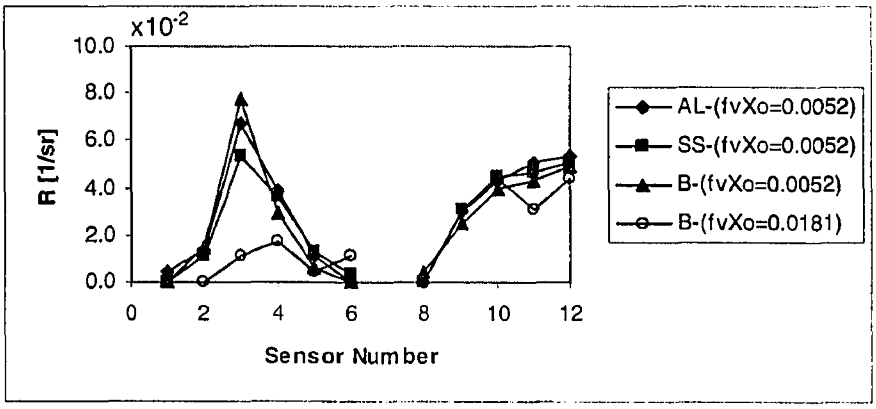
x10-2
R [1/sr]
Sensor Number
AL-(fvXo=0.0052)
SS-(fvXo=0.0052)
B-(fvXo=0.0052)
B-(fvXo=0.0181)

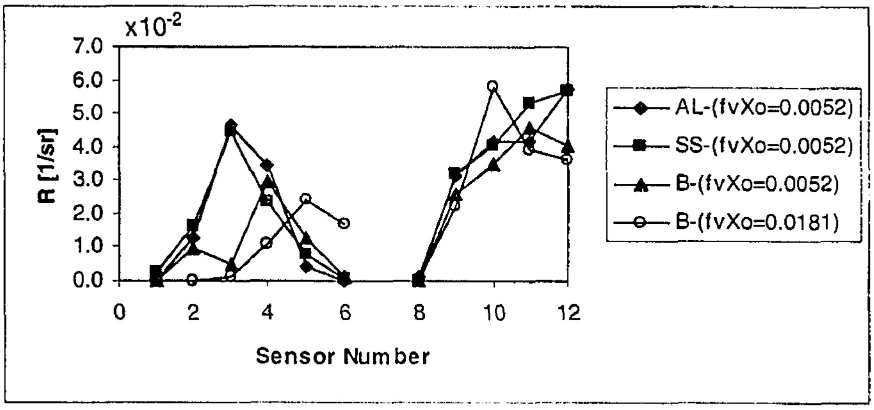
x10-2
R [1/sr]
Sensor Number
AL-(fvXo=0.0052)
SS-(fvXo=0.0052)
B-(fvXo=0.0052)
B-(fvXo=0.0181)

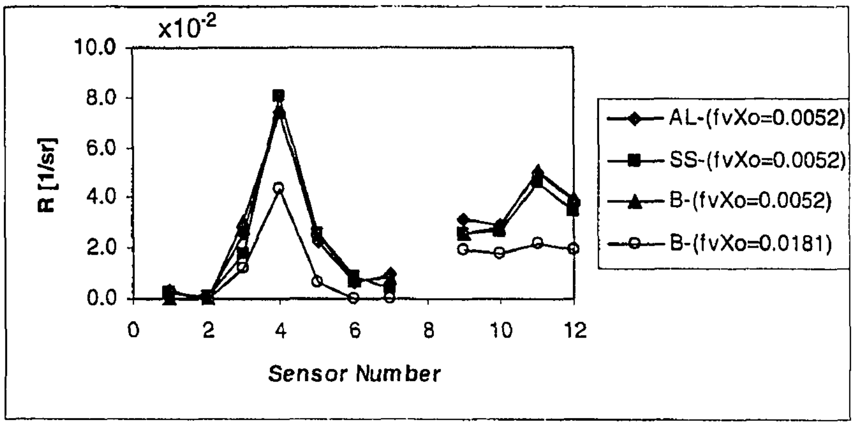

x10^-2
R [1/sr]
Sensor Number
AL-(fvXo=0.0052)
SS-(fvXo=0.0052)
B-(fvXo=0.0052)
B-(fvXo=0.0181)

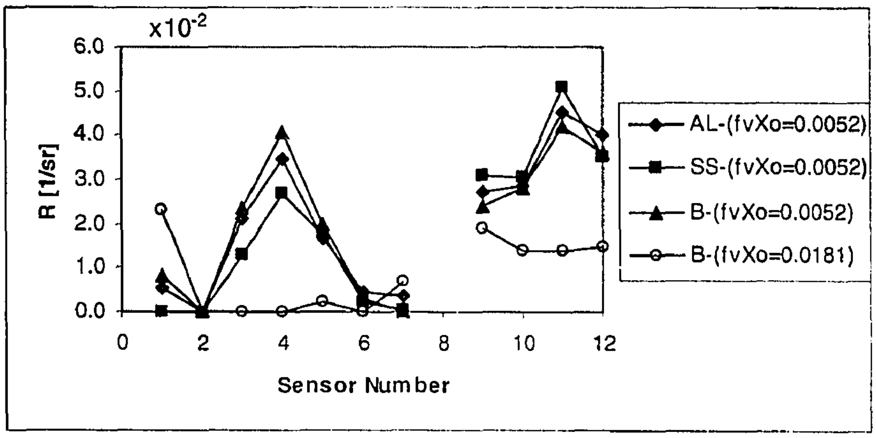

x10^-2
R [1/sr]
Sensor Number
AL-(fvXo=0.0052)
SS-(fvXo=0.0052)
B-(fvXo=0.0052)
B-(fvXo=0.0181)

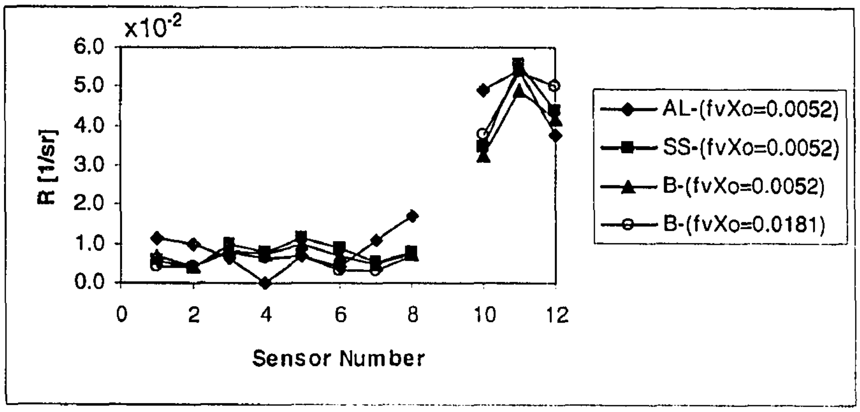

x10^-2
R [1/sr]
Sensor Number
AL-(fvXo=0.0052)
SS-(fvXo=0.0052)
B-(fvXo=0.0052)
B-(fvXo=0.0181)

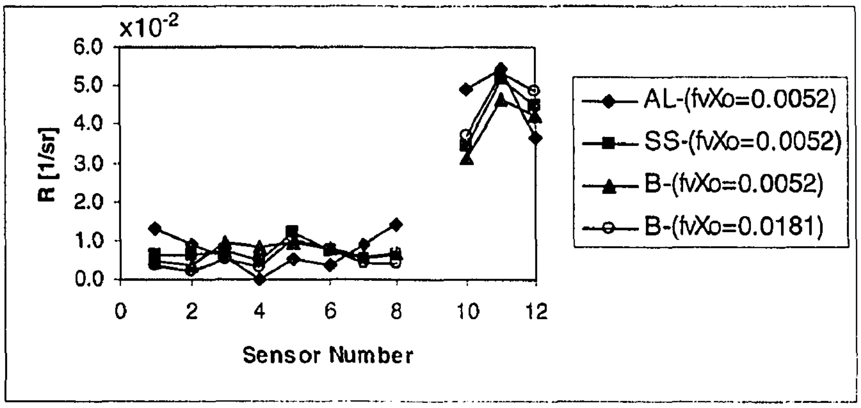

x10-2
R [1/sr]
Sensor Number
AL-(fvXo=0.0052)
SS-(fvXo=0.0052)
B-(fvXo=0.0052)
B-(fvXo=0.0181)

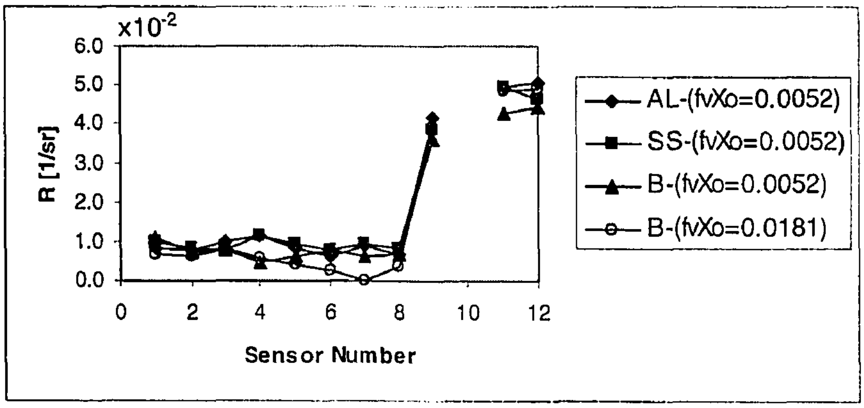

x10-2
R [1/sr]
Sensor Number
AL-(fvXo=0.0052)
SS-(fvXo=0.0052)
B-(fvXo=0.0052)
B-(fvXo=0.0181)

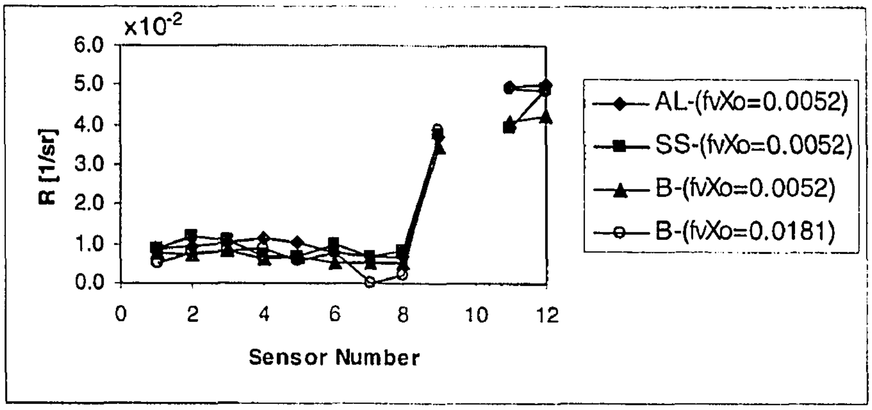

x10-2
R [1/sr]
Sensor Number
AL-(fvXo=0.0052)
SS-(fvXo=0.0052)
B-(fvXo=0.0052)
B-(fvXo=0.0181)

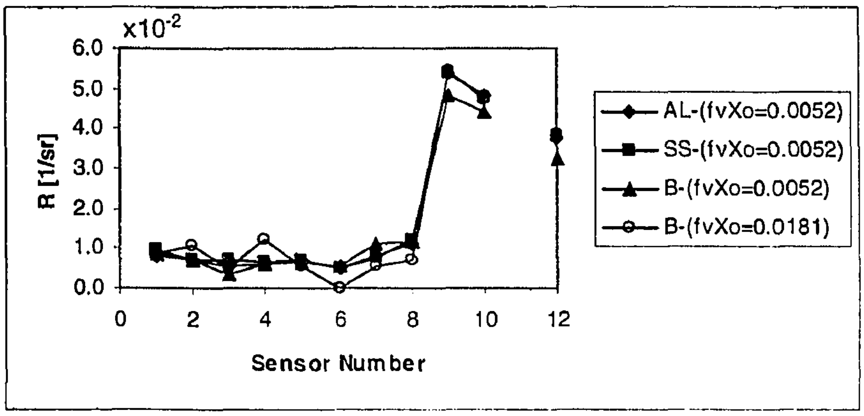
x10-2
R [1/sr]
Sensor Number
AL-(fvXo=0.0052)
SS-(fvXo=0.0052)
B-(fvXo=0.0052)
B-(fvXo=0.0181)

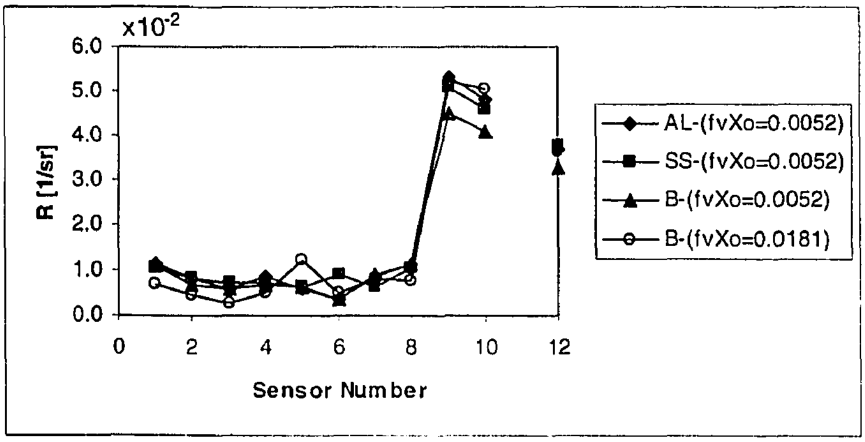
x10-2
R [1/sr]
Sensor Number
AL-(fvXo=0.0052)
SS-(fvXo=0.0052)
B-(fvXo=0.0052)
B-(fvXo=0.0181)

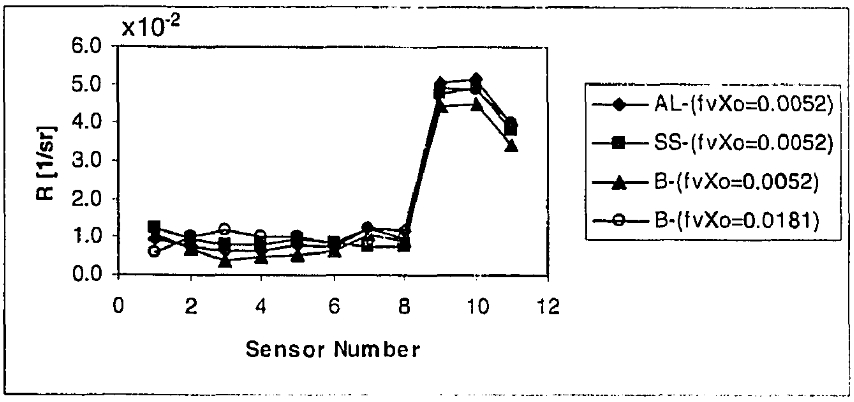
x10-2
R [1/sr]
Sensor Number
AL-(fvXo=0.0052)
SS-(fvXo=0.0052)
B-(fvXo=0.0052)
B-(fvXo=0.0181)

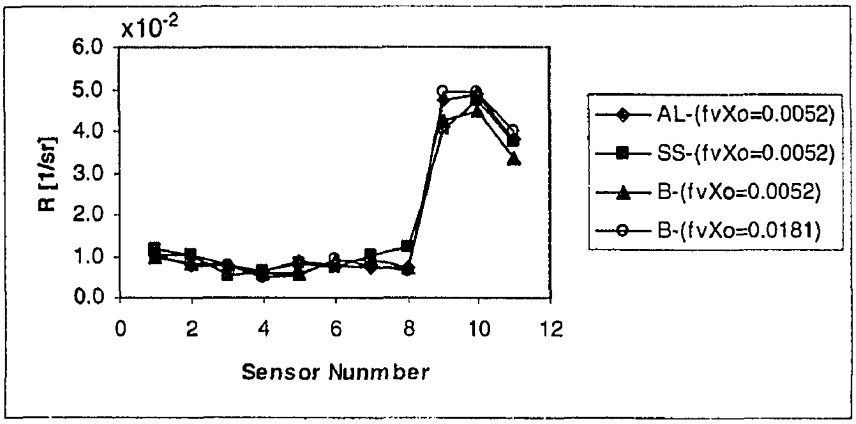

Fiber Insulation (TO-5)

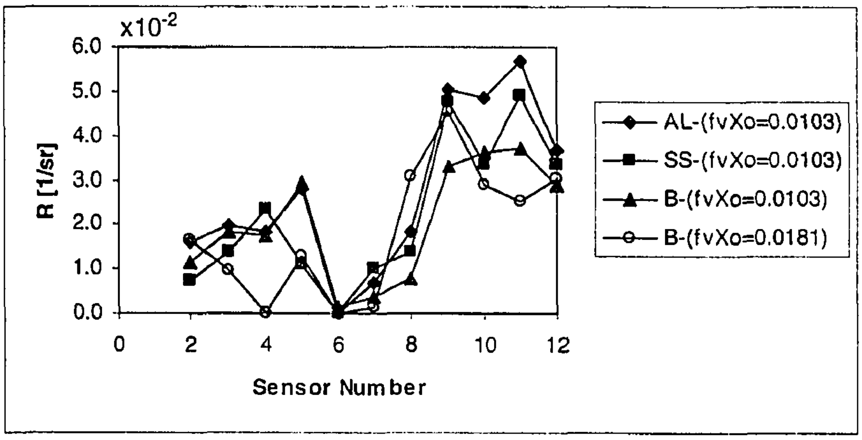

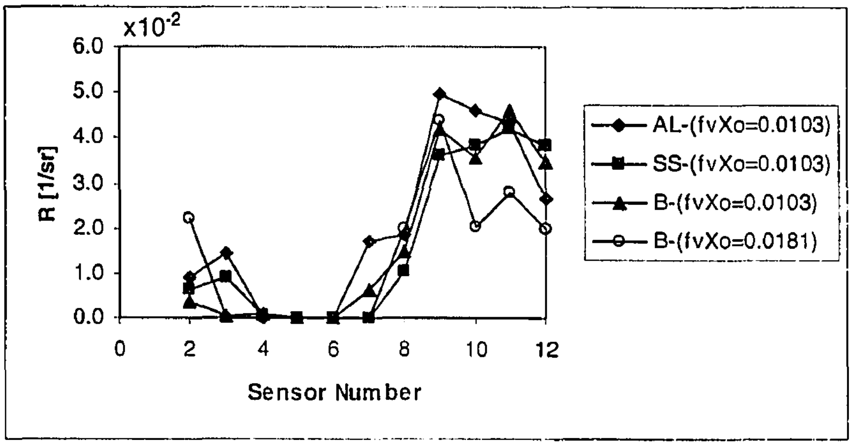

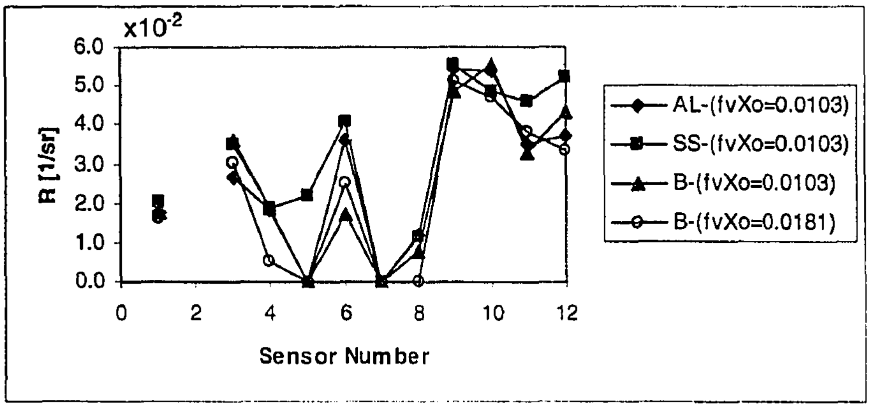
x10-2
R [1/sr]
Sensor Number
AL-(fvXo=0.0103)
SS-(fvXo=0.0103)
B-(fvXo=0.0103)
B-(fvXo=0.0181)

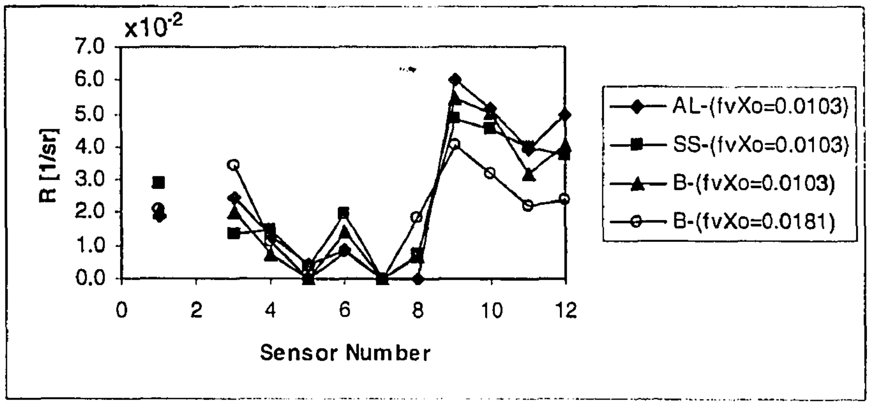
x10-2
R [1/sr]
Sensor Number
AL-(fvXo=0.0103)
SS-(fvXo=0.0103)
B-(fvXo=0.0103)
B-(fvXo=0.0181)

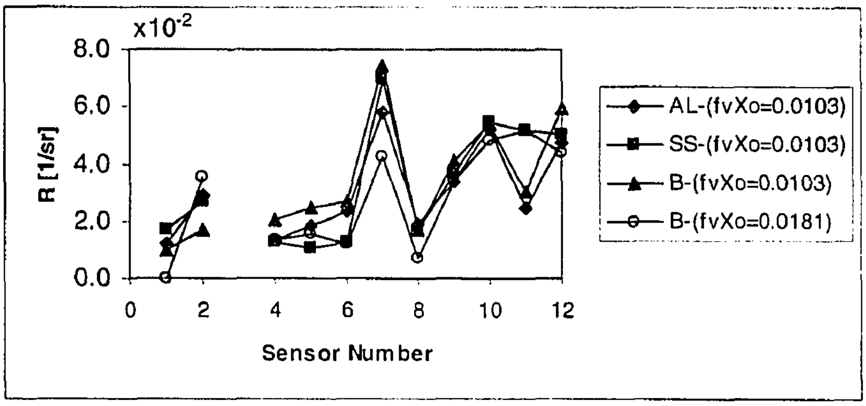
x10-2
R [1/sr]
Sensor Number
AL-(fvXo=0.0103)
SS-(fvXo=0.0103)
B-(fvXo=0.0103)
B-(fvXo=0.0181)

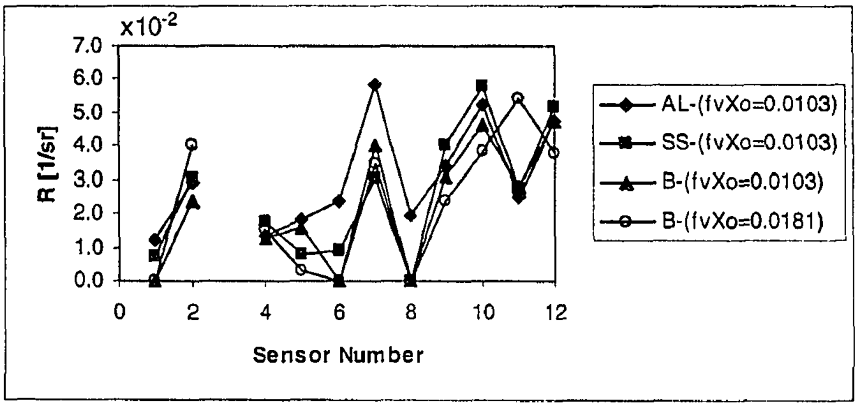
x10-2
R [1/sr]
Sensor Number
AL-(fvXo=0.0103)
SS-(fvXo=0.0103)
B-(fvXo=0.0103)
B-(fvXo=0.0181)

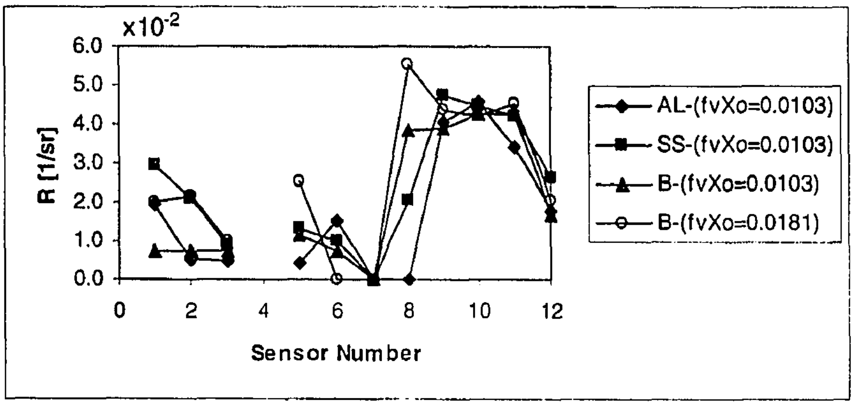
x10-2
R [1/sr]
Sensor Number
AL-(fvXo=0.0103)
SS-(fvXo=0.0103)
B-(fvXo=0.0103)
B-(fvXo=0.0181)

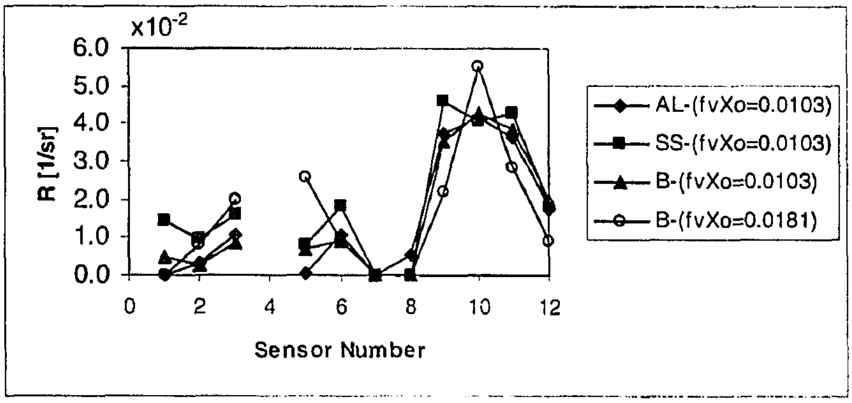
x10-2
R [1/sr]
Sensor Number
AL-(fvXo=0.0103)
SS-(fvXo=0.0103)
B-(fvXo=0.0103)
B-(fvXo=0.0181)

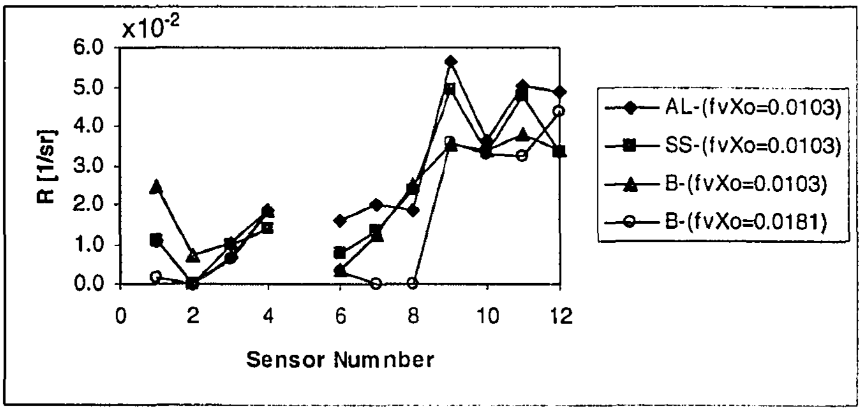
x10^-2
R [1/sr]
Sensor Numnber
AL-(fvXo=0.0103)
SS-(fvXo=0.0103)
B-(fvXo=0.0103)
B-(fvXo=0.0181)

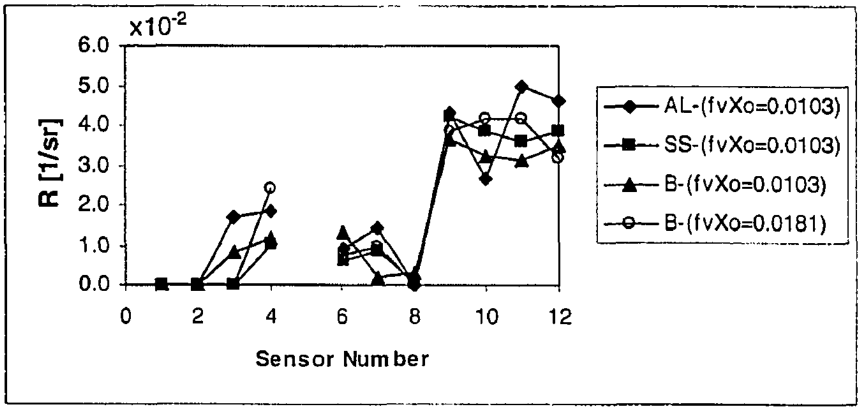
x10^-2
R [1/sr]
Sensor Number
AL-(fvXo=0.0103)
SS-(fvXo=0.0103)
B-(fvXo=0.0103)
B-(fvXo=0.0181)

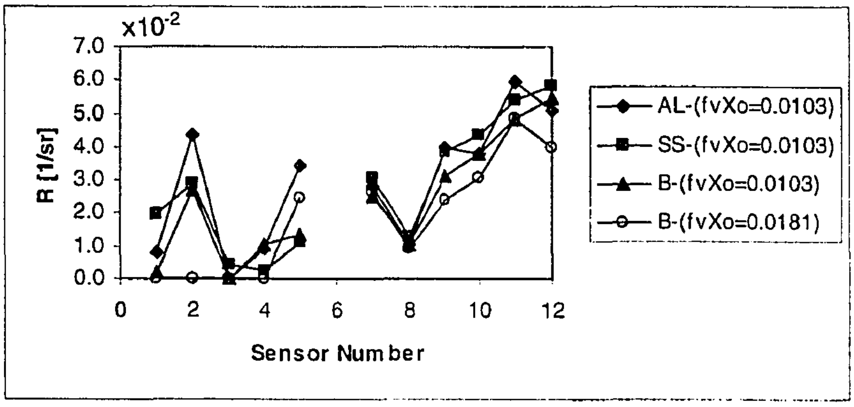
x10^-2
R [1/sr]
Sensor Number
AL-(fvXo=0.0103)
SS-(fvXo=0.0103)
B-(fvXo=0.0103)
B-(fvXo=0.0181)

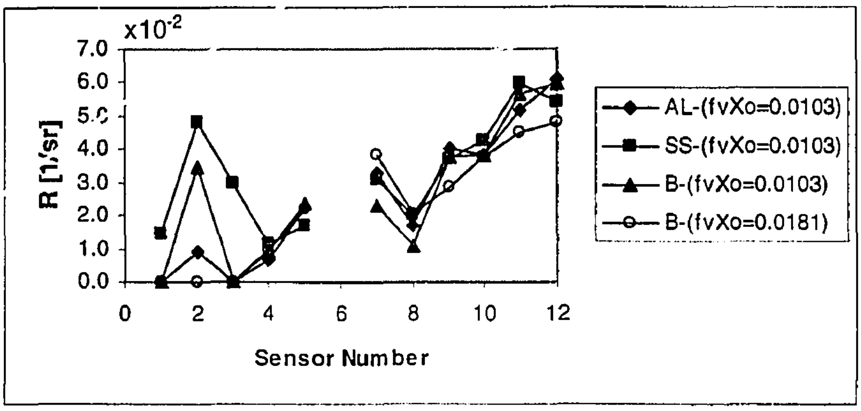
x10^-2
R [1/sr]
Sensor Number
AL-(fvXo=0.0103)
SS-(fvXo=0.0103)
B-(fvXo=0.0103)
B-(fvXo=0.0181)

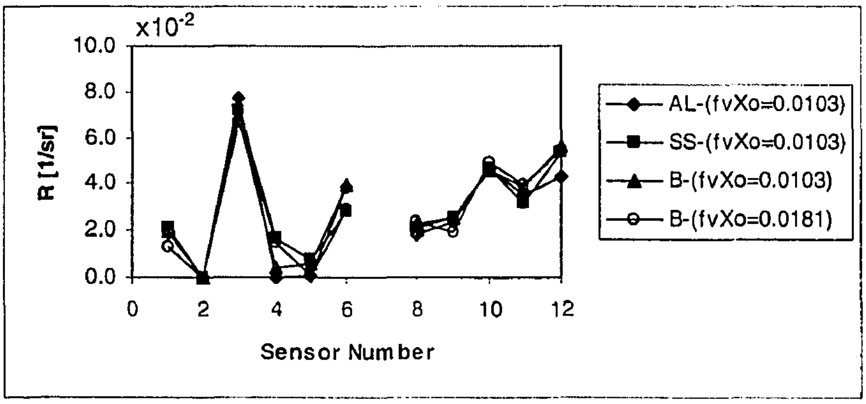
x10^-2
R [1/sr]
Sensor Number
AL-(fvXo=0.0103)
SS-(fvXo=0.0103)
B-(fvXo=0.0103)
B-(fvXo=0.0181)

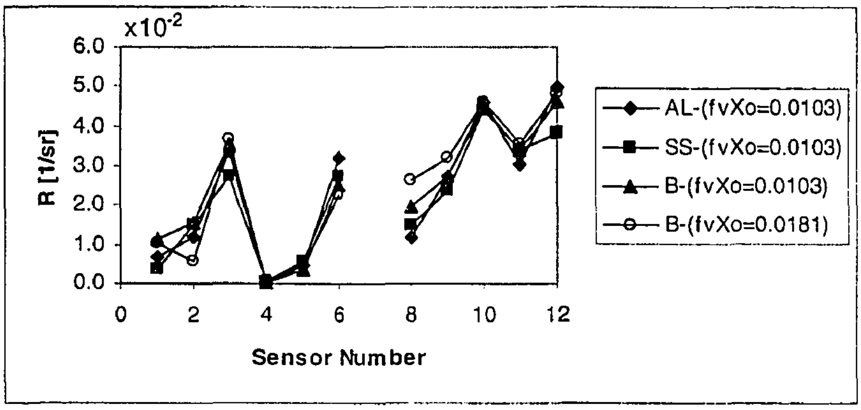
x10^-2
R [1/sr]
Sensor Number
AL-(fvXo=0.0103)
SS-(fvXo=0.0103)
B-(fvXo=0.0103)
B-(fvXo=0.0181)

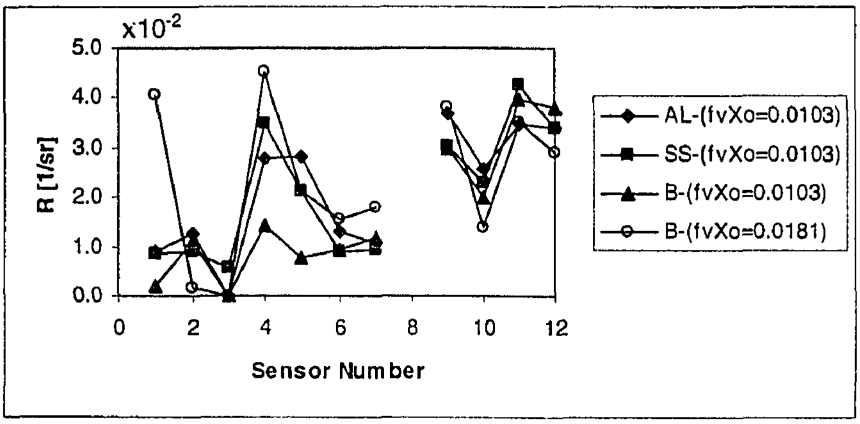
x10^-2
R [1/sr]
Sensor Number
AL-(fvXo=0.0103)
SS-(fvXo=0.0103)
B-(fvXo=0.0103)
B-(fvXo=0.0181)

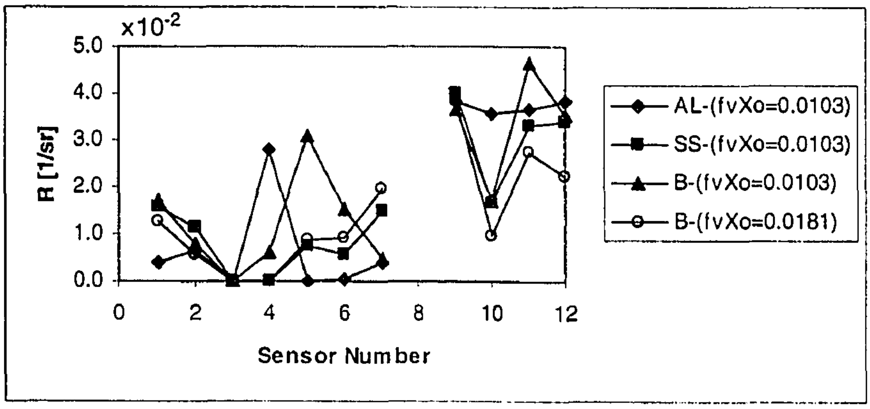
x10^-2
R [1/sr]
Sensor Number
AL-(fvXo=0.0103)
SS-(fvXo=0.0103)
B-(fvXo=0.0103)
B-(fvXo=0.0181)

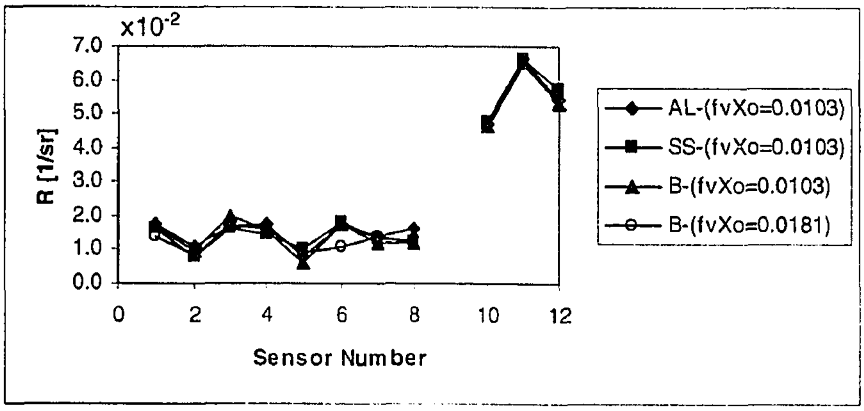
x10^-2
R [1/sr]
Sensor Number
AL-(fvXo=0.0103)
SS-(fvXo=0.0103)
B-(fvXo=0.0103)
B-(fvXo=0.0181)

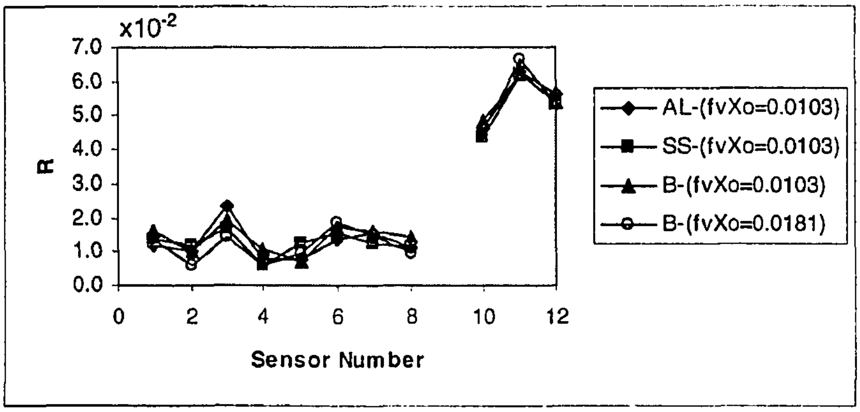
x10-2
R
Sensor Number
AL-(fvXo=0.0103)
SS-(fvXo=0.0103)
B-(fvXo=0.0103)
B-(fvXo=0.0181)

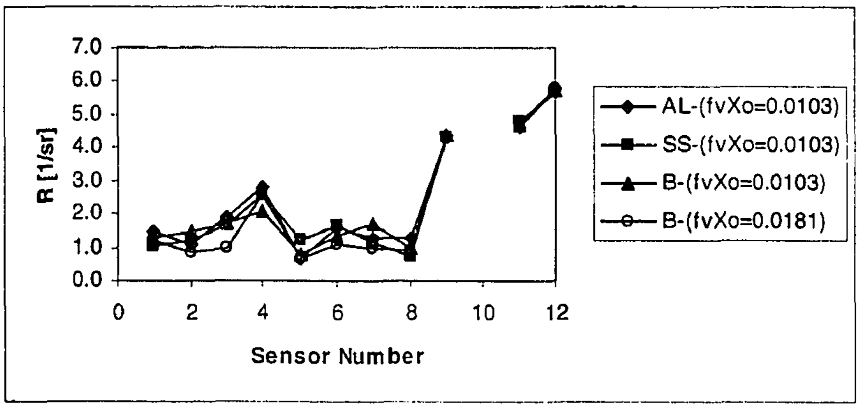
R [1/sr]
Sensor Number
AL-(fvXo=0.0103)
SS-(fvXo=0.0103)
B-(fvXo=0.0103)
B-(fvXo=0.0181)

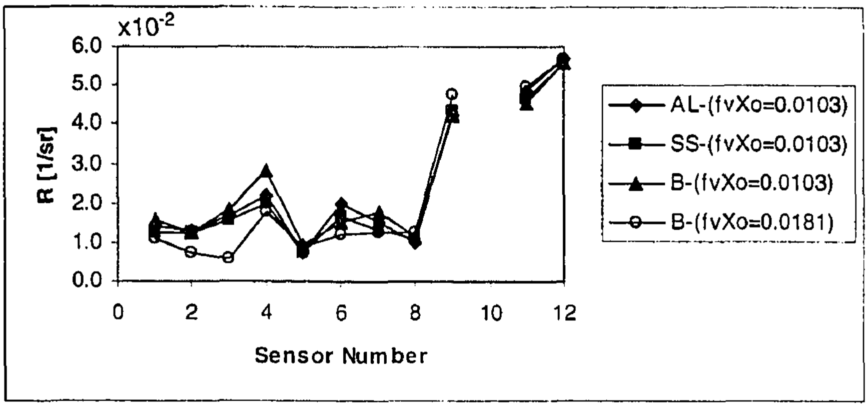
x10-2
R [1/sr]
Sensor Number
AL-(fvXo=0.0103)
SS-(fvXo=0.0103)
B-(fvXo=0.0103)
B-(fvXo=0.0181)

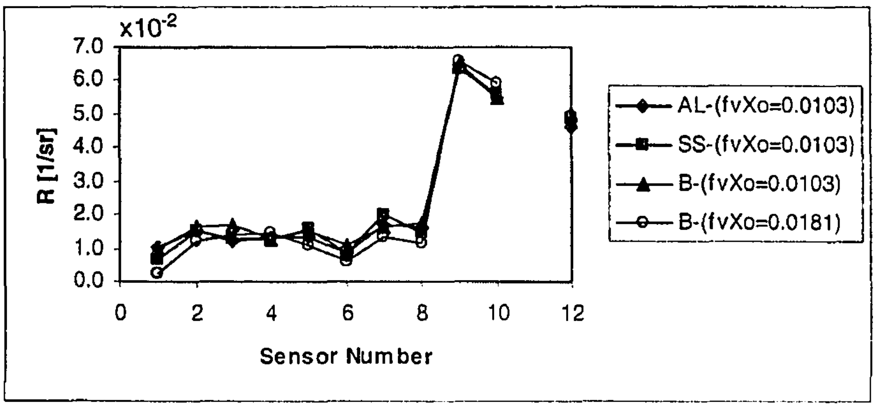
x10^-2
R [1/sr]
Sensor Number
AL-(fvXo=0.0103)
SS-(fvXo=0.0103)
B-(fvXo=0.0103)
B-(fvXo=0.0181)

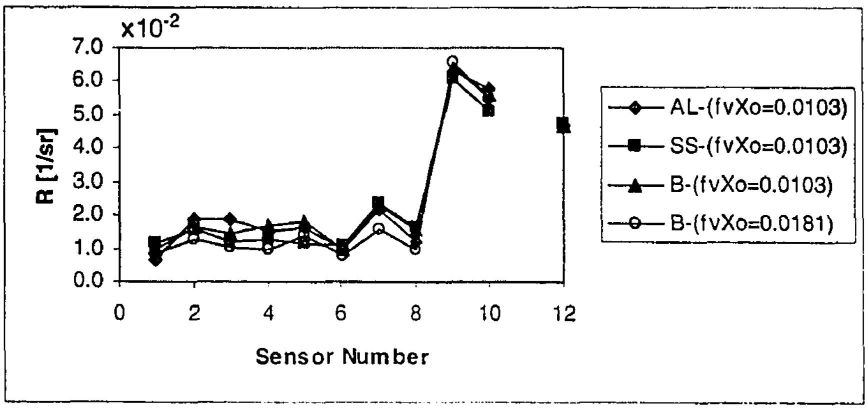
x10^-2
R [1/sr]
Sensor Number
AL-(fvXo=0.0103)
SS-(fvXo=0.0103)
B-(fvXo=0.0103)
B-(fvXo=0.0181)

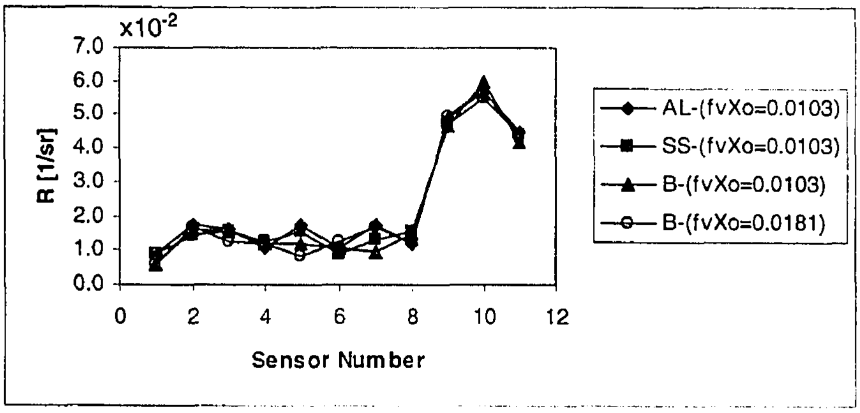
x10^-2
R [1/sr]
Sensor Number
AL-(fvXo=0.0103)
SS-(fvXo=0.0103)
B-(fvXo=0.0103)
B-(fvXo=0.0181)

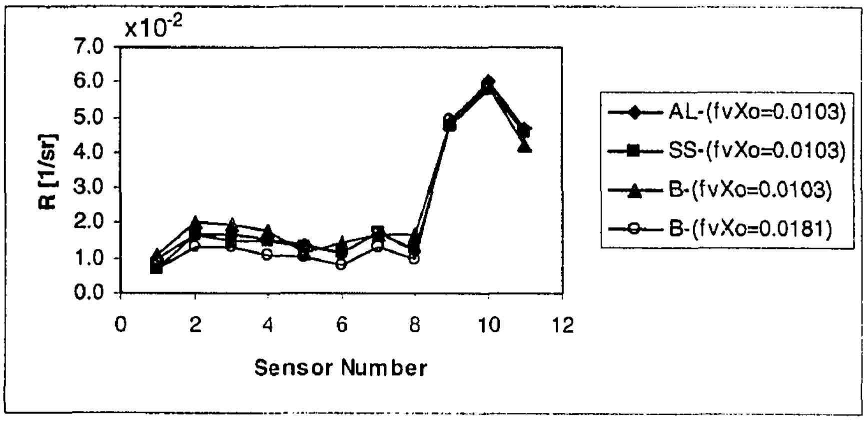
x10^-2
7.0
6.0
5.0
4.0
3.0
2.0
1.0
0.0
R [1/sr]
0
2
4
6
8
10
12
Sensor Number
AL-(fvXo=0.0103)
SS-(fvXo=0.0103)
B-(fvXo=0.0103)
B-(fvXo=0.0181)

APPENDIX C

DISCRETE-ORDINATES EQUATIONS

The discussion that follows is a representative of the approximations taken to formulate the discrete-ordinates equations for an absorbing, anisotropically scattering and reemitting media enclosed by wall that can either reflect specularly, diffuse or by some biangular distribution. The discretization of the equations is the same as presented in Chapter 5. Here there are formulated with more amplitude in the treatment of the boundary conditions. Note that rectangular geometry is used here in the analysis to represent the cylindrical sample; the assumed rectangle bounds the cylindrical shape. The rectangular geometry was taken to simplify the analysis, due to the need to specify a directed non-symmetric beam at the sample. The aspect ratio of the sample makes the actual problem geometrically 1-D; experimentally, edge effects (modeled as a cold bare sample) are also subtracted from the incident port beam. Since there are several competing ways to specify direction cosines in a cylindrical geometry (fixed coordinates or relative to the radial direction), this avoided potential difficulties in translating data.

C.1 Octal Intensity Discretization

A general formulation for the radiative transfer equation RTE is considered in this section. The RTE for an absorbing, anisotropically scattering and reemitting three-dimensional media (rectangular coordinate system) is given by

$$\begin{aligned}&\sin(\theta)\cos(\phi)\frac{\partial I}{\partial x}(x,y,z,\theta,\phi)+\sin(\theta)\sin(\phi)\frac{\partial I}{\partial y}(x,y,z,\theta,\phi)+\cos(\theta)\frac{\partial I}{\partial z}(x,y,z,\theta,\phi)=\\&-\beta I(x,y,z,\theta,\phi)+\frac{\sigma_s}{4\pi}\int_{4\pi}P(\Omega\rightarrow\Omega')I(x,y,z,\theta',\phi')d\Omega+\kappa I_b\left[T(x,y,z)\right]\end{aligned} \tag{C.1}$$

in $0<x<AL$, $0<x<BL$, $0<x<CL$, $0<\theta<\pi$, $0<\phi<2\pi$.

The geometry, coordinate system and the local spherical coordinate system are shown in Figure C.1.1.

Equation C.1 has singularities when $\sin(\theta)\cos(\phi)=0$, $\sin(\theta)\sin(\phi)=0$, and (ϕ)=0, hence, the analysis of the problem is split into eight octants, as shown in Figure C.1.2. Intensities for each octant are denoted as shown in Table C.1.1. After, mathematical rearrangement taking into account the respective angular ranges, the radiative intensities for each of the eight octants can now be written as:

Table C.1.1 Octal Intensity Distribution [88]

Octant 1	$=A(x,y,z,\theta,\phi)$	$0<\theta<\pi/2$	$0<\phi<\pi/2$	(C.2a)
Octant 2	$=B(x,y,z,\pi-\theta,\phi)$	$\pi/2<\theta<\pi$	$0<\phi<\pi/2$	(C.2b)
Octant 3	$=C(x,y,z,\pi-\theta,2\pi-\phi)$	$\pi/2<\theta<\pi$	$3\pi/2<\phi<2\pi$	(C.2c)
Octant 4	$=D(x,y,z,\theta,2\pi-\phi)$	$0<\theta<\pi/2$	$3\pi/2<\phi<2\pi$	(C.2d)
Octant 5	$=E(x,y,z,\theta,\pi-\phi)$	$0<\theta<\pi/2$	$\pi/2<\phi<\pi$	(C.2e)
Octant 6	$=F(x,y,z,\pi-\theta,\pi-\phi)$	$\pi/2<\theta<\pi$	$\pi/2<\phi<\pi$	(C.2f)
Octant 7	$=G(x,y,z,\pi-\theta,\frac{3\pi}{2}-\phi)$	$\pi/2<\theta<\pi$	$\pi<\phi<3\pi/2$	(C.2g)
Octant 8	$=H(x,y,z,\theta,\frac{3\pi}{2}-\phi)$	$0<\theta<\pi/2$	$\pi<\phi<3\pi/2$	(C.2h)

$$\sin(\theta)\cos(\phi)\frac{\partial A}{\partial x}+\sin(\theta)\sin(\phi)\frac{\partial A}{\partial y}+\cos(\theta)\frac{\partial A}{\partial z}=-\kappa_a A+\beta A+\frac{\sigma_s}{4\pi}S_A \tag{C.3a}$$

$$\sin(\theta)\cos(\phi)\frac{\partial B}{\partial x}+\sin(\theta)\sin(\phi)\frac{\partial B}{\partial y}-\cos(\theta)\frac{\partial B}{\partial z}=-\kappa_a B+\beta B+\frac{\sigma_s}{4\pi}S_B \tag{C.3b}$$

$$\sin(\theta)\cos(\phi)\frac{\partial C}{\partial x}-\sin(\theta)\sin(\phi)\frac{\partial C}{\partial y}-\cos(\theta)\frac{\partial C}{\partial z}=-\kappa_a C+\beta C+\frac{\sigma_s}{4\pi}S_C \tag{C.3c}$$

$$\sin(\theta)\cos(\phi)\frac{\partial D}{\partial x}-\sin(\theta)\sin(\phi)\frac{\partial D}{\partial y}+\cos(\theta)\frac{\partial D}{\partial z}=-\kappa_a D+\beta D+\frac{\sigma_s}{4\pi}S_D \tag{C.3d}$$

$$-\sin(\theta)\cos(\phi)\frac{\partial E}{\partial x}+\sin(\theta)\sin(\phi)\frac{\partial E}{\partial y}+\cos(\theta)\frac{\partial E}{\partial z}=-\kappa_a E+\beta E+\frac{\sigma_s}{4\pi}S_E \tag{C.3e}$$

$$-\sin(\theta)\cos(\phi)\frac{\partial F}{\partial x}+\sin(\theta)\sin(\phi)\frac{\partial F}{\partial y}-\cos(\theta)\frac{\partial F}{\partial z}=-\kappa_a F+\beta F+\frac{\sigma_s}{4\pi}S_F \tag{C.3f}$$

$$-\sin(\theta)\cos(\phi)\frac{\partial G}{\partial x}-\sin(\theta)\sin(\phi)\frac{\partial G}{\partial y}-\cos(\theta)\frac{\partial G}{\partial z}=-\kappa_a G+\beta G+\frac{\sigma_s}{4\pi}S_G \tag{C.3g}$$

$$-\sin(\theta)\cos(\phi)\frac{\partial H}{\partial x}-\sin(\theta)\sin(\phi)\frac{\partial H}{\partial y}-\cos(\theta)\frac{\partial H}{\partial z}=-\kappa_a H+\beta H+\frac{\sigma_s}{4\pi}S_H \tag{C.3h}$$

where S_i with $i = A..H$ represents the specific source function for the octal intensity.

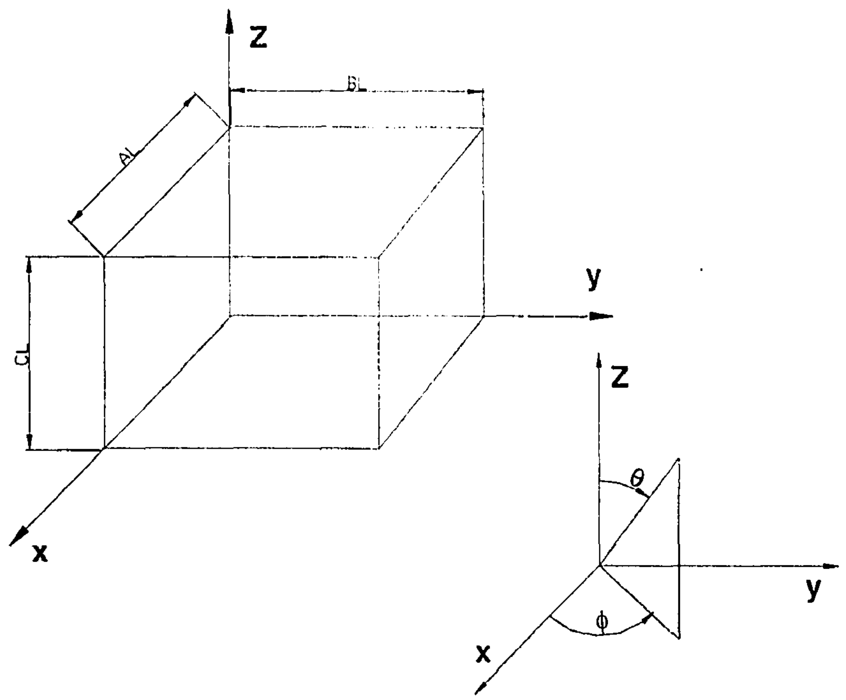

Figure C.1.1 Geometry, Coordinate system and the Local Spherical Coordinate System

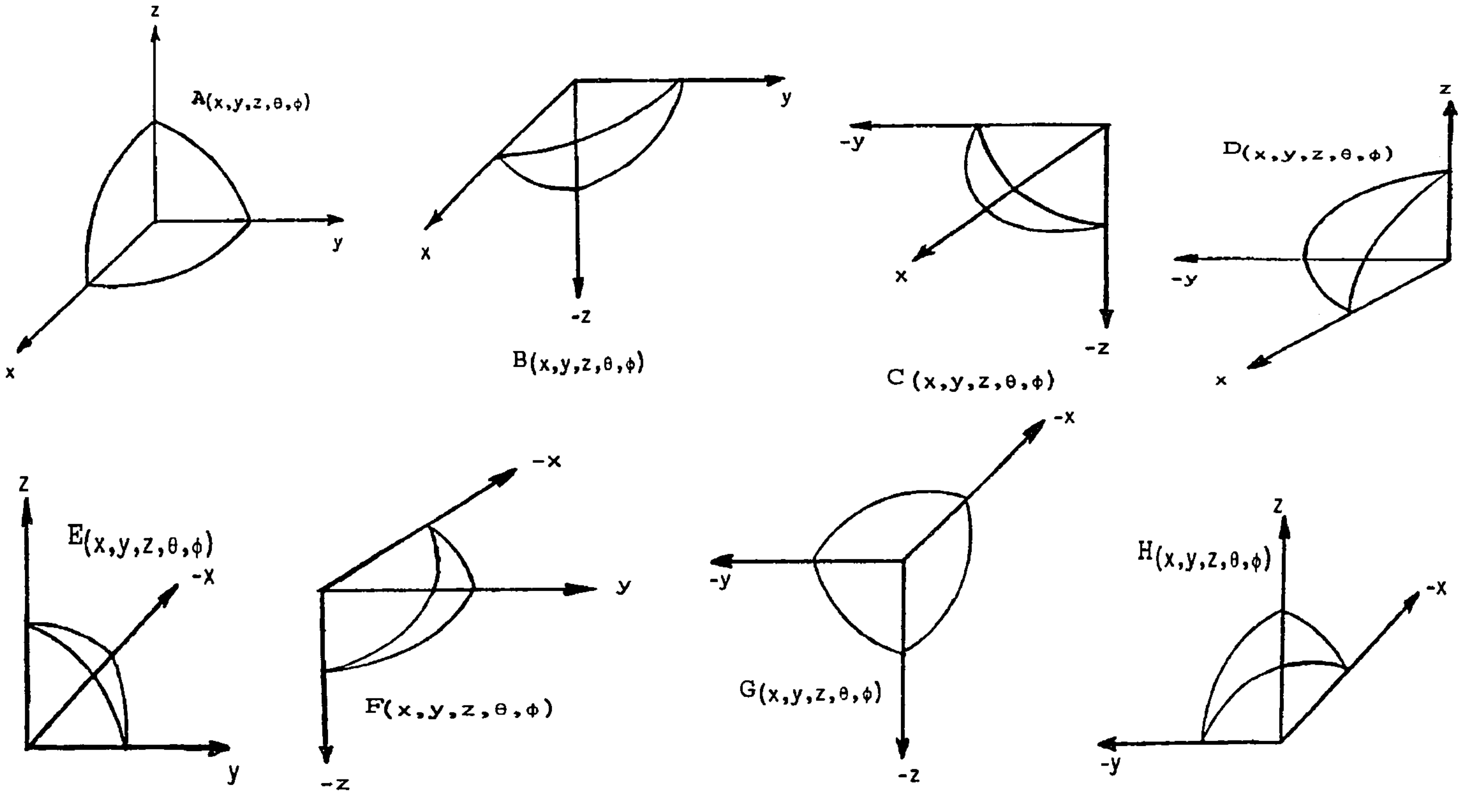

Figure C.1.2 Octal Intensity Distributions [75

For the discrete-ordinates method, the octal intensities are solved for a number of ordinates directions with the integral in the source functions replaced by a quadrature summed over the ordinate direction. Equations C.3 can be written in a positively manner taking into account the ordinates and the direction of the traveling intensity. Thus,

$$\xi_m \frac{\partial A'''}{\partial x} + \eta_m \frac{\partial A'''}{\partial y} + \mu_m \frac{\partial A'''}{\partial z} = -\kappa_a A''' + \beta A''' + \frac{\sigma_s}{4\pi} S_A''' \tag{C.4a}$$

$$\xi_m \frac{\partial B'''}{\partial x} + \eta_m \frac{\partial B'''}{\partial y} + \mu_m \frac{\partial B'''}{\partial z} = -\kappa_a B''' + \beta B''' + \frac{\sigma_s}{4\pi} S_B''' \tag{C.4b}$$

$$\xi_m \frac{\partial C'''}{\partial x} + \eta_m \frac{\partial C'''}{\partial y} + \mu_m \frac{\partial C'''}{\partial z} = -\kappa_a C''' + \beta C''' + \frac{\sigma_s}{4\pi} S_C''' \tag{C.4c}$$

$$\xi_m \frac{\partial D'''}{\partial x} + \eta_m \frac{\partial D'''}{\partial y} + \mu_m \frac{\partial D'''}{\partial z} = -\kappa_a D''' + \beta D''' + \frac{\sigma_s}{4\pi} S_D''' \tag{C.4d}$$

$$\xi_m \frac{\partial E'''}{\partial x} + \eta_m \frac{\partial E'''}{\partial y} + \mu_m \frac{\partial E'''}{\partial z} = -\kappa_a E''' + \beta E''' + \frac{\sigma_s}{4\pi} S_E''' \tag{C.4e}$$

$$\xi_m \frac{\partial F'''}{\partial x} + \eta_m \frac{\partial F'''}{\partial y} + \mu_m \frac{\partial F'''}{\partial z} = -\kappa_a F''' + \beta F''' + \frac{\sigma_s}{4\pi} S_F''' \tag{C.4f}$$

$$\xi_m \frac{\partial G'''}{\partial x} + \eta_m \frac{\partial G'''}{\partial y} + \mu_m \frac{\partial G'''}{\partial z} = -\kappa_a G''' + \beta G''' + \frac{\sigma_s}{4\pi} S_G''' \tag{C.4g}$$

$$\xi_m \frac{\partial H'''}{\partial x} + \eta_m \frac{\partial H'''}{\partial y} + \mu_m \frac{\partial H'''}{\partial z} = -\kappa_a H''' + \beta H''' + \frac{\sigma_s}{4\pi} S_H''' \tag{C.4h}$$

Following the finite difference form of the radiative transport equation [80], and taking into consideration the reference faces of the leaving intensities, as shown in Figure C.1.2, the above intensities can be transformed in:

$$A_p''' = \frac{|\xi_m| A_x A_b''' + |\eta_m| B_y A_w''' + |\mu_m| C_z A_s''' + \Psi S_A''' V_p}{|\xi_m| A_x + |\eta_m| B_y + |\mu_m| C_z + \Psi \beta V_p} \tag{C.5a}$$

$$B_p^m = \frac{|\xi_m| A_x B_b^m + |\eta_m| B_y B_w^m + |\mu_m| C_z B_n^m + \Psi S_B^m V_p}{|\xi_m| A_x + |\eta_m| B_y + |\mu_m| C_z + \Psi \beta V_p} \tag{C.5b}$$

$$C_p^m = \frac{|\xi_m| A_x C_b^m + |\eta_m| B_y C_e^m + |\mu_m| C_z C_n^m + \Psi S_C^m V_p}{|\xi_m| A_x + |\eta_m| B_y + |\mu_m| C_z + \Psi \beta V_p} \tag{C.5c}$$

$$D_p^m = \frac{|\xi_m| A_x D_b^m + |\eta_m| B_y D_e^m + |\mu_m| C_z D_s^m + \Psi S_D^m V_p}{|\xi_m| A_x + |\eta_m| B_y + |\mu_m| C_z + \Psi \beta V_p} \tag{C.5d}$$

$$E_p^m = \frac{|\xi_m| A_x E_f^m + |\eta_m| B_y E_w^m + |\mu_m| C_z E_s^m + \Psi S_E^m V_p}{|\xi_m| A_x + |\eta_m| B_y + |\mu_m| C_z + \Psi \beta V_p} \tag{C.5e}$$

$$F_p^m = \frac{|\xi_m| A_x F_f^m + |\eta_m| B_y F_w^m + |\mu_m| C_z F_n^m + \Psi S_F^m V_p}{|\xi_m| A_x + |\eta_m| B_y + |\mu_m| C_z + \Psi \beta V_p} \tag{C.5f}$$

$$G_p^m = \frac{|\xi_m| A_x G_f^m + |\eta_m| B_y G_e^m + |\mu_m| C_z G_n^m + \Psi S_G^m V_p}{|\xi_m| A_x + |\eta_m| B_y + |\mu_m| C_z + \Psi \beta V_p} \tag{C.5g}$$

$$H_p^m = \frac{|\xi_m| A_x H_f^m + |\eta_m| B_y H_e^m + |\mu_m| C_z H_s^m + \Psi S_H^m V_p}{|\xi_m| A_x + |\eta_m| B_y + |\mu_m| C_z + \Psi \beta V_p} \tag{C.5.h}$$

C.2. Octal Source Functions

For cases of anisotropic scattering the source function must be divided for the octal intensity in discussion. This octal function will collect all incoming intensities for the rest of the octants and it is modified by the respective phase function. For a linear anisotropic phase function, the octal source function for the octant 1 is stated as:

$$SA_p^m = \kappa I_b(r,T) + \frac{\sigma_s}{4\pi}[\sum_{m'} \varpi_{m'}(1 + a_1(\iota_1\xi_m\xi_{m'} + \iota_2\eta_m\eta_{m'} + \iota_3\mu_m\mu_{m'})A_p^{m'} +$$
$$\sum_{m'} \varpi_{m'}(1 + a_1(\iota_1\xi_m\xi_{m'} + \iota_2\eta_m\eta_{m'} - \iota_3\mu_m\mu_{m'})B_p^{m'} +$$
$$\sum_{m'} \varpi_{m'}(1 + a_1(\iota_1\xi_m\xi_{m'} - \iota_2\eta_m\eta_{m'} - \iota_3\mu_m\mu_{m'})C_p^{m'} +$$
$$\sum_{m'} \varpi_{m'}(1 + a_1(\iota_1\xi_m\xi_{m'} - \iota_2\eta_m\eta_{m'} + \iota_3\mu_m\mu_{m'})D_p^{m'} + \qquad \text{(C.6)}$$
$$\sum_{m'} \varpi_{m'}(1 + a_1(-\iota_1\xi_m\xi_{m'} + \iota_2\eta_m\eta_{m'} + \iota_3\mu_m\mu_{m'})E_p^{m'} +$$
$$\sum_{m'} \varpi_{m'}(1 + a_1(-\iota_1\xi_m\xi_{m'} + \iota_2\eta_m\eta_{m'} - \iota_3\mu_m\mu_{m'})F_p^{m'} +$$
$$\sum_{m'} \varpi_{m'}(1 + a_1(-\iota_1\xi_m\xi_{m'} - \iota_2\eta_m\eta_{m'} - \iota_3\mu_m\mu_{m'})G_p^{m'} +$$
$$\sum_{m'} \varpi_{m'}(1 + a_1(-\iota_1\xi_m\xi_{m'} - \iota_2\eta_m\eta_{m'} + \iota_3\mu_m\mu_{m'})H_p^{m'}]$$

where the expressions ι_1, ι_2, and ι_3 symbolize the direction of the axis coordinate when a different source function needs to be evaluated. For instance, to evaluate the source function at octant B, the above sign expressions must be, $\iota_1 = 1$, $\iota_2 = 1$, and $\iota_3 = -1$.

For isotropic radiation, the octal source functions could be replaced by one function that adds all the intensities.

C.3 Biangular Reflectance Boundary

The discrete boundary conditions can be formulated as

$$I^m(r,\Omega) = \sum_{\substack{m' \\ \xi_{m'} < 0}} \varpi_{m'}\xi_{m'}\rho''(r,m',m)I^{m'} \qquad x = 0 \qquad \text{(C.7)}$$

$$I^m(r,\Omega) = \sum_{\substack{m' \\ \xi_{m'} > 0}} \varpi_{m'}\xi_{m'}\rho''(r,m',m)I^{m'} \qquad x = AL \qquad \text{(C.8)}$$

$$I^m(r,\Omega) = \sum_{\substack{m' \\ \eta_{m'} < 0}} \varpi_{m'}\eta_{m'}\rho''(r,m',m)I^{m'} \qquad y = 0 \qquad \text{(C.9)}$$

$$I^{m}(r,\Omega)=\sum_{\substack{m' \\ \eta_{m'}>0}} \varpi_{m'}\eta_{m'}\rho''(r,m',m)I^{m'} \qquad y = BL \qquad (C.10)$$

$$I^{m}(r,\Omega)=\sum_{\substack{m' \\ \mu_{m'}<0}} \varpi_{m'}\mu_{m'}\rho''(r,m',m)I^{m'} \qquad z = 0 \qquad (C.11)$$

$$I^{m}(r,\Omega)=\sum_{\substack{m' \\ \mu_{m'}>0}} \varpi_{m'}\mu_{m'}\rho''(r,m',m)I^{m'} \qquad z = CL \qquad (C.12)$$

The term of the right hand side of equations (C.7 - C.12) represents the reflected incoming radiation flux, extended over the 2π incoming directions.

The octal incident and leaving intensities at the west boundary are the intensities pointing at the negative and positive y direction respectively. Thus,

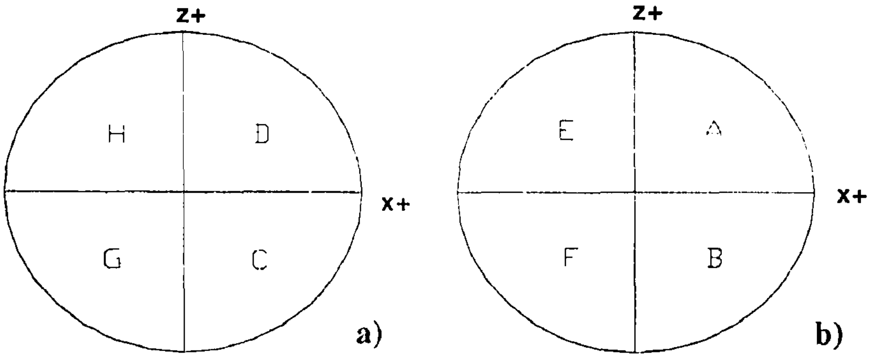

Figure C.3.1 a) Incident and b) Leaving Octal Intensities at the West Boundary Side

For leaving intensity A, Equation 5.8 is transformed into:

$$A_{p}^{m}(r,\Omega)=\sum_{\substack{m' \\ \eta_{m'}<0}} \varpi_{m'}\eta_{m'}\rho''(r_{p},m',m)\left[C_{p}^{m'}+D_{p}^{m'}+G_{p}^{m'}+H_{p}^{m'}\right] \qquad (C.13)$$

where r_p symbolizes that the reflectivity depends also of the octal intensity. Separating the second term of right hand side of equation C.13 into its components, then for the S_4 approximation one obtains

$$\sum_{\substack{m' \\ \eta_{m'}<0}} \varpi_{m'}\eta_{m'}\left[\rho_C(m',m)C_p^{m'} + \rho_D(m',m)D_p^{m'} + \rho_G(m',m)G_p^{m'} + \rho_H(m',m)H_p^{m'}\right] \quad \text{(C.14)}$$

expanding for all leaving and incident directions, one obtains

for m'=1..3, m=1,

$$\begin{aligned}
&\rho_C(1,1).\varpi_1\eta_1C_p^1 + \rho_D(1,1).\varpi_1\eta_1D_p^1 + \rho_G(1,1).\varpi_1\eta_1G_p^1 + \rho_H(1,1).\varpi_1\eta_1H_p^1 && + \\
&\rho_C(2,1).\varpi_2\eta_2C_p^2 + \rho_D(2,1).\varpi_2\eta_2D_p^2 + \rho_G(2,1).\varpi_2\eta_2G_p^2 + \rho_H(2,1).\varpi_2\eta_2H_p^2 && + \\
&\rho_C(3,1).\varpi_3\eta_3C_p^3 + \rho_D(3,1).\varpi_3\eta_3D_p^3 + \rho_G(3,1).\varpi_3\eta_3G_p^3 + \rho_H(3,1).\varpi_3\eta_3H_p^3 && = sA1
\end{aligned}$$

for m'=1..3, m=2,

$$\begin{aligned}
&\rho_C(1,2).\varpi_1\eta_1C_p^1 + \rho_D(1,2).\varpi_1\eta_1D_p^1 + \rho_G(1,2).\varpi_1\eta_1G_p^1 + \rho_H(1,2).\varpi_1\eta_1H_p^1 && + \\
&\rho_C(2,2).\varpi_2\eta_2C_p^2 + \rho_D(2,2).\varpi_2\eta_2D_p^2 + \rho_G(2,2).\varpi_2\eta_2G_p^2 + \rho_H(2,2).\varpi_2\eta_2H_p^2 && + \\
&\rho_C(3,2).\varpi_3\eta_3C_p^3 + \rho_D(3,2).\varpi_3\eta_3D_p^3 + \rho_G(3,2).\varpi_3\eta_3G_p^3 + \rho_H(3,2).\varpi_3\eta_3H_p^3 && = sA2
\end{aligned}$$

for m'=1..3, m=3

$$\begin{aligned}
&\rho_C(1,3).\varpi_1\eta_1C_p^1 + \rho_D(1,3).\varpi_1\eta_1D_p^1 + \rho_G(1,3).\varpi_1\eta_1G_p^1 + \rho_H(1,3).\varpi_1\eta_1H_p^1 && + \\
&\rho_C(2,3).\varpi_2\eta_2C_p^2 + \rho_D(2,3).\varpi_2\eta_2D_p^2 + \rho_G(2,3).\varpi_2\eta_2G_p^2 + \rho_H(2,3).\varpi_2\eta_2H_p^2 && + \\
&\rho_C(3,3).\varpi_3\eta_3C_p^3 + \rho_D(3,3).\varpi_3\eta_3D_p^3 + \rho_G(3,3).\varpi_3\eta_3G_p^3 + \rho_H(3,3).\varpi_3\eta_3H_p^3 && = sA3
\end{aligned}$$

$$A_p^m = sA1 + sA2 + sA2 \quad \text{(C.15)}$$

The same development is done for intensities B, E, and F.

Thus, the biangular reflectance distribution function for the octal intensity A can be represented as a square matrix

$$\rho_A(\Omega_{3'},\Omega_3)_i = \begin{bmatrix} (1,1) & (1,2) & (1,3) \\ (2,1) & (2,2) & (2,3) \\ (3,1) & (3,2) & (3,3) \end{bmatrix} \quad \text{(C.16)}$$

with i representing the respective incident intensity The rest of boundary conditions follows the above procedure and are re-written as

<u>West Boundary</u> (y=0)

$$I_p^m(r,\Omega)=\sum_{\substack{m' \\ \eta_{m'}<0}} \varpi_{m'}\eta_{m'}\left[\rho_{wC}^{m',m} C_p^{m'}+\rho_{wD}^{m',m} D_p^{m'}+\rho_{wG}^{m',m} G_p^{m'}+\rho_{wH}^{m',m} H_p^{m'}\right] \tag{C.17}$$

where $I_p^m(r,\Omega)\mapsto A_w^m, B_w^m, E_w^m, F_w^m$

<u>East Boundary</u> (y=BL)

$$I_p^m(r,\Omega)=\sum_{\substack{m' \\ \eta_{m'}<0}} \varpi_{m'}\eta_{m'}\left[\rho_{eA}^{m',m} A_p^{m'}+\rho_{eB}^{m',m} B_p^{m'}+\rho_{eE}^{m',m} E_p^{m'}+\rho_{eF}^{m',m} F_p^{m'}\right] \tag{C.18}$$

where $I_p^m(r,\Omega)\mapsto C_e^m, D_e^m, G_e^m, H_e^m$

<u>Back Boundary</u> (x=0)

$$I_p^m(r,\Omega)=\sum_{\substack{m' \\ \xi_{m'}<0}} \varpi_{m'}\xi_{m'}\left[\rho_{bE}^{m',m} E_p^{m'}+\rho_{bF}^{m',m} F_p^{m'}+\rho_{bG}^{m',m} G_p^{m'}+\rho_{bH}^{m',m} H_p^{m'}\right] \tag{C.19}$$

where $I_p^m(r,\Omega)\mapsto A_b^m, B_b^m, C_b^m, D_b^m$

<u>Forward Boundary</u> (x=AL)

$$I_p^m(r,\Omega)=\sum_{\substack{m' \\ \xi_{m'}<0}} \varpi_{m'}\xi_{m'}\left[\rho_{fA}^{m',m} A_p^{m'}+\rho_{fB}^{m',m} B_p^{m'}+\rho_{fC}^{m',m} C_p^{m'}+\rho_{fD}^{m',m} D_p^{m'}\right] \tag{C.20}$$

where $I_p^m(r,\Omega)\mapsto E_f^m, F_f^m, G_f^m, H_f^m$

<u>South Boundary</u> (z=0)

$$I_p^m(r,\Omega)=\sum_{\substack{m' \\ \mu_{m'}<0}} \varpi_{m'}\mu_{m'}\left[\rho_{sB}^{m',m} B_p^{m'}+\rho_{sC}^{m',m} C_p^{m'}+\rho_{sG}^{m',m} G_p^{m'}+\rho_{sF}^{m',m} F_p^{m'}\right] \tag{C.21}$$

where $I_p^m(r,\Omega)\mapsto A_s^m, D_s^m, E_s^m, H_s^m$

<u>North Boundary</u> (z=CL)

$$I_p^m(r,\Omega)=\sum_{\substack{m' \\ \mu_{m'}<0}} \varpi_{m'}\mu_{m'}\left[\rho_{nA}^{m',m}A_p^{m'}+\rho_{nD}^{m',m}D_p^{m'}+\rho_{nE}^{m',m}E_p^{m'}+\rho_{nH}^{m',m}H_p^{m'}\right] \qquad \text{(C.22)}$$

where $I_p^m(r,\Omega)\mapsto B_n^m, C_n^m, F_n^m, G_n^m$

C.4 Specularly Reflecting Boundary

The treatment of specularly reflecting, diffusively emitting opaque boundary conditions is formulated by taking into account the incoming direction intensity for the respective octant that will produce a specular reflection at the octal concerning the boundary and summing all contributions for diffuse reflection.

At the west boundary wall, intensity A is formulated as:

$$A_w^m=\varepsilon I_b+\rho^s H_p^m+\frac{\rho^d}{\pi}\sum_{\substack{m' \\ \eta_{m'}<0}} \varpi_{m'}\eta_{m'}\left[C_p^{m'}+D_p^{m'}+G_p^{m'}+H_p^{m'}\right] \qquad \text{(C.22)}$$

where intensity H_p^m is the intensity that will produce a specular reflection leaving in direction of A_w^m. By looking at Figure C.3.1, it is seen that any particular leaving direction from the A intensity, the incident specular ray must had came from the respective direction of intensity B in octant 2 on the plane x+, z+. However, intensity B is an intensity leaving the west boundary, as shown in Figures C.3.1 and C.4.1. The only way a specular reflection can leave through intensity A is by looking at the opposite octant of B. In this case is H. Following this mechanism; the other specular striking intensities can be calculated for the rest of the 4 intensities that leave the west boundary. Thus,

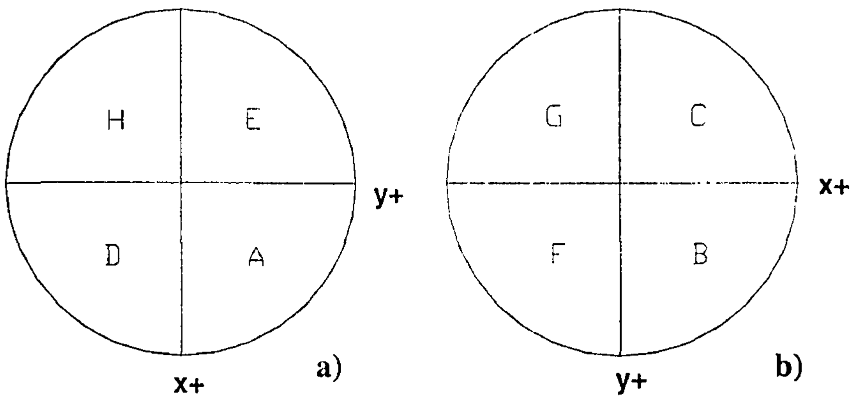

Figure C.4.1 Octal intensity distribution seen through a) top plane (z+) and b) bottom plane (z-)

$$\left[A_w^m, B_w^m, E_w^m, F_w^m\right] = \varepsilon I_b + \rho_w^s\left[H_p^m, G_p^m, D_p^m, C_p^m\right] + \frac{\rho_w^d}{\pi}\sum_{\substack{m' \\ \eta_{m'}<0}} \varpi_{m'}\eta_{m'}\left[C_p^{m'} + D_p^{m'} + G_p^{m'} + H_p^{m'}\right] \tag{C.23}$$

<u>East Boundary</u> (y=BL)

$$\left[C_e^m, D_e^m, E_e^m, H_e^m\right] = \varepsilon I_b + \rho_e^s\left[F_p^m, E_p^m, D_p^m, A_p^m\right] + \frac{\rho_e^d}{\pi}\sum_{\substack{m' \\ \eta_{m'}<0}} \varpi_{m'}\eta_{m'}\left[A_p^{m'} + B_p^{m'} + E_p^{m'} + F_p^{m'}\right] \tag{C.24}$$

<u>Back Boundary</u> (x=0)

$$\left[A_b^m, B_b^m, C_b^m, D_b^m\right] = \varepsilon I_b + \rho_b^s\left[E_p^m, F_p^m, G_p^m, H_p^m\right] + \frac{\rho_b^d}{\pi}\sum_{\substack{m' \\ \xi_{m'}<0}} \varpi_{m'}\xi_{m'}\left[E_p^{m'} + F_p^{m'} + G_p^{m'} + H_p^{m'}\right] \tag{C.25}$$

<u>Forward Boundary</u> (x=AL)

$$\left[E_f^m, F_f^m, G_f^m, H_f^m\right] = \varepsilon I_b + \rho_f^s\left[A_p^m, B_p^m, C_p^m, D_p^m\right] + \frac{\rho_f^d}{\pi}\sum_{\substack{m' \\ \xi_{m'}<0}} \varpi_{m'}\xi_{m'}\left[A_p^{m'} + B_p^{m'} + C_p^{m'} + D_p^{m'}\right] \tag{C.26}$$

<u>South Boundary</u> (z=0)

$$\left[A_s^m, D_s^m, E_s^m, H_s^m\right] = \varepsilon I_b + \rho_s^s \left[B_p^m, C_p^m, F_p^m, G_p^m\right]$$
$$+\frac{\rho_s^d}{\pi} \sum_{\substack{m' \\ \mu_{m'}<0}} \varpi_{m'} \mu_{m'} \left[B_p^{m'} + C_p^{m'} + F_p^{m'} + G_p^{m'}\right] \tag{C.27}$$

<u>North Boundary</u> (z=CL)

$$\left[B_n^m, C_n^m, F_n^m, G_n^m\right] = \varepsilon I_b + \rho_s^s \left[A_p^m, D_p^m, E_p^m, H_p^m\right]$$
$$+\frac{\rho_s^d}{\pi} \sum_{\substack{m' \\ \mu_{m'}<0}} \varpi_{m'} \mu_{m'} \left[A_p^{m'} + D_p^{m'} + E_p^{m'} + H_p^{m'}\right] \tag{C.28}$$

C.5 Collimated Irradiation

Considering the problem of a collimated incident flux of magnitude q_o incident on a medium with suspended particles (or fibers) having a relative refractive index of unity with respect to the surrounding boundaries as depicted in figure C.5.1.

The direction of incidence is given by the coordinate system (ξ_o, η_o, μ_o). Treating the collimated irradiation flux as a source term in the transfer equation then $q_o \exp\left(\int \beta d(C_L - z)\right)$ is the attenuated flux at any specific depth. The contribution to the scattered radiation field in the direction (ξ_o, η_o, μ_o) is [95,96]

$$Sc = \frac{\sigma_s}{4\pi} P(\Omega' \to \Omega) q_o \exp\left(\int \beta d(C_L - z)\right) \tag{C.29}$$

and the RTE becomes

$$(\Omega \bullet \nabla) I_\lambda(r,\Omega) = -(\kappa_\lambda + \sigma_{s\lambda}) I_\lambda(r,\Omega) + \kappa_\lambda I_b(r) +$$
$$\frac{\sigma_{s\lambda}}{4\pi} \int_{\Omega' \to 4\pi} I_\lambda(r,\Omega) P(\Omega' \to \Omega) d\Omega' + Sc \tag{C.30}$$

Discretizing the above equation leads to the same octal equations as shown before except that the source function will have the collimated term to be evaluated. Since the intensity was spilt into eight octants the collimated incident flux of magnitude q_o must also be divided into the same number of octants. Thus, equation 5.15 is transformed into:

$$S_{ip}^{m} = \kappa I_b + \frac{\sigma_s}{4\pi}[\sum_{m'} \varpi_{m'}(1 + a_1(\xi_m \xi_{m'} + \eta_m \eta_{m'} + \mu_m \mu_{m'})).$$

$$(A_p^{m'} + B_p^{m'} + C_p^{m'} + D_p^{m'} + E_p^{m'} + F_p^{m'} + G_p^{m'} + H_p^{m'})] +$$

$$\frac{\sigma_s}{4\pi}\left({q_o}\big/{8} \right)\exp\left(\int \beta d(C_L - z) \right)\left((1 + a_1(\xi_m \xi_o + \eta_m \eta_o + \mu_m \mu_o) \right) \quad \text{(C.31)}$$

The last term in equation C.31 is the source function due to the collimated irradiation flux. Where i represent the octal intensity (from A to H) in discussion. Equation C.31 must be set for each one of the eight octal intensities in order to account for the angular variation in linear anisotropic phase function.

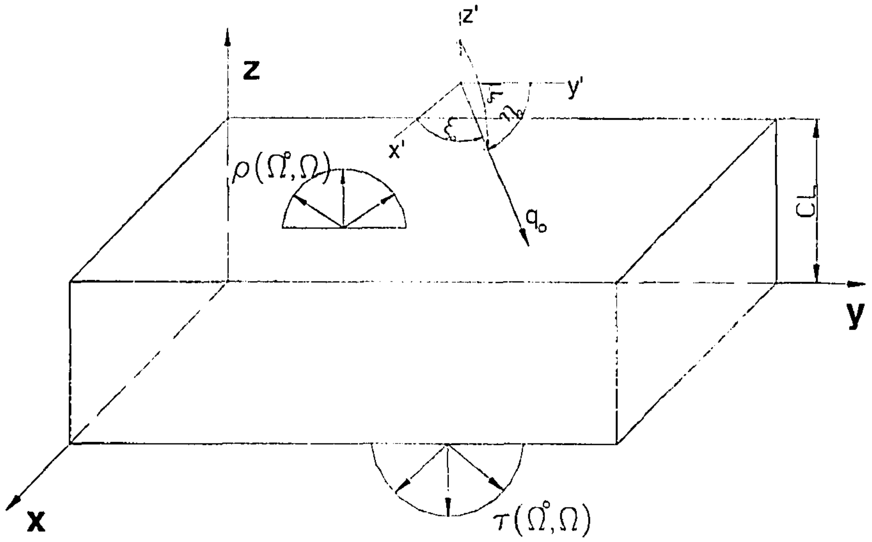

Figure C.5.1 Three-dimensional Medium Subject to Collimated Mono-directional Flux

For instance, the source function for octant A is written as:

$$
\begin{aligned}
SA_p^m = \kappa I_b(r,T) + \frac{\sigma_s}{4\pi}[\sum_{m'} \varpi_{m'}(1 + a_1(\iota_1\xi_m\xi_{m'} + \iota_2\eta_m\eta_{m'} + \iota_3\mu_m\mu_{m'})A_p^{m'} + \\
\sum_{m'} \varpi_{m'}(1 + a_1(\iota_1\xi_m\xi_{m'} + \iota_2\eta_m\eta_{m'} - \iota_3\mu_m\mu_{m'})B_p^{m'} + \\
\sum_{m'} \varpi_{m'}(1 + a_1(\iota_1\xi_m\xi_{m'} - \iota_2\eta_m\eta_{m'} - \iota_3\mu_m\mu_{m'})C_p^{m'} + \\
\sum_{m'} \varpi_{m'}(1 + a_1(\iota_1\xi_m\xi_{m'} - \iota_2\eta_m\eta_{m'} + \iota_3\mu_m\mu_{m'})D_p^{m'} + \\
\sum_{m'} \varpi_{m'}(1 + a_1(-\iota_1\xi_m\xi_{m'} + \iota_2\eta_m\eta_{m'} + \iota_3\mu_m\mu_{m'})E_p^{m'} + \\
\sum_{m'} \varpi_{m'}(1 + a_1(-\iota_1\xi_m\xi_{m'} + \iota_2\eta_m\eta_{m'} - \iota_3\mu_m\mu_{m'})F_p^{m'} + \\
\sum_{m'} \varpi_{m'}(1 \div a_1(-\iota_1\xi_m\xi_{m'} - \iota_2\eta_m\eta_{m'} - \iota_3\mu_m\mu_{m'})G_p^{m'} + \\
\sum_{m'} \varpi_{m'}(1 + a_1(-\iota_1\xi_m\xi_{m'} - \iota_2\eta_m\eta_{m'} + \iota_3\mu_m\mu_{m'})H_p^{m'}] + \\
\frac{\sigma_s}{4\pi}\left(q_o/8\right)\exp\left(\int \beta d(C_L - z)\right) * [\sum_{m'} \varpi_{m'}(1 + a_1(\iota_1\xi_m\xi_o + \iota_2\eta_m\eta_o + \iota_3\mu_m\mu_0) + \\
\sum_{m'} \varpi_{m'}(1 + a_1(\iota_1\xi_m\xi_o + \iota_2\eta_m\eta_o - \iota_3\mu_m\mu_o) + \\
\sum_{m'} \varpi_{m'}(1 + a_1(\iota_1\xi_m\xi_o - \iota_2\eta_m\eta_o - \iota_3\mu_m\mu_o) + \\
\sum_{m'} \varpi_{m'}(1 + a_1(\iota_1\xi_m\xi_o - \iota_2\eta_m\eta_o + \iota_3\mu_m\mu_o) + \\
\sum_{m'} \varpi_{m'}(1 + a_1(-\iota_1\xi_m\xi_o + \iota_2\eta_m\eta_o + \iota_3\mu_m\mu_o) + \\
\sum_{m'} \varpi_{m'}(1 + a_1(-\iota_1\xi_m\xi_o + \iota_2\eta_m\eta_{m'} - \iota_3\mu_m\mu_o) + \\
\sum_{m'} \varpi_{m'}(1 + a_1(-\iota_1\xi_m\xi_o - \iota_2\eta_m\eta_o - \iota_3\mu_m\mu_o) + \\
\sum_{m'} \varpi_{m'}(1 + a_1(-\iota_1\xi_m\xi_o - \iota_2\eta_m\eta_o + \iota_3\mu_m\mu_o)]
\end{aligned}
\tag{C.32}
$$

where the expressions ι_1, ι_2, and ι_3 symbolize the direction of the axis coordinate when a different source function needs to be evaluated as done previously.

APPENDIX D

FIRE BARRIER PROBLEM

D.1 Fire Barrier Assessment

Fluent 6.0 is general-purpose computational fluid dynamics (CFD) and computational heat transfer software with unique capabilities in unstructured, finite volume based solvers which are near-ideal in parallel performance. Two years ago, the School of Aerospace and Mechanical Engineering adopted this software as a standard for the sequence of graduate courses in fluids and heat transfer. Recently, a discrete ordinates solver has been added to solve for participating radiation. In solving problems of the type contained in this dissertation, it should be noted that a number of features of the code are marginally documented. It should also be noted that variable properties require the use of Microsoft® .NET C-compiler for Windows® PC platforms.

This commercial software has been used to predict the transient combined heat transfer in a inverted L-shaped geometry fire barrier with full dimensions given in Chapter 5. This problem possesses the following characteristics:

Geometry:

- 768 nodes, 625 quadrilateral Elements, 7 Zones (3 Faces)

Boundary conditions:

- Fire Wall (Horizontal & Vertical) Mixed Boundaries (Convection-Radiation)

  $h = 0.044 * (\Delta T)^{0.333} / 5.677$ [W/m²/K]

  $$T = \left((80.0 + 460 + 1350 * \left(1 - \exp^{\left[-3.79533\sqrt{t/3600}\right]} \right) + 306.74 * \sqrt{t/3600}) \right) / 1.8 \text{ [K]}$$

- Unexposed Wall (Horizontal & Vertical) Mixed Boundaries (Convection-Radiation)

  $h = 0.044 * (\Delta T)^{0.333} / 5.677$ W/m²/K

  T = 313 [K]

Time Step Conditions

- Time step size(s) 108
- Number time of steps 100
- Iteration per step size 10000

Material parameters:

- Durablanket® S
    - Density 128 kg/m3
    - Specific Heat 1130 J/kg-K
    - Thermal Conductivity 0.2 W/mK
    - Absorption Coefficient 291.84 1/m
    - Scattering Coefficient 4572.16 1/m
    - Scattering Phase Function: Linear Anisotropic 0.12
- Aluminum
    - Density 2719 kg/m3
    - Specific Heat 871 J/kg-K
    - Thermal Conductivity 202.4 W/mK
    - Absorption Coefficient 0.01 1/m
    - Thickness 0.00041 m
    - Emissivity 0.03

C.6.1 Additional Result

When the fire is located at the inside of the fire barrier, the hot "spots" are located away from the corner of the geometry after 3 hours of fire, as shown in Figure D.1. There is a cold "spot" opposite the fire in the corner. For outside fire, this would be the hot "spot".

The figure shows that the longer plates are the weakest points of the barrier for these conditions. This analysis might result in redesign, based on the requirements of the barrier and the geometry.

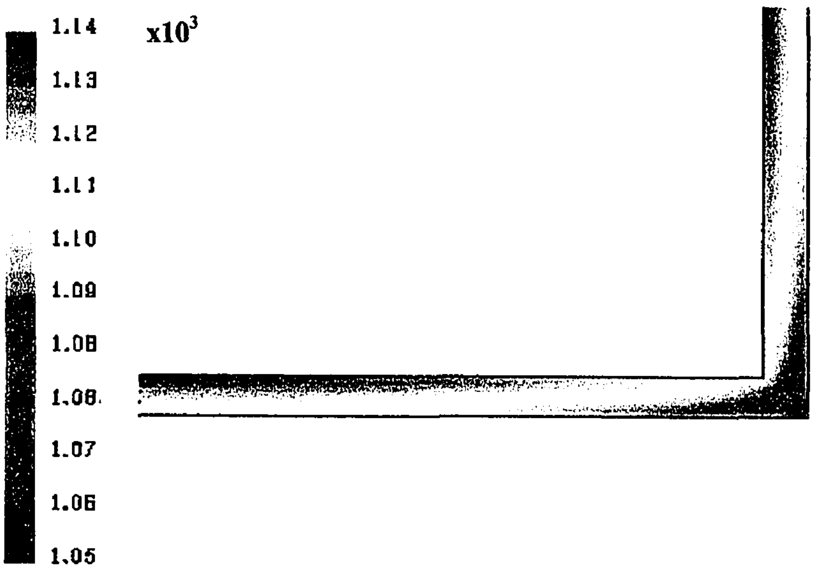

Figure D.1 Total Temperature Color Contour Plot, (t=3h)